A New Method of Mapping Cosmic Flow Fields: Evaluating the Suitability of the Infrared bands Tully-Fisher Relation for ZoA Work

Affadi Ikechukwu Patrick

January 2015

Declaration of Authorship

I, Affadi Ikechukwu Patrick, declare that this thesis titled, "A New Method of Mapping Cosmic Flow Fields: Evaluating the Suitability of the Infrared bands Tully-Fisher Relation for ZoA Work" and the work presented in it are my own. I confirm that:

- This work was done wholly or mainly while in candidature for a research degree at this University.
- Where any part of this thesis has previously been submitted for a degree or any other qualification at this University or any other institution, this has been clearly stated.
- Where I have consulted the published work of others, this is always clearly attributed.
- Where I have quoted from the work of others, the source is always given. With the exception of such quotations, this thesis is entirely my own work.
- I have acknowledged all main sources of help.
- Where the thesis is based on work done by myself jointly with others, I have made clear exactly what was done by others and what I have contributed myself.

Signed by candidate

Signed: Signature Removed

Date: 4^{th} of March 2014

"Human beings are awesome, if you teach them to do good they will do good."

Prof. Affadi Ikechukwu Patrick

UNIVERSITY OF CAPE TOWN

Abstract

Faculty of Science
Department of Astronomy

Masters of Astrophysics & Space Science

by Affadi Ikechukwu Patrick

This thesis aims at using the Infrared Survey Facility (IRSF) JHK_s bands, Two Micron All Sky Survey (2MASS) JHK_s bands and Wide Field Infrared Survey Explorer (WISE) W1-W4 bands isophotal magnitudes to understand the cosmic flow associated with Zone of Avoidance (ZoA) galaxies. We started with determining the Galactic absorption associated with 2MASS JHK_s bands and WISE W1-W4 bands. We found that the K_s band Galactic absorption is about $\sim$ 8.8 % of the Galactic absorption in the B band, while the WISE bands Galactic absorption is $\lesssim$ 1.0 % of the Galactic absorption in the B band. We found that the maximum additional correction to isophotal magnitudes for foreground extinction levels of $A_B = 1^{\rm m}$ for J, H, K_s, WISE W1 and W2 bands spiral galaxy magnitudes are $1^{\rm m}.20 \pm 0^{\rm m}.010$, $0^{\rm m}.55 \pm 0^{\rm m}.010$, $0^{\rm m}.30 \pm 0^{\rm m}.010$, $0^{\rm m}.02 \pm 0^{\rm m}.001$ & $0^{\rm m}.035 \pm 0^{\rm m}.001$ respectively. The radii correction to isophotal magnitudes for foreground extinction levels of $A_B = 1^{\rm m}$ for J, H, K_s, WISE W1 and W2 bands spiral galaxy magnitudes are 3.55 $\pm$ 0.01, 2.00 $\pm$ 0.01, 1.50 $\pm$ 0.01, 1.14 $\pm$ 0.01 & 1.12 $\pm$ 0.01 respectively. We found that different morphological types of spiral galaxies are affected differently by Galactic absorption. Therefore, Galactic absorption corrections are important in ZoA galaxies magnitudes corrections especially for IRSF and 2MASS JHK_s bands, for WISE bands these effects are small. Using the IRSF K_s, 2MASS K_s and WISE W1 and W2 bands isophotal magnitudes with the Tully-Fisher relation calibrations of Said (2013) for the K_s band, Lagattuta et al. (2013); Sorce et al. (2013) and Cosmic Flow Program calibrations of Neill et al. (2014) for WISE W1 band and Cosmic Flow Program calibrations of Neill et al. (2014) for WISE W2 band. We observed that the cosmic flow associated with density distribution in the ZoA galaxies arises from two major flow. An inflow into the Great Attractor and an outflow into a more massive concentration. This massive concentration is not within the ZoA covered by this work, but have been identified by other authors to be Shapley supercluster.

The major source of the density distribution in the ZoA are mostly associated with the region around the Great Attractor ($l = 307^{\circ}.0$, $b = 9^{\circ}.0$), the region near Puppis cluster ($240^{\circ}.0$, $0^{\circ}.0$) and the region between Hydra ($270^{\circ}.0$, $+27^{\circ}.0$) and Antlia ($273^{\circ}.0$, $+19^{\circ}.0$) clusters. We also found that the Great Attractor is the primary over density strongly influencing the motion of galaxies in the ZoA region. We have also shown that cosmic flow associated with the ZoA galaxies can well be approximated by the peculiar velocity model of the Local Universe. In general, WISE W1 and W2 bands as compared to near-infrared IRSF JHK_s and 2MASS JHK_s bands provide the best bands for mapping flow field analysis for density distribution in the ZoA region due to small effect of extinction.

Acknowledgements

I would like to thank my God for his strength, wisdom, guidance and protection throughout my stay in South Africa. Special thank to my supervisor Prof. Renée C. Kraan-Korteweg and my co-supervisor Prof. Thomas Jarrett for their constructive advice throughout this project work. I would like to thank Dr. Christina Magoulas who assisted in preparing the faint WISE photometry and all those who in one way or the other have contributed to the success of this project. Also, I would like to appreciate my family for their support and understanding, your love kept me going. Big thanks to my classmates and the entire management of National Astrophysics and Space Science Programme (NASSP) you gave me the step-up that I needed in life. ...

Contents

List of Figures

List of Tables

Abbreviations

2dFGRS	**2dF G**alaxy **R**edshift **S**urvey
2MASS	**2** Micron **A**ll **S**ky **S**urvey
CfA	**C**enter **f**or **A**strophysics
CMB	**C**osmic **M**icrowave **B**ackground
COBE	**CO**smic **B**ackground **E**xplorer
ESO	**E**uropean **S**outhern **O**bservatory
HEALPIX	**H**ierarchical **E**qual **A**rea **I**so **L**atitude **PIX**elation
HIZoA	**HI Z**one **o**f **A**voidance
IRAC	**I**nfra**R**ed **A**rray **C**amera
IRAS	**I**nfra**R**ed **A**stronomical **S**atelite
IRSF	**I**nfra**R**ed **S**urvey **F**acility
IPAC	**I**nfrared **P**rocessing **A**stronomical **C**enter
ISM	**I**nter**S**tellar **M**edium
LAMBDA	**L**agacy **A**rchive for **M**icrowave **B**ackground **D**ata **A**nalysis
NGC	**N**ew **G**eneral **C**atalogue
NED	**N**ASA/IPAC **E**xtragalactic **D**atabase
PAH	**P**olycyclic **A**romatic **H**ydrocarbon
POSS	**P**alomar **O**bservatory **S**ky **S**survey
SAAO	**S**outh **A**frica **A**stronomical **O**bservatory
SDSS	**S**loan **D**igital **S**ky **S**urvey
SIRIUS	**S**imultaneous **I**nfra**R**ed **I**mager for **U**nbaised **S**urvey
SINGS	**S**pitzer **I**nfrared **N**earby **G**alaxies **S**urvey
WISE	**W**ide-field **I**nfrared **S**urvey **E**xplorer
ZoA	**Z**one **o**f **A**voidance

Physical Constants

Speed of Light	c	=	2.998×10^8 m s^{-1}
Hubble Constant	H_0	=	$100\ h$ km s^{-1} Mpc^{-1}
Electron Volt	eV	=	1.602×10^{-12} erg
Avogadro's Number	N_A	=	6.022×10^{23}
Earth Radius	$R_\oplus$	=	6.378×10^8 cm
Earth Mass	$M_\oplus$	=	5.974×10^{27} g
Solar Mass	$M_\odot$	=	1.989×10^{33} g
Solar Luminosity	$L_\odot$	=	3.939×10^{33} erg s^{-1}
Solar Temperature	$T_\odot$	=	5.780×10^3 K
Parsec	pc	=	3.086×10^{18} cm
Light-Year	ly	=	9.461×10^{17} cm
Year	yr	=	3.156×10^7 s
Astronomical Unit	AU	=	1.496×10^{13} cm
Planck's Constant	h	=	6.626×10^{-27} erg s
Gravitational Constant	G	=	6.674×10^{-8} cm^3 g^{-1} s^{-2}

Symbols

d	distance	m
ω	angular frequency	rad s^{-1}
R	radius	arcsec
λ	wavelength	cm
b	galactic latitude	deg
l	galactic longitude	deg
F	flux	Jy km s^{-1}
I	intensity	W m^{-3} sr^{-1}
m	apparent magnitude	mag
M	absolute magnitude	mag
μ	surface brightness	mag $arcsec^{-2}$
W	line width	km s^{-1}
V	velocity	km s^{-1}

Dedicated to Mom and Dad ...

Chapter 1

Introduction

The application of the theory of general relativity to large-scale structures of the Universe lead to various cosmological theories and postulates. Most of these cosmological theories are based on a local unverifiable assumptions (Ellis, 1975). One of such cosmological assumptions is the Cosmological Principle. The cosmological principle states that, on sufficiently large scale the Universe is homogeneous and isotropic, in other words there is no preferred direction or preferred place in the Universe (Ellis, 1975). This is not clearly true for scales less than 100 h^{-1} Mpc. Observations of large-scale structures in the Universe have shown that galaxies in the Universe are not uniformly distributed in space. Galaxy redshift survey from Center for Astrophysics (CfA) in the 80's by Geller & Huchra (1983, 1989), 2dF Galaxy Redshift Survey (2dFGRS) by Colless et al. (2001, 2003), the Sloan Digital Sky Survey (SDSS) by Newman et al. (2004), the current DEEP2 Redshift Survey and the VIMOS-VLT Deep Survey (VVDS) have shown that rich galaxies clusters can be observed to a scale of $\sim$ 100 h^{-1} Mpc. Bulk motion of $\sim$ 600 km s^{-1} relative to the cosmic microwave background (CMB) radiation (Lynden-Bell et al., 1988), for sphere of galaxies and galaxies clusters have been observed to a scale of $\sim$ 100 h^{-1} Mpc. Galaxy redshift survey to a scale of $\sim$ 100 h^{-1} Mpc reveals a netlike or spongy structures and vast regions of relative empty space known as voids, which contain very few galaxies and span the volume in between well known structures in the Universe (Lindner et al., 1995). Particularly, is the high redshift clustering observed in astronomical object such as quasar (Webster, 1982; Komberg et al., 1996; Horvath et al., 2013). All these contributions have become fundamental to our understanding of large-scale structures since structures in the Universe evolve slowly with time.

The major difficulty encountered in the study of the large-scale structure of the Universe is the difficult in mapping the distribution of galaxies and galaxies clusters at low Galactic latitude (Kraan-Korteweg & Juraszek, 2000). The obscuration due to dust in the

optical survey and the high stellar density in the infrared survey result in a substantial Zone of Avoidance (ZoA) and therefore contribute to the uncertainties in our understanding of the dynamics of the local Universe, cosmic flow field and the convergence of the CMB dipole (Kraan-Korteweg & Lahav, 2000; Kraan-Korteweg & Jarrett, 2005). The effect of dust in the low Galactic latitude obscure approximately 20 per cent of the extragalactic sky at optical wavelengths and more than one tenth of the infrared extragalactic sky observed by Infrared Astronomical Satellite (IRAS) (Kraan-Korteweg & Lahav, 2000; Donley et al., 2005). The Milky Way obscures the full extent in the Supergalactic plane (Kraan-Korteweg & Lahav, 2000). The most luminous galaxies clusters such as the Great Attractor, the Puppis clusters and others are inherently known to be bisected by the Galactic plane (Kraan-Korteweg & Lahav, 2000). The detection of new structures in these region affect the cosmic flow as determined from redshift surveys in regions away from the Local Group (Yahil et al., 1991; Lavaux et al., 2010). Thereby, preventing us from fully understanding the origin of the motion of the Local Group with respect to the CMB. The incomplete coverage of the extragalactic sky, limits our understanding of several key issues associated with the distribution of large-scale structures in the Universe. Because the observed large-scale structure depends both on the cosmological parameters and on the formation and evolution of galaxies (Kraan-Korteweg & Lahav, 2000). One approach to overcoming the hindrance in mapping large-scale structures distribution in the Galactic plane is the multi-wavelength observation and study of extragalactic structures in these regions. Recently, enormous effort and observation time have been devoted to establish the extragalactic large-scale structure of the Universe.

1.1 Zone of Avoidance Galaxy Surveys

If we look in the plane of own galaxy, the Milky Way, we will observe bright stars and luminous galaxies obscured by dust. The effect of dust and stellar crowding at low Galactic latitude $|b| < 10^{\circ}$ makes optical observation of extragalactic objects difficult in this region (Kraan-Korteweg & Jarrett, 2005). The obscured region of the night sky beyond the disk of our Galaxy reveal few galaxies: the numerous stars and cloud of dust along the line of sight make their observation at visible wavelength very difficult resulting in the so-called Zone of Avoidance (ZoA) (Kraan-Korteweg & Lahav, 2000).

The first reference to the ZoA was made by Proctor in 1837, based on the distribution of nebulae in the New General Catalogue (NGC) of Nebulae and was defined by Shapley in 1961 as the region delimited by "the isopleth of five galaxies per square degree from Lick and Harvard surveys" (Shapley, 1961; Proctor, 1878). The concept of ZoA was created by Hubble in 1936, where he emphasize that hardly any extragalactic nebulae were found

along the disk of the Milky Way (Hubble, 1936). In recent times, the development of highly sensitive near and mid-infrared detectors, together with spacecraft been launch into outer space to take mid-infrared observations have increasingly help to overcome the shortcomings caused by the ZoA in investigating extragalactic sky beyond the plane of the Milky Way. Several surveys have searched for hidden mass concentration of galaxies in the ZoA, mainly to discover and observe objects beyond it.

1.1.1 Optical Observations

The absorption by dust and the presence of numerous bright stars render optical observation of extragalactic source in the direction of the disk difficult. Therefore, optical galaxy catalogs are mainly limited by Galactic extinction (Kraan-Korteweg, 2000b; Kraan-Korteweg & Jarrett, 2005). In the optical, Hauschildt (1987); Kraan-Korteweg et al. (1994); Weinberger et al. (1995); Seeberger et al. (1996); Lercher et al. (1996); Saurer et al. (1997); Lahav et al. (1998); Kraan-Korteweg (2000b) and others, survey the ZoA and discovered large number of optically visible galaxies in regions of very small opacity. Using the existing optical surveys such as the First and Second Palomar Observatory Sky Survey (POSS I & POSS II) in the northern sky and ESO/SERC[1] surveys in the southern sky. The search of galaxies in the visible wavelength have help to detect quite a few number of galaxies in the ZoA at $A_B \sim 3^{\mathrm{m}}$. Moreover, these search for galaxies in the ZoA have become considerably ineffective at extinction[2] levels of over $A_B = 3^{\mathrm{m}}$ with an apparent diameter[3] of $D = 14''$ (Kraan-Korteweg & Lahav, 2000; Kraan-Korteweg & Jarrett, 2005).

1.1.2 Infrared Observations

As we move from visible light towards longer wavelengths of light, we enter the infrared region. The hot blue stars seen clearly in visible light fade out and cooler stars come into view. Infrared surveys are less affected by dust absorption due to infrared radiation penetrate through dust clouds. In the near-infrared, Deep Near Infrared Survey (DENIS) catalogue (Epchtein et al., 1997) and 2MASS catalogue (Skrutskie et al., 2006; Jarrett et al., 2003) and others have contributed considerably in detecting galaxies in the ZoA. The near-infrared surveys are less affected by dust absorption when compared to optical surveys, thereby reducing the confusion with Galactic objects (Kraan-Korteweg & Jarrett, 2005). 2MASS has considerably reduced the size of the ZoA, especially in the regions away from the Galactic bulge (Jarrett et al., 2000a).

[1] European Southern Observatory (ESO) and Southern Galactic Plane Survey (SERC)
[2] Extinction is explained in Section 1.2.
[3] Apparent diameter is the diameter a galaxy would have if it was obscured.

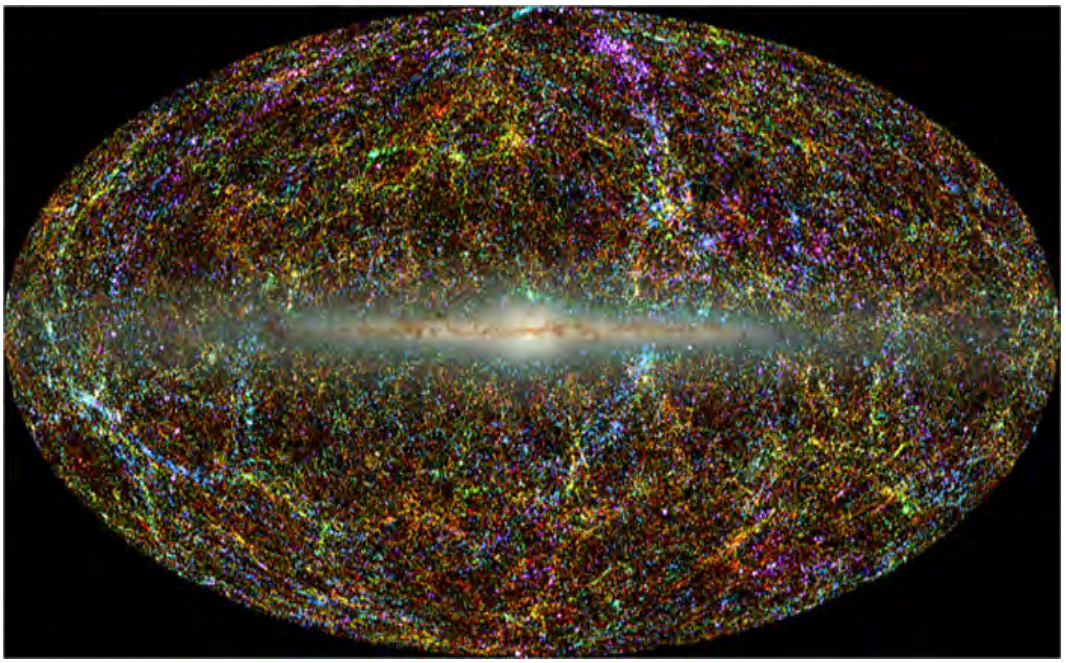

FIGURE 1.1: 2MASS extended source catalog coverage from Cutri et al. (2003). Aitoff projection of more than 1.5 million galaxies from the extended source catalog and nearly 0.5 billion Milky Way stars from the point source catalog color-coded by its redshift z. The galaxy are color-coded by redshift photometrically reduced from K_s band (K-short band). The blue dots are the nearest source ($z < 0.01$), the red dots are the most distant galaxies ($0.04 < z < 0.1$) and the green dots are galaxy at intermediate distance ($0.01 < z < 0.04$).

In the mid & far-infrared, IRAS[4] (Takata et al., 1996), WISE W1 (3.4 μm), W2 (4.6 μm), W3 (12 μm), & W4 (22 μm) bands (Wright et al., 2010), Spitzer (Infrared Array Camera (IRAC) 3.6 μm, 4.5 μm, 5.8 μm & 8 μm) (Werner et al., 2004), this project work and others have also improved the search of galaxies at the highest extinction levels. WISE provide a new window to explore the ZoA with vast improvement over earlier IRAS missions. The mid-infrared of wavelength $\lambda > 5$ μm, is sensitive to the interstellar medium, notably the warm dust continuum and emission from Polycyclic Aromatic Hydrocarbon (PAH) molecules (Wright et al., 2010). The mid-infrared region between 8-24 μm have shown strong emission from PAH molecules and warm dust (Wright et al., 2010). In the far-infrared, the stars have all vanished. Instead we now see very cold matter with temperature of 140 Kelvin or less. Huge cold clouds of gas and dust in our own galaxy as well as in nearby galaxies, glow in the far-infrared light (Wright et al., 2010).

[4]Infrared Astronomy Satellite

1.1.3 X-ray Observations

Exploring X-ray wavelengths, we have the X-ray all-sky survey carried by Uhuru[5] in the energy range 2-20 keV, Ariel V in the energy range 0.3-40 keV, HEAO-1[6] in the energy range 0.2-10 MeV band, R*ö*ntgensatellit (ROSAT) in the energy range 0.1-2.5 keV bands and others. X-ray surveys provide an excellent tool to study the large scale structures in the ZoA, because the Milky Way is transparent to the hard X-ray emission above a few keV and also because rich clusters are strong X-ray emitters (Böhringer et al., 2000; Fabian, 1994; Arnaud, 2005; Johnston et al., 1981). Though, the effect of dust and stellar obscuration are unimportant in the X-ray band, photoelectric absorption of X-ray by Galactic hydrogen atom does limit detection of extragalactic object close to the Galactic plane (Böhringer et al., 2000).

1.1.4 HI Observations

Galaxies in the low Galactic latitude are fully transparent to the 21 cm line radiation of neutral hydrogen as seen in FIGURE 1.2. HI surveys immediately makes available rotational properties of a detected galaxy, which provide insight into the properties of the obscured galaxies such as distance and peculiar velocity of the galaxy used in Tully-Fisher relation. Also, HI observation will be of great value for studying the large scale distribution of dust and galaxies in the Universe. The major setback of HI surveys is the inability to identify early-type galaxies which are tracers of massive groups and clusters, because they are gas-poor (Donley et al., 2005). Also, galaxies close to radio continuum sources and galaxies with very low velocity extragalactic source might be missed due to strong Galactic emission (Donley et al., 2005).

HI observation in the ZoA by Staveley-Smith et al. (1998); Donley et al. (2005); Doyle et al. (2005); Henning et al. (1998) and others led to the HI Zone of Avoidance (HIZoA) galaxies. This was done using radio telescope like the 25 m Dwingeloo in the northern ZoA sky, and the 64 m Parkes deep radio telescope in the southern ZoA sky. FIGURE 1.3 & 1.4 shows the whole sky distribution of HI detected galaxies by Meyer et al. (2004). The dots in FIGURE 1.3 & 1.4 are galaxies color-coded based on their velocity. The solid lines are the equatorial coordinates, the dotted lines are the Galactic coordinates and the thick solid line is the supergalactic plane.

[5] also known as Small Astronomical Satellite 1 (SAS-1)
[6] High Energy Astronomy Observatories

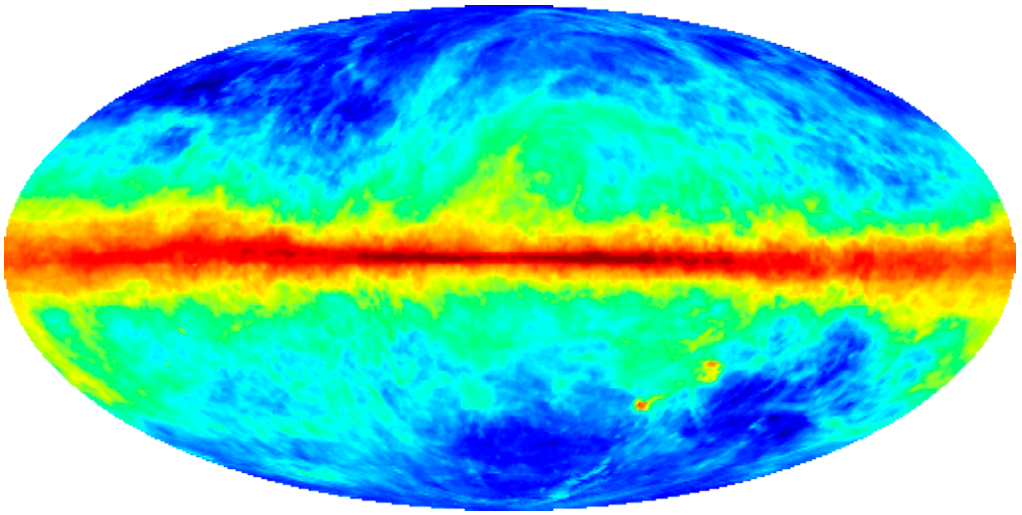

FIGURE 1.2: The Hierarchical Equal Area Iso Latitude Pixelation (HEALPIX) resampling of Leiden/Argentine/Bonn (LAB) survey of Galactic HI. Kalberla et al. (2005) observations of 21 cm emission from Galactic neutral hydrogen over the entire sky obtained from Lagacy Archive for Microwave Background Data Analysis (LAMBDA).

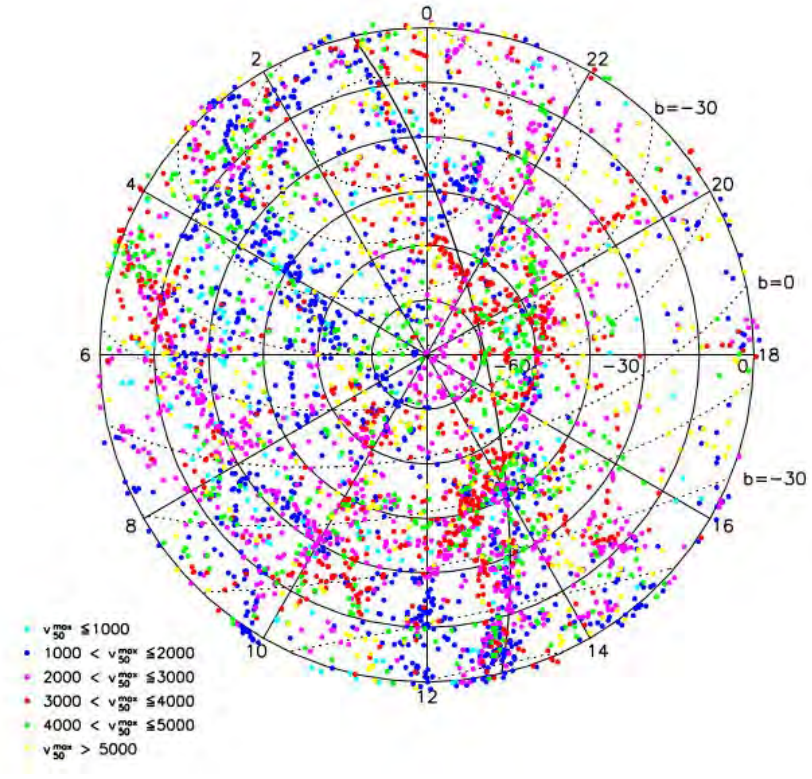

FIGURE 1.3: Polar projection of HI catalogue from Meyer et al. (2004). Objects are color-coded based on their velocity. The solid lines are the equatorial coordinates, the dotted lines are the Galactic coordinates and the thick solid line is the supergalactic plane.

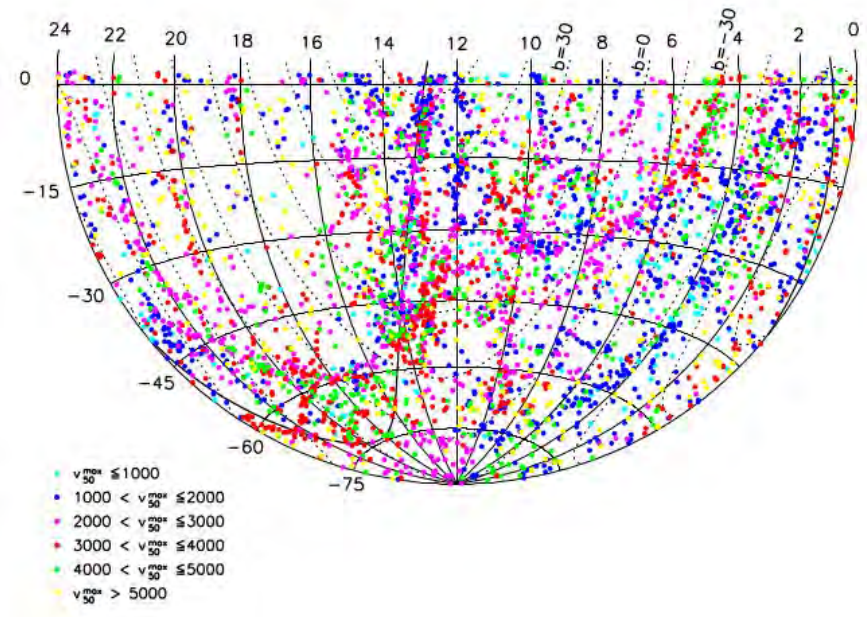

FIGURE 1.4: Aitoff projection of HI catalogue from Meyer et al. (2004). Objects are color-coded based on their velocity. The solid lines are the equatorial coordinates, the dotted lines are the Galactic coordinates and the thick solid line is the supergalactic plane.

1.1.4.1 HI Line Profile

The line profile of a galaxy is the HI line flux over the frequency range which corresponds to the radial velocities of all the HI atoms in the galaxy (Ewen & Purcell, 1951). The width of the HI profile are mostly measured at 20 per cent (W_{20}) or 50 per cent (W_{50}) of either mean or peak flux. The width parameter can be used to estimate the maximum rotational velocity of the gas in a galaxy, since for disk galaxies the 50 per cent linewidth $W_{50} = 2V_{max} \sin i$. The systemic velocity of the galaxy in km s^{-1} can be calculated from the midpoint of the HI line profile and can be used to make an estimate of the redshift-distance using Hubble's law. The total HI line flux integrated over the signal in Jy km s^{-1} can be used to obtain the total HI mass. The observed width of HI line profile gives the Doppler broadening which is due to the galaxy rotation. Also the total dynamical mass of a galaxy can be estimated from the width parameters, in combination with the galaxy's size and inclination (Juraszek et al., 2000; Staveley-Smith et al., 1996; Juraszek et al., 2000). The HI line profile used in this work have varied shape with a few displaying an asymmetric line profile. Some of the HI profile have double horn shape, some have a Gaussian shape while others have a peculiar features in them. As an example FIGURE 1.5 shows a double horn HI profile of J0741-22 with W_{50} linewidth of 466 ± 9 km s^{-1} and W_{20} linewidth of 510 ± 13 km s^{-1} and a recessional velocity of

3073 ± 4 km s^{-1}. The double horn profile makes it a suitable candidate for cosmic flow analysis, because it is an indication of a large inclined spiral galaxy.

FIGURE 1.5: Double horn HI profile of ZoA galaxy J0741-22. Plot of HI flux in Jy km s^{-1} on heliocentric velocity in km s^{-1}.

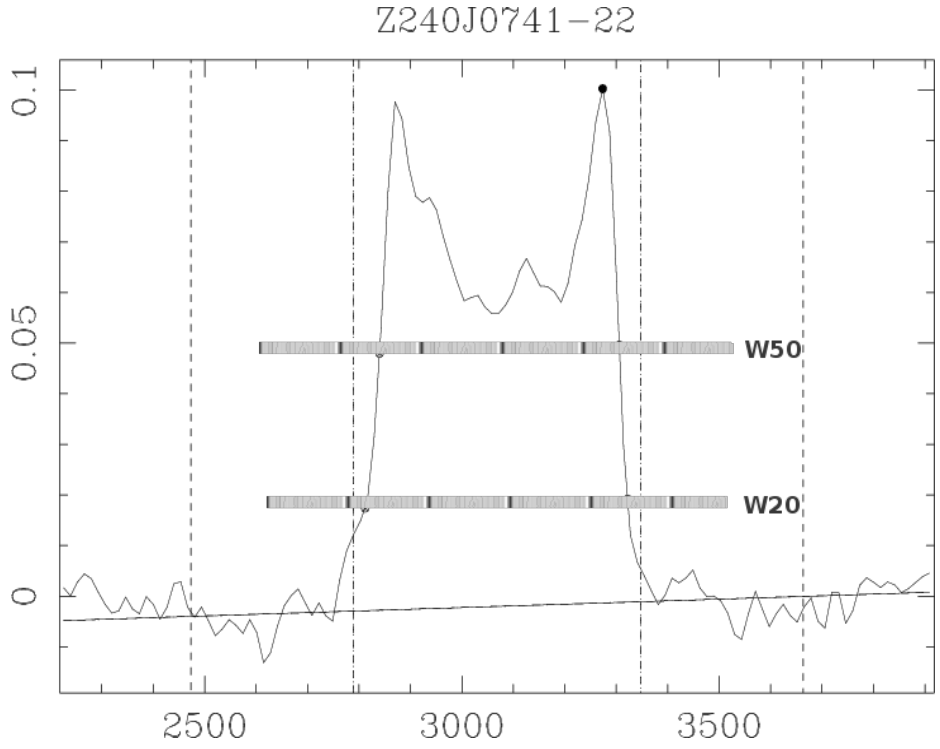

1.1.4.2 HI Parameters

Hubble demonstrated that all galaxies are moving away from us, and that the velocity of their recession were proportional to their distance. The Local Group velocity V_{LG} is the radial velocity of galaxies corrected for motion with respect to the Local Group which can be written as

$$V_{LG} = V_{obs} + 300 \sin l \cos b, \tag{1.1}$$

where l and b are Galactic coordinates, $V_{obs} = cz$ is the heliocentric velocity, where c is the speed of light and z is the redshift. The Local Group velocity is $V_{LG} = H_0 d$, where $H_0 = 75$ km s^{-1}Mpc^{-1} is the value of Hubble constant used throughout this research work and d is distance in Mpc. The CMB velocity V_{CMB} is the radial velocity in the frame of the CMB given by the model of Fixsen et al. (1996) as

$$V_{CMB} = V_{obs} + V_{apex}[\sin b \cos b_{apex} + \cos b \cos b_{apex} \cos(l - l_{apex})]. \tag{1.2}$$

Where $V_{apex} = 371$ km s^{-1}, $l_{apex} = 264.14°$, $b_{apex} = 48.26°$ are the velocity and Galactic position components of the apex vector describing the relative motion of the Sun with

respect to the CMB. The peculiar velocity of a galaxy is its velocity relative to the motion due to the isotropic expansion of the Universe as described by the Hubble flow given as $V_{pec} = V_{obs} - H_0 d$. The total velocity of a galaxy is the sum of the velocity due to the Hubble flow and the local motion of the galaxy within its cluster or group environment due to local gravitational effects. The mass of HI $M_\odot$ was calculated as

$$M_{HI} = 2.356 \times 10^5 d^2 I_{HI}, \tag{1.3}$$

where I_{HI} is the integrated flux in Jy km s^{-1} and d is the distance in Mpc (Donley et al., 2005).

1.1.5 Theoretical and Statistical Views

Hoffman et al. (1992); Zaroubi et al. (1995, 1999); Dekel et al. (1999); Webster et al. (1997); Bertschinger & Dekel (1989); Hoffman (1994); Enßlin et al. (2009); Branchini et al. (1996); Bistolas & Hoffman (1998); Lahav et al. (1994) and others showed that various mathematical method exist to reconstruct the distribution of galaxy in the ZoA without having direct access to observational data. One of such possibilities is the expansion of galaxy distributions adjacent to the ZoA into spherical harmonics to recover the structures in the ZoA either with a 2-dimensional (sky positions) or 3-dimensional (redshift catalog) (Lahav et al., 1994; Scharf et al., 1992; Fisher et al., 1995). Also, there exist statistical method known as Weiner Filter which could be used to reconstruct structures behind the Milky Way. It was developed explicitly for reconstruction of corrupt or incomplete data (Hoffman, 1994; Fisher et al., 1995; Webster et al., 1997). Using Weiner Filter with linear theory allows the determination of the real-space density of galaxies, as well as their velocity and potential fields (Fisher et al., 1995). Furthermore, POTENT analysis can be used to reconstruct the potential field (mass distribution) from peculiar velocity fields in the ZoA (Dekel et al., 1999). The reconstruction of the potential fields versus density field have advantage that they can locate hidden over density even if unseen (Fisher et al., 1995). The raw data for POTENT analysis are distances, redshifts, and angular positions for a set of galaxies. The distance can be estimated from Tully-Fisher relation and the difference between the redshift and the estimated distance is the estimated radial peculiar velocity. The velocity field is recovered under the assumption of potential flow given as

$$\mathbf{v}(\mathbf{x}) = \nabla \mathbf{\Phi}(\mathbf{x}), \tag{1.4}$$

where the velocity potential can be calculated by integrating the radial velocity along the radial direction given as

$$\mathbf{\Phi}(\mathbf{x}) = \int_0^r u(r', \theta, \phi) dr'. \tag{1.5}$$

Differentiating $\mathbf{\Phi}$ in the transverse directions recovers the two missing components the underlying mass density fluctuation field $\delta(x)$, which is computed as

$$\delta(x) = \left\| \mathbf{I} - f(\Omega)^{-1} \frac{\partial \mathbf{v}}{\partial x} \right\| - 1, \tag{1.6}$$

where the bars denote Jacobian determinant, $\mathbf{I}$ is the unit matrix and $f(\Omega) \equiv \dfrac{\dot{D}}{D} \simeq \Omega^{0.6}$, with $D(t)$ denoting the linear growth factor (Peebles, 1976). The non-linear approximation in equation 1.6 reduces to $\delta = -f(\Omega)^{-1} \nabla \cdot \mathbf{v}$ in the linear regime (Dekel et al., 1999; Bertschinger & Dekel, 1989).

1.2 Stellar Density

Variation of the star density across the sky was the first observable indication of presence of dust in the Galaxy (Robin & Creze, 1986). Star counts involves counting stars in magnitude intervals in each cell of a regular grid in an obscured field and comparing this number with the counts in a reference field, supposedly free of absorption. Stellar density is the average number of stars within a unit volume, measured in cubic parsec (pc^3). Stellar density when counted on a rectangular grid on the sky is called the surface density. FIGURE 1.6 shows the 2MASS Point Source Catalogue stellar number density metric, $\log(N_{K_s<14}/\deg^2)$, where $N_{K_s<14}$ is the number of stars brighter than $A_B \sim 14^{\mathrm{m}}$ in K_s-band. The locations within the Milky Way that have the highest stellar density are the central core and the interior of globular clusters (Robin & Creze, 1986; Robin et al., 2012). In FIGURE 1.6 we can observe the Galactic bulge as an ellipse of stars above and below the Galactic plane. The closer you get to the center of the galaxy, the greater the density of both stellar dust and stellar bodies (Jarrett et al., 2000b; Jurić et al., 2008). Multiple stars can be found within distances of far less than a light year. The ZoA is obscured from us by thick interstellar clouds of gas and dust. As we move into the near-infrared the effect of dust obscuration becomes much weaker, since the effect of absorption becomes less stringent as one move to the redder wavebands. Moreover, the major delimiting factor affecting near-infrared observation of the ZoA is the star density. 2MASS and IRSF observation of the ZoA do not uncover galaxies at low Galactic latitudes in the Galactic Bulge region (Jarrett et al., 2000b; Kraan-Korteweg & Jarrett, 2005). This effect is not associated with extinction, but due

to star crowding and stellar confusion noise. From FIGURE 1.6 we could see that the effect of stellar obscuration is higher at the center of the Galactic plane and decreases northward or southward to the pole. At Galactic latitude $|b| > 25°$ the star density metric $\log(N_{K_s<14}/\deg^2)$ is less than 3.2 which is the light gray point. The gray points with stellar density metric $\log(N_{K_s<14}/\deg^2)$ between 3.2 and 3.6 correspond roughly with $10° < |b| < 25°$. For region with dark gray points the stellar density metric $\log(N_{K_s<14}/\deg^2)$ is between 3.6 and 4, while for the black point the stellar density metric $\log(N_{K_s<14}/\deg^2)$ is greater than 4. The white gap centered about the Galactic center is mostly devoid of 2MASS extended source catalogue objects due to the extreme density of stars. However, there is a spur of high density Orion Nebula points at $l = 210°$ & $b = -20°$. The Great Attractor field, including the galaxy cluster of Abell 3627 at $l = 325.^\circ 6$ & $b = -7.^\circ 2$ have a high stellar density metric $\log(N_{K_s<14}/\deg^2)$ of $\sim 4 - 4.3$. WISE observations of the ZoA galaxies using the WISE online database at http://irsa.ipac.caltech.edu/Missions/wise.html have shown that the effect of stellar crowding becomes minimal at low Galactic latitude when compared to 2MASS and IRSF observations. From the observation of WISE W1 band images, the effect of stellar crowding are quite obvious and start to vanishes as we observe through the other WISE bands (WISE W2, W3 & W4) space telescope image. In the WISE W4 image the star have all vanish, we can only observe thick dust of cloud around stellar objects.

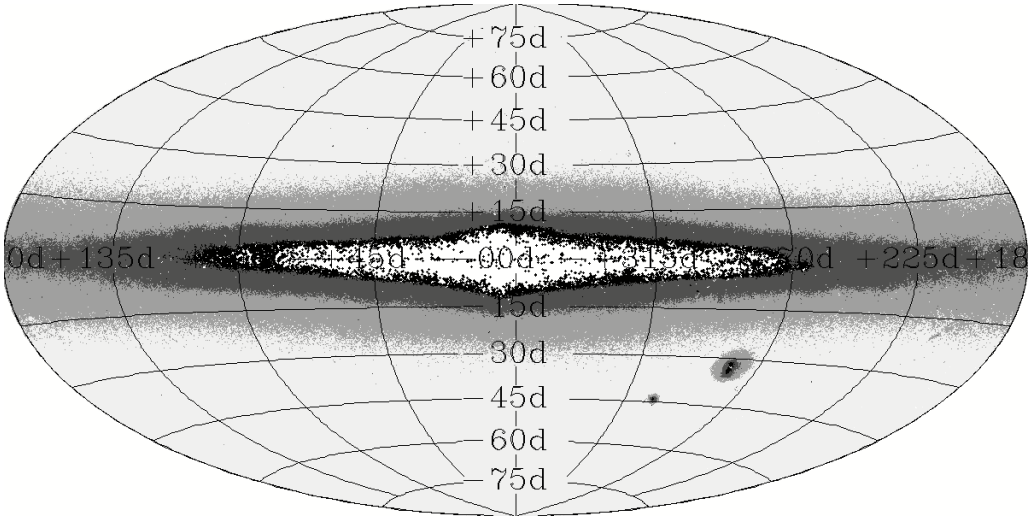

FIGURE 1.6: Aitoff projection of the extended source catalog in Galactic coordinates, coded according to the foreground stellar number density for each source. The density star count metric ($\log(N_{K_s<14}/\deg^2)$) is defined as logarithm of number of stars brighter than 14^{th} magnitude in the K_s band. The image is obtained from Cutri et al. (2003) at http://www.ipac.caltech.edu/2mass/releases/allsky/doc/sec4_5c.html.

1.3 Extinction in the Zone of Avoidance

Extinction is the absorption and scattering of electromagnetic radiation by matter between an emitting astronomical object and the observer (Trumpler, 1930). Extinction affect the colors of stars as well as limit the apparent magnitude of galaxies and makes observation of astronomical object difficult. It becomes very significant when observing astronomical objects in the ZoA. Extinction arises both from the interstellar medium (ISM) and the Earth's atmosphere for ground based observers; it may also arise from circumstellar dust around an observed object (Trumpler, 1930).

1.3.1 Atmospheric Extinction

We do not measure directly the flux f_ν that reach the Earth from the galaxy, since the atmosphere absorbs some photons, while others are lost in the telescope operation. Instead, we measure raw flux $\mathcal{F}$ given as

$$\mathcal{F} = \int_0^\infty f_\nu T_\nu F_\nu R_\nu d\nu. \tag{1.7}$$

Where T_ν is the transmission of the atmosphere, F_ν is the transmission of any filter, which has been put into the system to isolate a particular range of frequencies, and R_ν is the instrumental efficiency (Diplas & Savage, 1994; Binney & Merrifield, 1998; Burke et al., 2010). The transmission of the atmosphere satisfies $T_\nu \propto e^{-a}$, where a is proportional to the column density of air along the line of sight. The ratio of the actual value of a to its value a_0 at the zenith is the air mass $\equiv a/a_0$. For a plane-parallel atmosphere, airmass $a/a_0 = \sec z_d$, where z_d is the zenith distance of the object been observed. Atmospheric extinction produces a dimming of light from galaxies according to the relation

$$m(z_d) = C \sec z_d + \text{const.} \tag{1.8}$$

Where C is a constant and $m(z_d)$ is the observed galaxies magnitude at zenith distance. We can correct for atmospheric extinction by observing the magnitude of a galaxy at several values of z_d. Also, strong atmospheric extinction in some wavelength regions such as in X-ray, ultraviolet and infrared requires the use of space-based observatories (Diplas & Savage, 1994; Binney & Merrifield, 1998; Burke et al., 2010). The Earth's upper atmosphere is opaque to most electromagnetic radiation except for radio wavebands, the entire visible region, the near ultraviolet and near infrared wavebands. Much of the infrared suffers absorption from water molecules, carbon dioxide and oxygen molecules.

Most ultraviolet undergoes absorption by ozone, while gas atoms and molecules absorb X-ray and gamma rays (Binney & Merrifield, 1998). WISE wavebands cannot be observed from the Earth as compared to the optical and near-infrared wavebands.

1.3.2 Galactic Dust Extinction

The space between stars in a galaxy is not empty, but filled with smoke-like particles called dust. A vest majority of these dust particle hang around interstellar space obscuring our view of celestial objects (Whittet, 1988). Dust not only dims (absorbs) the light from distant star, it scatters and reddens it. Galactic or Interstellar extinction is the absorption and scattering of light by the Milky Way dust and gas particles between an emitting astronomical object and the observer (Schultz & Wiemer, 1975). The extinction A_λ associated with a galaxy in some waveband λ is the difference between the observed λ-band magnitude $m(\lambda)$ and the magnitude $m_0(\lambda)$ that would be observed in the absence of dust given as

$$A_\lambda \equiv m(\lambda) - m_0(\lambda). \tag{1.9}$$

Color is the difference in magnitude measured in two different bands, while the color index in two different filters is given as

$$CI \equiv \ m_{\lambda_1} - m_{\lambda_2} = \text{const.} - 2.5 \log \frac{\int_0^\infty d\lambda S_\lambda(\lambda_1) f_\lambda}{\int_0^\infty d\lambda S_\lambda(\lambda_2) f_\lambda}. \tag{1.10}$$

Where S_λ denotes the combined telescope-receiver-filter sensitivity and f_λ is the average fluxes at wavelength λ. The reddening or color excess $E(\lambda_1 - \lambda_2)$ in some color $\lambda_1 - \lambda_2$ is the difference between the observed color A_{λ_1} and the intrinsic color A_{λ_2} given as

$$E(\lambda_1 - \lambda_2) \equiv A_{\lambda_1} - A_{\lambda_2}. \tag{1.11}$$

Where $A_{\lambda_1} = m(\lambda_1) - m(\lambda_2)$ is the Color index which essentially measures a property of an objects spectrum that is independent of its distance. (Schultz & Wiemer, 1975; Diplas & Savage, 1994; Binney & Merrifield, 1998).

1.3.3 Extinction Correction

The energy flux we receive at the Earth from an astronomical object need to be corrected for, in other to be able to estimate true brightness and distance of the astronomical object. If F_1 is the flux received when the object is at a distance D_1, the flux F_2 that

would be received if it were at some other distance D_2 is given by the inverse square law

$$F_2 = \left(\frac{D_1}{D_2}\right)^2 F_1. \tag{1.12}$$

In principle, the farther away an object is, the fainter it will appear. Therefore, we can obtain information about the relative intrinsic brightness of an objects. The absolute magnitude of an object M is the apparent magnitude an object would have if it were located at a distance of 10 pc. The distance modulus $m - M$ is given as

$$m - M = -2.5 \log\left(\frac{F_2}{F_1}\right) = 5 \log d - 5. \tag{1.13}$$

In astronomical measurements, we correct galaxy magnitude for absorption and scattering of photon and for object moving rapidly away from us, because it lies at a cosmological-significant distance. The relation in equation (1.13) can be written as

$$m - M = 5 \log d - 5 + A_\lambda + k. \tag{1.14}$$

Where A_λ is the extinction, and the quantity $k(z)$ is related to k the K-correction[7] as

$$k(z) = k - 2.5 \log(1 + z), \tag{1.15}$$

where z is the redshift of the object. K-correction are reliable only for nearby galaxies, for which $k \simeq 0$ (Poggianti, 1997; Binney & Merrifield, 1998). In reality we should compare the brightness of a distant galaxy with the brightness of a nearby galaxy in the waveband at which the photons collected from the distant galaxy were emitted.

1.3.4 Extinction Curve & Map

The extinction at any two frequency are not always the same, because dust type varies at each waveband (Schultz & Wiemer, 1975). In the visual band, at shorter wavelengths, the extinction curve is found to vary from one line of sight to another. This is actually as a result of variations in the size-distribution of grains in different wavelength regions (Schultz & Wiemer, 1975). Extinction rises strongly in the ultraviolet region, but has a negligible effect on infrared radiation. The extinction laws was parameterized using

$$R_V \equiv \frac{A_V}{E(B - V)}. \tag{1.16}$$

R_V is known to be correlated with the average size of the dust grains causing the extinction. Consequently, R_V quantifies whether the extinction curve is rising steeply

[7] K-correction is not applied to stars.

in the ultraviolet wavelength or not. For a steeply rising extinction curve $R_V \simeq 3$, while $R_V \simeq 5$ for a slowly rising one. Small values of R_V generally apply for line of sight that do not penetrate deeply into a molecular cloud (Cardelli et al., 1989). The extinction studies by Schultz & Wiemer (1975); Sneden et al. (1978) and others derived

$$R_V = 3.1, \tag{1.17}$$

for line of sight that do not pass through dense clouds. The equation (1.17) is mostly used because it allows one to estimate A_V from the much more readily measured quantity $E(B-V)$. Unfortunately these studies does not allow for estimation of the error associated with R_V. Cardelli et al. (1989) showed that along the line of sight A_λ/A_V can be well approximated by

$$\frac{A_\lambda}{A_V} = a(\lambda) + \frac{b(\lambda)}{R_V}, \tag{1.18}$$

where a and b are polynomial in λ^{-1}. Standard extinction curve depends on the composition of the interstellar medium, which varies from galaxy to galaxy as seen in FIGURE 1.7.

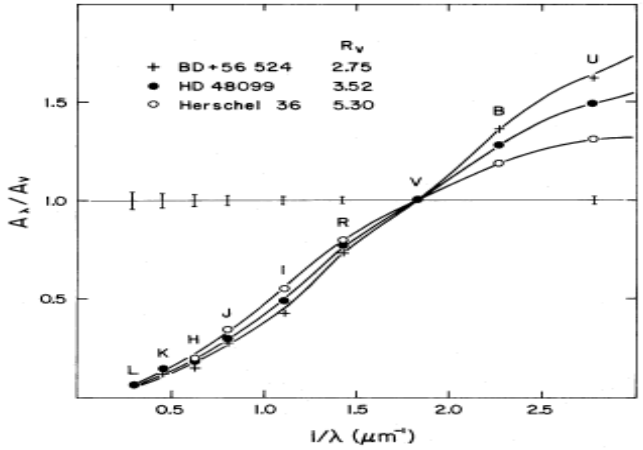

FIGURE 1.7: Mean Optical and Near-infrared R_V-dependent extinction law of (Cardelli et al., 1989). The errorbars represent the computed standard deviation of the data about the best fit of $A(\lambda)/A(V)$ versus R_V^{-1} with $a(\lambda) + b(\lambda)/R_V$, where $x \equiv \lambda^{-1}$.

In the Local Group, the best determined extinction curves are those of the Milky Way, the Small Magellanic Cloud (SMC) and the Large Magellanic Cloud (LMC) (Gordon et al., 2003).

In general extinction makes galaxies fainter and it reduces the number of galaxies counted in any zone to some given limiting magnitude. Extinction is often associated with neutral hydrogen that can be detected through 21 cm line. The extinction along the line of sight out of the Milky Way generally diminishes as $|b|$ increases, it varies very irregularly over

the sky. Away from the direction of the Galactic center $E(B-V)$ tends to be small in the North at $b > 20°$, while in the South there is a great spur of high $E(B-V)$, which reaches to $b = 40°$ at $l = 170°$ (Gordon et al., 2003; Stecher, 1965, 1969). Along the line of sight $E(B-V)$ is approximately proportional to the column density N_H of interstellar hydrogen atoms which is given as

$$E(B-V) = \frac{N_H}{5.8 \times 10^{25}\ \mathrm{m}^{-2}}, \tag{1.19}$$

where $\frac{E(B-V)}{N_H}$ is the dust/gas ratio. The equation in (1.19) implies that a fixed number and size distribution of dust grains is associated with a given mass of interstellar hydrogen (Bohlin et al., 1978; Diplas & Savage, 1994).

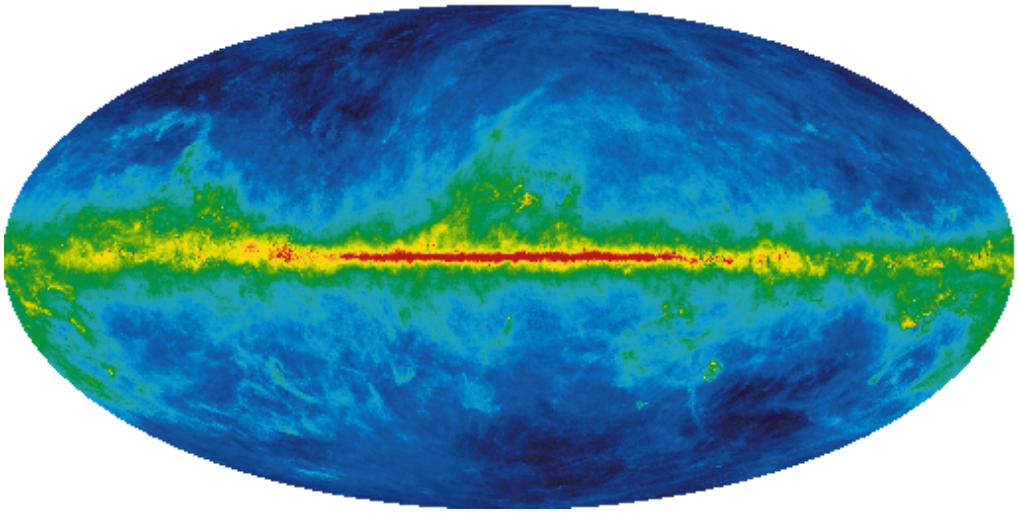

FIGURE 1.8: LAMBDA Map of Galactic reddening, $E(B-V)$ derived using IRAS and COBE/DIRBE data by Schlegel et al. (1998). The $E(B-V)$ values are given in logarithmic scale from $0^{\mathrm{m}}.004$-$6^{\mathrm{m}}.3$. Low dust extinction are coded with blue while high dust region are coded with red.

There exist extensive maps of both the neutral hydrogen gas (HI) and the distribution of dust (IRAS 100 μm) within the Galaxy. The good correspondence between these two maps indicates that the HI gas and dust trace each other (Schlegel et al., 1998). The amounts of the extinction which correspond to these two components have been calibrated from detailed, multicolor observations of distant galaxies. Therefore, the Galactic extinction for any galaxy can be estimated given its position on these maps. The map in FIGURE 1.8 provides a direct measure of column density. Also, this map can be used, in conjunction with a spectral template for the background, to derive the dust temperature opacity, and hence, the extinction along the line of sight. As the Galactic latitude falls below about 25°-30°, the corrections for Galactic extinction become large with correspondingly large uncertainties (Schlegel et al., 1998). The effect of dust extinction is quite prominent in the optical wavebands. As we move to the near

infrared the effect of dust extinction is greatly reduced, while for WISE wavebands the effect of dust extinction become very negligible.

1.4 Cosmic Flow Fields

If we look beyond the plane of our own galaxy, the clearest structure we will see in the Universe are other galaxies. Unfortunately, these galaxies are not standard candles. Observation of telescope image of galaxies which approximately lie at the same distance reveal that they have an enormous range of apparent magnitude and angular diameter. Therefore, to understand the physics behind this astronomical phenomena, we need to quantify the basic properties (e.g peculiar velocity) of the system under observation, and many of these properties cannot be determined unless we know the distance to the object in question. Clearly, we have to look at more subtle properties of these galaxies, if we are to use them as distance indicator. One of the wide array of different techniques that can be used to measure distances to galaxies is the Tully-Fisher relation.

1.4.1 Tully-Fisher Relation

Tully-Fisher relation is a secondary distance indicator which make use of the strong correlation between the luminosity of spiral galaxies and their rotational velocities (Tully & Fisher, 1977). Also, this technique has proved extremely valuable for the mapping of large-scale structure, the Hubble flow and associated peculiar velocity field (Giovanelli et al., 1997). The correlation between the derived total mass using HI linewidths and optical luminosity was noticed in the late 60's to 80's by Roberts (1969); Rogstad & Shostak (1972); de Vaucouleurs (1972); Sandage (1973); Balkowski et al. (1974); Shostak (1975) and others. Tully & Fisher (1977) suggested a luminosity-linewidth relation of the form $L \propto V^{\alpha}$, to measure distances to spiral galaxies. They demonstrated that using some nearby spiral galaxies for which the distances are known accurately, the luminosity-linewidth relation can be calibrated to infer distances to clusters of galaxies as well as obtain a value for Hubble constant. The value of index α is found to be ~ 3 in the optical and ~ 4 in the near-infrared (Aaronson et al., 1979). Tully-Fisher relation study are more preferable done with infrared bands luminosities due to low dust extinction, but the Tully-Fisher relation best results have been achieved with I band luminosity (Masters et al., 2006).

1.4.2 Peculiar Velocity Field

The cosmic flow is the use of distances to determine peculiar velocities and subsequently mass fluctuation. Peculiar velocity[8] refers to the components of a receding galaxy's velocity that cannot be explained by Hubble's law (Giovanelli et al., 1998). According to Hubble's law, the relationship between a receding velocity and distance should have an exact value in the absence of any effect. Galaxies in the Universe are not evenly distributed in the observable Universe, but are found in clusters with size ranging from fewer dozens to thousands. Therefore, observed velocity will add or subtract from the radial velocity that one would expect from Hubble's law. In principle, peculiar velocities are departures from the cosmic mean expansion which arises due to density fluctuation (Giovanelli et al., 1998). Therefore, in determining the distance of a single galaxy, a possible error must be assumed. This error becomes smaller, relative to the total speed, as the distance increases. Accurate distance estimate can be made by taking into consideration the average velocity of a group of galaxies. The assumed peculiar velocities which is essentially random, will cancel each other, leaving a much more accurate measurement of distance (Aaronson et al., 1982a,b; Giovanelli et al., 1998; Nusser & Davis, 1995).

1.5 Research Work Motivation

It is general accepted that the CMB dipole is due to a Doppler effect arising from the motion of the Local Group through the cosmological reference frame. Kogut et al. (1993) showed that the CMB dipole indicates that our Local Group moves with a velocity of 627 ± 22 km s^{-1} towards the direction of $l = 276°$, $b = 30°$ in Galactic coordinates. Although, the direction and amplitude of this Local Group motion is known to high accuracy, its source has yet to be conclusively determined. Resolving the source of the Local Group's motion and the bulk flow in which it participates carries many interesting cosmographical and cosmological implications.

The 2MASS survey and the data release from WISE telescope in 2009 opens up the possibility to obtain near-mid infrared data of the Galactic sky and especially to study the cosmic flow field associated with galaxy distribution in the Universe. Masters et al. (2003, 2008) studied the near-infrared correction to spiral galaxies and then apply these corrections to determine the Tully-Fisher relation using J, H & K_s bands total magnitudes from 2MASS catalogue and HI data from Cornell HI Digital Archives. They

[8] Peculiar velocity $V_{pec} = V_{obs} - H_0 d$, where V_{obs} is the observed velocity, H_0 is the Hubble's constant and d is the distance of the galaxies. More detailed description is given in Chapter 5

constructed a global template of near-infrared Tully-Fisher relation with total magnitudes using 888 galaxies. Said (2013) used the same 888 galaxies of Masters et al. (2008) with isophotal magnitudes to construct the J, H & K_s bands Tully-Fisher template relation. Lagattuta et al. (2013) used WISE W1 galaxies magnitudes and the publicly available line-width data from Cornell HI Digital Archives and HYPERLEDA samples. They applied an approach similar to the paper of Masters et al. (2008) to correct for WISE W1 band galaxies magnitudes. They constructed a WISE W1 Tully-Fisher template relation using a sample of 568 galaxies. Lagattuta et al. (2013) showed that using W1 and 2MASS K_s band photometry that the galaxy colors $(K_s - W1) \sim 0$, which suggest that these two bands trace similar stellar populations and possibly the same star formation history. Sorce et al. (2013) used a sample of 213 galaxies in 13 clusters that define the slope and 26 galaxies with Cepheid or tip of the red giant branch distances that define the zero point to obtain the 3.6 μm Tully-Fisher template relation. Currently, the Cosmic Flow Program (Neill et al. (2014)) used a sample of WISE W1 and W2 bands galaxies to obtain WISE W1 and W2 bands Tully-Fisher template relation and the I band conversion of WISE W1 and W2 bands Tully-Fisher template relation.

In this project work, we are going to extract a subsample of HIZoA galaxy catalogue suitable for Tully-Fisher work in the ZoA. This will involve inclined galaxies with strong rotational velocity. We will use the imaging from the IRSF, online WISE and possibly online 2MASS bands data to search for their counterparts and then measure their resolved galaxy WISE photometry. We will combine the IRSF, 2MASS and WISE data and cross correlate them with their respective Deep Parkes HIZoA survey data. Also, from this we will derive the peculiar velocity analysis for K_s, WISE W1 and W2 bands using the Tully-Fisher relation calibration of Said (2013) for the K_s band, Lagattuta et al. (2013); Sorce et al. (2013) and Cosmic Flow Program calibrations for WISE W1 band and Cosmic Flow Program calibrations for WISE W2 band. We then compared the WISE W1 and W2 bands results with the IRAF and 2MASS K_s bands results. To do this, we first investigate the effect of Galactic dust extinction on 2MASS JHK_s bands and WISE W1 and W2 bands. We applied spiral galaxies Galactic extinction correction to isophotal magnitudes based on the analysis of Cameron (1990) and Riad et al. (2010). Initially, Cameron (1990) used this analysis to correct for B band galaxies magnitudes, while Riad et al. (2010) applied this method to correct for JHK_s bands near-infrared galaxies. We then apply this method to correct near-infrared spiral galaxies magnitudes of IRSF JHK_s bands data and 2MASS JHK_s bands online data and resolved galaxies WISE W1-W4 bands magnitudes.

Our aim in this project is to understand the cosmic flow associated with the ZoA galaxies and to compare the suitability of using the WISE bands over the Near-infrared 2MASS JHK_s bands and IRSF JHK_s bands in mapping cosmic flow of the ZoA galaxies. These

will help us to ascertain whether the K_s band and the WISE W1 band traces the same cosmic flow using our dataset.

1.6 Thesis Outline

Chapter one is based on the literature review on topic relevant to understanding the research topic. The chapter two is based on data analysis which include comparison of IRSF JHK_s bands, 2MASS JHK_s bands and WISE W1-W4 bands observations and data. Chapter three describes the Galactic absorption correction of JHK_s bands and WISE W1-W4 bands isophotal magnitudes using the method of Cameron (1990) and Riad et al. (2010). Chapter four applies to Tully-Fisher relation parameters. In chapter five we obtained the cosmic flow analysis for K_s band, WISE W1 and W2 bands associated with ZoA galaxies. The last chapter is based on discussion of results and the future work.

Chapter 2

Zone of Avoidance Data Description

We combine HI data from three separate surveys of the ZoA obtained with the multibeam of the Parkes 64 m radio telescope. The main criteria for inclusion of galaxies from these subsamples are that their linewidth are of good quality. We chose to study cosmic flow field using IRSF bands, 2MASS bands and WISE bands photometry. Infrared photometry has a number of clear advantages over conventional optical data. Foremost, the effects of dust extinction are strongly reduced. Also, for WISE photometry the effect of stellar crowding are greatly reduced and vanishes for WISE W4 band photometry. In addition, recent bursts of star formation can have a large effect on the optical luminosity of a galaxy, whereas in the infrared bands luminosities, these have a negligible effect (Savage et al., 1985). Several galaxies in our sample are highly inclined with respect to the line of sight, such that a large fraction of the light can also be absorbed by internal dust. In the optical bands, this effect can be very significant ($\gtrsim 1^{\mathrm{m}}$) leading to large uncertainties in the derived absolute luminosities but, in the infrared bands, these uncertainties are less severe.

2.1 Data Selection

The initial HIZoA data[1] contains 1109 possible galaxies, while the observed IRSF counterpart has 555 possible galaxies. FIGURE 2.1 shows the HIZoA data positions which consist of the reduced data from different surveys and the red star ($\star$) indicate the observed IRSF counterpart with the 1.4 m IRSF telescope of South Africa Astronomical

[1]It was observed by Renée Kraan-Kowteweg and collaborators (Donley et al., 2005; Henning et al., 1998, 2000).

Observatory (SAAO) in Sutherland. For WISE W1 and W2 analysis we focused on the 555 galaxies detected from IRSF observations[2]. We used the IRSF imaging, the WISE online imaging, HI profile and photometric properties which are all displayed in the project website at http://www.ast.uct.ac.za/~affadi/patrick/patrick.html[3] to select our candidates galaxies. We obtained the resolved galaxy WISE W1-W4 bands photometric data using the IRSF detected 451 possible counterparts of the HIZoA galaxies. We closely compared IRSF photometry of these possible galaxies with the WISE resolved galaxies photometry. Also, the HI profile of the selected galaxies are of a reasonable and good quality. In the final selection, we found 196 WISE photometry of the HIZoA galaxies positions which have a counterpart in IRSF observations and are suitable for cosmic flow analysis. We cross checked these galaxies with 2MASS extended source online catalogue and found 155 galaxies as seen in FIGURE 2.2[4].

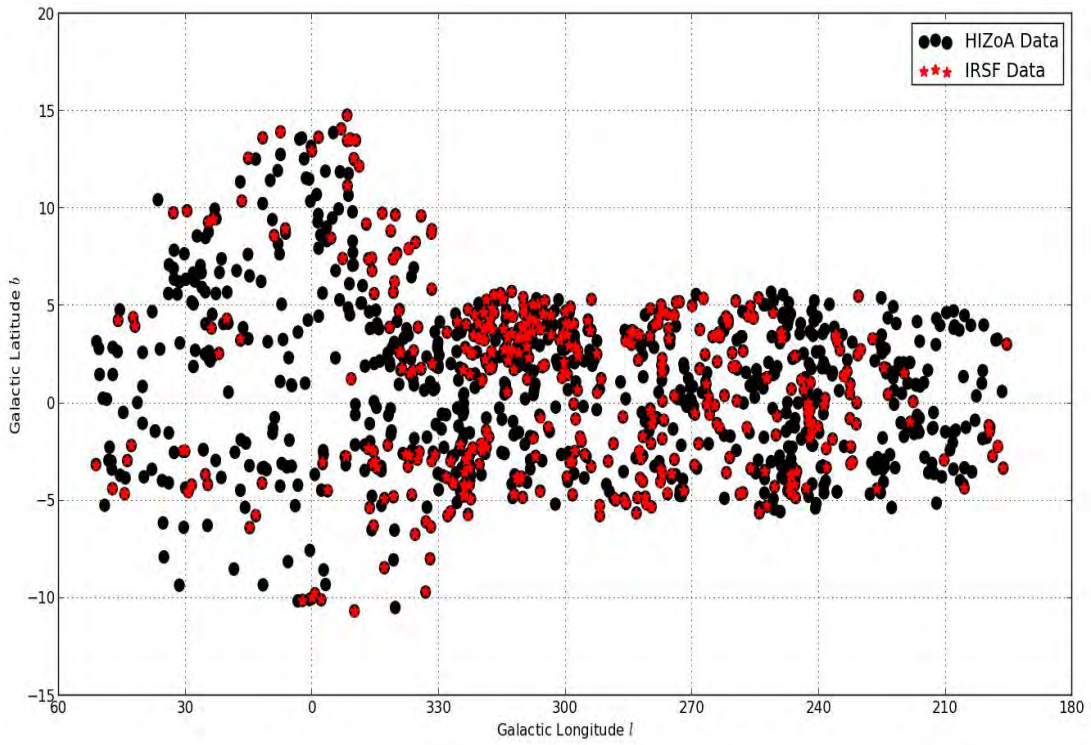

FIGURE 2.1: The positions of 1109 HIZoA galaxies with the corresponding 451 detected IRSF counterparts.

A secondary consideration was that our selected galaxies should be well distributed around the ZoA, in order for their average motions to represent the true bulk motion of the ZoA region. Furthermore, for ZoA Tully-Fisher relation analysis we selected galaxies with high rotational velocity of $\log W \geq 2.0$ to reduce Tully-Fisher relation

[2]Observed and reduced by William Wendy, Nabiha Shafi and others (Williams, 2011).
[3]See Section 2.5 for more details.
[4]The complete dataset can be downloaded at http://www.ast.uct.ac.za/~affadi/patrick/patrick.html

scatter and minimize bias (Masters et al., 2008). In the case of cosmic flow analysis, we restricted our samples to ZoA galaxies with IRSF K_s band axial ratio less than 0.7 to ensure that mostly edge-on spiral galaxies are selected. These samples were cross-checked with NASA/IPAC Extragalactic Database (NED) and other published works. Also, we obtained the online WISE and 2MASS photometry to compare our data sample. For the cosmic flow analysis in this work, we used absolute magnitudes that are unique to each calibrator[5].

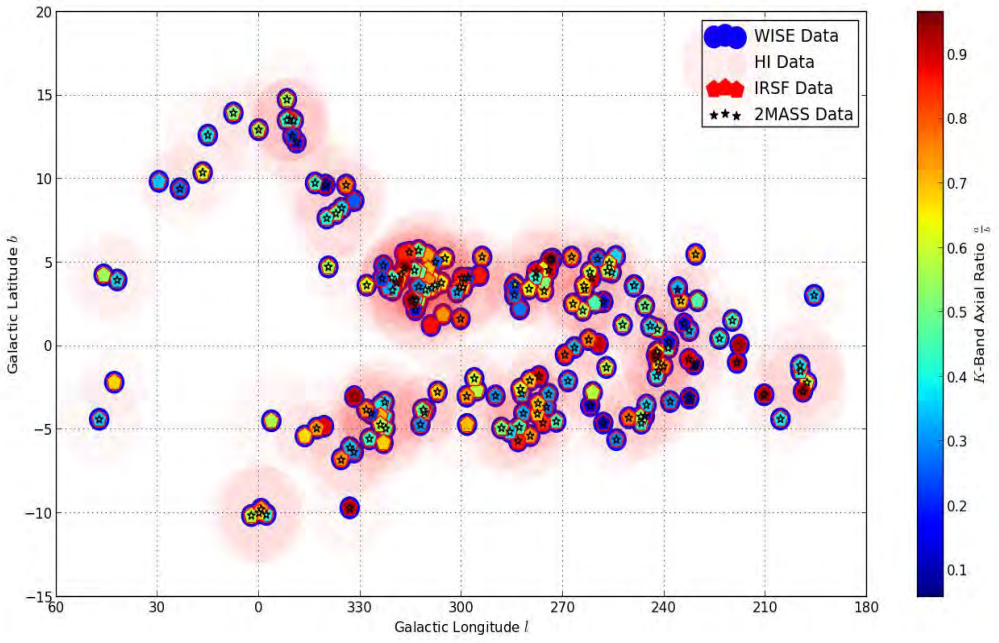

FIGURE 2.2: The positions of selected ZoA galaxies. The HI Data with red blobs are plotted with respect to their rotational velocity.

2.2 HIZoA Data Description

HI observations of ZoA galaxies was carried out with the multibeam of the Parkes 64 m radio telescope. The Parkes 64 meter radio telescope installed in 1967 is the largest single-dish telescope in the southern hemisphere dedicated to astronomy (Staveley-Smith et al., 1996). It can observe at frequencies from 0.3 to 43 GHz. In 1997, it was equipped with a 13-beam Multibeam Receiver which provides unprecedented efficiency for large-scale radio surveys of the sky (Staveley-Smith, 1997). The HI observation were made using Parkes radio telescope to scan the sky at constant Galactic latitude. Each scan covered 8° in Galactic longitude, with offset of 35° in latitude, thereby mapping out a

[5]All the calibrations used in this work were calibrated with isophotal magnitudes.

strip of $8^\circ \times 1\overset{\circ}{.}7$. The receiver is rotated to achieve maximum sky coverage. The raw data obtained were bandpass-corrected, Doppler corrected, calibrated and gridded with a resulting pixel of $4' \times 4'$ and a beam sizes of $15\overset{'}{.}5$. The resulting data cubes were Hanning smoothed to reduce the effects of ringing by strong continuum emission. The first ZoA survey covers ($212^\circ \leq l \leq 36^\circ; |b| < 5^\circ$) (Henning et al., 2000; Meyer et al., 2004). It was later extended to include the Northern region which is called the Northern Extension (NE) covering ($36^\circ \leq l \leq 52^\circ$) and ($196^\circ \leq l \leq 212^\circ$) having ($|b| < 5^\circ$) (Donley et al., 2005). Furthermore, this surveys was further extended to include the Galactic Bulge region (GB extension) which covers ($332^\circ \leq l \leq 36^\circ; 5^\circ < |b| < 10^\circ$) and ($352^\circ \leq l \leq 24^\circ; 10^\circ < |b| < 15^\circ$) (Juraszek et al., 2000; Donley et al., 2005). The HIZoA is a combination of ZoA survey, Northern Extension and Galactic Bulge extension with velocity coverage of $-1200 \leq cz \leq 12700$ km s^{-1} and velocity resolution of 27 km s^{-1} with an average noise of 6 mJy beam^{-1} (Donley et al., 2005; Doyle et al., 2005).

2.3 Infrared Data Description

Infrared radiation span from 0.75 to 300 μm. Importantly, any object that has a temperature over absolute zero emits infrared radiation. Infrared observation from ground based telescope is quite difficult. This is especially true for wavelength beyond two microns, reason being that our atmosphere absorbs many wavelengths of infrared light and also, air and warm telescope glow with infrared light (Wright et al., 2010). Therefore, most observations in the infrared are done with a space based telescope. We combined data from space based telescope; which include WISE telescope and Earth bound telescopes; which include 2MASS and IRSF. In this Section we will describe the infrared bands data that was used in the subsequent cosmic flow analysis.

2.3.1 2MASS

2MASS is a homogeneous survey which uses two identical highly-automated 1.3 m telescopes to uniformly survey the entire sky in J (1.24 μm), H (1.66 μm) & K_s (2.16 μm) near-infrared bands. One of the telescopes is located at Mt. Hopkins, Arizona to survey the northern sky, while the other telescope is located at Cerro Tololo, Chile to survey the southern sky. Each telescope was equipped with a three channel camera, each channel consisting of 256×256 array HgCdTe detectors, capable of surveying the sky simultaneously at J, H & K_s bands. The survey of the northern sky was carried out between 1997-2000, while the southern survey was done between 1998-2001. The 2MASS survey covers about 99.998 % of the sky with about 1.6 million extracted extended objects. Galaxies have unique colors relative to stars in the 2MASS JHK_s bands, owing to the

effects of internal extinction and star formation. 2MASS penetrate the Galactic interstellar medium and detects a substantial number of galaxies, even in the midst of the Galactic plane. Its extended sources have about 90 % free obscuration. The major limitation of 2MASS in the ZoA is noise from starlight which originate from background galaxies which is revealed in the near-infrared bands. Interstellar reddening and source confusion dominate the appearance of the 2MASS within the Galactic plane as seen in FIGURE 2.3. The end result is a loss of sensitivity, as the surface density of stars increases exponentially and a profusion of multiple surface groupings of stars. The reliability of 2MASS Extended Source Catalog in the Galactic plane ranges from 20-80 %, while for region out of the Galactic plane the reliability is greater than 98 %. Therefore, 2MASS ability to find source in the ZoA is quite limited particularly around the Galactic Bulge. For this research work, we used the online 2MASS data reduced by the 2MASS team (Cutri et al., 2003).

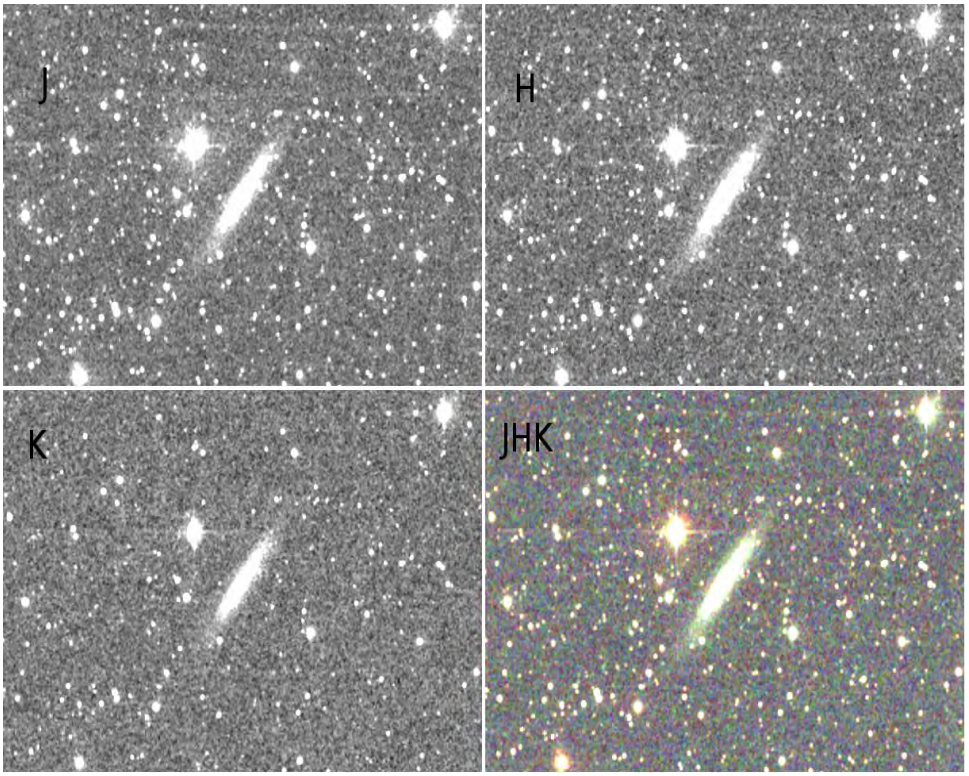

FIGURE 2.3: 2MASS JHK_s bands and RGB reduced online images of J0746-18. The panel J is observed with the 2MASS J-band, panel H is observed with the 2MASS H-band, panel K is observed with the 2MASS K_s-band and panel JHK is the RGB image created from 2MASS J, H, & K_s-bands images.

2.3.2 IRSF

The Infrared Survey Facility (IRSF) of SAAO in Sutherland is a 1.4 m reflector fitted with a Simultaneous Infrared Imager for Unbiased Survey called SIRIUS. It was designed specifically, to survey the southern hemisphere sky in the infrared J (1.25 μm), H (1.65 μm) and K_s (2.15 μm) bands. SIRIUS is incorporated with three 1024 $\times$ 1024 pixel format of HgCdTe detectors and has a field of approximately 7.′8 $\times$ 7.′8 with a resolution of 3″ (Glass & Nagata, 2000). Observation of HIZoA galaxies using the IRSF were done between March 2006 to date with an exposure time of 30-40 s and a signal-to-noise ratio of $\sqrt{N}$, where N is the number of frame (Williams, 2011). The raw image was reduced using the SIRIUS pipeline[6]. The reduction include the dark current subtraction, determination of master flat fields and flat correction, sky determination and subtraction and frame to frame offset determination and combination[7]. The major problem with this IRSF is high source confusion and high stellar crowding as seen in FIGURE 2.4.

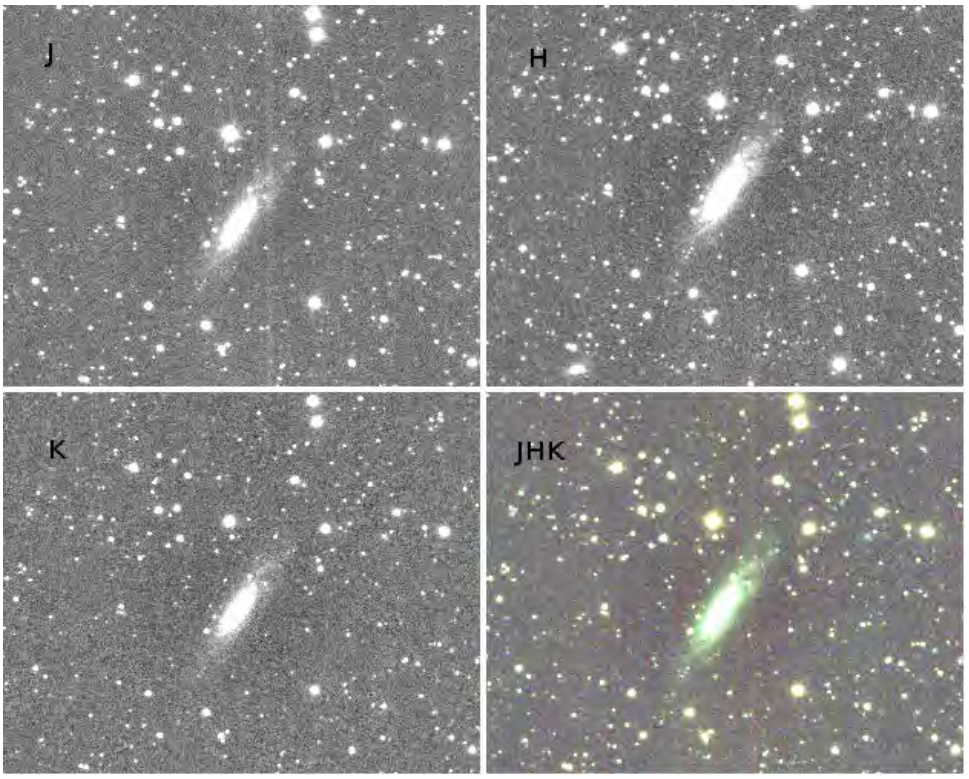

FIGURE 2.4: IRSF JHK_s bands and RGB reduced images of J0746-18 with star density of 3.591 and E(B-V) of 0.468. The panel J is observed with the IRSF J-band, panel H is observed with the IRSF H-band, panel K is observed with the IRSF K_s-band and panel IRSF JHK is the RGB image created from IRSF J, H, & K_s-bands images.

[6]Developed by Yasushi Nakajima

[7]The clear and simple explanation of flat correction and sky background subtraction is given in Subsection 2.4.1

2.3.3 WISE

The Wide-field Infrared Survey Explorer (WISE) is a space-based telescope designed primarily to scan the entire sky at mid-infrared wavelengths with vastly improved sensitivity and resolution over past missions. The instrument includes a 40-centimeter-diameter (16-inch) telescope and four infrared detectors containing one million pixels each, all kept cold inside an outer cylindrical, vacuum-tight tank filled with frozen hydrogen, called a cryostat. WISE orbits the earth 15 times per day and detect four distinct bands of mid-infrared light with wavelengths of 3.4, 4.6, 12 and 22 microns. It has an orbital inclination of $97^{\circ}.5$ and the field of view is $47'$ wide. WISE could detect glowing objects with temperature range between $73^{\circ}.15K - 973^{\circ}.15K$. This includes cool dust, dim stars, dusty galaxies and other objects that might otherwise be hidden from optical telescopes. WISE can find objects buried in blankets of dust (Wright et al., 2010).

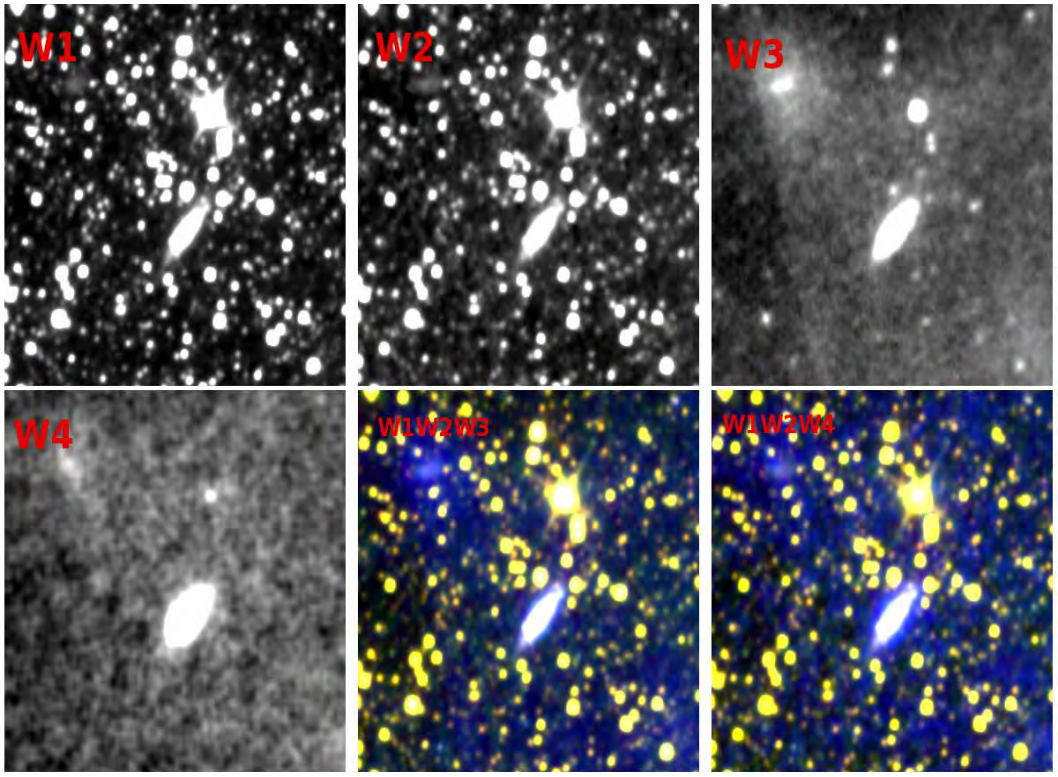

FIGURE 2.5: WISE W1-W4 bands, RGB W1W2W3 and W1W2W4 reduced images of J0746-18. The panel $W1$ is observed with the WISE W1 band, Panel $W2$ is observed with the WISE W2 band, Panel $W3$ is observed with the WISE W3 band, Panel $W4$ is observed with the WISE W4 band, panel $W1W2W3$ is the RGB image created from WISE W1, W2, & W3 bands images and panel $W1W2W4$ is the RGB image created from WISE W1, W2, & W4 bands images.

The image quality or resolution of WISE is about $6''$ in its 3.4, 4.6 and 12 microns bands. At 22 microns, the resolution is $12''$. Therefore, WISE can distinguish features about

five times smaller than the Infrared Astronomical Satellite could at 12 and 25 microns, and many hundred times smaller than NASA's Cosmic Background Explorer (COBE) could at 3.5 and 4.9 microns (Wright et al., 2010).

The WISE online images in FIGURE 2.5 consist of an image atlas with four colors that cover each part of the sky. Also, a catalog of sources extracted from these images are produced. The WISE online image can be used as a tool to properly identify a galaxy and to ascertain their true position. For this report the WISE reduced image was obtained online using the HIZoA positions, and then corrected to get the true positions of the WISE counterparts. We compared the online WISE data with the resolved galaxy WISE data to check our results.

2.4 WISE Data & Characterization Pipeline

We measured the WISE W1-W4 bands photometry of the considered HIZoA galaxies using a special designed WISE Pipeline[8] (Jarrett et al., 2013). The WISE resolved galaxies data consist of WISE W1-W4 bands special constructed mosaics which maintain the original angular resolution of WISE imaging with pixel scale of $1''$ and FWHM of $6''$. One major task of this Pipeline is to automatically measure resolved stars and remove the foreground stars. However, manual help is needed to remove additional stars, masking and initial shape constraints. The WISE Pipeline is a python script that can be run with the code 'python WISSfuzzyphot.py <Folder I.D> w', it immediately display photometry properties of the galaxy and other parameters for further analysis such as

- r : redisplay.
- m : to mark stars.
- ma : to mark stars for clobber masking.
- sp : diffraction spike masking.
- u : undo a star subtraction.
- u2 : undo star masking (but subtraction ok).
- s : set a fixed aperture as a first guess fit to the isophote.
- sm : set the Self-Model flag.

[8]Designed by Tom Jarrett IPAC/UCT in Jarrett et al. (2013)

- x : run again.
- z : run again *later*.
- y : make a png image.
- w : radial plot.
- c : comment/classify.
- <return> to move on to the next source.

The source characterization consists of

- Source positions -centroid
- Shape -elliptical fit to the 3-sigma isophote with fixed axis ratio and position angle
- Size -elliptical fits to the 1-sigma isophote which include other size matrics include convergence, half-light & total light
- Surface Brightness -mean and radial-axis-symmetry
- Double Sérsic fits to the 1-D surface brightness for bulge and disk
- Photometry -Isophotal, Convergence and Curve of growth analysis
- Colors -optimal based on apertures with W1 matched to W2, W4 matched W3

The resolved galaxy WISE photometry outputs consist of

- Photometry table
- Curve of Growth table
- Axis-symmetry Surface Brightness
- Foreground WISE source removed list
- Additional identified non-catalogue sources removed list
- Fits images -stamps centered on the measured resolved source including the original, cleaned and uncertainty fits images
- Processed image, plots and fits from the Pipeline

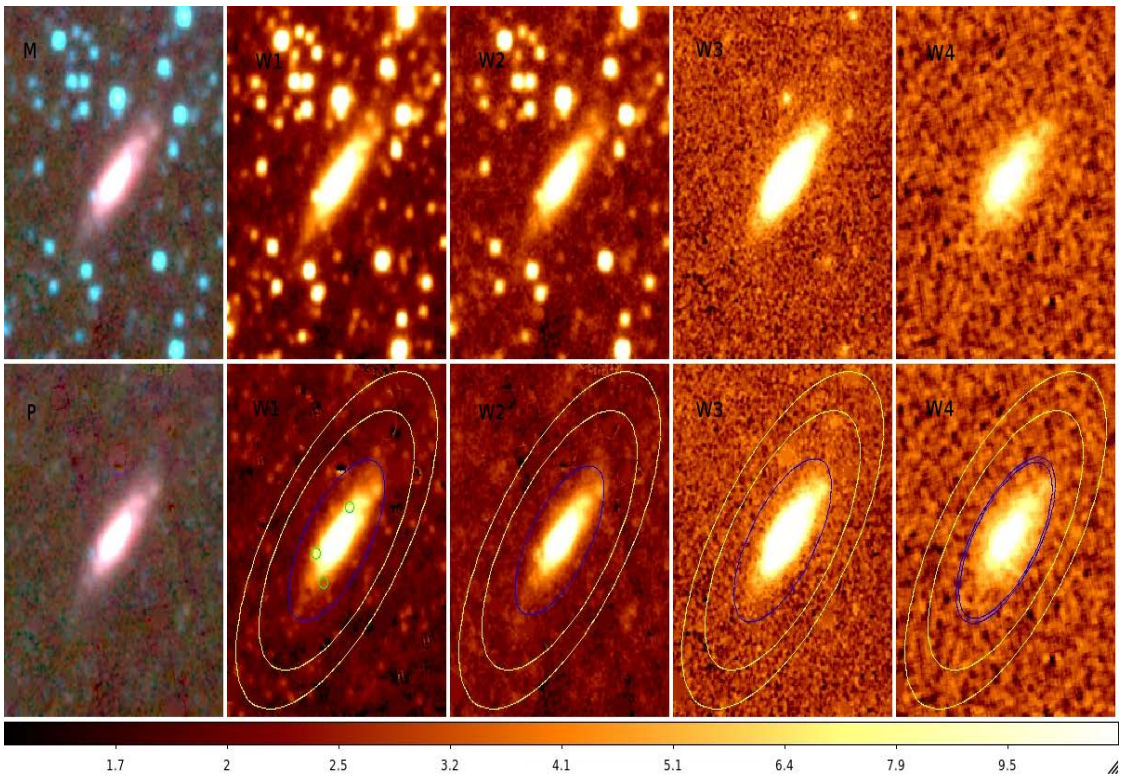

FIGURE 2.6: WISE resolved galaxy images of J0746-18 from the resolved galaxy WISE pipeline. The panel *M* is the unprocessed mosaic image of WISE W1, while the panel *P* is the processed mosaic image of WISE W1 from the WISE pipeline. The upper panels are the unprocessed images for various WISE bands, while the lower panels are the processed images for various WISE bands.

FIGURE 2.6 shows the resolved galaxy WISE images from the pipeline. The top roll images include the unprocessed mosaic colored image with label 'M' and the unprocessed mosaic WISE W1-W4 bands. The down roll images include the processed mosaic colored image with label 'P' and the processed mosaic images for the WISE W1-W4 bands.

2.4.1 Derived Parameters

When measuring light from an object using an astronomical detector, the astronomer must compensate for the fact that the pixels are not exactly uniform. Some pixels in a detector are more sensitive than others. The process of correcting for the effect of dimming of images towards the edge of telescope field of view[9] and the unequal sensitivity of each pixel is known as flat fielding. Also, the detector must be calibrated, by observing stars of known brightness to determine how many counts correspond to a given flux or magnitude. To produce an image of a galaxy, we must subtract out the contribution of the night sky, since only the brightest parts of the galaxies are brighter

[9] vignetting of the field

than the sky. This is done by measuring surface brightnesses down to $\lesssim 1.0$ % of the sky level by using dome or sky flat fields. Surface brightness is the measure of the flux concentration in units of mag arcsec^{-2} given as $\mu \propto \mu_0 - 2.5\log(I)$, where I is the intensity. Isophotal magnitude is the light measured within an isophote with surface brightness of 25 mag arcsec^{-2} given as $m_{ISO} \propto m_{ISO,0} - 2.5\log(f)$, where f is the integrated flux. One of the method for measuring the flux of a galaxy is to measure its profile by fitting a Sérsic function and then derive its flux. The Sérsic profile is a mathematical function that describe how the intensity of a galaxy varies with distance from its center expressed as

$$I(R) = I_0 \exp\Big[- \Big(\frac{R}{\alpha}\Big)^{1/n}\Big]. \tag{2.1}$$

Where $I(R)$ is the intensity at radius R, I_0 is the central intensity, α is the scale length at which the intensity drops by $\exp(-1)$ and n is the Sérsic index which varies with galaxy morphology. Sérsic index determines the concentration of the profile. For an elliptical galaxies with $n = 4$, the scale length α in equation (2.1) is too small to measure, therefore one often redefines the profile in terms of half-light radius also known as the effective radius. Therefore, the Sérsic profile in equation (2.1) can be rewritten in terms of de Vaucouleur's $r^{1/4}$ law commonly used for elliptical galaxies as

$$I(R) = I_e \exp\Big[- 7.67\Big(\frac{R}{R_e}\Big)^{1/4} - 1\Big], \tag{2.2}$$

where R_e radius containing half total light. The profile in equation (2.1) can be written as a generalization of de Vaucouleur's law for all n as

$$I(R) = I_e \exp\Big[- b_n\Big(\frac{R}{R_e}\Big)^{1/n} - 1\Big], \tag{2.3}$$

where b_n is a constant which is obtained from fitting the profile. For $n = 1$, profiles are fitted by an exponential profile, when $n = 4$, profiles are fitted by a de Vaucouleur's law. In reality, profiles are a combination of bulge profile which exhibit Sérsic fit and a disc profile which exhibit an exponential profile given as

$$I(R) = I_0^{disc} \exp\Big(- \frac{R}{R_d}\Big) + I_e^{bulge} \exp\Big[- 7.67\Big(\frac{R}{R_e}\Big)^{1/4} - 1\Big]. \tag{2.4}$$

Therefore to fit spiral/SO galaxy profiles requires the sum of $r^{1/4}$ plus exponential disk model (Sérsic, 1963, 1968; Ciotti, 1991; Caon et al., 1993; Cutri et al., 2003). FIGURE 2.7 shows the WISE W1-W4 bands surface brightness profile with Sérsic fit from the resolved galaxy WISE pipeline and surface brightness profile extraction from the WISE pipeline is similar to the description given in Section 3.3.

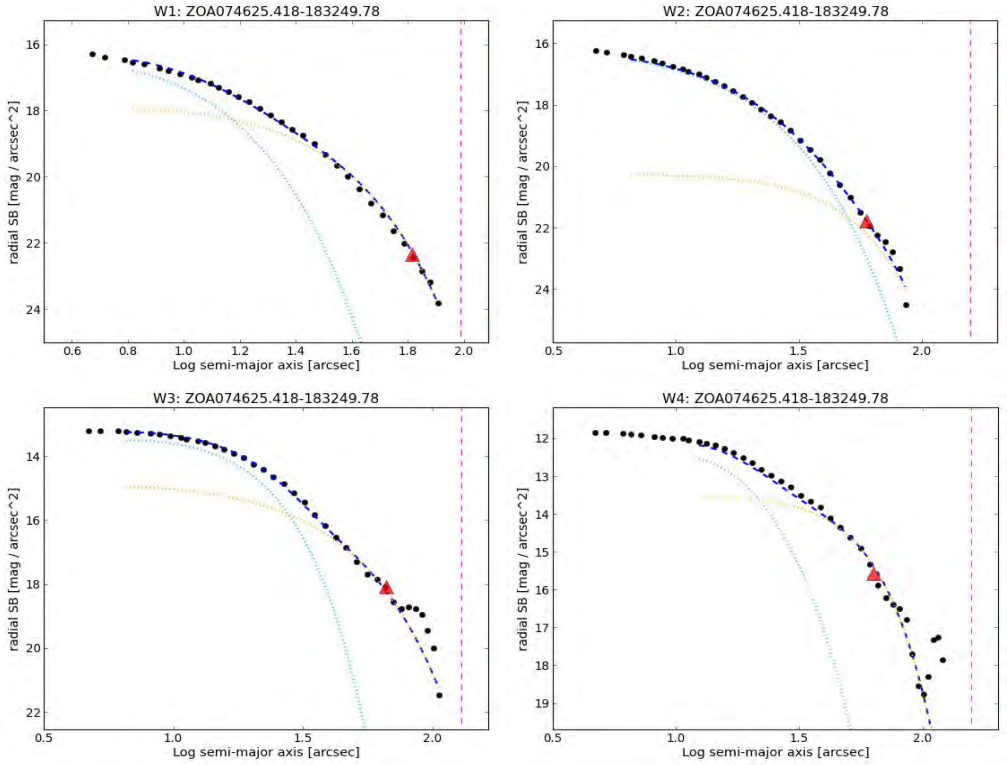

FIGURE 2.7: WISE W1-W4 bands surface brightness profile with Sérsic fit of J0746-18 from the resolved galaxy WISE pipeline. The blue dashed line is the 'bulge' component and the magenta dashed line is the 'disk' component of the double Sérsic function.

2.5 Project Website

I designed a project website using a bash script, that automatically reads data from a list, arranges the images and data tables, input links to astronomical data site and create an html web page. The project website consist of all the 1109 HIZoA possible galaxies, this includes the galaxy spectrum, the WISE online color image and the RGB image of the IRSF JHK_s bands observations and data. This site contains all the 451 possible resolved galaxies WISE W1-W4 bands photometry, their HI profile and IRSF observation and photometry. Also, this site consist of the resolved galaxy WISE photometry of observed IRSF brightest samples with $K_{s20fe} \leq 12^{\mathrm{m}}$. Furthermore, this website contains the full galaxies which have been carefully selected for cosmic flow analysis. These samples consist of the complete resolved galaxy WISE images, their surface brightness profile WISE W1-W4 bands, their IRSF and WISE photometry and links to NED and WISE online for each galaxy position. Furthermore, the website consist of the complete results of the effect of internal absorption on the magnitudes and radii for 2MASS JHK_s and WISE W1-W4 bands galaxies. The link to the project website can be found at http://www.ast.uct.ac.za/~affadi/patrick/patrick.html. One use

of this website is to provide a comprehensive view, easy comparisons between HI, IRSF and WISE observations of the ZoA galaxies.

2.6 Data Analysis

In this Section, we compared, analyzed and check the reliability of IRSF, 2MASS, online WISE and the resolved galaxy WISE data.

2.6.1 Near-Infrared and WISE Passbands

Astronomers notice that it was quite impossible to compare the measurements made by different observers with different equipment and different detectors. Therefore, they defined a series of standard passbands which could help observers to compare their results. Photometric system are mostly characterized by the widths of their passbands. Passbands wider than 30 nm are broadband filters, intermediate band filters are between 10 nm and 30 nm and narrow band filters are less than 10 nm wide (Binney & Merrifield, 1998). The main advantage of broadband filters is that they transmit lots of light which means one can detect faint objects with short exposure times or with a small telescopes. The narrow band filters cover a smaller range of wavelengths. Although, this set requires longer exposure times or larger telescopes to reach the same signal-to-noise (SNR) as the broadband filters. In reality, passbands are affected by the Earth's atmosphere, telescope optics, filters and detector types. The FIGURE 2.8 shows relative spectral response per photon for 2MASS JHK_s and WISE W1-W4 bands filters. Based on the width of the filters we could associate the 2MASS JHK_s band filters are narrow band as compared to WISE W3 and W4 filters which are broadband, while WISE W1 and W2 can be considered as an intermediate band as compared to WISE W3 and W4. In general the filters in FIGURE 2.8 are all broadband filters. The difference in the filters transmission can be attributed to the fact that there is no atmosphere transmission associated with WISE filters since they are space based. The filter transmission of WISE W1 and W2 are very high when compared to other filters. The image quality in the WISE W1 and W2 bands filters are suitable for photometric purposes as compared to other WISE bands.

2.6.2 Data and Observations Comparison

When we observe the HIZoA galaxies closely using the project website we can assume that the effect of dust in the near infrared bands are quite small. Although, we have observe some Galactic emissions close to the Galactic equator. The major problem

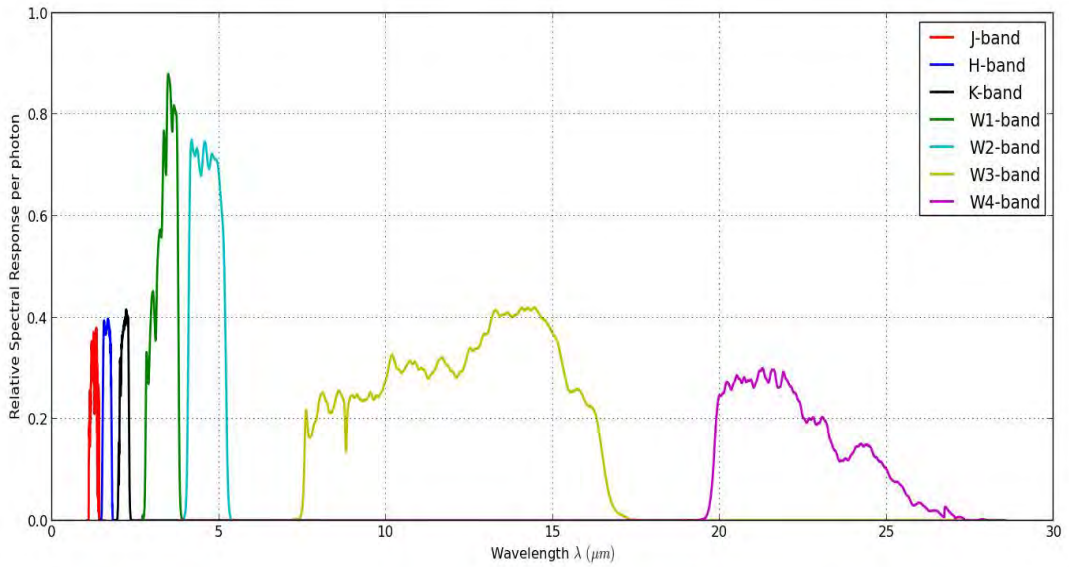

FIGURE 2.8: Filter transmission for JHK_s 2MASS & WISE W1-W4 bands. WISE data from Jarrett et al. (2011) and 2MASS data from Cutri et al. (2003) and Jarrett et al. (2003).

in this region is the effect of stellar crowding. This is quite obvious in the previous IRSF and 2MASS images of FIGURE 2.9(b) & (c). WISE observations of ZOA galaxies have shown that the effect stellar crowding is reduced as seen in FIGURE 2.9(a) & 2.5. Importantly, stellar obscuration vanishes when observing with WISE W4 band as seen in FIGURE 2.5. Galaxy identification in the IRSF, 2MASS and WISE images are unique in their own way, since the detection of a galaxy depends on the emission coming out from the galaxy. From the observed HIZoA galaxies, 152 HI galaxies revealed no counterpart on the IRSF images. These are mostly highly obscured with high stellar density. To see if WISE can improve on cross identification. We searched for 152 undetected IRSF HIZoA galaxies in WISE image, we found 30 possible WISE counterpart. Though, most of these sources are very faint with a red blob. A few of them appear as good candidate samples for further investigation and study. In general WISE observations provide a better galaxy identification when compared to IRSF and 2MASS observations for region in the low Galactic plane, this can be seen in FIGURE 2.4, 2.3, 2.5 & 2.9.

We compared the difference between resolved galaxy WISE photometry magnitude and the online WISE magnitude using the brightest ZoA galaxies. We found a strong offset between the online values and the resolved galaxy WISE values with high dispersion towards the faint magnitude as seen in TABLE 2.1. These shows that the online WISE photometry based on point source photometry, would not be good for cosmic flow field analysis. Also, we compared the 2MASS data with the IRSF data we found a slight

FIGURE 2.9: WISE, 2MASS, IRSF image of J1514-53 with position $l = 323.^{\circ}6$ & $b = 4.^{\circ}04$ and $A_V = 2.^{m}63$.

(a) WISE image of J1514-53 with image scale 1024 × 1024 pixel.

(b) 2MASS image of J1514-53 with image scale 512 × 1024 pixel.

(c) IRSF image of J1514-53 with image scale 1024 × 1024 pixel.

offset between the two data with slight dispersion about the mean as seen in TABLE 2.1. This shows that the 2MASS magnitudes are under estimated as compared to IRSF measurement. The summary of the comparison between 2MASS and IRSF data and between online WISE and resolved galaxy WISE data is given in the TABLE 2.1.

TABLE 2.1: Summary table of data comparison.

Difference between 2MASS & IRSF data				
Band	Slope	Mean	σ	Intercept
J	-0.1640	-0.0131	0.8390	2.0459
H	-0.1290	-0.0738	0.7018	1.4366
K	-0.1227	-0.0754	0.6901	1.3131
Difference between WISE resolved galaxy & online WISE data				
Band	Slope	Mean	σ	Intercept
W1	-0.1009	-0.1053	0.4155	0.9356
W2	-0.0971	-0.1827	0.4028	0.8065
W3	-0.0128	-0.3031	0.4360	-0.2124
W4	0.1181	-0.0655	0.5070	-0.7039

Chapter 3

Galactic Absorption in Spiral Galaxies

Galaxies behind the Milky Way suffer size reduction and dimming due to the obscuration by dust in the disc of our Galaxy (Riad et al., 2010). The isophotal magnitude of an obscured galaxy appears fainter than they really are. Therefore, additional correction on isophotal magnitudes are required to correct for the effect of extra dimming due to loss of their fainter outer regions in the disk. Extinction correction studies in the optical band by Fisher & Tully (1981); Hauschildt (1987); Cameron (1990) and in the Infrared, by Nagayama et al. (2004) and Riad et al. (2010) have shown that non-linear extra dimming correction on isophotal magnitude can be approximated by a linear relation for extinction levels $A_{Ks} \lesssim 1^{\rm m}$. Using the radial profile of a galaxy of a given type it is well possible to calculate the inward shift of that isophote towards the center of the galaxy in case of front absorption. This involve artificially absorbing the galaxy so that the limiting surface brightness decreases with the diameter of the galaxy. Cameron (1990) artificial absorbed a sample of elliptical and spiral galaxies in the B band magnitude and found that for absorption larger than $1^{\rm m}$, the correction due to diameter reduction becomes very significant. At B band absorption of $3^{\rm m}.5$, an elliptical galaxies will be additionally dimmed by $0^{\rm m}.8$, while a spiral galaxy by as much as $1^{\rm m}.6$. Thus, ZoA galaxies within their B band 25 mag arcsec^{-2} isophote, are actually brighter than their magnitudes would suggest. Riad et al. (2010) extended this study to include near-infrared bands galaxies and found that as compared to the optical band, the near-infrared K_s band is approximately 10 percent of the B band extinction values. In this research work we extended this study with 2MASS JHK_s bands and WISE W1-W4 bands. We adopted the method of Riad et al. (2010) and Cameron (1990) to obtain the Galactic absorption associated with galaxy in these bands. This method involve simulating extinction in

each band to correct for galaxy isophotal magnitude. We then compared the results obtained in each wave band with the K_s band extinction value at 1^{m} and 3^{m}.

3.1 Procedures

In Riad et al. (2010), the reduced radii $f(R)$ and isophotal magnitude Δm_{iso} were calculated as a function of extinction for each galaxy. These quantities can be expressed as

$$f(R) = \frac{R^{\circ}}{R}, \tag{3.1}$$

$$\Delta m_{iso} = m_{iso} - m^{\circ}_{iso}, \tag{3.2}$$

where m_{iso}, m°_{iso}, R, & R° are the total (intrinsic) and effective (absorbed) isophotal magnitude and radii respectively. The different values of $f(R)$ and Δm_{iso} corresponding to the simulated extinction value, were calculated and fitted with an empirical relation given by Cameron (1990) as,

$$f(R) = 10^{a(A_\lambda)^b}, \tag{3.3}$$

$$\Delta m_{iso} = F(A_\lambda)^v, \tag{3.4}$$

where F, v, a, b are the fitting parameters and A_λ is the Galactic extinction. The equation above was applied directly to correct for isophotal absolute magnitude M_{iso} given as,

$$M_{iso} = m_{iso,0} - A_\lambda - \Delta m_{iso} - 5\log V_{LG} - 15, \tag{3.5}$$

while the correction for isophotal apparent magnitude m_{iso} is given as,

$$m_{iso} = m_{iso,0} - A_\lambda - \Delta m_{iso}, \tag{3.6}$$

where $m_{iso,0}$ is the observed magnitude, A_λ is the Galactic dust extinction and Δm_{iso} is the Galactic absorption correction by Riad et al. (2010). Equation 3.5 implicitly uses a Hubble constant of 100 km/s/Mpc. The JHK_s and WISE bands isophotal magnitude correction was based on the optimized correction based on central surface brightness μ_c given by Riad et al. (2010). In Riad et al. (2010) the central surface brightness is a specific parameter from the 2MASS XSC $r \leq 5''$ of the mean surface brightness. The optimized correction for central surface brightness is given as,

$$f(R, \mu_c) = 10^{a(\mu_c)A_\lambda^{b(\mu_c)}}, \tag{3.7}$$

$$\Delta m_{iso}(\mu_c) = F(\mu_c)A_\lambda^{v(\mu_c)}, \tag{3.8}$$

with parameters defined as,

$$a(\mu_c) = a_0 \exp(\mu_c \cdot a_1), \tag{3.9}$$

$$b(\mu_c) = b_0 \exp(\mu_c \cdot b_1), \tag{3.10}$$

$$F(\mu_c) = F_0 \exp(\mu_c \cdot F_1), \tag{3.11}$$

$$v(\mu_c) = v_0 \exp(\mu_c \cdot v_1). \tag{3.12}$$

This formalism entails using an optimized correction based on central surface brightness to determine the fitting parameters a_0, a_1, b_0, b_1, F_0, F_1, v_0 & v_1 for each of the bands.

3.2 Candidate Sample Selection

To understand the effect of Galactic absorption on 2MASS JHK_s and WISE W1-W4 bands isophotal magnitude we selected 10 galaxies from the Spitzer Infrared Nearby Galaxies Survey (SINGS) which are common to Riad et al. (2010) selected galaxies. We obtain the JHK_s bands photometry as well as fits files of our selected galaxies from Jarrett et al. (2003) 2MASS extended source catalogue in the 2MASS online image server. For the WISE bands, we obtained a resolved galaxy photometry and mosaics fits of the selected galaxies using the WISE pipeline (Jarrett et al., 2013).

TABLE 3.1: Candidate samples selection from 2MASS JHK_s & WISE W1-W4 bands spiral galaxies. These spiral galaxies were selected to determine the effect of Galactic absorption in 2MASS JHK_s & WISE W1-W4 bands.

Candidate samples selection from 2MASS & WISE bands spiral galaxies				
Galaxy	RA	Dec	Morphology	Inclination
NGC 0024	2.485583	-24.963139	SA(s)c	edge-on
NGC 4321	185.728463	15.821818	SAB(s)bc	face-on
NGC 4501	187.996503	14.420387	SA(rs)b	face-on
NGC 4569	189.207470	13.162940	SAB(rs)ab	face-on
NGC 4594	189.9976325	-11.6230544	SA(s)a	edge-on
NGC 4736	192.721088	41.120458	SA(r)ab	face-on
NGC 4826	194.181837	21.682970	SA(rs)ab	face-on
NGC 5055	198.955542	42.029278	SA(rs)bc	face-on
NGC 0628	24.1739458	15.7836619	SA(s)c	face-on
NGC 6861	301.831167	-48.370222	SA(s)0-	edge-on

3.3 Surface Brightness Profile Extraction

We extracted the surface brightness profile of the selected candidate galaxies using IRAF software. This was done using an IRAF package called isophote, and then applying

IRAF sub-task called ellipse. To obtain the surface brightness profile, we set the ellipse and geompar parameters sub-task in IRAF software using the information from the fit image header. From the parameters generated we converted the intensity I into surface brightness μ using

$$\mu = \mu_0 - 2.5\log(I), \tag{3.13}$$

where μ_0 is the zero point surface brightness. The isophotal magnitude m_{ISO} was obtained using

$$m_{ISO} = m_{ISO,0} - 2.5\log(f), \tag{3.14}$$

where f is the integrated flux of the elliptical aperture measured in mag arcsec^{-2} and $m_{ISO,0}$ is the zero point isophotal magnitude.

FIGURE 3.1: 2MASS JHK_s bands surface brightness profile of NGC 4501. These was obtained using IRAF software sub-task called ellipse using the output parameter "intensity" and the equation in (3.13), we obtained the surface brightness.

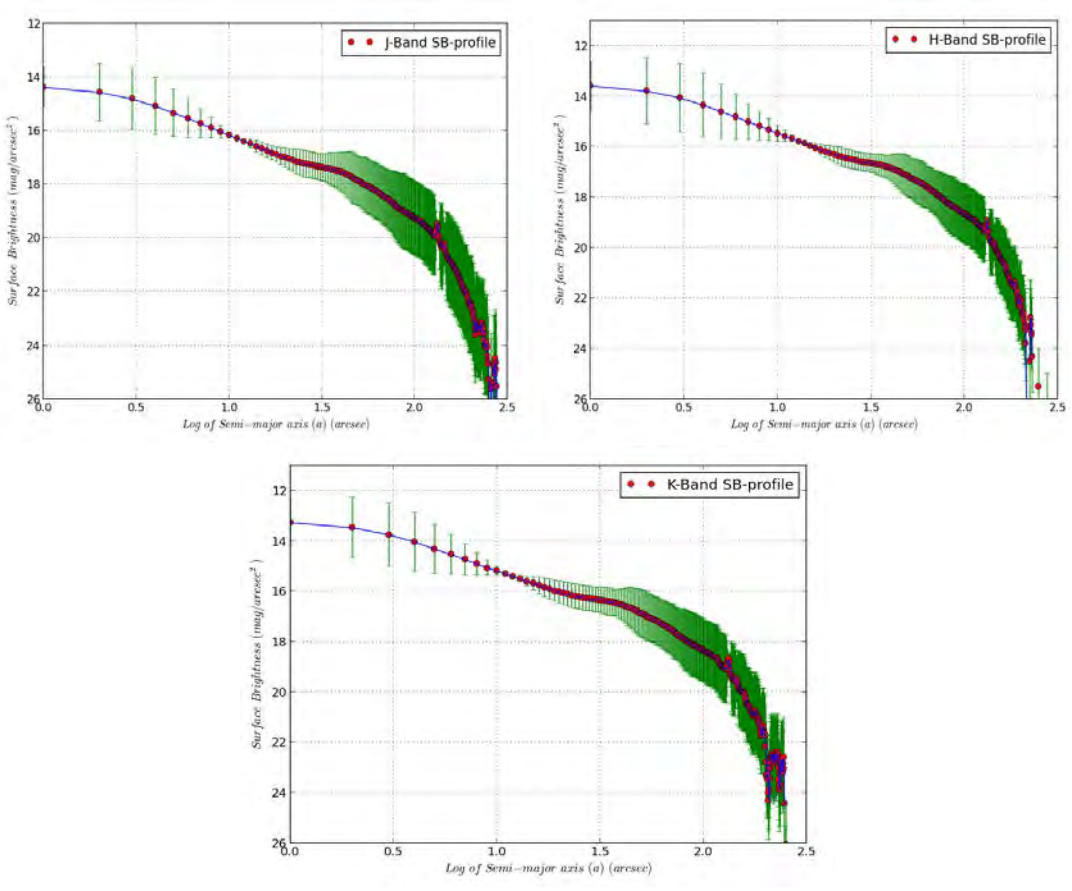

FIGURE 3.2: WISE W1-W4 bands surface brightness profile of NGC 4501. These was obtained using IRAF software sub-task called ellipse using the output "intensity" we obtained the surface brightness.

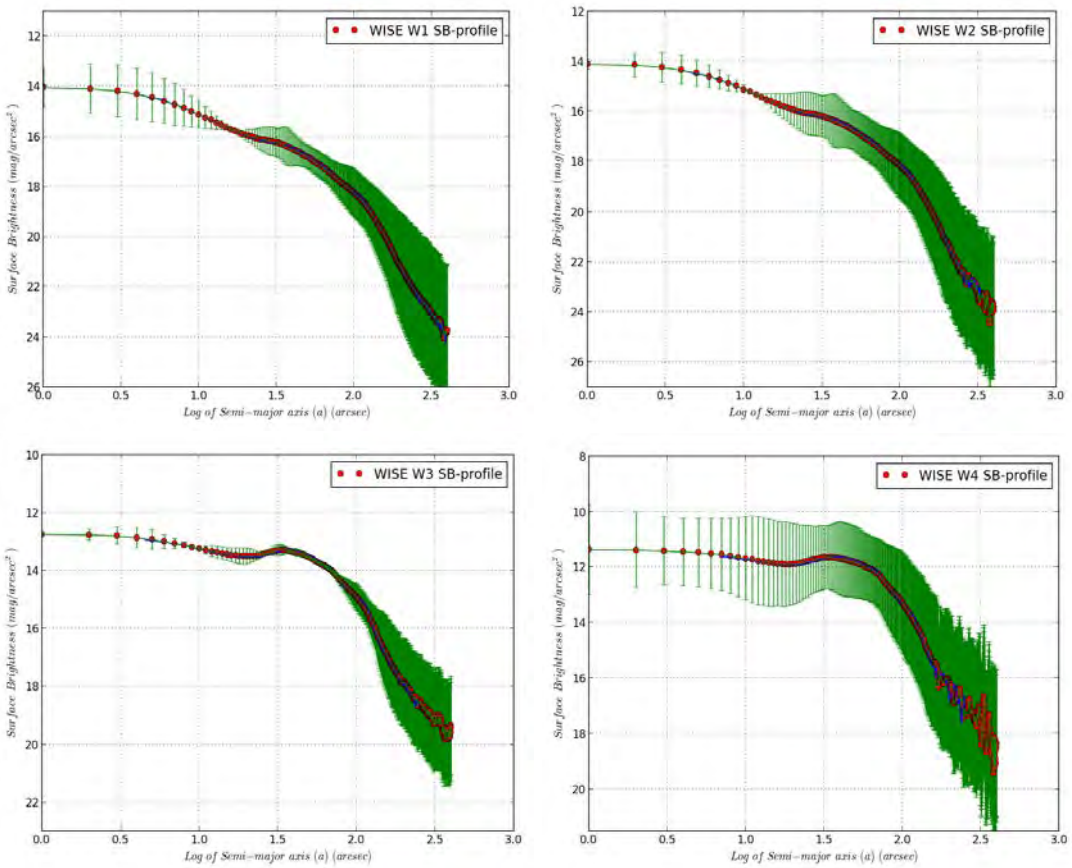

3.3.1 K_s Band Galactic Dust Conversion

For the Galactic extinction estimate used in this method we used a standard extinction map by Schlafly & Finkbeiner (2011) which take into consideration some of the flaws encountered in IRAS/DIRBE maps of Schlegel et al. (1998). The Galactic dust extinction in Equation 3.16−3.3.1 is obtained using the Cardelli et al. (1989) equations described in Section 1.3.4. The Galactic extinction equivalence to K_s band extinction was obtained from the calculated values in equations (4.15-4.20)[1] using the infrared band Galactic dust extinction estimate of Cardelli et al. (1989) and $E(B-V)$ values of Schlafly & Finkbeiner (2011). We obtained the K_s band Galactic dust extinction equivalence to other band as

[1] A clear description of Galactic dust extinction is given in Chapter 1&4

$$A_J = 2.3943\, A_{Ks}, \tag{3.15}$$

$$A_H = 1.5312\, A_{Ks}, \tag{3.16}$$

$$A_K = 1.0000\, A_{Ks}, \tag{3.17}$$

$$A_{W1} = 0.4362\, A_{Ks}, \tag{3.18}$$

$$A_{W2} = 0.2938\, A_{Ks}, \tag{3.19}$$

$$A_{W3} = 0.0627\, A_{Ks}, \tag{3.20}$$

$$A_{W4} = 0.0235\, A_{Ks}. \tag{3.21}$$

3.4 Extinction Simulation in JHK_s and WISE Bands

The effect of Galactic absorption on the isophotal magnitude and radii of a galaxy was performed by applying an inward displacement of the limiting isophote along the surface brightness profile. The limiting isophotal was shifted in uniform steps along the galaxy light profile with each step being equivalent to a certain extinction level in the investigated band. Starting from the 1σ background level obtained from the fit image header, we simulated a maximum of 3^{m} of extinction in the each waveband for our selected galaxy samples. We determined the radius of intercept of the 1σ background $R_\circ$ and the radius of intercept of the 0^{m} - 3^{m} simulation extinction levels of the each waveband to the surface brightness profile as seen in FIGURE 3.3-3.9[2]. Therefore, using equation (3.1 & 3.2) we determined the f-ratio $f(R)$ and extinction Δm. We plotted these quantities $f(R)$ and Δm as a function of simulated extinction in each waveband. We then fit the resulting plots of $f(R)$ and Δm with the formalism of Cameron (1990) given in equation (3.3 & 3.4) respectively to derive the fitting parameters a_0, a_1, b_0, b_1, F_0, F_1, v_0 & v_1 for each of the wavebands. The fitting of the simulated extinction made use of package called curve_fit in the scipy.optimize module in python. The 1σ fits to the data were good, but the assumed initial values varies with each fits. The fitting parameters for 2MASS JHK_s and WISE W1-W4 bands based on optimized correction for central surface brightness obtained from fitting the quantities $f(R)$ and Δm_{iso} as a function of simulated extinction value in each waveband is given in TABLE 3.2. The Galactic absorption analysis and the plots and fits for 2MASS JHK_s and WISE W1-W4 bands is given in FIGURE 3.3-3.16.

[2]The complete analysis for all selected galaxies can be found at http://www.ast.uct.ac.za/~affadi/patrick/patrick.html

FIGURE 3.3: 2MASS J band isophotal magnitude analysis of NGC 4501. In the surface brightness plot the lines represent the simulated extinction between 0^{m}-3^{m} in each waveband.

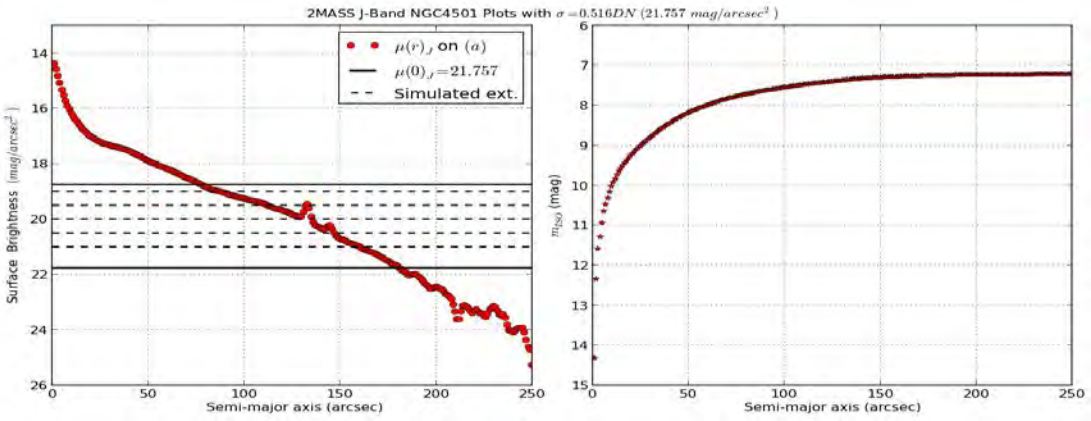

FIGURE 3.4: 2MASS H band isophotal magnitude analysis of NGC 4501. In the surface brightness plot the lines represent the simulated extinction between 0^{m}-3^{m} in each waveband.

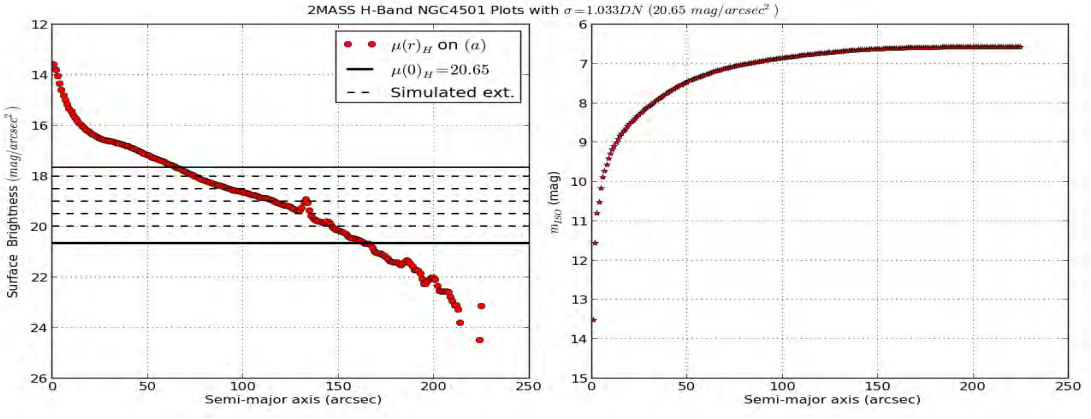

FIGURE 3.5: 2MASS K_s band isophotal magnitude analysis of NGC 4501. In the surface brightness plot the lines represent the simulated extinction between 0^{m}-3^{m} in each waveband.

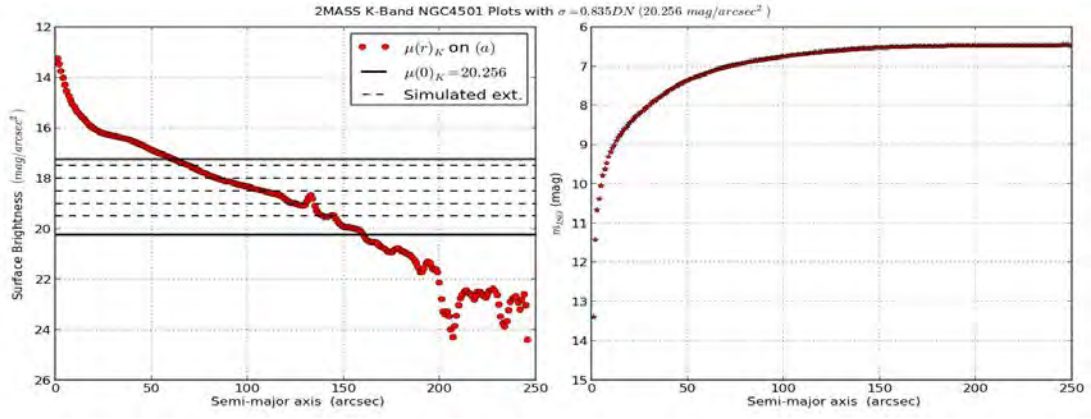

FIGURE 3.6: WISE W1 band isophotal magnitude analysis of NGC 4501. In the surface brightness plot the lines represent the simulated extinction between 0^m-3^m in each waveband.

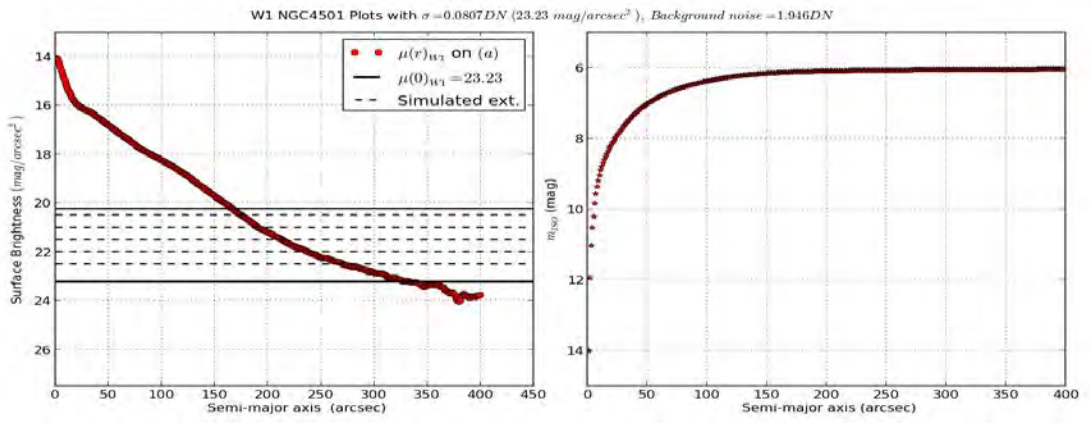

FIGURE 3.7: WISE W2 band isophotal magnitude analysis of NGC 4501. In the surface brightness plot the lines represent the simulated extinction between 0^m-3^m in each waveband.

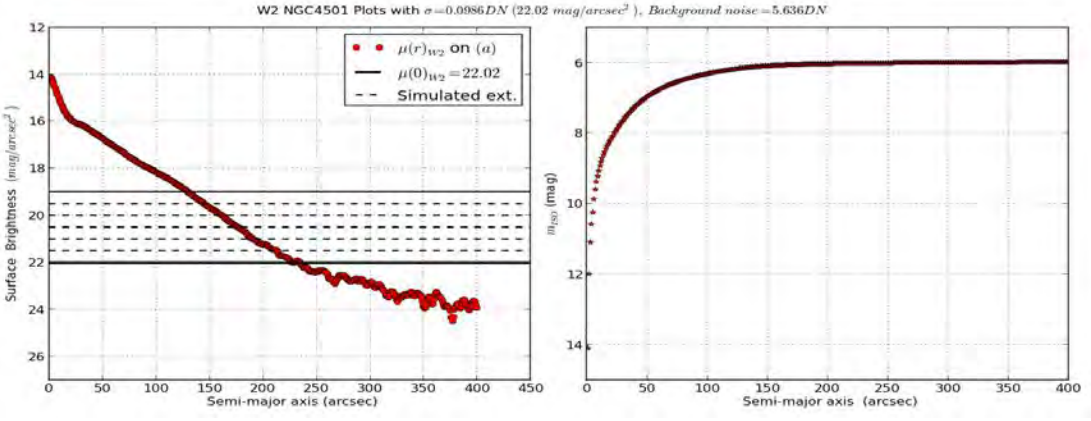

FIGURE 3.8: WISE W3 band isophotal magnitude analysis of NGC 4501. In the surface brightness plot the lines represent the simulated extinction between 0^m-3^m in each waveband.

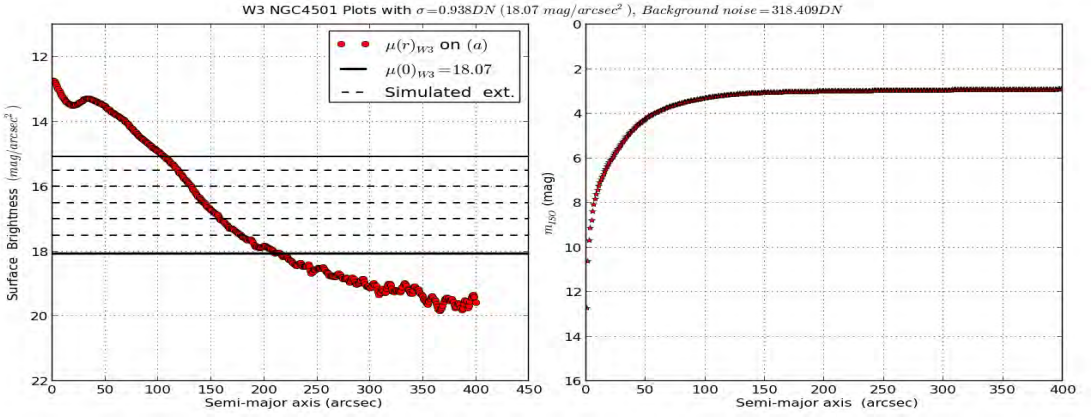

FIGURE 3.9: WISE W4 band isophotal magnitude analysis of NGC 4501. In the surface brightness plot the lines represent the simulated extinction between 0^{m}-3^{m} in each waveband.

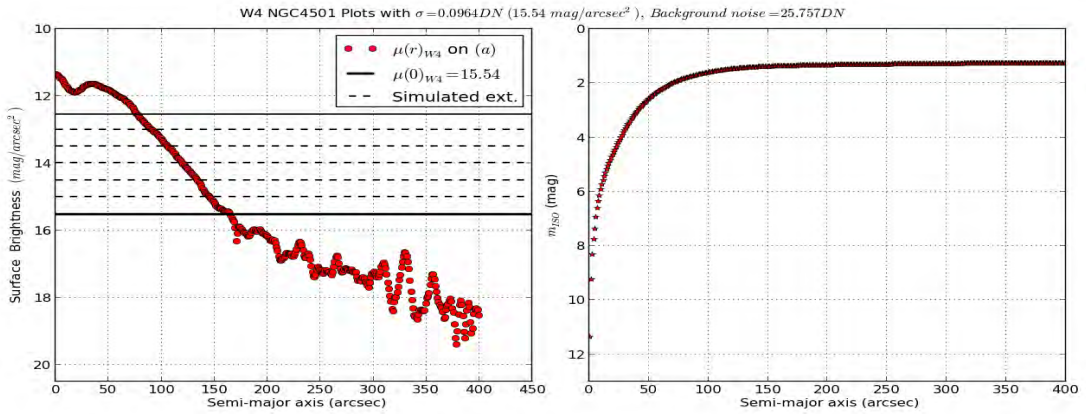

FIGURE 3.10: 2MASS J band fitting plots of $\Delta m \,\&\, f(R)$ for NGC 4501. Using the equation in (3.3-3.4) we fitted the simulated extinction Δm and reduced radii $f(R)$ as a function of K_s band Galactic extinction.

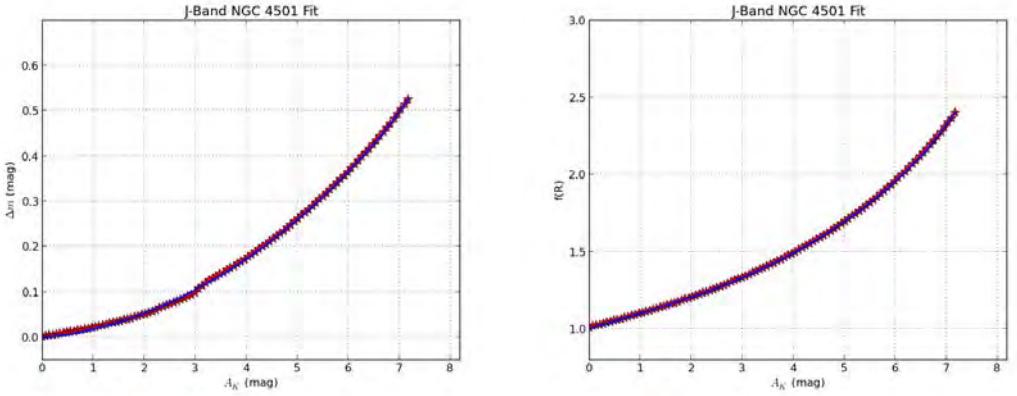

FIGURE 3.11: 2MASS H band fitting plots of $\Delta m \,\&\, f(R)$ for NGC 4501. Using the equation in (3.3-3.4) we fitted the simulated extinction Δm and reduced radii $f(R)$ as a function of K_s band Galactic extinction.

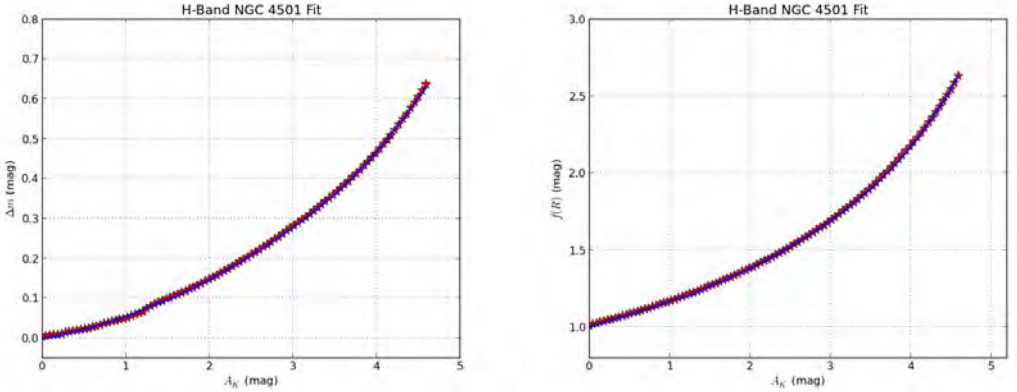

FIGURE 3.12: 2MASS K_s band fitting plots of Δm & $f(R)$ for NGC 4501. Using the equation in (3.3-3.4) we fitted the simulated extinction Δm and reduced radii $f(R)$ as a function of K_s band Galactic extinction.

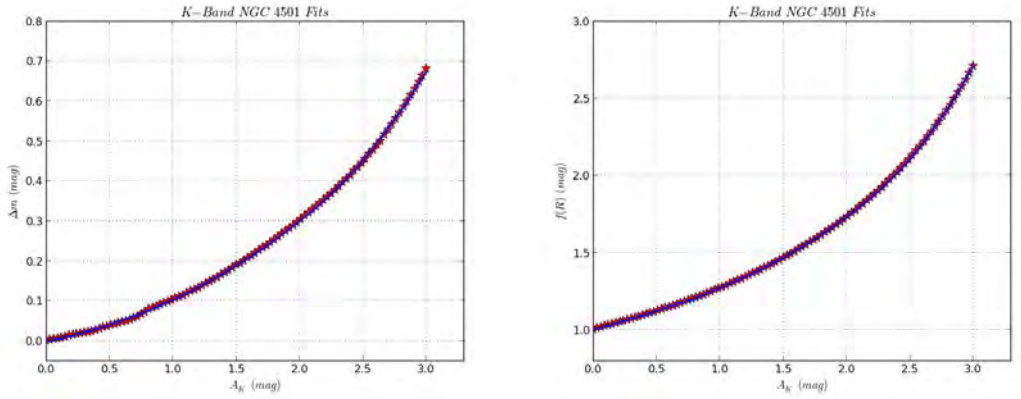

FIGURE 3.13: WISE W1 fitting plots of Δm & $f(R)$ for NGC 4501. Using the equation in (3.3-3.4) we fitted the simulated extinction Δm and reduced radii $f(R)$ as a function of K_s band Galactic extinction.

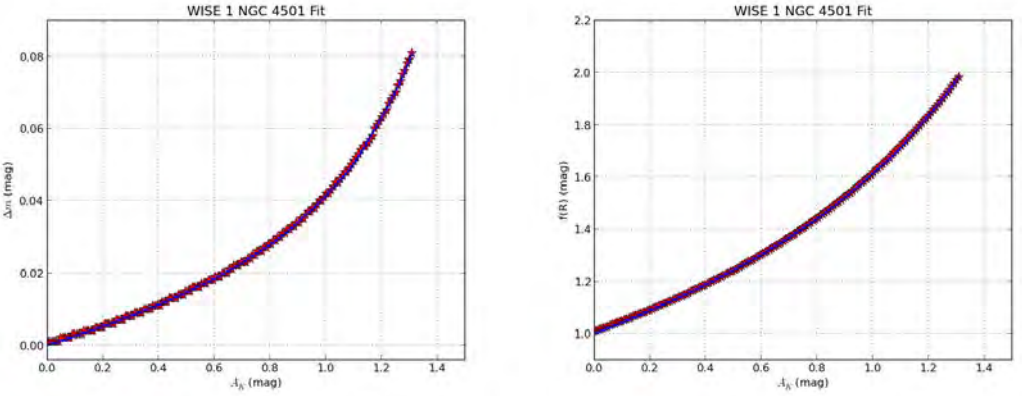

FIGURE 3.14: WISE W2 fitting plots of Δm & $f(R)$ for NGC 4501. Using the equation in (3.3-3.4) we fitted the simulated extinction Δm and reduced radii $f(R)$ as a function of K_s band Galactic extinction.

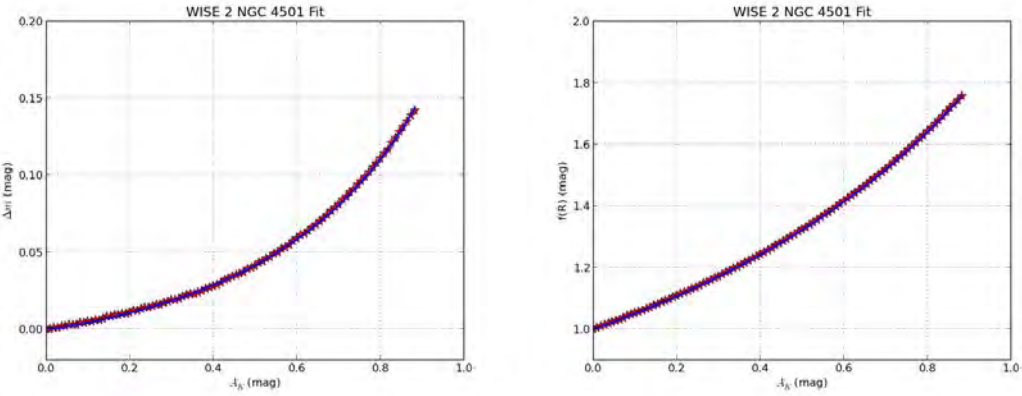

FIGURE 3.15: WISE W3 fitting plots of Δm & $f(R)$ for NGC 4501. Using the equation in (3.3-3.4) we fitted the simulated extinction Δm and reduced radii $f(R)$ as a function of K_s band Galactic extinction.

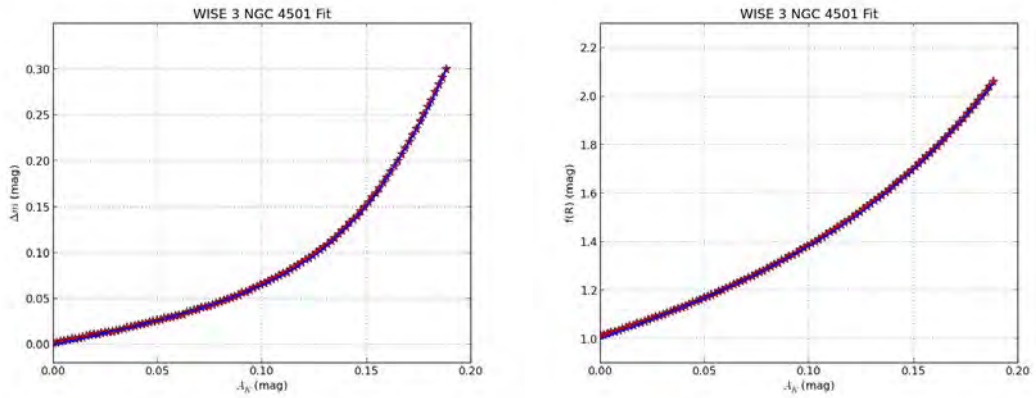

FIGURE 3.16: WISE W4 fitting plots of Δm & $f(R)$ for NGC 4501. Using the equation in (3.3-3.4) we fitted the simulated extinction Δm and reduced radii $f(R)$ as a function of K_s band Galactic extinction.

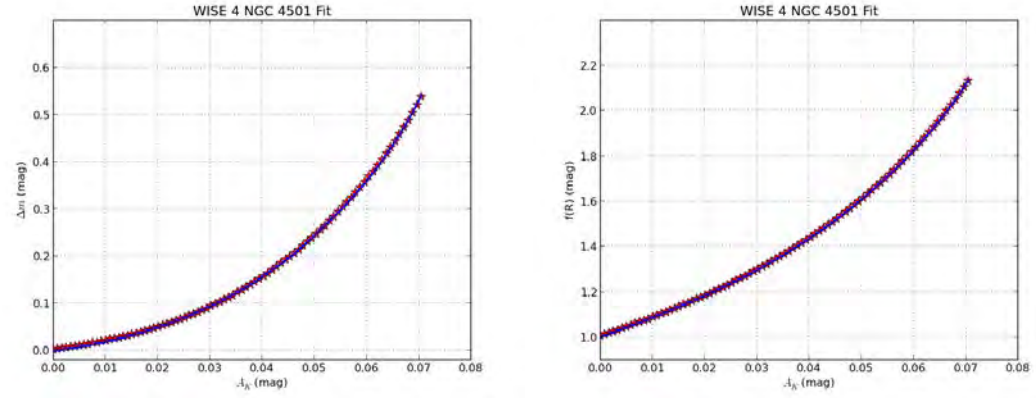

TABLE 3.2: Fitting parameters of 2MASS JHK_s & WISE W1-W4 bands for selected spiral galaxies candidates. Fitting parameters for WISE bands based on optimized correction for central surface brightness obtained from fitting the quantities $f(R)$ and Δm_{iso} as a function of simulated extinction value in each waveband. The fitting parameter obtained is not constant, this shows that the effect of internal absorption varies with each galaxies.

Fitting parameters of 2MASS JHK_s & WISE W1-W4 band spiral galaxies

Galaxy	Band	a_0	a_1	b_0	b_1	F_0	F_1	v_0	v_1
	J	49554.6	-0.6138	0.3076	1e-11	1.3252e+8	-0.9777	0.2044	1e-11
	H	10178064	-0.9176	9.6623	-2.1665	9.9737e+9	-1.2427	10.0745	-1.5556
	K_s	0.6246	-0.0839	12.5739	-0.1336	9.8451	-0.1911	39.8305	-0.1895
NGC 0024	W1	0.0830	0.0046	5.7057	-0.0781	1.5633	-0.1657	16.7586	-0.1185
	W2	0.7047	-0.0832	5.5428	-0.0897	0.2210	-0.0311	54.7333	-0.1875
	W3	0.1750	1e-12	555.19	-0.3940	0.2394	1e-12	324.2384	-0.3299
	W4	0.0309	1e-12	0.0807	0.2753	0.3549	1e-12	1692.18	-0.4895
	J	821.341	-0.4236	0.9824	1e-12	0.0005	0.2947	45.4803	-0.1542
	H	29.8924	-0.2761	1.2613	1e-12	6.3394	-0.1642	1.5662	6.4034e-13
	K_s	11.9008	-0.2356	1.3833	2.3685e-12	8.77e-4	0.3022	24.0585	-0.1366
NGC 4321	W1	0.1433	-0.0256	1.8168	-0.0223	40.6204	-0.3226	0.9806	1.2849e-13
	W2	0.01878	0.0868	13.9134	-0.1279	0.0069	0.1104	53.1068	-0.1713
	W3	0.0127	0.1158	4.1648	-0.0723	0.0351	0.0310	7.0431	-0.0782
	W4	0.0256	0.0922	5.5063	-0.1088	0.0463	0.0517	3.2280	-0.0441
	J	0.0451	0.0380	8.4600	-0.1004	0.0815	-0.0066	4.5068	-0.0489
	H	0.0392	0.0511	7.7768	-0.09998	0.4954	-0.0832	5.3516	-0.0705
	K_s	0.0467	0.04262	6.8175	-0.0939	0.1401	-0.0161	8.9590	-0.0975
NGC 4501	W1	1.7371	-0.1357	0.4705	0.0313	0.1481	-0.1098	17.4767	-0.1231
	W2	0.0851	-0.0111	2.3366	-0.0372	0.0181	1e-12	23.5522	-0.1333
	W3	0.1093	-0.0140	2.3610	-0.0482	0.0458	-0.0165	39.3293	-0.2011
	W4	0.0818	0.0043	2.9058	-0.0697	0.4801	-0.1409	5.6585	-0.0962
	J	26.2204	-0.2583	0.9042	4.4493e-12	295.0301	-0.3770	1.1451	1.2297e-14
	H	23.6168	-0.2628	0.9407	2.7934e-13	213.3643	-0.3691	1.1399	3.4572e-13
	K_s	0.0149	0.1167	19.7808	-0.1451	143.1008	-0.3521	1.1258	1.8438e-13
NGC 4569	W1	12.3133	-0.2371	0.7667	-1.3975e-13	0.0231	1e-13	10.9332	-0.0906
	W2	0.0085	0.1213	9.5413	-0.1007	0.0664	1e-12	36.4279	-0.1637
	W3	0.0339	0.0578	4.0199	-0.0722	0.0427	1e-11	11.0175	-0.1217
	W4	45.0492	-0.4121	0.0037	0.3570	0.0235	0.0388	25.4714	-0.2032
	J	0.0144	0.0906	7.5878	-0.0909	0.0184	0.0551	71.6712	-0.2001
	H	0.0185	0.0828	6.8778	-0.0892	0.0160	0.0557	21.8827	-0.1368
	K_s	0.0695	0.0234	6.5436	-0.0949	0.0175	0.0757	12.8502	-0.1131
NGC 4594	W1	10.1999	-0.2112	0.8632	-6.9484e-14	191.3887	-0.4055	0.9759	3.5208e-13
	W2	6.9906	-0.1938	0.8392	1.0496e-13	88.3828	-0.3570	0.8673	2.1767e-13
	W3	0.0213	0.1076	12.7110	-0.1384	0.4386	-0.0540	3.3359	-0.0453
	W4	0.0770	0.0391	8.3121	-0.1335	0.0198	0.1848	24.5479	-0.2065
	J	0.1108	3.9464e-13	12.6934	-0.1257	1.4591	-0.1623	1.4241	2.1793e-13
	H	6.5156	-0.2120	1.0005	2.2675e-12	0.6416	-0.1207	1.4555	4.8065e-13
	K_s	2.2999	-0.1583	1.0575	5.8845e-13	0.0120	0.0970	8.0137	-0.0912
NGC 4736	W1	1.3862	-0.1143	1.1525	3.9278e-13	0.00542	0.0905	4.1454	-0.0473
	W2	0.1209	-0.00015	3.4528	-0.0524	1.3585	-0.1527	0.9482	1.0534e-13
	W3	0.1375	0.00043	8.0457	-0.1283	1.6157	-0.2030	37.4051	-0.2234
	W4	0.0014	0.2931	14.3332	-0.1632	0.0014	0.2362	13.8200	-0.1552
	J	14.8357	0.8152	-0.2471	6.3054e-13	3068.41	-0.5299	0.8885	1e-12
	H	0.0117	0.1080	8.1504	-0.0965	1.1745	-0.1463	8.2661	-0.0940
	K_s	19.1682	-0.2733	0.8500	6.3552e-13	0.2871	-0.0616	12.1674	-0.1157
NGC 4826	W1	0.1178	-0.0248	2.6324	-0.0440	0.0066	0.0215	17.1643	-0.1111
	W2	0.0718	0.0099	4.1069	-0.0643	0.1157	-0.0646	12.2248	-0.1068
	W3	1.1194	-0.1328	1.0854	-1.4766e-13	0.0034	0.1560	13.7292	-0.1321
	W4	0.6064	-0.1191	0.9031	0.0056	0.5959	-0.1937	3.2454	-0.0768
	J	66.8813	-0.3112	0.8085	2.8014e-12	1.2340	-0.1051	10.9280	-0.1077
	H	62.9299	-0.3211	0.8256	5.4007e-13	0.3827	-0.0572	11.6367	-0.1085
	K_s	95.0186	-0.3413	0.6770	7.6694e-12	1658.29	-0.4889	0.8125	7.1343e-14
NGC 5055	W1	0.1980	-0.0318	4.0412	-0.0636	0.2277	-0.0925	12.1188	-0.1034
	W2	0.3552	-0.0586	3.3882	-0.0599	0.8734	-0.1407	17.2193	-0.1299
	W3	0.0370	0.0494	3.9137	-0.0709	0.0053	0.1160	14.8070	-0.1255
	W4	0.0176	0.1353	11.0352	-0.1580	0.0077	0.1837	13.6691	-0.1466
	W1	0.03575	0.0393	6.4959	-0.0826	4.1220e+9	-1.1607	9.1655e-05	-2.2725
NGC 0628	W2	59.3031	-0.3019	0.7536	1e-12	5345.43	-0.5214	0.9460	1e-12
	W3	0.0125	0.1295	9.9006	-0.1261	17.2952	-0.3020	1.6124	1e-13
	W4	2.7370	-0.2532	2.1632	1e-13	7.1605e-05	0.5982	68.3681	-0.2426
	W1	0.8947	-0.0887	3.1246	-0.0530	0.1612	-0.0583	11.5186	-0.1057
NGC 6861	W2	7.5688	0.8690	-0.1882	-2.1162e-13	139.2984	-0.3632	0.7446	7.6912e-14
	W3	0.3425	-0.0613	2.0264	-0.0389	0.0267	0.0623	22.3427	-0.1699
	W4	0.0817	0.0359	6.3310	-0.1201	10.6457	-0.2636	1.0898	5.6791e-13

3.5 Isophotal Magnitudes and Radii Correction

The magnitudes and radii of infrared galaxies are mostly affected by stellar light with a minimized distorting effects due to gas and dust extinction (Kraan-Korteweg & Jarrett, 2005). The optimized correction based on central surface brightness requires knowledge of the galaxy's light profile. The use of optimized corrections based on central surface brightness to estimate the internal absorption associated with galaxy magnitudes and radii is useful as it can be independently used to categorize galaxies into early or late type (Cameron, 1990; Riad et al., 2010). The Galactic absorption associated with 2MASS JHK_s and WISE W1-W4 bands isophotal magnitude and radii were obtained using the method described by Cameron (1990) & Riad et al. (2010). By using the fitting parameters obtained based on optimized correction for central surface brightness to correct for the magnitudes and radii of IRSF JHK_s bands, 2MASS JHK_s bands and WISE W1-W4 bands spiral galaxies. The additional correction in the 2MASS JHK_s and WISE W1-W4 bands magnitudes and radii for different absorption values are plotted in FIGURE 3.17−3.23 for all the galaxies in our samples. While the spiral galaxies correction at $1^{\rm m}$ K_s band equivalence conversion for each waveband is given in TABLE 3.3. From the plots in FIGURE 3.17 one could observed that the maximum correction for a spiral galaxies at $1^{\rm m}$ K_s band equivalence for J band magnitudes is about $1^{\rm m}.2$, while the radii correction is about 3.55. For K_s band spiral galaxies the maximum additional correction at $1^{\rm m}$ for K_s band galaxy magnitude is $0^{\rm m}.3$, while the radii correction is about 1.5. The plot in FIGURE 3.20 shows that the maximum K_s band equivalence correction required for WISE W1 band magnitudes is about $0^{\rm m}.02$ and the radii correction is about 1.14. The maximum K_s band equivalence correction required for WISE W2 band magnitudes is about $0^{\rm m}.035$ and the radii correction is about 1.12. The magnitude and radii corrections for other bands is given in TABLE 3.3.

Therefore, a spiral galaxy with observed radius R and isophotal magnitude m in the IRSF JHK_s, 2MASS JHK_s and WISE W1-W4 bands is corrected using the relation $m_{cor} = m - A_\lambda - \Delta m$ in equation (3.6), where A_λ is the Galactic dust extinction and Δm is the Galactic absorption associated with the isophotal magnitude observed at wavelength λ. The total radii R° for galaxy observed at wavelength λ is $R^\circ = f(R)\, R$ given in equation (3.1). The analysis above shows that the correction to internal absorption are quite obvious for JHK_s bands magnitudes and radii. This corrections become very negligible for WISE W1-W4 isophotal magnitudes and radii. The values obtained for 2MASS JHK_s bands were used to correct for IRSF JHK_s bands. Using Cameron (1990) Galactic absorption values for B band galaxies as comparison. We found that the K_s band Galactic absorption is about 8.8 % of the Galactic absorption in the B band, while the WISE W1 band is about 1.03 % of the Galactic absorption

in the B bands. The Galactic absorption of K_s band in this work agrees with what is obtained by Riad et al. (2010) for Near-Infrared bands.

TABLE 3.3: Spiral galaxies maximum additional corrections at 1^m K_s band equivalence from our selected galaxies for 2MASS JHK_s & WISE W1-W4 bands and the extinction equivalent percentage in the B band given by Cameron (1990).

Spiral galaxies maximum correction at 1^m K_s band equivalence				
Survey	band	Δm	$f(R)$	B band estimate in %
	J	$1^m.200 \pm 0^m.010$	3.55 ± 0.01	35.25
2MASS	H	$0^m.550 \pm 0^m.010$	2.00 ± 0.01	16.15
	K_s	$0^m.300 \pm 0^m.010$	1.50 ± 0.01	8.81
	W1	$0^m.020 \pm 0^m.001$	1.14 ± 0.01	0.59
WISE	W2	$0^m.035 \pm 0^m.001$	1.12 ± 0.01	1.03
	W3	$0^m.015 \pm 0^m.002$	1.05 ± 0.01	0.44
	W4	$0^m.015 \pm 0^m.002$	1.02 ± 0.01	0.43

Other bands Galactic absorption equivalent for B band is given in TABLE 3.3. Also, we have shown that the different morphological types of spiral galaxies are affected differently by Galactic absorption as seen in FIGURE 3.17 – 3.23. Galaxies with an exponential light profile bulge requires larger correction as compared to galaxies with a de Vaucouleurs profile or a bulge plus disc profile that require a lesser correction (Riad et al., 2010).

FIGURE 3.17: 2MASS J band isophotal magnitude correction for various galaxies.

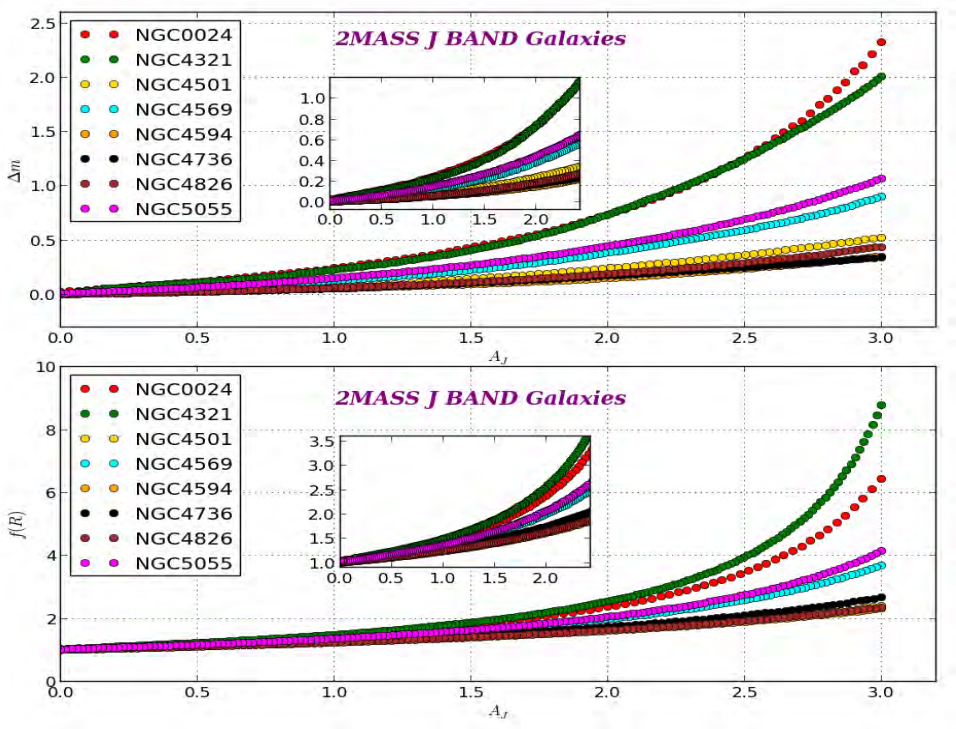

FIGURE 3.18: 2MASS H band isophotal magnitude correction for various galaxies.

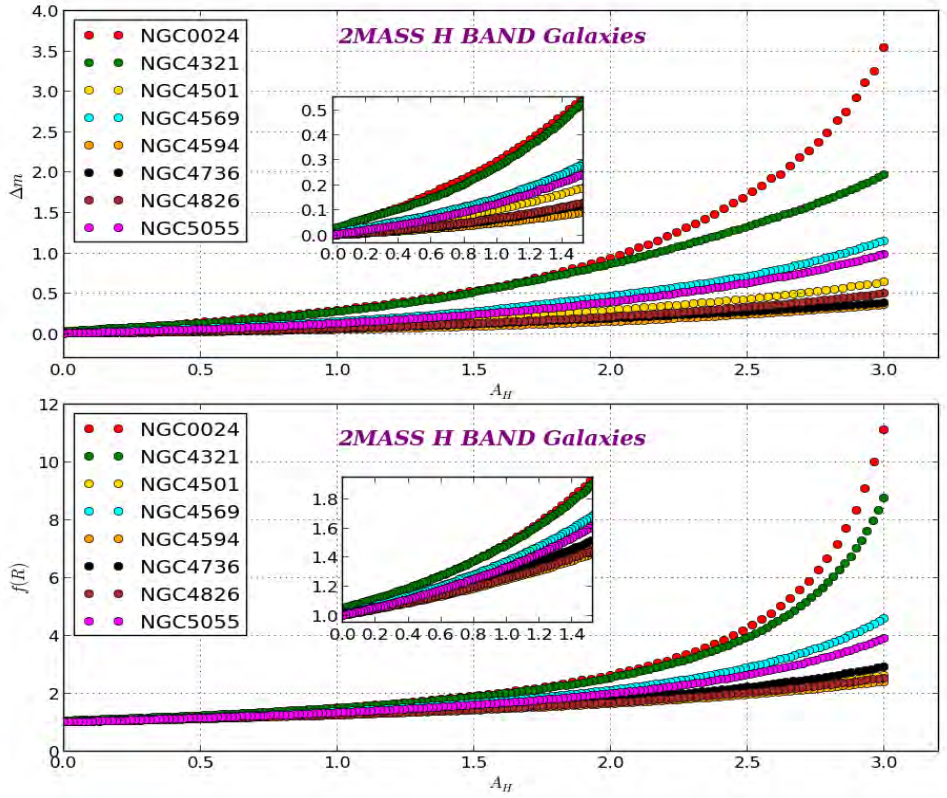

FIGURE 3.19: 2MASS K_s band isophotal magnitude correction for various galaxies.

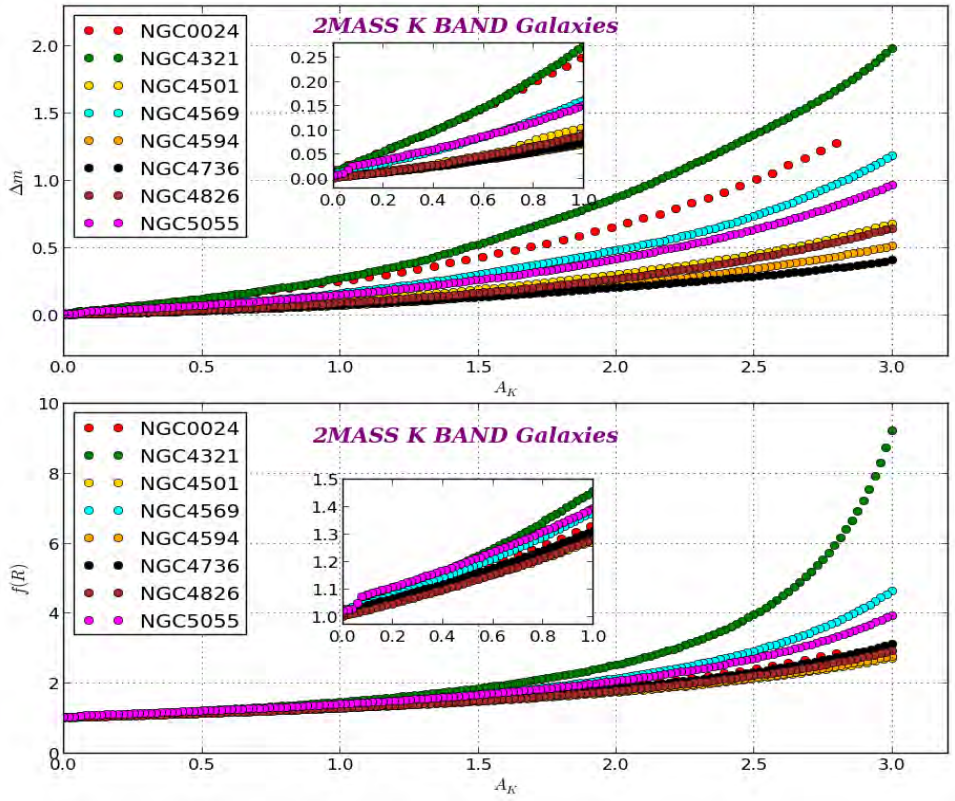

FIGURE 3.20: WISE W1 band isophotal magnitude correction for various galaxies.

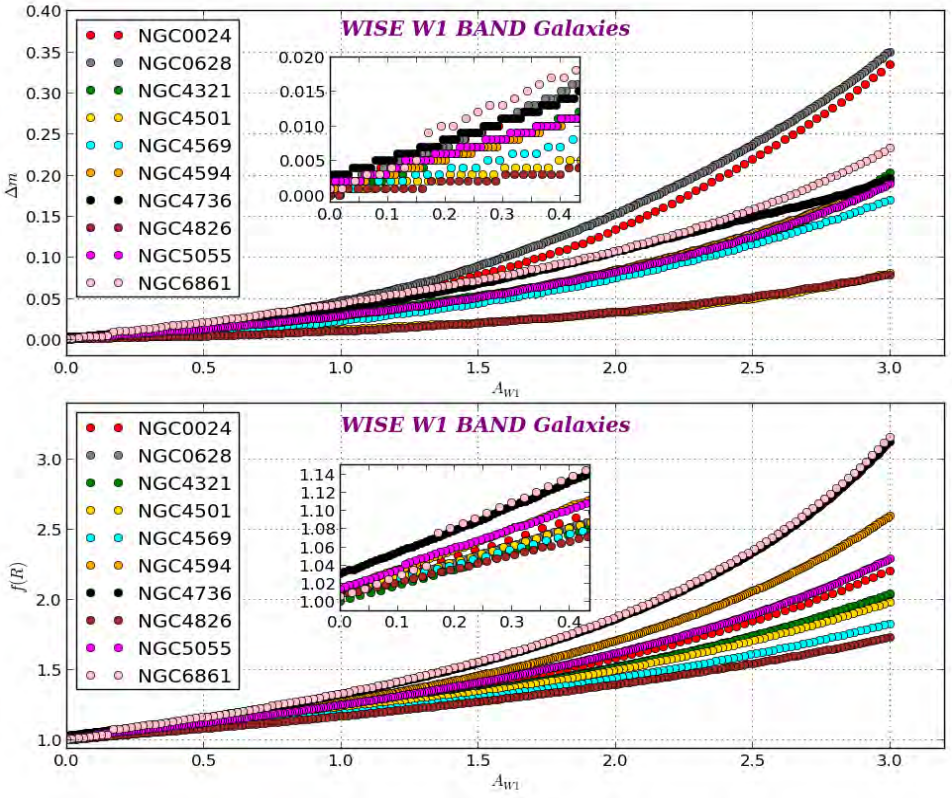

FIGURE 3.21: WISE W2 band isophotal magnitude correction for various galaxies.

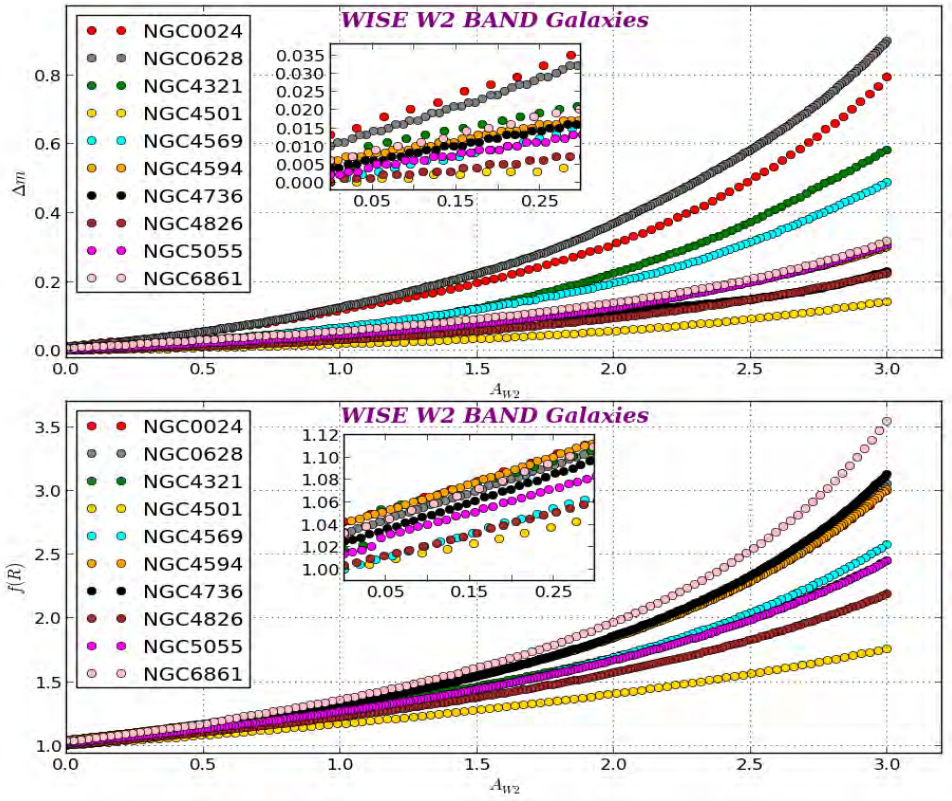

FIGURE 3.22: WISE W3 band isophotal magnitude correction for various galaxies.

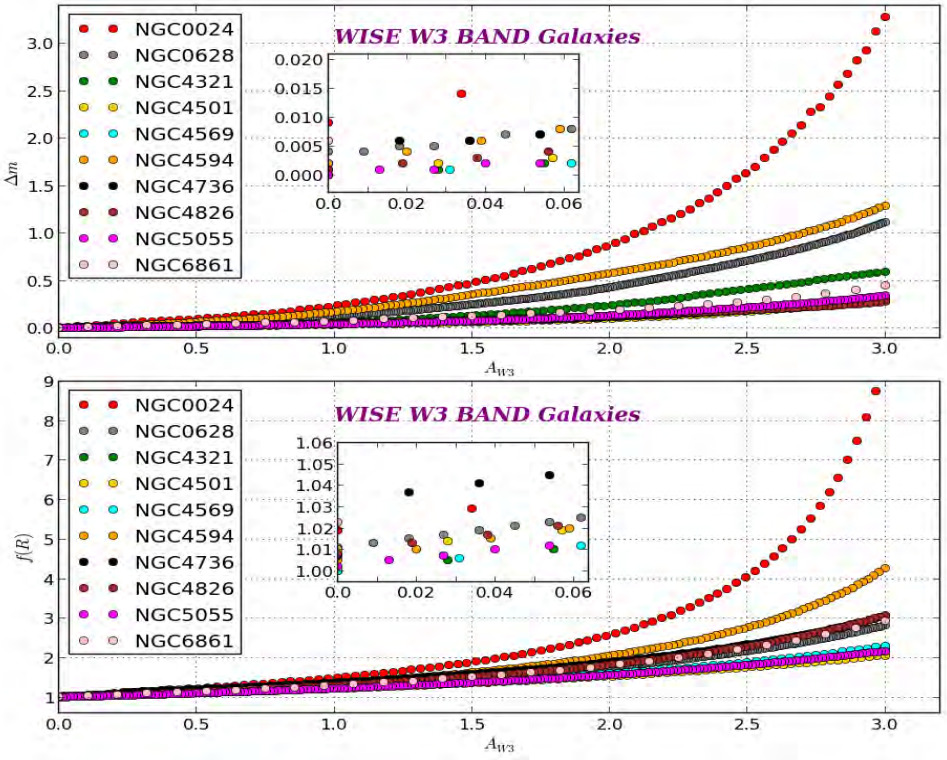

FIGURE 3.23: WISE W4 band isophotal magnitude correction for various galaxies.

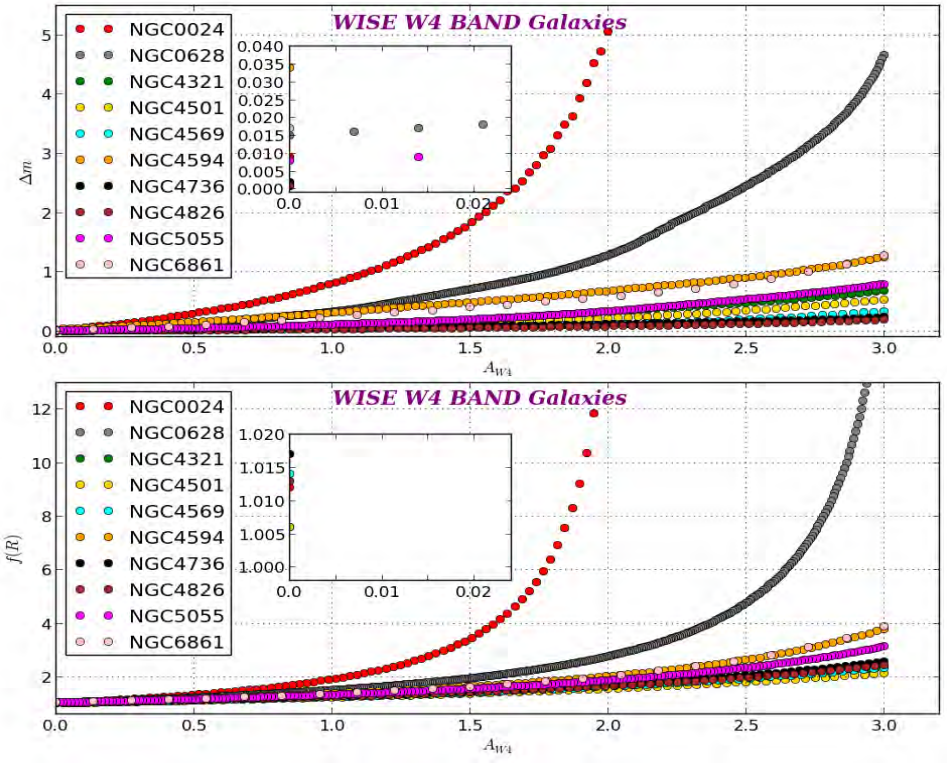

Chapter 4

Tully-Fisher Relation Parameters

Galaxies in the ZoA are quite difficult to observe due to obscuration by dust in the disk of our Galaxy and stellar crowding close to the Galactic plane (Kraan-Korteweg & Juraszek, 2000). The degree of dust obscuration is wavelength dependent. Therefore, extinction corrections are important when relating spiral galaxy magnitude to their velocity linewidth for the Tully-Fisher relation (Riad et al., 2010). Tully-Fisher relation is an empirical correlation which predicts that the luminosity L of a disk galaxy is proportional to its maximum rotational velocity V_{max}^{α}, where α is the Tully-Fisher relation slope (Tully & Fisher, 1977). Tully-Fisher relation studies have been carried out in the optical bands up to the infrared bands by Tully & Fisher (1977); Courteau et al. (2007); Masters et al. (2008); Sorce et al. (2013); Lagattuta et al. (2013) and others using different galaxies with different correction technique. Their results have shown that the Tully-Fisher relation of spiral galaxies do not obey a single luminosity-linewidth correlation. The Tully-Fisher slope α have been observationally established to be around $\sim 3-4$ (Aaronson et al., 1979). Tully-Fisher relation has been widely used as a distance indicator, in the studies of cosmic distance scales and large scale peculiar velocity field (Willick, 1990; Mathewson et al., 1992; Willick et al., 1997; Courteau et al., 2000). In this research work, we specifically selected galaxies from the ZoA and used the Tully-Fisher relation calibrations given by Said (2013) for the K_s bands, the Lagattuta et al. (2013); Sorce et al. (2013) and Cosmic Flow Program Tully-Fisher relation calibrations of Neill et al. (2014) for WISE W1 band and the Cosmic Flow Program calibrations of Neill et al. (2014) for WISE W2 band to map the ZoA cosmic flow.

4.1 Linewidth Correction

The parameter of choice for predicting the luminosity of a disk galaxy is the maximum amplitude of the rotation curve V_{max}. This is especially convenient given that most galaxies have flat rotation curves over much of their extent (Pierce, 2006). The most common method to measure the HI linewidth is the width at 20 per cent (W_{20}) or 50 per cent (W_{50}) of either mean or peak flux. Tully and Fisher advocated using the Doppler width of the 21 cm line profile measured at 20 % of peak intensity, corrected for inclination. However, if the Tully-Fisher relation is to be applied to low-luminosity spiral and irregular galaxies a more complicated correction is required in order to account for the effects of internal turbulence and subtle variations in line-profile shape (Pierce, 2006). When optical spectra are used, the maximum rotational velocity can be measured directly from the rotation curve. W_{50} is a good choice for Tully-Fisher relation work because it best avoid noise at both the top and bottom of the profile. If we measure W_{50} from a double-horned profile rather than from a Gaussian profile, provide a method that is less prone to noise (Pierce, 2006). To use the observed linewidth for Tully-Fisher study we need to correct for relativistic effect, instrumental broadening and smoothing, turbulent motion and galaxy inclination. These corrections are discussed in the sections below. In this research work, the 50 per cent linewidth W_{50} was used and corrected using the most general correction for linewidth given as

$$W_{cor} = \left[\frac{W_{50} - \Delta_s}{1+z} - \Delta t\right] \frac{1}{\sin i}, \tag{4.1}$$

where Δ_s is the systematic instrumental correction which is likely very small[1], $1+z$ is the correction for cosmological broadening, where z is the redshift, i is the inclination and Δt is the potential turbulent motion broadening.

4.1.1 Axial Ratio Correction

The axial ratio a/b is the ratio of the major axis radius a divided by the minor axis radius b. The axial ratio correction by Masters et al. (2008) was used to correct IRSF JHK_s bands and 2MASS JHK_s bands ZoA galaxies. Masters et al. (2003) correction to axial ratio is given as

$$\left(\frac{a}{b}\right)_{cor} = \left(\frac{a}{b}\right)(1 - 0.02x + 0.21x^2 - 0.01x^3). \tag{4.2}$$

[1]The width correction that accounts for the effects of instrumental broadening, signal-to-noise distortions and data processing smoothing

Where the value

$$x = FWHM\left(\frac{a/b}{r_{20}}\right). \tag{4.3}$$

$FWHM$ is the full width at half maximum of the seeing discs and r_{20} is the waveband semi-major axis measured at the 20th mag arcsec^{-2} isophotal elliptical aperture preferably in the J band. The $FWHM$ of 2MASS galaxies is about $2''.5$, while the $FWHM$ of IRSF data varies with each galaxies, but is typically much smaller from $1'' - 2''$. Using this inclination correction method, we can account for the blurring of the galaxy discs by seeing. Also face-on galaxy have $a/b > 0.7$, while edge-on galaxies are less than this value. For WISE axial ratio we used the axial ratio from the WISE resolved galaxy photometry.

4.1.2 Inclination Correction

Spiral galaxies can be described as a thin disks which is fundamentally axisymmetric (van Dokkum et al., 1994). When viewed as an edge-on, the disk of galaxy appear elliptical and inclined with respect to our line of sight. In practice, we measure the ellipticity from examining the galaxy isophote[2]. The inclination of a galaxy are mostly estimated using the approach suggested by (Holmberg, 1958). Holmberg (1958) showed that the inclination of a galaxy i can be measured from the observed axial ratio using this relation

$$\cos^2 i = \frac{(1-\epsilon)^2 - q_0^2}{1 - q_0^2}, \tag{4.4}$$

where $\epsilon = 1 - a/b$ is the ellipticity of the galaxy and q_0 is the axial ratio for an edge-on system. Masters et al. (2003) estimated this value $q_0 = 0.2$ for the intrinsic axial ratio for all type of galaxies, for spiral galaxies the value $q_0 = 0.13$. The inclination of face-on is zero while a perfectly edge-on galaxy the inclination is 90°. Complications arise from the fact that some galaxies do not have perfectly circular isophotes at face-on orientation. As a result, most investigations restrict these sample to those systems whose inclinations are at least 30° - 45° in order to minimize the resulting uncertainties on the deprojected rotational velocities (Pierce, 2006). For inclination correction of galaxies in this ZoA work, we used equation 4.4.

[2]Contours of equal surface brightness

4.1.3 Relativistic Correction

HI profile appear broader than they really are as a result of Hubble flow. To correct for this relativistic effect we use the standard factor given as

$$W_{50}^{z} = (1+z)^{-1} W_{50}. \tag{4.5}$$

The measured velocity width can be converted to a rotational velocity with the following relation $W_{50}^{cor} = 2\ v_{50}^{max}$. Importantly, this correction is insignificant for our sample.

4.1.4 Instrumental Broadening and Smoothing

The finite velocity resolution of the telescope correlator and any smoothing that is applied to the data can cause a broadening of the observed HI profile. We can account for the combined instrumental and noise effects by subtracting an offset from the measured width. For HIZoA galaxies the velocity resolution is $\Delta v = 27$ km s^{-1}. We use the method in Springob et al. (2005) to calculate the instrumental broadening which is given as

$$\Delta_s = 2\Delta v \lambda. \tag{4.6}$$

The broadening of the width measurement λ is one-half the difference between the measured width and the width that would be measured in the absence of instrumental effects. Also, λ is a defined function of the signal-to-noise ratio given as

$$\log(SNR) < 0.6: \qquad \lambda = \lambda_1(\Delta v), \tag{4.7}$$

$$0.6 < \log(SNR) \leq 1.1: \quad \lambda = \lambda_2(\Delta v) + \lambda_2'(\Delta v)\log(SNR), \tag{4.8}$$

$$\log(SNR) > 1.1: \qquad \lambda = \lambda_3(\Delta v). \tag{4.9}$$

The values $\lambda_1(\Delta v)$, $\lambda_2(\Delta v)$, $\lambda_2'(\Delta v)$ & $\lambda_3(\Delta v)$ are constants for both $\Delta v < 5$ km s^{-1} and $\Delta v > 11$ km s^{-1}, but depend linearly on Δv within the range 5 km s^{-1} $< \Delta v <$ 11 km s^{-1}. For this research work, the HI spectral were only Hanning smoothed. The velocity width instrumental correction parameters are given in Table 4.1.

To account for the spectral noise, the true signal-to-noise ratio (SNR) of the spectrum can be characterized by $SNR = (f_p - \text{rms})/\text{rms}$, where f_p is the peak flux density (Springob et al., 2005). For HIZoA galaxies the SNR can be approximately given as

$$SNR = \frac{\text{HI Flux}}{W_{50} \times 0.006} \tag{4.10}$$

TABLE 4.1: The velocity width instrumental correction parameters as given by Springob et al. (2005). The 'H' code indicate that HI spectral were Hanning smoothed once, while the 'B' code indicate that a three-channel "boxcar" average plus Hanning smoothing were applied to the HI spectral.

Velocity width instrumental correction parameters					
Δv(km s^{-1})	smoothing	$\lambda_1(\Delta v)$	$\lambda_2(\Delta v)$	$\lambda'_2(\Delta v)$	$\lambda_3(\Delta v)$
> 11	H	0.227	-0.1523	0.623	0.533
> 11	B	0.332	-0.2323	0.940	0.802

4.1.5 Turbulent Motion Correction

The turbulent motion within the disc contribute to the observed velocity profile of the galaxy. It was found that HI clouds in a disk do not move strictly along circular orbits, even in the absence of large-scale anomalies, such as warps, bars and with its associated small-scale dispersion and streaming motions near the spiral arms. Springob et al. (2005) correction for this effect involves linearly subtracting the turbulence correction from the linewidth. For this reseach work we used the calculated valued for turbulent motion in Springob et al. (2005), which is given as $\Delta t = 6.5$ km s^{-1}.

4.1.6 Corrected Linewidth

Equation 4.1 was used to correct the linewidth in this ZoA work. Doppler-broadened of 21 cm line of HI are very important in measuring the rotation of late-type galaxies (Pierce, 2006). This is because spiral galaxies are HI rich, so their spectrum has HI line that is relatively strong. Also, HI within these sources has an extended distribution such that the outer, flat portion of the rotation curve is well sampled, providing an accurate measurement of the maximum rotational velocity. This will equal zero near $W_{50} = 316$ km s^{-1}, where W_{50} is an estimate of twice the maximum rotational velocity of a galaxy. This convention is dictated by the practice of deriving W_{50} from Doppler-broadened single-dish 21 cm line global profiles of galaxies. The 21 cm measurements are usually the best choice for nearby galaxies. Hα measurements are optimal for redshifts beyond about 10000 km s^{-1}. At higher redshift $\sim$ 60000 km s^{-1}, Hα line becomes contaminated by increasingly strong emission lines from the night sky. Currently, several investigation have been conducted to ascertain the suitability of using other lines such as [O II] (λ3727 Å) and [O III] (λ5007 Å) inorder to apply Tully-Fisher relation to larger distances galaxies (Pierce, 2006).

4.2 Infrared Band Extinction Correction

Recent extinction studies have shown that the IRAS/DIRBE extinction maps were overestimated at low Galactic latitudes (Nagayama et al., 2004; Schröder et al., 2007). Schröder et al. (2007) estimated the true reddening in the area of the Galactic plane to be about 87 % of the IRAS/DIRBE estimate of Schlegel et al. (1998). Currently, there exist a standard extinction map by Schlafly & Finkbeiner (2011) which take into consideration some of the flaws encounter in the previous estimate to correct for Galactic dust extinction caused by the Milky Way. The dust maps of Schlafly & Finkbeiner (2011) were used along side with the waveband conversions calculated from (Cardelli et al., 1989). $R_V = 3.1$[3] is adopted and used to calculate the values of A_λ/A_V. These are then normalized using Schlafly & Finkbeiner (2011) extinction values to obtain the value for $A_\lambda/E(B-V)$ for each galaxy sample. Cardelli et al. (1989) Galactic extinction estimate in the infrared range $0.3\ \mu\text{m}^{-1} \leq x \leq 1.1\ \mu\text{m}^{-1}$ is given as,

$$\left\langle \frac{A_\lambda}{A_V} \right\rangle = a(x) + \frac{b(x)}{R_V}, \tag{4.11}$$

where $a(x)$ & $b(x)$ is given as,

$$a(x) = \quad 0.574\, x^{1.61}, \tag{4.12}$$

$$b(x) = \quad -0.527\, x^{1.61}. \tag{4.13}$$

Also, we extended the limit given by Cardelli et al. (1989) Galactic extinction estimate to calculate the Galactic extinction for WISE bands. We did a theoretical simulation to determine the effect of dust size R_V on extinction in the optical-infrared bands as seen in FIGURE 4.1. This was done using the equations in (4.11 – 4.13) and plotting $\frac{A_\lambda}{A_V}$ as a function of $\lambda^{-1}\mu$m. This imply that equation (4.11) can be extended to determine the Galactic extinction associated with WISE wavelengths. The extinction studies of Cardelli et al. (1989); Schlafly & Finkbeiner (2011) and all other optical studies were never designed for the mid-infrared, hence there is some uncertainty to this curve.

[3] R_V may be higher for molecular clouds i.e the dark ZoA

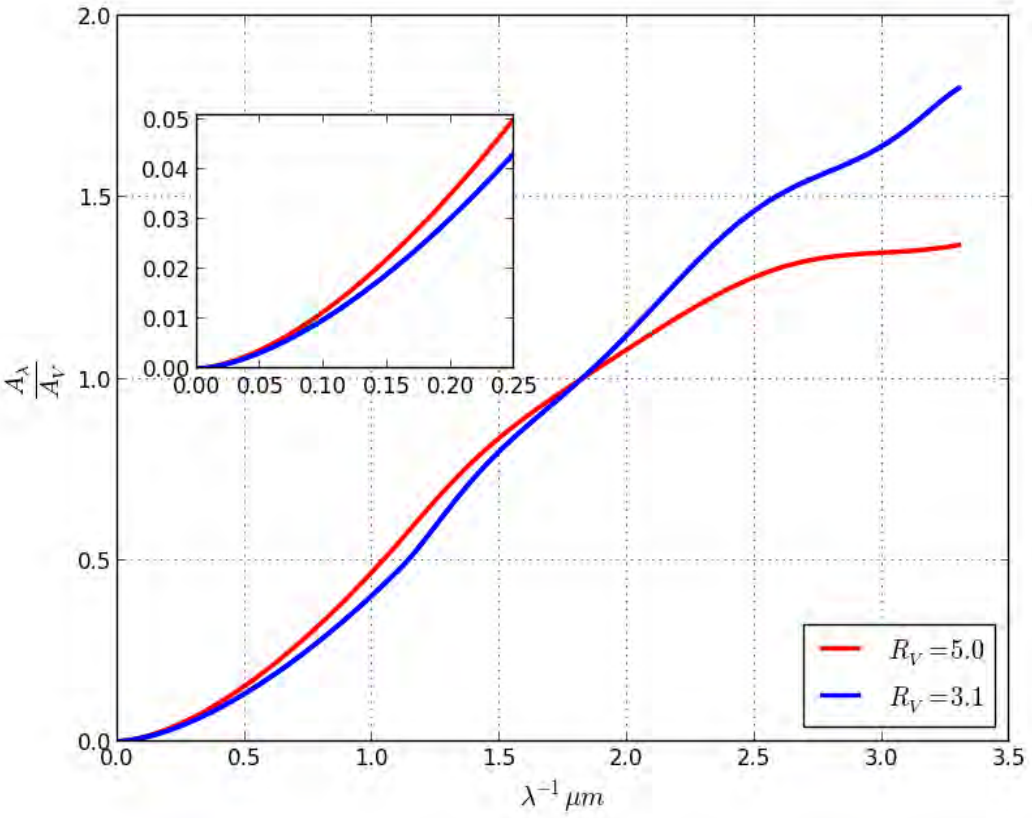

FIGURE 4.1: Plots showing the variation of dust size R_V with extinction for infrared to optical wavelengths.

The effect of Galactic dust extinction in W3 and W4 WISE bands are very small and could be neglected. In this research work we corrected for Galactic dust extinction for all bands. We obtained the Galactic extinction in JHK_s and WISE bands from the Cardelli et al. (1989) equations in (4.11 – 4.13) as

$$A_J = 0.8744\,E(B-V), \tag{4.14}$$
$$A_H = 0.5592\,E(B-V), \tag{4.15}$$
$$A_K = 0.3652\,E(B-V), \tag{4.16}$$
$$A_{W1} = 0.1593\,E(B-V), \tag{4.17}$$
$$A_{W2} = 0.1073\,E(B-V), \tag{4.18}$$
$$A_{W3} = 0.0229\,E(B-V), \tag{4.19}$$
$$A_{W4} = 0.0086\,E(B-V). \tag{4.20}$$

These results compare favorably with the results obtained by Flaherty et al. (2007) for 3.6 μm ($A_{3.6} = 0.203\,E(B-V)$) and 4.5 μm ($A_{4.5} = 0.156\,E(B-V)$) bands of IRAC 1 and IRAC 2.

4.2.1 Cosmological K-correction

The cosmological correction is made on magnitude to account for the wavelength shift in galaxy spectra caused by Hubble flow. We corrected for cosmological K-correction using a simple linear fit to the low-redshift end of the models of Poggianti (1997) given as

$$k(z) = m_{z(i)} - m_{z(0)} - 2.5 \log 10(1+z), \tag{4.21}$$

where $m_{z(0)}$ is the magnitude at zero redshift and $m_{z(i)}$ is the magnitude at any other redshift, where the redshift $z = V_{obs}/c$. V_{obs} is the heliocentric velocity and c is the speed of light given as 3×10^5 km s^{-1}. Importantly, the cosmic flow analysis in this research work is confined to the non-relativistic Local Universe with redshift $z < 0.1$. Also, for gas-rich disks like Sb and Sc spiral galaxies the K-correction is small for redshift $z \ll 0.1$. Therefore, the K_s band flux increases with redshift $z(< 0.1)$, so that the K-correction would reduce the observed flux as seen in equation (4.23 – 4.28).

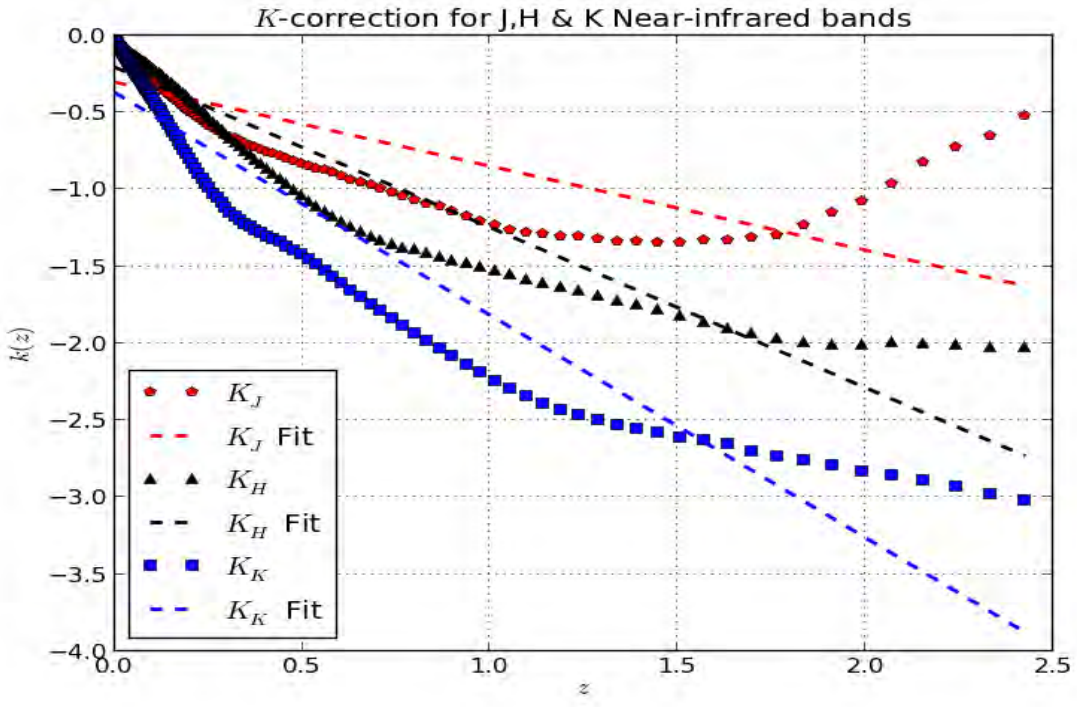

FIGURE 4.2: Cosmological K-correction for J, H & K_s bands.

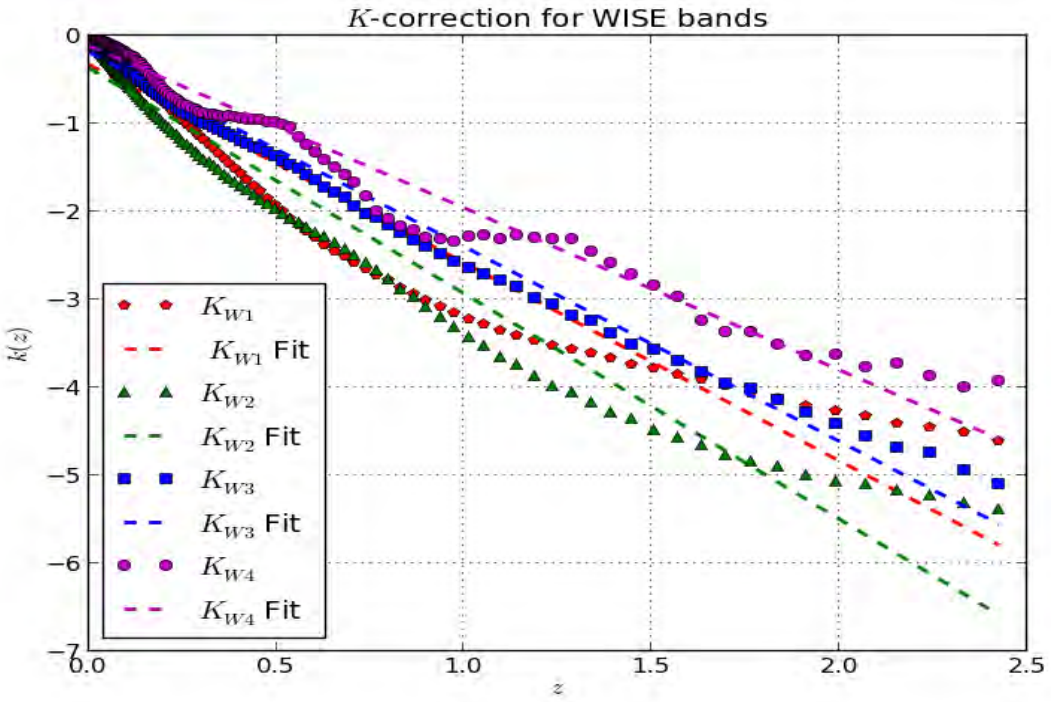

FIGURE 4.3: Cosmological K-correction for WISE W1-W4 bands.

We obtained the cosmological K-correction used in this research work using the S0 redshift template of Jarrett et al. (2013)[4] with the low-z cosmological K-correction equation in (4.21). Then, we applied a linear fit to the plot of $k(z)$ data on z. The slope of the linear fits plus the offset was used to parameterized the K-correction for each waveband.

The plots and fits of the parameterized K-correction for JHK_s and WISE W1-W4 bands are given in FIGURE 4.2 & 4.3. We obtain the cosmological K-correction for JHK_s band as

$$K_J = -0.8498\, z, \tag{4.22}$$

$$K_H = -1.2483\, z, \tag{4.23}$$

$$K_K = -1.8178\, z. \tag{4.24}$$

[4]Data could be downloaded at http://www.ast.uct.ac.za/~affadi/patrick/patrick.html

For the WISE bands, we obtain the cosmological K-correction as

$$K_{W1} = -2.5854\, z, \tag{4.25}$$

$$K_{W2} = -2.9358\, z, \tag{4.26}$$

$$K_{W3} = -2.4028\, z, \tag{4.27}$$

$$K_{W4} = -1.9615\, z. \tag{4.28}$$

We compare our results with the values obtained in Masters et al. (2003) low-z cosmological K-correction for JHK_s bands given as

$$K_J = -0.68\, z, \tag{4.29}$$

$$K_H = -1.40\, z, \tag{4.30}$$

$$K_K = -1.52\, z. \tag{4.31}$$

Also, for WISE bands we compared our result with the low-z formulation of K-correction for 3.6 μm IRAC channel by Huang et al. (2007) given as

$$K_{3.6} = -2.27\, z. \tag{4.32}$$

Our results agree closely with the value obtained by Masters et al. (2003) for JHK_s 2MASS bands and with Huang et al. (2007) for 3.6 μm IRAC channel.

4.2.2 Internal Extinction Correction

The estimation of the internal dust extinction in galaxies is quite uncertain. It depends on their dust geometry which include orientation, morphological type, size, and luminosity. For Tully-Fisher relation studies, edge-on spiral galaxies are preferentially used in other to minimize systematic distance error (Tully & Fisher, 1977). To compute the internal extinction correction that is, the extinction due to the galaxy itself. We used a more general empirical model given by Giovanelli et al. (1998) as

$$A_i = \gamma_i \log(a/b), \tag{4.33}$$

where a/b is the axial ratio. The constant γ_i values for JHK_s IRSF and 2MASS bands was obtained using the values given by Masters et al. (2003) for JHK_s bands as

$$\gamma_J = \begin{cases} 0.48 \pm 0.15, & \text{for} \quad \log(a/b) \leq 0.5, \\ 1.60 \pm 0.2 + 0.24/\log(a/b), & \text{otherwise}, \end{cases} \tag{4.34}$$

$$\gamma_H = \begin{cases} 0.39 \pm 0.15, & \text{for} \quad \log(a/b) \leq 0.5, \\ 1.4 \pm 0.2 + 0.20/\log(a/b), & \text{otherwise}, \end{cases} \tag{4.35}$$

$$\gamma_K = \begin{cases} 0.26 \pm 0.15, & \text{for} \quad \log(a/b) \leq 0.5, \\ 1.10 \pm 0.20 + 0.13/\log(a/b), & \text{otherwise}. \end{cases} \tag{4.36}$$

For the WISE bands we apply the method of Lagattuta et al. (2013). This method involves scaling the K_s band slope of Masters et al. (2003) by $1/\lambda$ scaling law, since internal extinction is much less prevalent as wavelength increases (Lagattuta et al., 2013). We approximated the WISE internal extinction as

$$\gamma_{W1} = \begin{cases} 0.166 \pm 0.096, & \text{for} \quad \log(a/b) \leq 0.5, \\ 0.702 \pm 0.128 + 0.083/\log(a/b), & \text{otherwise}. \end{cases} \tag{4.37}$$

$$\gamma_{W2} = \begin{cases} 0.123 \pm 0.071, & \text{for} \quad \log(a/b) \leq 0.5, \\ 0.519 \pm 0.094 + 0.061/\log(a/b), & \text{otherwise}. \end{cases} \tag{4.38}$$

$$\gamma_{W3} = \begin{cases} 0.047 \pm 0.027, & \text{for} \quad \log(a/b) \leq 0.5, \\ 0.199 \pm 0.036 + 0.024/\log(a/b), & \text{otherwise}. \end{cases} \tag{4.39}$$

$$\gamma_{W4} = \begin{cases} 0.026 \pm 0.015, & \text{for} \quad \log(a/b) \leq 0.5, \\ 0.109 \pm 0.020 + 0.013/\log(a/b), & \text{otherwise}. \end{cases} \tag{4.40}$$

If the disks of galaxies are completely transparent all the way to the center, then there should be no change in the total magnitude with inclination and also the isophotal radius should increase as the disk is tilted. If a galaxy is completely opaque, then the total and isophotal magnitude should decrease, while the measured radius do not change with inclination (Masters et al., 2008). The correction for edge-on galaxies are too extreme and can cause over-corrections.

4.2.3 Galactic Absorption Correction

It is widely accepted that the disc of a galaxy is optically thin. If the disc of a galaxy is optically thick, then the observed luminous mass is greatly affected by internal absorption (Masters et al., 2003). Internal absorption in a galaxy describes the degree of absorption of its emitted light by dust inside the galaxy. Galactic absorption are due to the extinction cause by the dust in the Milky Way. Spiral galaxies magnitudes measured in the ultraviolet, optical, infrared wavelengths are affected by foreground extinction especially in the ZoA region. This extra dimming associated with ZoA galaxies

were corrected using the method of Cameron (1990) and Riad et al. (2010) based on optimized correction for central surface brightness obtained from fitting the quantities $f(R)$ and Δm_{iso} as a function of simulated extinction value in each waveband as seen in FIGURE 3.3-3.16. We specifically used NGC 4501 galaxy fitting parameter given in TABLE 3.2 to correct for Galactic absorption in our Tully-Fisher relation sample galaxies. This was because the NGC 4501 has the best curve fitting with most having an initial values of zero.

4.2.4 Morphology Correction

Morphology studies by de Vaucouleurs (1982) and others have shown that different Morphology type follow different Tully-Fisher relation slope. Brighter galaxies show more internal extinction at a given inclination than the dimmer ones. Which can be attributed to the increase in the physical size and metallicity of the brighter galaxies. The morphology correction for IRSF JHK_s and 2MASS JHK_s bands was based on the values given by Masters et al. (2008) as

$$J \text{ band} \begin{cases} M_{Sa} = & 0.02 - 1.31(\log W_{cor} - 2.5) \text{ If } 2 \leq T \leq 4, \\ M_{Sb} = & 0.23 - 2.86(\log W_{cor} - 2.5) \quad \text{If} \quad T \leq 2, \end{cases} \tag{4.41}$$

$$H \text{ band} \begin{cases} M_{Sa} = & 0.01 - 1.26(\log W_{cor} - 2.5) \text{ If } 2 \leq T \leq 4, \\ M_{Sb} = & 0.21 - 2.92(\log W_{cor} - 2.5) \quad \text{If} \quad T \leq 2, \end{cases} \tag{4.42}$$

$$K_s \text{ band} \begin{cases} M_{Sa} = & 0.01 - 1.46(\log W_{cor} - 2.5) \text{ If } 2 \leq T \leq 4, \\ M_{Sb} = & 0.19 - 3.16(\log W_{cor} - 2.5) \quad \text{If} \quad T \leq 2. \end{cases} \tag{4.43}$$

For the WISE bands we used the WISE morphology correction given by Lagattuta et al. (2013).

$$\text{WISE band} \begin{cases} \Delta M_{S0/Sa} = -0.61 - 5.54(\log W_{cor} - 2.5) \\ \Delta M_{Sb} = -0.30 - 2.84(\log W_{cor} - 2.5) \end{cases} \tag{4.44}$$

Each galaxy morphological type T was analyzed using the formalism of Jarrett et al. (2003) and NED morphological classification for our sample galaxies. Jarrett et al. (2003) showed a dependence between optical to Infrared effective surface brightness or effective radius on morphological type T. Jarrett et al. (2003) method was used because most of the galaxies used in this research work do not have a clear morphological type.

4.2.5 Magnitude Correction

To correct for isophotal magnitude in the JHK_s & WISE bands we adopted the standard magnitude correction to spiral galaxies. This correction involves correcting for Galactic dust extinction, internal extinction, Galactic absorption, cosmological K-correction and morphological correction. The corrected isophotal absolute magnitude equation is given as

$$M_\lambda - 5\log h = m_{obs} - A_\lambda + k_z - A_{int} - 5\log V_{LG} - 15 \tag{4.45}$$

or

$$M_\lambda - 5\log h = m_{obs} - A_\lambda + k_z - A_{int} - 5\log V_{CMB} - 15 \tag{4.46}$$

While, the corrected isophotal apparent magnitude equation is given as

$$m_{apparent} = m_{obs} - A_\lambda + k_z - A_{int} \tag{4.47}$$

where m_{obs} is the observed magnitude, V_{LG} is the Local Group velocity, V_{CMB} is the CMB velocity, A_λ is Galactic extinction, A_{int} is the internal extinction, k_z is the cosmological K-correction that accounts for the shift of the spectral energy distribution of the galaxy. For the conversion of apparent magnitude to absolute magnitude in this work we used the Local Group velocity V_{LG}.

4.3 Bias Correction

Obtaining a reliable Tully-Fisher relation fit requires bias corrections which in turn require the knowledge of the characteristics of the scatter. In this research work, we explicitly described the various form of bias apply to our selected Tully-Fisher relation calibrations. If the selected galaxies for a Tully-Fisher relation are from the same clusters, they should roughly lie at the same distance. Even when the data sample is limited in some way independent of magnitude, the fit to this data sample will reproduce the true Tully-Fisher relation. The brightest galaxies in the sample will tend to lie above the true correlation line. Moreover, if the sample is magnitude limited, the lower magnitude end will be pulled up to correlation line.

4.3.1 Incompleteness Bias

Incompleteness bias correction to galaxies magnitude is important, because it takes into consideration the flaws encounter in the measurements of galaxies magnitudes. Also, it can correct for the fact that more distant galaxy groups should lie closer than they

actually are, which is obviously a problem for determining peculiar velocities using Hubble flow. For our selected Tully-Fisher relation calibrations, the incomplete bias used was based on the method of Willick (1994). These entails applying Monte carlo simulation between the expected magnitude and the observed magnitude. We use the luminosity function of spiral galaxies with an assumed scatter as an input parameters to the Monte carlo simulation (Masters et al., 2008).

4.3.2 Cluster Size and Mean Distance Bias

The correction for mean distances to cluster which arises because a small fixed bias for all galaxies in a given cluster. This arises because the logarithm of the average of the distance is not equal to the average of the logarithm of the distance. Lower luminosity galaxies in the closest part of the cluster introduce a small bias to the Tully-Fisher slope (Masters et al., 2008). For most of our selected Tully-Fisher relation calibrations this value was quite small.

4.3.3 Malmquist Bias

The effect of Malmquist bias arises when observing in a small solid angle, there may be a different number of galaxies at a distance $r+\delta r$ than at r, even for a homogeneous spatial distribution. The approximate Malmquist idealized value is $M_0 - M(m) = 1.386\ \sigma(M)^2$ which is derived from the luminosity function (Masters et al., 2008). The correction for Malmquist bias is quite similar to the correction of incompleteness bias. Giovanelli et al. (1997); Masters et al. (2006) argue that this correction are quite small and can be neglected.

4.4 Error Analysis and Calculation

The error analysis is concerned with the changes in the output of the model as the parameters to the model vary with the mean. The measurements of physical quantities especially in astronomy is highly uncertain. Therefore, inorder to draw valid conclusions errors must be indicated and dealt with properly. The error associated with corrected absolute magnitude σ_m and linewidth σ_{W50} are taken from the relation in Koribalski et al. (2004). The uncertainty associated with absolute magnitude is given as

$$\sigma_M^2 = \sigma_{m_{obs}}^2 + \sigma_A^2 + \sigma_{A_i}^2 + \left(\frac{5}{V}\ln 10\right)^2 \sigma_V^2, \tag{4.48}$$

where V represent either the CMB velocity (V_{CMB}) or the Local Group velocity (V_{LG}). The uncertainty associated with linewidth is given as

$$\sigma^2_{W_{50}} = \left(\frac{1}{1+z}\right)^2 \sigma^2_{W_{50}} + \left(W_{50}\frac{\cos i}{\sin i}\right)^2 \sigma_i^2, \tag{4.49}$$

where

$$\sigma_i^2 = \left(\frac{1-\epsilon}{(1-q_0^2)\cos i \sin i}\right)^2 \sigma_\epsilon^2. \tag{4.50}$$

The uncertainty in systemic velocity is given from Koribalski et al. (2004) as

$$\sigma_{vsys} = 3\left(\frac{\sigma_{Speak}}{S_{peak}}\right)(P\Delta v)^{1/2}, \tag{4.51}$$

where $P = 0.5\ (W_{20} - W_{50})$ measures the steepness of the profile edges. Therefore, the uncertainty associated with W_{50} and W_{20} can be deduced from Koribalski et al. (2004) as

$$\sigma_{W_{50}} = 2\sigma_{vsys} \tag{4.52}$$

$$\sigma_{W_{20}} = 3\sigma_{vsys} \tag{4.53}$$

4.4.1 Effects of Errors on Tully-Fisher Slope

The main source of error in the Tully-Fisher relation is mostly associated with the errors in the corrected linewidth (Jacoby et al., 1992; Bothun & Mould, 1987). Most of the HI profile linewidth are asymmetric. Asymmetric line profile raise several questions on the calibration of Tully-Fisher relation, since calculating linewidth profile of such asymmetric profiles may not accurately estimate the maximum rotational velocity of these galaxies (Bothun & Mould, 1987). The variation in line profile shape could introduce additional errors in the Tully-Fisher relation calibration. It is mostly assumed that the measured linewidth represent the maximum rotational velocity V_{max}. There is no comprehensive model that could explain how reliable one could predict the maximum rotation velocity from the linewidth profile. The most commonly used inclination correction method are not very reliable and introduce unnecessary errors to Tully-Fisher calibration. Different method exist for linewidth correction which are explained explicitly in Tully & Fisher (1977); Haynes et al. (1998); Tully & Fouque (1985) and others. There is no comprehensive model that have been developed to date to compare the differences between these models. Tully-Fisher relation has an intrinsic scatter that appears to be impossible to beat down. This section may be important to such multiple causes. There is some additional uncertainty introduced while applying aperture correction to obtaining the magnitudes of an astronomical objects. Schneider et al. (2002) showed using the 2MASS

extended source catalogue sample galaxies, that the uncertainties in aperture correction applied to obtaining the total magnitudes is much larger than the uncertainty required in obtaining magnitudes from the fudicial isophotal magnitude measured at K_s mag of the 20 mag arcsec^{-2}. In general, there is no standard or reliable way of correcting galaxies magnitude without introducing additional uncertainty to the results.

4.5 Conclusion

In this research work, we have obtained the extinction corrected magnitude for the IRSF JHK_s and 2MASS JHK_s bands and WISE W1-W2 bands. Using the S0 K-correction template we calibrated the K-correction by plotting the dependence of k_z on redshift z for JHK_s bands and WISE W1-W2 bands. Also, we calculated the Galactic extinction for the JHK_s bands and WISE bands. Furthermore, we obtained the fitting parameters for the 2MASS JHK_s Bands and WISE W1 and W2 bands using the method of Cameron (1990) and Riad et al. (2010) which was based on optimized correction for central surface brightness. We applied these corrections to determined the Galactic absorption associated with 2MASS JHK_s and WISE W1-W4 bands and then use it to correct our selected galaxies. In the next chapter we would use the Tully-Fisher relation calibration of Said (2013) for the K_s band, Lagattuta et al. (2013); Sorce et al. (2013) and Cosmic Flow Program[5] calibrations for WISE W1 band and the Cosmic Flow Program calibrations for WISE W2 band for the ZoA cosmic flow analysis in this research work.

[5]The Cosmic Flow Program calibrations is given by Neill et al. (2014).

Chapter 5

Cosmic Flow Analysis

Galaxies move coherently in the Hubble expansion. They also have velocities relative to the Hubble expansion known as peculiar velocities (Jacoby et al., 1992). On scales that are small compared to the Hubble radius, galaxy motions result from deviations of the idealized isotropic cosmological expansion (Feldman et al., 2010). Cosmic flows are deviations from a smooth Hubble flow due to large-scale gravitational perturbations and are driven by gravity (Jacoby et al., 1992; Zaroubi et al., 1999). The amplitude of such coherent large-scale motions are therefore among the most sensitive probes of both the large-scale structure of the Universe and the initial conditions of galaxy formation. Galaxy clustering on small scales are highly non-linear and peculiar velocities of most galaxies can be expected to be incoherent and random. For large scales these clustering properties of galaxies are mostly linear, with a well define peculiar velocity field (Feldman et al., 2010).

The ZoA is a region mostly obscured by dust in the optical wavelengths and characterized by high stellar crowding in the infrared wavelengths thereby, making some regions devoid of galaxies (Kraan-Korteweg & Juraszek, 2000). The full distribution of matter, especially in the Local Universe, is essential in understanding the motion of the Local Group relative to the CMB and the inflow of galaxies towards the Great Attractor. Studies have shown that galaxy peculiar velocity data can provide important dynamical clues to the large scale structures obscured by the ZoA with resolution $\lesssim 500$ km s^{-1} (Kolatt et al., 1995). The Tully-Fisher relation for spirals can be used to obtain distances, which can be applied to determine the radial component of the peculiar velocity. Though, this method is limited to $cz/H_0 \sim 100$ Mpc, corresponding to velocity expansion $cz \sim 6000$ km s^{-1}, it can be used to determine distance to a relative accuracy of v/cz which is similar to 60 per cent (Pierce, 2006). Importantly, cosmic flow involves the measurement of distances, peculiar velocities and proper motion

using peculiar velocity field models and constructions. In this chapter we used the K_s band linewidth-magnitude calibration of Said (2013), WISE W1 linewidth-magnitude calibrations of Lagattuta et al. (2013); Sorce et al. (2013) and Comic Flow Program and WISE W2 linewidth-magnitude calibrations of the Cosmic Flow Program to show the cosmic flow associated with ZoA galaxies. We did not include the IRSF J & H bands and 2MASS J & H bands for the cosmic flow analysis because the effects of extinction are very high in these bands.

5.1 Previous Work

Early studies to determine the source of Local Group peculiar velocity have suggested a local origin. The Virgo cluster which is the nearest large-scale over density has an infall velocity of 240 km s^{-1} (Jerjen & Tammann, 1993), which can only account for the 27 % of the Local Group velocity of 627 km s^{-1} toward the CMB dipole (Kogut et al., 1993). Therefore, the inability for Virgo cluster to explain the Local Group motion led Shaya (1984) to suggest an additional flow toward the Hydra-Centaurus supercluster. This inflow into the Great Attractor was detected by Lynden-Bell et al. (1988) as a systematic distortion in the peculiar velocities of 400 early-type galaxies within 40 h^{-1} Mpc. Several work by various author have come all the way to suggest that the Local Group is as a result of two flows, one into the Hydra-Centaurus region and a second flow toward a more distant source (Tonry et al., 2000). They estimated the amplitude for the flow motion in the Local Group to be in the range $\sim 150-400$ km s^{-1} and suggested that the peculiar motions arose from a relatively local[1] mass density perturbations (Schechter, 1980; Aaronson et al., 1982a; de Vaucouleurs et al., 1981; Hart & Davies, 1982; Shaya, 1984; Dressler & Sandage, 1983; Tonry et al., 2000). Cosmic flows beyond the Great Attractor suggested that some fraction of the motion is due to infall into the Shapley supercluster located at ~ 100 h^{-1} Mpc behind the Hydra-Centaurus supercluster (Tonry et al., 2000; Kocevski & Ebeling, 2006). The dynamic significance of the Shapley supercluster and the Great Attractor on the motion of the Local Group has been a matter of debate. Recent studies by Lucey et al. (2005) have shown that the Great Attractor and the Shapley supercluster generate the same amount of peculiar velocity. Though, these results are still highly controversial and a consensus has still not been reached. In this work our aim is to use various cosmic flow models and the well calibrated Tully-Fisher relation to map the cosmic flow associated with galaxy data in the ZoA described in the previous chapter.

[1] Scales $\lesssim 5000$ km s^{-1}

5.2 ZoA Peculiar Velocity Distribution

The galaxy samples used for the peculiar velocity analysis was initially selected from HIZoA galaxies which have counterparts in both IRSF and WISE data derived here. We only regarded galaxies with $\log W \geq 2.0$. For optimal results and to ensure that our selected galaxies are mostly edge-on galaxies, we only applied the cosmic flow analysis to galaxies having K_s band axial ratio less than 0.7. We preferable used the corrected K_s band and WISE W1 and W2 isophotal magnitude for the cosmic flow analysis. This is partly due to K_s band have less foreground extinction and also because the photometry of K_s band and WISE W1 and W2 band are optimal for this analysis. We compared our work with the published work of Kolatt et al. (1995); Tonry et al. (2000); Pomarède et al. (2013); Kocevski & Ebeling (2006); Said (2013); Tully et al. (2008) and Tully et al. (2008).

Peculiar velocities are vital probes of the underlying mass distribution in the Local Universe under the assumption that galaxies are unbiased tracers of the large-scale gravitationally induced velocity field (Kocevski & Ebeling, 2006). Furthermore, analysis of the peculiar velocity field have shown that they can provide additional information on different regions not actually covered by the data since they are non-local (Kolatt & Dekel, 1995; Zaroubi et al., 1999). More importantly, they can provide additional information on scales larger than the sampled regions (Hoffman & Zaroubi, 2000). To measure peculiar velocities we need a known distance indicator which can be determined from Tully-Fisher relation. For the cosmic flow field analysis in this research work, we used the Tully-Fisher relation calibration of Said (2013) for the K_s band, Lagattuta et al. (2013); Sorce et al. (2013) and Cosmic Flow Program calibrations of Neill et al. (2014) for WISE W1 band and Cosmic Flow Program calibrations of Neill et al. (2014) for WISE W2 band. The major criteria for selection of these calibrations are based on the large sample of galaxies used for the Tully Fisher relation analysis. For the calibrations used in this work, isophotal magnitudes was used to obtain its calibrations. The cosmic flow analysis entails using the data offset obtained by subtracting the absolute magnitude from a standard Tully-Fisher relation calibration from the corrected absolute magnitude and subsequently applying the formalism of Masters et al. (2008) to calculate the distance and peculiar velocities of our sample galaxies using the data offset. Where necessary, we converted the Tully-Fisher relation calibration given in Vega photometric system to AB photometric system using the transformation of Frei & Gunn (1994) for J, H, K_s & 3.6 μm bands Tully-Fisher relation calibrations and Jarrett et al. (2011) for WISE W1-W4 calibrations. The IRSF K_s band, 2MASS K_s band, WISE W1 and W2 bands extinction corrected isophotal magnitudes with the Tully-Fisher relation

calibrations of various published work were used to understand the cosmic flow of ZoA galaxies.

FIGURE 5.1: Offset in IRSF K_s band, 2MASS K_s band, WISE W1 and W2 band isophotal magnitudes with comparison between various selected calibrations with $\log W \geq 2.0$.

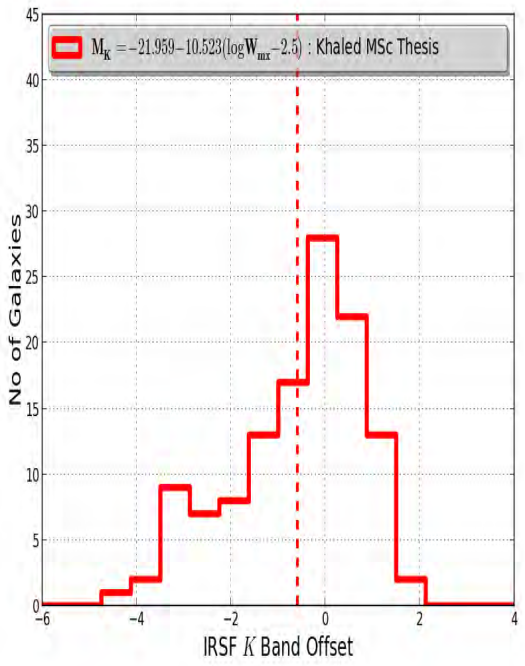

(a) IRSF K_s band Offset.

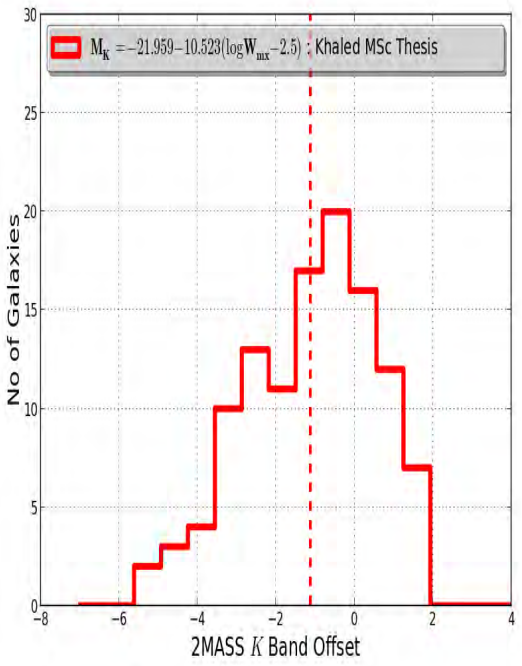

(b) 2MASS K_s band Offset.

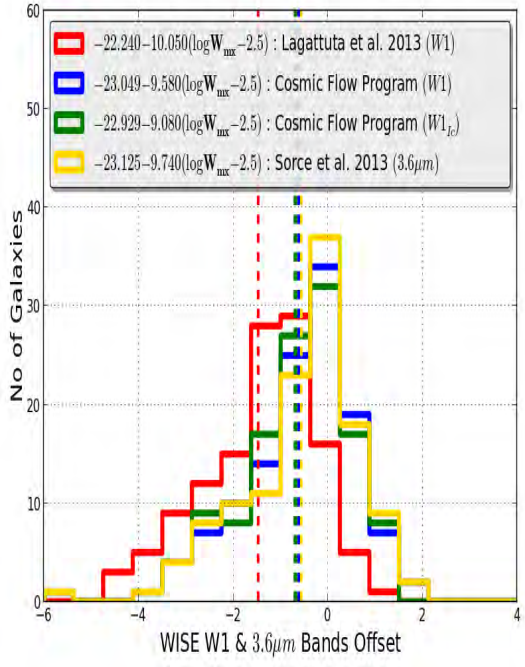

(c) WISE W1 band Offset.

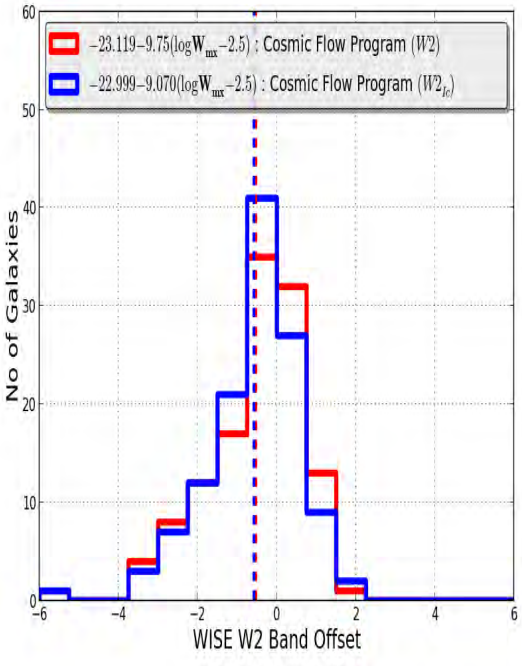

(d) WISE W2 band Offset.

FIGURE 5.2: Offset in IRSF K_s band, 2MASS K_s band, WISE W1 and W2 band isophotal magnitudes with comparison between various selected calibrations with $\log W \geq 2.3$.

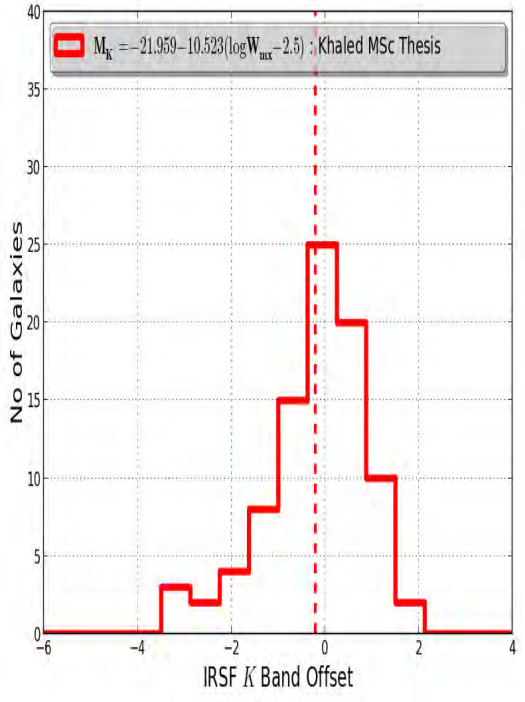

(a) IRSF K_s band Offset.

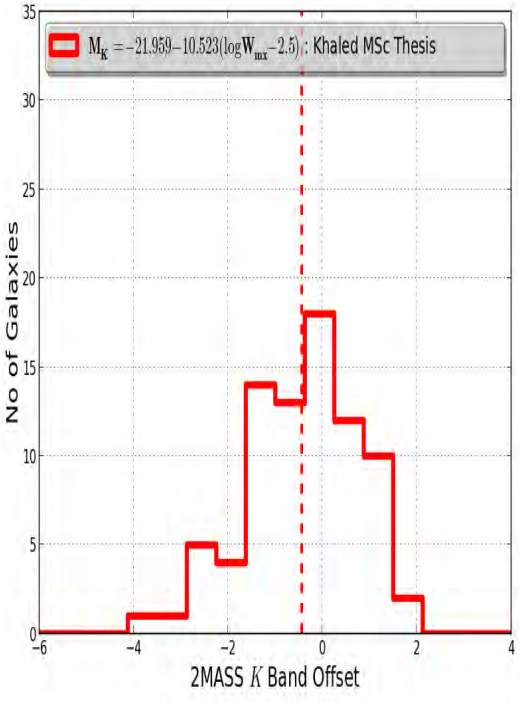

(b) 2MASS K_s band Offset.

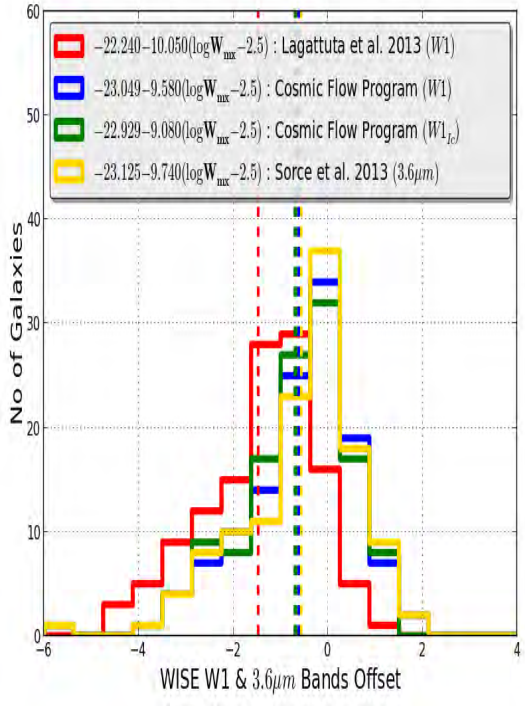

(c) WISE W1 band Offset.

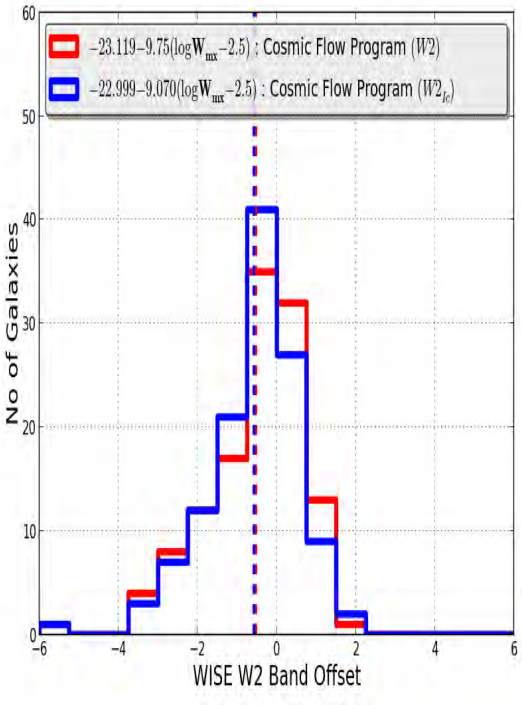

(d) WISE W2 band Offset.

The magnitude used for the cosmic flow analysis was corrected based on the calibrator corrections given in equation 4.45 and the linewidth was corrected using equation 4.1. We obtained the data offset and the peculiar velocity distribution of ZoA galaxies for each of these wavebands as seen in FIGURE 5.1, 5.2, 5.3, 5.4, 5.5 & 5.6. FIGURE 5.1 & 5.2 shows a negative mean offset. This imples that the flows are towards a more dense region. FIGURE 5.3, 5.4, 5.5 & 5.6 show a positive mean peculiar velocity distribution associated with ZoA galaxies. The Great Attractor region ($270° < l < 360°$; Kolatt et al. (1995)) and the region near Puppis with $220° 0 < l < 270°$ also indicate a positive mean peculiar velocity. The Great Attractor regions when compare to the entire ZoA region and the region near Puppis has the highest mean peculiar velocity distribution as seen in FIGURE 5.3, 5.4, 5.5 & 5.6. This suggest that galaxy dynamics in the ZoA are strongly dominated by the infall into Great Attractor. The Great Attractor is the most pronounced feature in the ZoA and it is mostly characterized with a high mass concentration as compared to ZoA region near Puppis which has a lower mass concentration as seen in the histograms in FIGURE 5.3, 5.4, 5.5 & 5.6. FIGURE 5.11 shows that most of the mean peculiar velocities are within the range predicted from the Local Group motion with respect to the CMB. Therefore, the velocity range of $2000-6000$ km s^{-1} with an isophotal absolute magnitude offset of 0.2-0.4 may cause a systemic flow of $100-650$ km s^{-1} as seen in FIGURE 5.11.

FIGURE 5.3: Peculiar velocity distribution of ZoA galaxies using IRSF K_s band isophotal magnitudes.

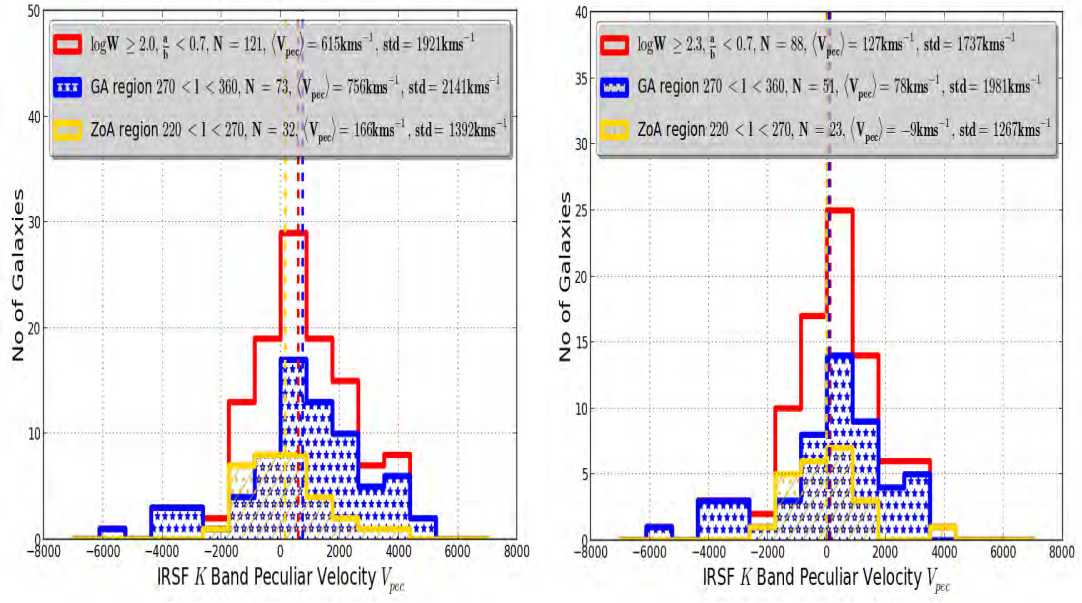

(a) Peculiar velocity distribution of ZoA galaxies using Said (2013) K_s band Tully-Fisher relation calibration and IRSF K_s band isophotal magnitudes with $\log W \geq 2.0$.

(b) Peculiar velocity distribution of ZoA galaxies using Said (2013) K_s band Tully-Fisher relation calibration and IRSF K_s band isophotal magnitudes with $\log W \geq 2.3$.

FIGURE 5.4: Peculiar velocity distribution of ZoA galaxies using 2MASS K_s band isophotal magnitudes.

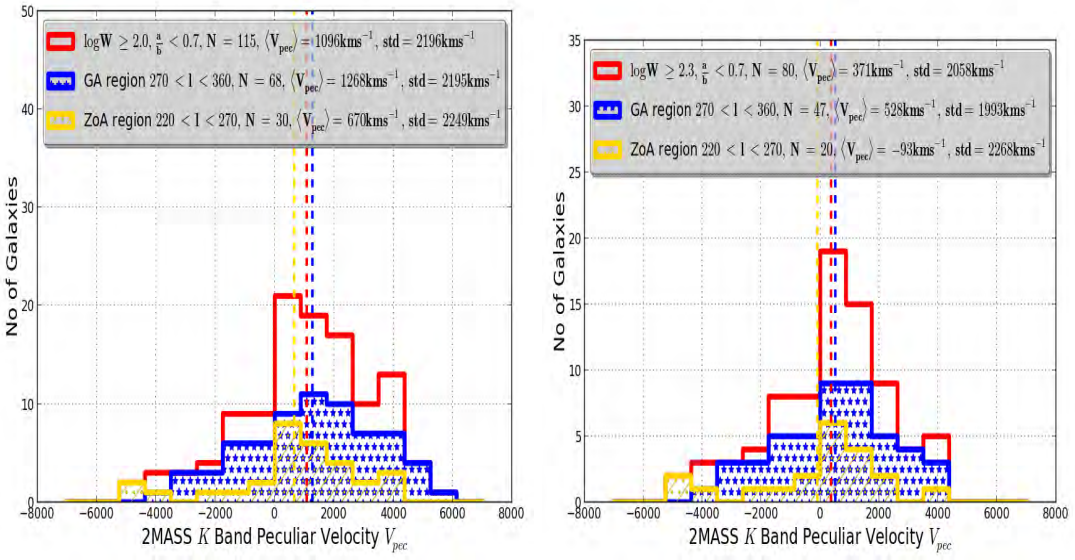

(a) Peculiar velocity distribution of ZoA galaxies using Said (2013) K_s band Tully-Fisher relation calibration and 2MASS K_s band isophotal magnitudes with $\log W \geq 2.0$.

(b) Peculiar velocity distribution of ZoA galaxies using Said (2013) K_s band Tully-Fisher relation calibration and 2MASS K_s band isophotal magnitudes with $\log W \geq 2.3$.

FIGURE 5.5: Peculiar velocity distribution of ZoA galaxies using WISE W1 band isophotal magnitudes.

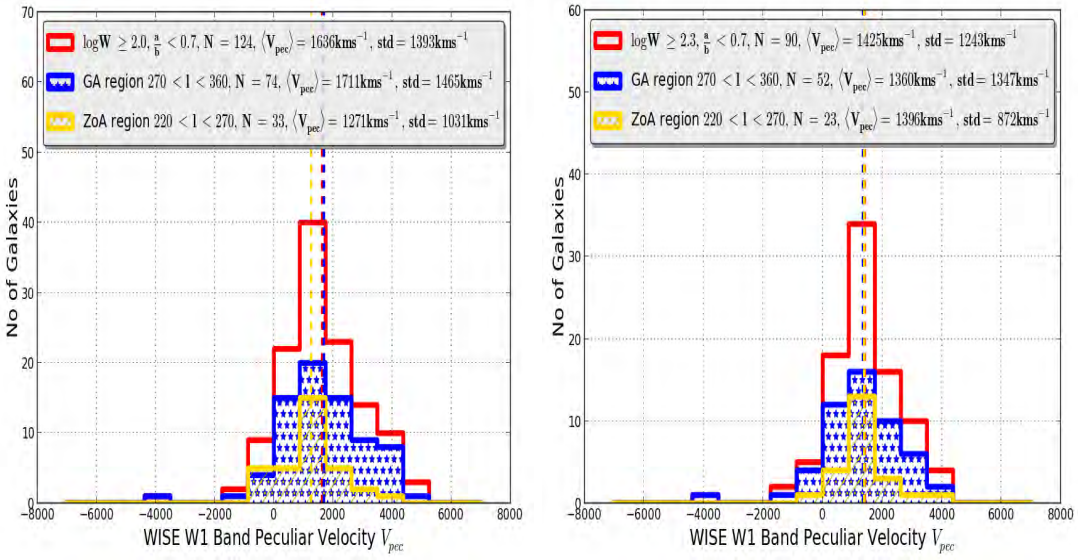

(a) Peculiar velocity distribution of ZoA galaxies using Lagattuta et al. (2013) WISE W1 Tully-Fisher relation calibration and WISE W1 band isophotal magnitudes with $\log W \geq 2.0$.

(b) Peculiar velocity distribution of ZoA galaxies using Lagattuta et al. (2013) WISE W1 Tully-Fisher relation calibration and WISE W1 band isophotal magnitudes with $\log W \geq 2.3$.

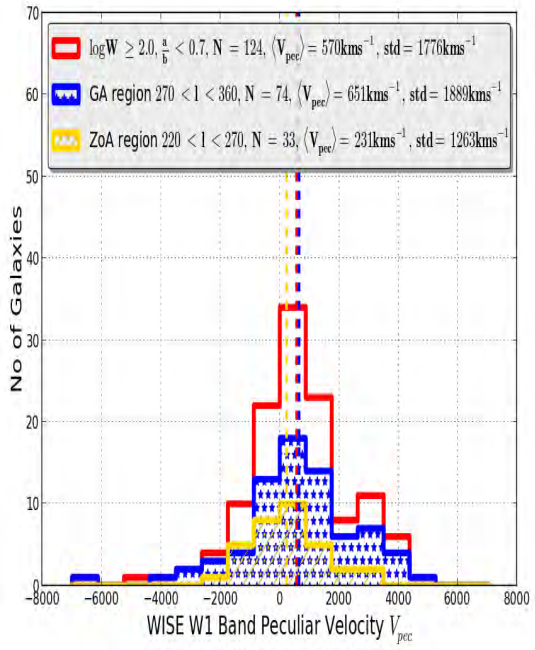

(c) Peculiar velocity distribution of ZoA galaxies using Cosmic Flow Program WISE W1 Tully-Fisher relation calibration and WISE W1 band isophotal magnitudes with $\log W \geq 2.0$.

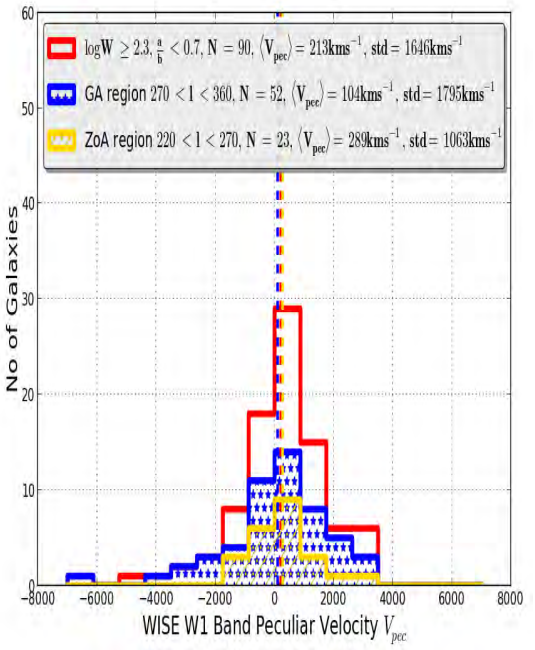

(d) Peculiar velocity distribution of ZoA galaxies using Cosmic Flow Program WISE W1 Tully-Fisher relation calibration and WISE W1 band isophotal magnitudes with $\log W \geq 2.3$.

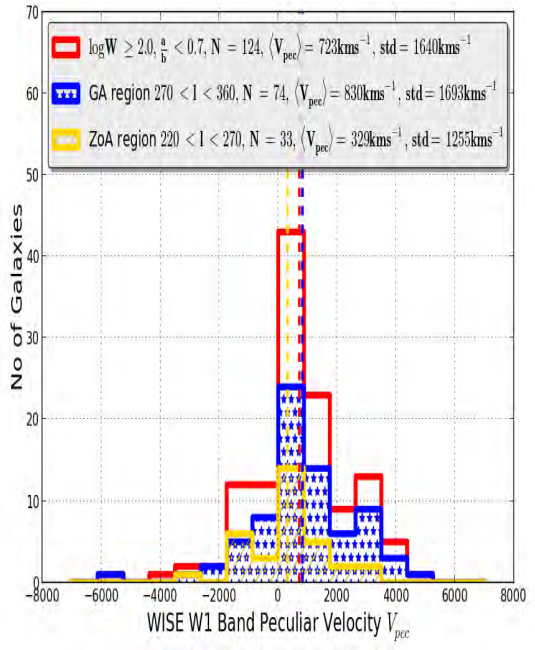

(e) Peculiar velocity distribution of ZoA galaxies using Cosmic Flow Program I band conversion of WISE W1 Tully-Fisher relation calibration and WISE W1 band isophotal magnitudes with $\log W \geq 2.0$.

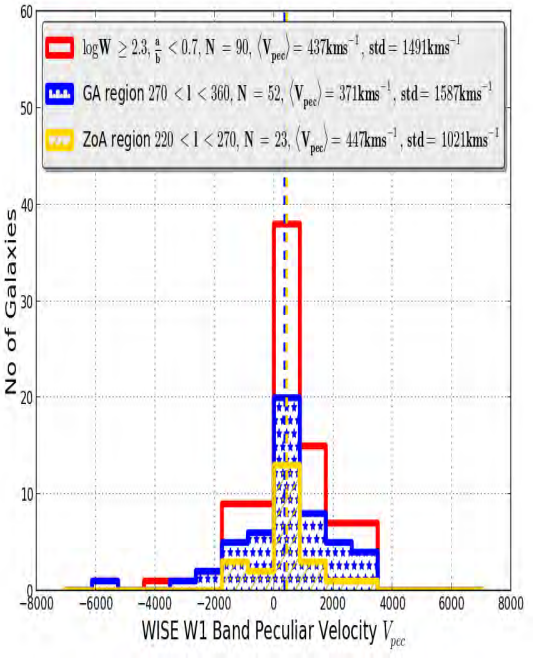

(f) Peculiar velocity distribution of ZoA galaxies using Cosmic Flow Program I band conversion of WISE W1 Tully-Fisher relation calibration and WISE W1 band isophotal magnitudes with $\log W \geq 2.3$.

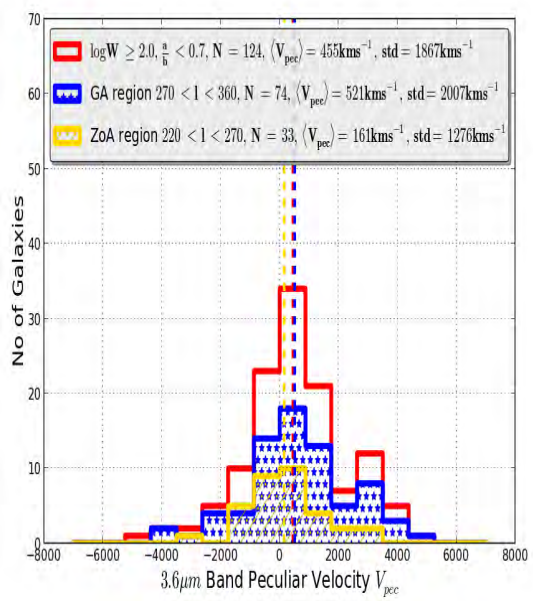

(g) Peculiar velocity distribution of ZoA galaxies using Sorce et al. (2013) 3.6 μm Tully-Fisher relation calibration and WISE W1 band isophotal magnitudes with $\log W \geq 2.0$.

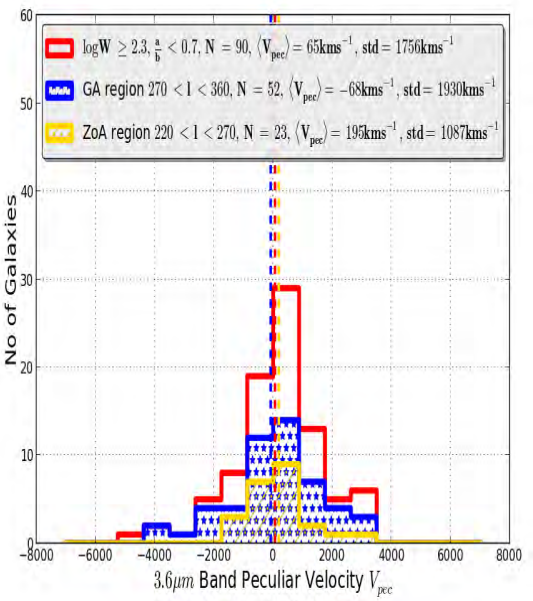

(h) Peculiar velocity distribution of ZoA galaxies using Sorce et al. (2013) 3.6 μm Tully-Fisher relation calibration and WISE W1 band isophotal magnitudes with $\log W \geq 2.3$.

FIGURE 5.6: Peculiar velocity distribution of ZoA galaxies using WISE W2 band isophotal magnitudes.

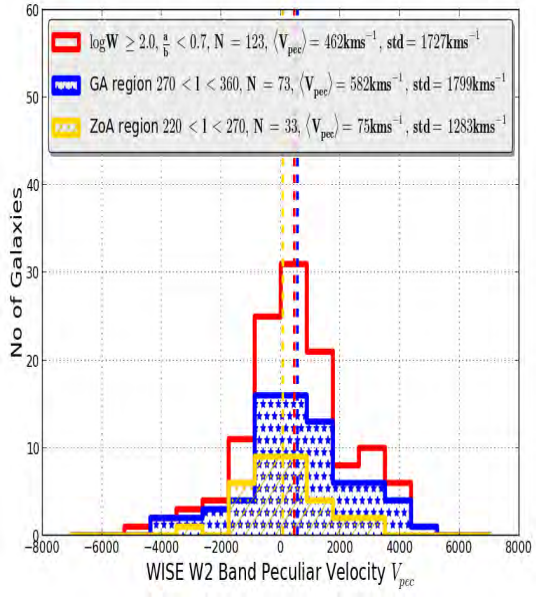

(a) Peculiar velocity distribution of ZoA galaxies using Cosmic Flow Program WISE W2 Tully-Fisher relation calibration and WISE W2 band isophotal magnitudes with $\log W \geq 2.0$.

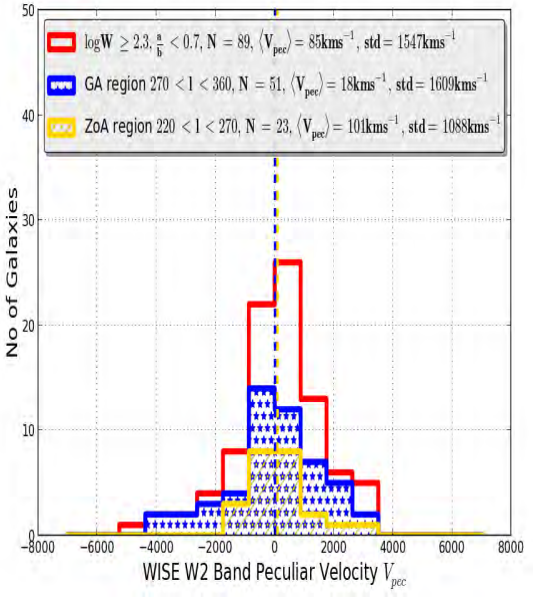

(b) Peculiar velocity distribution of ZoA galaxies using Cosmic Flow Program WISE W2 Tully-Fisher relation calibration and WISE W2 band isophotal magnitudes with $\log W \geq 2.3$.

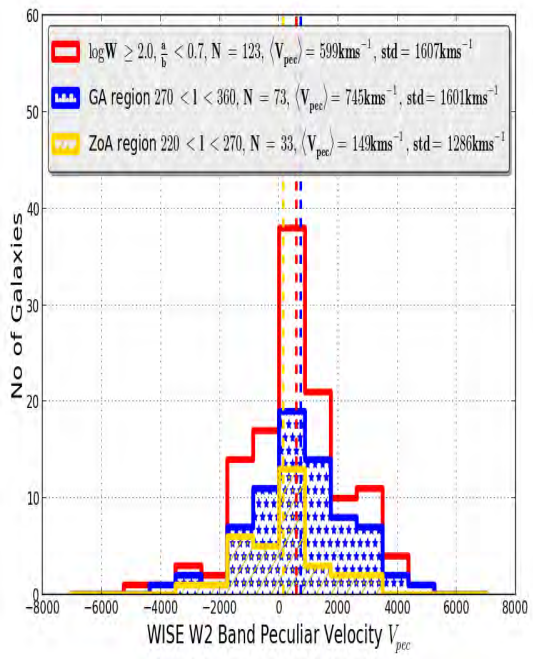

(c) Peculiar velocity distribution of ZoA galaxies using Cosmic Flow Program I band conversion of WISE W2 Tully-Fisher relation calibration and WISE W2 band isophotal magnitudes with $\log W \geq 2.0$.

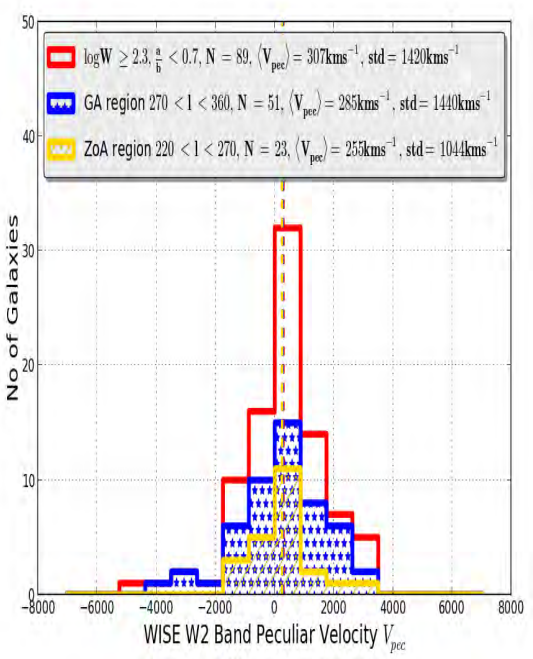

(d) Peculiar velocity distribution of ZoA galaxies using Cosmic Flow Program I band conversion of WISE W2 Tully-Fisher relation calibration and WISE W2 band isophotal magnitudes with $\log W \geq 2.3$.

5.2.1 Peculiar Velocity Models

In this research work, we consider basically some models of peculiar velocity. We started with the basic linear model given by Peebles (1976) and then extended it to include the cluster infall of various Attractor models. We considered the Attractor models of Hudson et al. (2004) which include the Great Attractor, Virgo Attractor and the Shapley Concentration.

5.2.2 Linear Theory

If we assume that density fluctuation appear at some very early time, then at a later time we can describe the density contrast $\bar{\delta}(x,t)$ of the growing mode $D(t)$ as

$$\bar{\delta}(x,t) = \bar{\delta}(x,t_i)\frac{D(t)}{D(t_i)}, \qquad D(t) \propto a(t) \propto t^{2/3}, \quad \text{for} \quad \Omega_m = 1. \tag{5.1}$$

Therefore, density contrast simply grows in a comoving coordinate when $\delta \ll 1$. From the continuity equation the divergence of the peculiar velocity could be written as

$$\vec{\nabla} \cdot \mathbf{v} = -a\delta H f(\Omega_m). \tag{5.2}$$

where $f(\Omega_m) = \Omega_m^{0.6}$ [2], a is the present value of the expansion factor and H is the Hubble parameter. Peebles (1976) showed that linear theory of gravitational instability dictates that the peculiar velocity of a reference frame can be related to the gravitational acceleration $\mathbf{g}$ induced by the mass distribution as

$$V_{pec} = \frac{H_0\beta}{4\pi\bar{n}} \int \frac{n(r)}{r^2}\hat{\mathbf{r}}\, dr = \frac{H_0 f}{4\pi G\rho_b}\mathbf{g}, \tag{5.3}$$

where $\bar{n}$ is the average mass tracer number density. However, there is both theoretical (Dekel & Lahav, 1999; Kaiser, 1984; Davis et al., 1985; Kauffmann et al., 1997) and observational (Davis & Geller, 1976; Dressler, 1980; Tegmark & Bromley, 1999) evidence that galaxies are biased tracers of the matter distribution. As a result, comparisons between the density and velocity fields within linear theory cannot yield an estimate of Ω_m. The quantity that is estimated is $\beta = \Omega_m^{0.6}/b$, where b is the biasing parameter relating mass tracers to the underlying mass distribution. Equation (5.3) can be rewritten as $V_{pec} = \beta\mathbf{D}_{cl}$, where $\mathbf{D}_{cl}$ is the cluster dipole. This equation tells us that the dipole moment of a mass-tracer distribution is proportional to the peculiar velocity that the galaxy sample will induce. Linear theory gives a relation between galaxy density and peculiar velocity, which can be used to derive a velocity field from a redshift survey (Peebles, 1976). The linear cluster infall model focus on measuring the peculiar velocity field by comparing it to models of what is expected given the density field. Early studies on cosmic flow involves the measurements of cluster infall. Which is based on the idea that a spherically symmetric cluster embedded in a homogeneous medium induces a spherically symmetric radial velocity field (Hudson et al., 2004). Prediction from the cluster infall velocity model are often used for cluster mass estimation (Kaiser, 1984).

5.2.3 Bulk Flow Model

For an idealized densely sampled survey, the bulk flow or the dipole moment of the peculiar velocity field would reflect the gravitational pull of mass near and beyond the survey limits. This model is more sensitive to the distribution of mass on the largest scales, which is carried out by fitting the radial components of the cluster peculiar velocities with the flow model

$$V_{pec}(r) = \mathbf{V}\cdot\hat{\mathbf{r}} + \frac{\triangle H}{H}\mathbf{r}. \tag{5.4}$$

The free parameter V is the bulk flow vector, $\mathbf{r}$ is the distance expressed in km s^{-1} and $\triangle H/H$ is a perturbation to the assumed Hubble constant (Hudson et al., 2004).

[2] We have known for almost a decades that $\Omega_m \ll 1$, and have known for over a decade that the index to Ω_m is modified from 0.6 by the presence of dark energy.

Giovanelli et al. (1999) found a statistically insignificant Hubble bubble of $\triangle H/H = 1 \pm 2$ % using the Tully-Fisher relation. In this research work we fitted this model to our dataset using a Local Group Bulk flow of 627 km s^{-1} given by Kogut et al. (1993).

5.2.4 Attractor Models

Several authors have consider the spherically symmetric infall into the Attractor, one of such Attractor model was given by Hudson et al. (2004). The Hudson et al. (2004) model for the radial infall component towards an Attractor is given as

$$V^a_{pec}(r) = \left(v_a \frac{r_a}{d_a} \left[\frac{(d_a^2 + c_a^2)}{(r_a^2 + c_a^2)} \right]^{\frac{(n_a+1)}{2}} \right) \cdot \hat{r}, \tag{5.5}$$

where d_a is the distance from the Local Group to the Attractor, $\mathbf{r}_a = \mathbf{d}_a - \mathbf{r}$ is the vector from the point $\mathbf{r}$ to the center of the Attractor. c_a is the core radius and v_a is the velocity of infall towards the Attractor at position of the Local Group. From equation (5.5) we observe there is no infall at $r_a \sim 0$, and the infall peaks at $r_a \sim c_a$ and falls off as $V^a_{pec} \sim r_a^{-n_a}$. The parameters used for the Great Attractor model are given by Faber & Burstein (1988), as $n_{GA} = 1.7$, $r_{GA} = 4200$ km s^{-1}, $c_{GA} = 1430$ km s^{-1} & $v_{GA} = 535$ km s^{-1} (Hudson et al., 2004). For the second Great Attractor model we assumed a $n_{GA} = 1.7$, $r_{GA} = 4848$ km s^{-1}, $c_{GA} = 1430$ km s^{-1} & $v_{GA} = 535$ km s^{-1} (Kraan-Korteweg et al., 1996; Kraan-Korteweg & Lahav, 2000; Hudson et al., 2004). For the Virgo Attractor model, we used Tonry et al. (2000) and Hudson et al. (2004) assumed parameters given as $n_{VA} = 1.7$, $r_{VA} = 2300$ km s^{-1}, $c_{VA} = 1430$ km s^{-1} & $v_{VA} = 240$ km s^{-1}. Furthermore, we consider other Attractor models at larger distance, Since the Great Attractor at ($l = 307°$, $b = 9°$) is not the only primary source inducing large scale motions in our Local Group (Mathewson & Ford, 1994). There are other bigger structures located beyond this region which could induce bulk flows at very large-scales. The Shapley supercluster, a massive cluster centered on the rich cluster Abell 3558 at $l = 312°$, $b = 31°$ which is at a distance of 145 h^{-1} Mpc (Lynden-Bell et al., 1988; Tonry et al., 2000; Hudson et al., 2004). The parameters for Shapley supercluster model are $n_{SC} = 1.7$, $r_{SC} = 14500$ km s^{-1} and $c_{SC} = 2250$ km s^{-1}. The Shapley Concentration predicts an inflow at the Local Group of 200 ± 60 km s^{-1} with no bulk flow, while Shapley Concentration plus bulk flow predict an inflow of 140 ± 80 km s^{-1} (Hudson et al., 2004). However large uncertainties are present in the distance measurements due to inhomogeneous Malmquist bias and other effects. We used these models to investigate the peculiar velocities that would be associated with our selected ZoA galaxies. The Attractor models plots on the distribution of peculiar velocity for each waveband with various calibrations is given in FIGURE 5.7, 5.8, 5.9 & 5.10.

5.2.5 Local Group Peculiar Velocity Field Model

The Local Group velocity model is a generalized model for all observed nearby mass concentration that contribute to the galaxies flow motion in the Local Universe. Mould et al. (2000a,b) Local Universe peculiar velocity is the sum of the Sun peculiar velocity $V_{\odot}$ with respect to its neighborhood star which is 16 km s^{-1}, the peculiar velocity of the Local Group centroid ΔV_{LG} of about 100 km s^{-1}, the peculiar velocity of the Great Attractor ΔV_{GA}, the peculiar velocity of the Virgo cluster ΔV_{Virgo} and the Shapley supercluster peculiar velocity $\Delta V_{Shapley}$. The biggest contribution to solar motion is the Galactic rotation. Using the Attractor models of Hudson et al. (2004) described in Subsection 5.2.4, we obtained the peculiar velocity distributions for the Great Attractor, Virgo cluster and the Shapley supercluster for the Mould et al. (2000a,b) model. The parameters are similar to the parameter used in Subsection 5.2.4. The corrected cosmic peculiar velocity with respect to the Local Universe can be expressed as

$$V_{pec}^{LG} = V_{\odot} + \Delta V_{LG} + \Delta V_{GA} + \Delta V_{Virgo} + \Delta V_{Shapley} + \cdots . \tag{5.6}$$

We plotted this model on our dataset to understand the distribution of ZoA galaxies peculiar velocities. The model given by Mould et al. (2000a,b) is a combination of the model given by Hudson et al. (2004) in equation 5.5. This model provide a general ideal for understanding the dynamics of the Local Universe. We neglected other Attractor models because they have a very small contribution to Local Group motion.

FIGURE 5.7: IRSF K_s band peculiar velocity analysis of ZoA data and plots of various peculiar velocity models. The selected ZoA data have $\log W \geq 2.3$ with K_s band axial ratio $\frac{a}{b} \leq 0.7$. The K_s band axial ratio was used for colorbar calibration the plots.

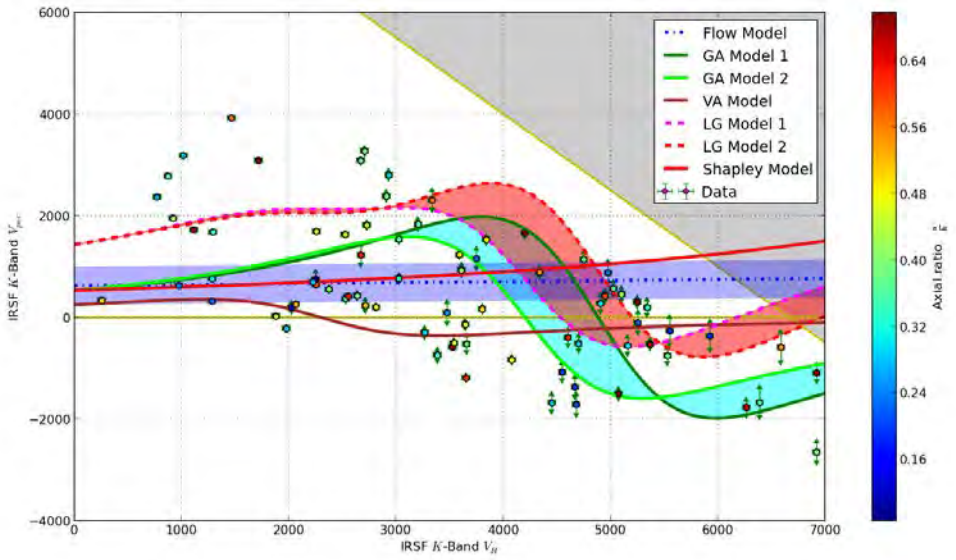

(a) Peculiar velocity models distribution of ZoA galaxies using Said (2013) Tully-Fisher relation calibration and IRSF K_s band magnitudes.

FIGURE 5.8: 2MASS K_s band peculiar velocity analysis of ZoA data and plots of various peculiar velocity models. The selected ZoA data have $\log W \geq 2.3$ with K_s band axial ratio $\frac{a}{b} \leq 0.7$.

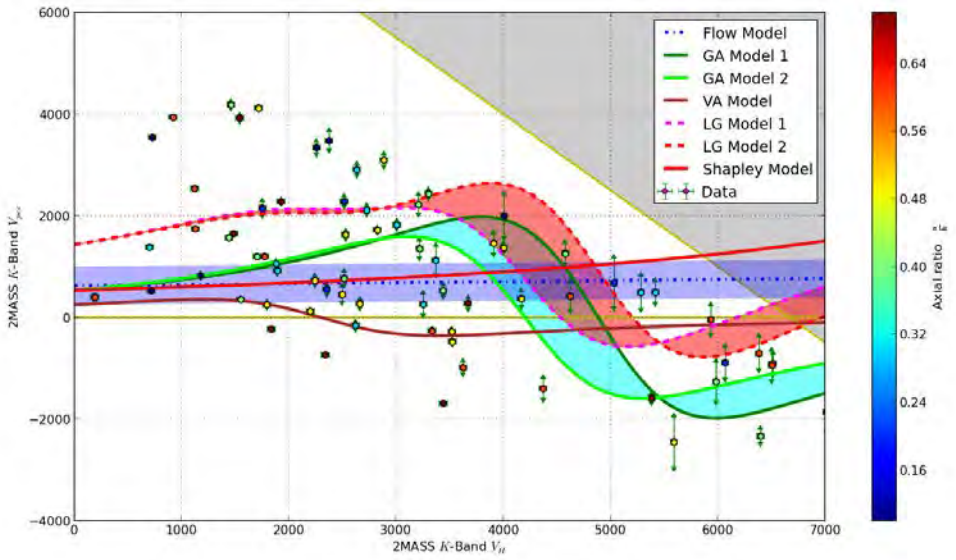

(a) Peculiar velocity models distribution of ZoA galaxies using Said (2013) Tully-Fisher relation calibration and 2MASS K_s band magnitudes.

FIGURE 5.9: WISE W1 band peculiar velocity analysis of ZoA data and plots of various peculiar velocity models. The selected ZoA data have $\log W \geq 2.3$ with K_s band axial ratio $\frac{a}{b} \leq 0.7$.

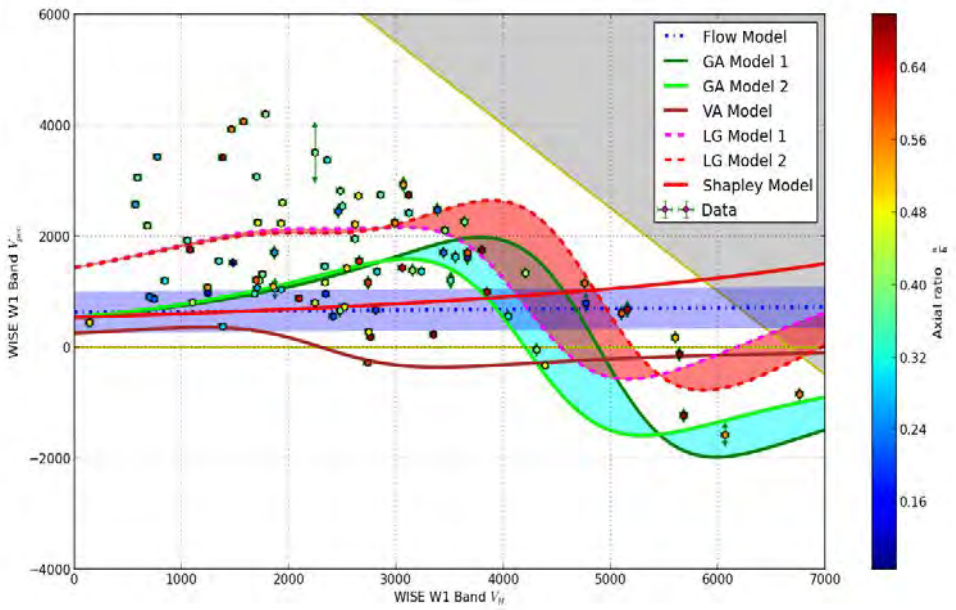

(a) Peculiar velocity models distribution of ZoA galaxies using Lagattuta et al. (2013) WISE W1 Tully-Fisher relation calibration and WISE W1 band magnitudes.

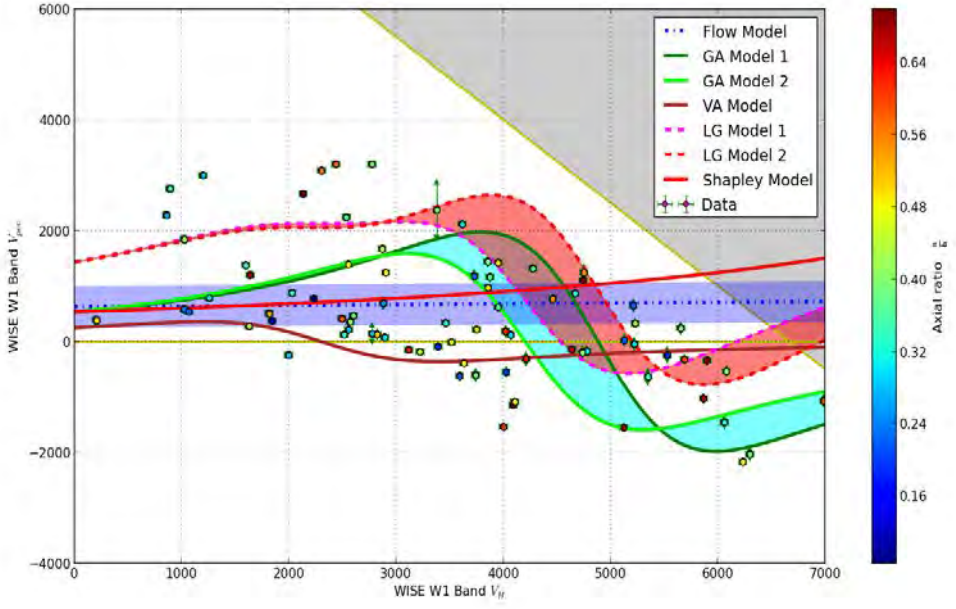

(b) Peculiar velocity models distribution of ZoA galaxies using Sorce et al. (2013) 3.6 μm Tully-Fisher relation calibration and WISE W1 band magnitudes.

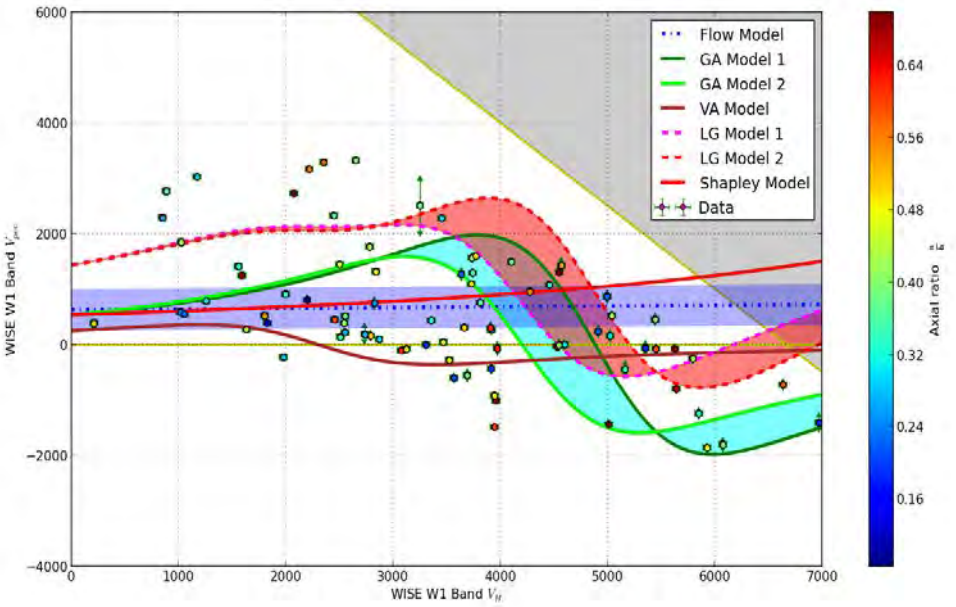

(c) Peculiar velocity models distribution of ZoA galaxies using Cosmic Flow Program WISE W1 Tully-Fisher relation calibration and WISE W1 band magnitudes.

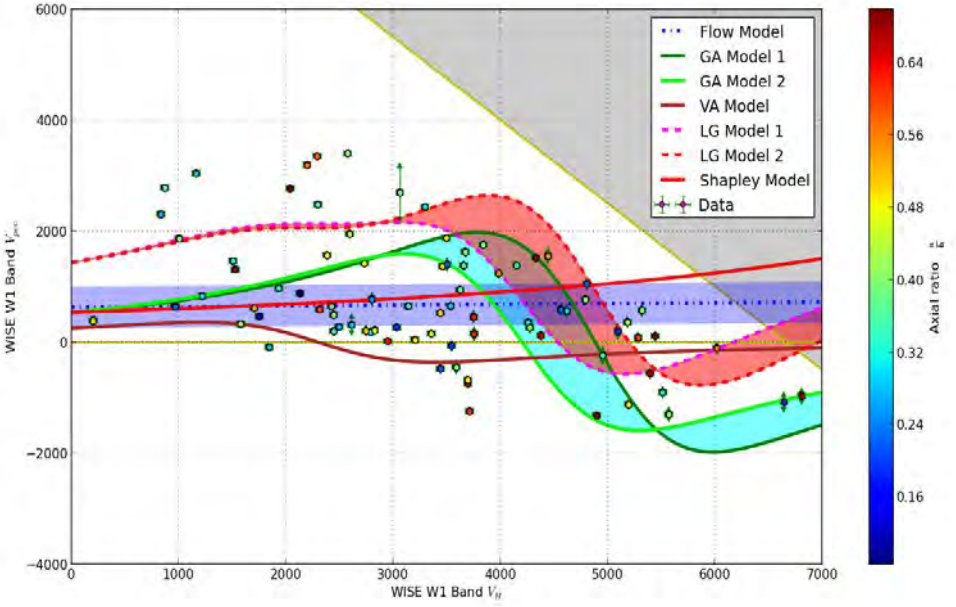

(d) Peculiar velocity models distribution of ZoA galaxies using Cosmic Flow Program I band conversion of WISE W1 Tully-Fisher relation calibration and WISE W1 band magnitudes.

FIGURE 5.10: WISE W2 band peculiar velocity analysis of ZoA data and plots of various peculiar velocity models. The selected ZoA data have $\log W \geq 2.3$ with K_s band axial ratio $\frac{a}{b} \leq 0.7$.

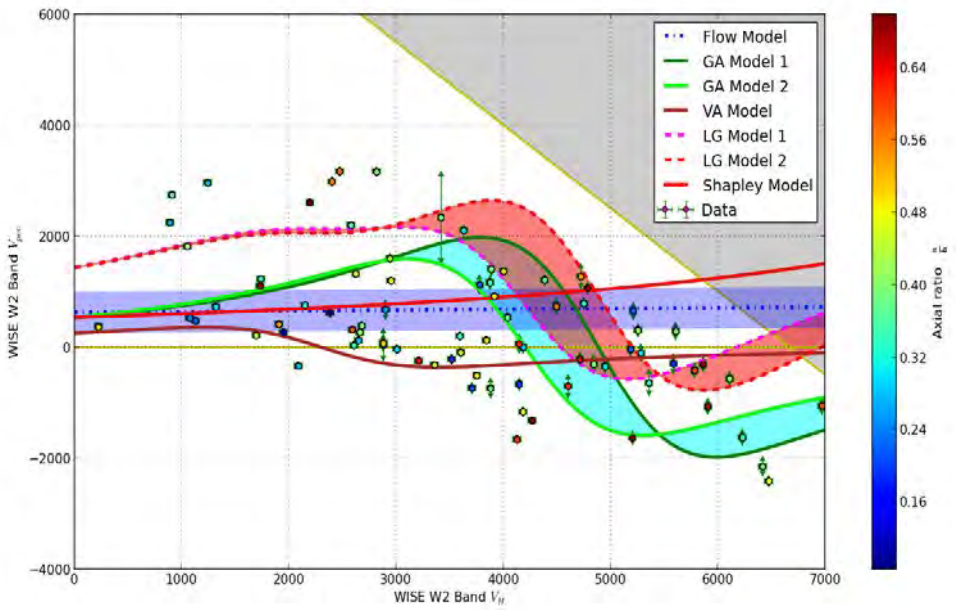

(a) Peculiar velocity models distribution of ZoA galaxies using Cosmic Flow Program WISE W2 Tully-Fisher relation calibration and WISE W2 band magnitudes.

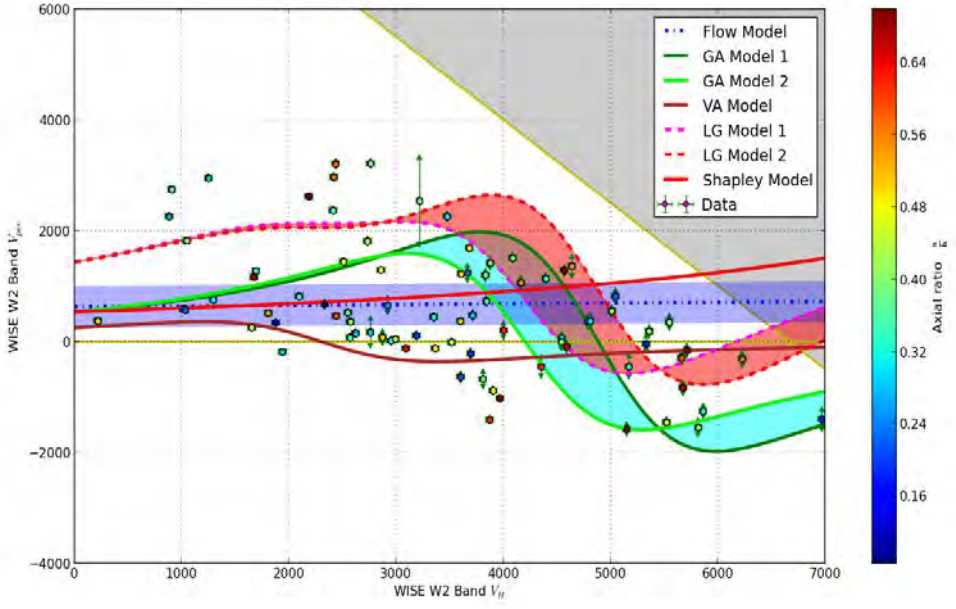

(b) Peculiar velocity models distribution of ZoA galaxies using Cosmic Flow Program I band conversion of WISE W2 Tully-Fisher relation calibration and WISE W2 band magnitudes.

5.3 Peculiar Velocity Field

If we can measure the redshift of a source, then we could determine the total or observed velocity and subsequently determine the peculiar velocity using this relation

$$V_{pec} = V_{obs} - V_H. \tag{5.7}$$

Peculiar velocities enable a reconstruction of the large scale matter distribution independent of galaxy surveys (Kolatt et al., 1995). One can compare the measured velocity field with the inferred velocities from the matter distribution. In this research work we determine the peculiar velocity associated with the ZoA using the formalism of (Masters et al., 2008) given as

$$V_{pec} = V_{CMB}\left(1 - 10^{\frac{\Delta M}{5}}\right), \tag{5.8}$$

and the distance was calculate as

$$d = \frac{V_{CMB}}{H_0} 10^{\frac{\Delta M}{5}}. \tag{5.9}$$

Where $\Delta M = M_{obs} - M(W)$ is the offset which was obtained using the difference between the observed absolute magnitude M_{obs} and $M(W)$. $M(W)$ is the linewidth-magnitude dependent correction from a standard calibration. The error in the peculiar velocity is given as

$$\sigma^2_{V_{pec}} = \frac{V^2_{pec}}{V^2_{CMB}}\sigma^2_{V_{CMB}} + (0.2H_0 d \ln 10)^2 \sigma^2_{\triangle M}, \tag{5.10}$$

while the error in distance is given as

$$\sigma^2_d = \frac{d^2}{V^2_{CMB}}\sigma^2_{V_{CMB}} + (0.2d \ln 10)^2 \sigma^2_{\triangle M}. \tag{5.11}$$

The error associated with the offset is given as

$$\sigma^2_{\Delta M} = \sigma^2_{m_{obs}} + \sigma^2_A + \sigma^2_{A_i} + \left(\frac{5}{V}\ln 10\right)^2 \sigma^2_V + \left(\frac{b}{W \ln 10}\right)^2 \sigma^2_W + \epsilon^2_{int}. \tag{5.12}$$

The parameters are clearly defined and explained in Chapter 4 (Masters et al., 2008). From FIGURE 5.7, 5.8, 5.9 & 5.10 shows a plot of peculiar velocity on Hubble velocity $V_H = H_0 d$ with a specification of the galaxies axial ratio. The models discussed above were over plotted on the ZoA peculiar velocity distribution with Hubble flow. The galaxies used for the peculiar velocity model analysis had axial ratio of 0.7 with $\log W \geq 2.3$. FIGURE 5.7, 5.8, 5.9 & 5.10 shows a good agreement with various peculiar velocity models. The region color-coded with cyan is region between Great Attractor model 1 and 2, while the region color-coded with blue is the observed range of bulk flows in the Local Group of galaxies. The region color-coded with red is the region between the Local

Universe model 1 and 2. The region color-coded with grey is the observational limit. The models in FIGURE 5.7 – 5.10 are the Great Attractor models, the Virgo model, the Local Universe models and the Shapley model discussed above. We could observe that the cosmic peculiar velocity field model with respect to the Local Universe provide the best model for understanding the dynamics of ZoA galaxies. Therefore, at low Hubble's velocities we would observe a positive peculiar velocity, while at large Hubble's velocities we would observe a negative peculiar velocities as seen in FIGURE 5.7 – 5.10. The region 1 and 2 are regions having average and maximum velocities of the Great Attractor. FIGURE 5.11 shows the mean peculiar velocities values for various regions of ZoA with $\log W \geq 2.0$ and $\log W \geq 2.3$ using the calibration of Said (2013) for the K_s band, Lagattuta et al. (2013); Sorce et al. (2013) and Cosmic Flow Program calibrations for WISE W1 band and the Cosmic Flow Program calibrations for WISE W2 band. From FIGURE 5.11(a) & (b) shows that the more inclined estimate of mean peculiar velocities are distributed around zero mean peculiar velocity as compared to less inclined estimate of mean peculiar velocities.

FIGURE 5.11: Mean peculiar velocities values of various ZoA regions for IRSF K_s, 2MASS K_s, WISE W1 and W2 bands using Infrared bands Tully-Fisher relation calibrations. The 'K' stand for Said (2013) calibration, 'L' represent Lagattuta et al. (2013) calibration, 'C1' represent the Cosmic Flow Program calibration and 'C2' I band conversion of Cosmic Flow Program calibration. The grey horizontal solid line is the mean peculiar velocity obtained by Kogut et al. (1993).

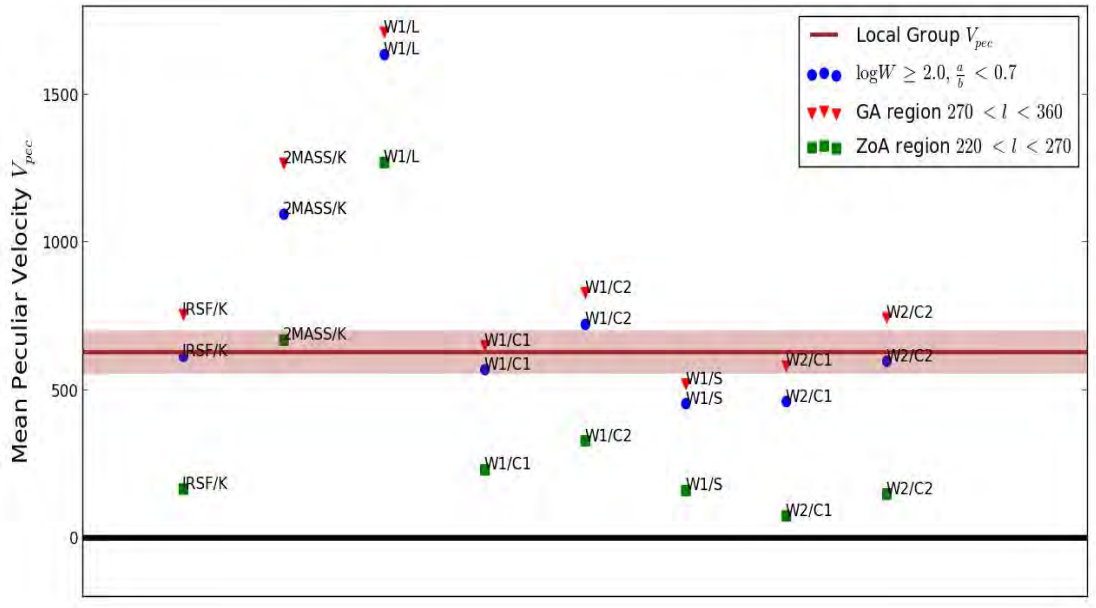

(a) Mean peculiar velocities values of various ZoA regions with $\log W \geq 2.0$.

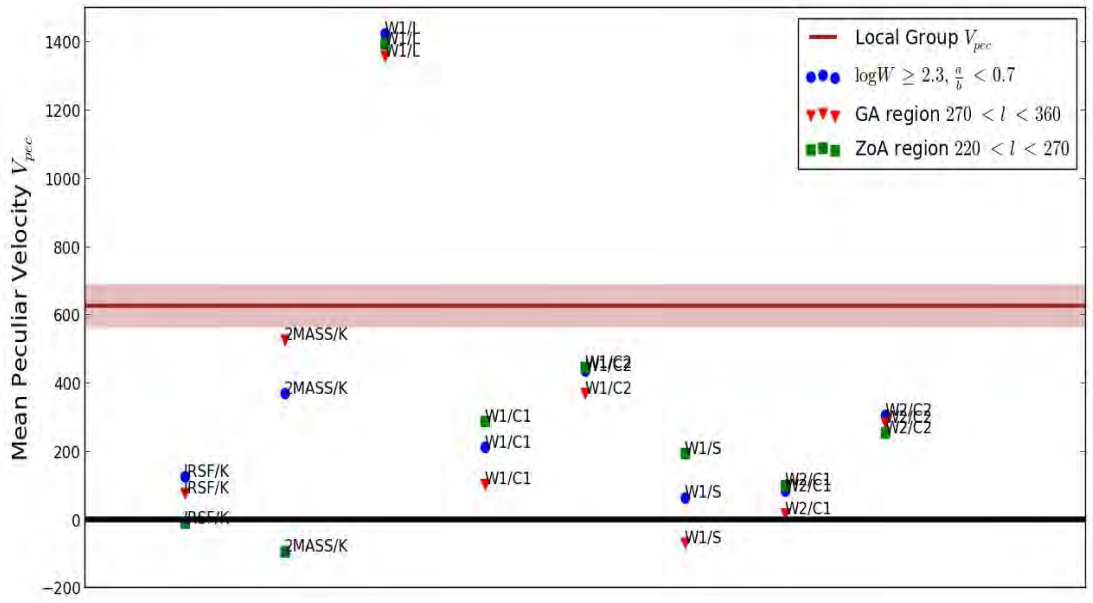

(b) Mean peculiar velocities values of various ZoA regions with $\log W \geq 2.3$.

5.3.1 Mapping Peculiar Velocity Field

The peculiar velocity equation in (5.3) cannot be explained by Hubble's law. Thus, the farther away a light source is, the bigger the value of Hubble's velocity V_H. If we measure an object that is very far away, the peculiar velocity is quite small as compared to the Hubble's velocity. Also, if we measure an object that is nearby, then the Hubble's velocity is not very large and so we correct for peculiar velocity. Observed galaxies do not exactly follow Hubble's law. This is because of the observed peculiar velocities associated with galaxies will make Hubble's law useless. However, galaxy peculiar velocity are quite small $\sim$ 300 km s^{-1} and rarely exceed 1000 km s^{-1}. When the value of $H_0 d$ is much larger than 1000 km s^{-1}, Hubbles law become accurate for galaxies that are far away (Pierce, 2006; Tully et al., 2008). Hubbles law is very important in mapping the 3-dimensional distribution of galaxies. This is because we can estimate the galaxy's distance from its redshift. FIGURE 5.12-5.19 are linear peculiar velocity maps obtained using K_s band linewidth-magnitude calibration of Said (2013), WISE W1 linewidth-magnitude calibrations of Lagattuta et al. (2013); Sorce et al. (2013) and Cosmic Flow Program and WISE W2 linewidth-magnitude calibrations of the Cosmic Flow Program.

The peculiar velocity map in this research work was produced by using ZoA galaxies with $\log W \geq 2.3$ and a linear interpolation of the peculiar velocities across the Galactic longitude and recession velocity plane, using the scipy interpolation module in python called griddata. If we look closely at the linear map in FIGURE 5.12-5.19, it show the northward local streaming associated with the non-uniform distribution of matter

within the ZoA region. The region with very high positive peculiar velocities are regions mostly associated with galaxy clusters or supercluster as seen in the peculiar velocity map in FIGURE 5.12-5.19. The stars in the plots are galaxy clusters and superclusters associated with the ZoA. The stars are areas of high peculiar velocities mostly associated with galaxy clusters. The blue star (★) is the Great Attractor region, the cyan star (★) is the Galactic center, the yellow star (★) is the region close to Hydra (270°, +27°) and Antlia (273°, +19°) clusters given by Radburn-Smith et al. (2006) and the red star (★) is the Puppis cluster at (240°, 0°) given by Lahav et al. (1993). The color-coded dots in the map are galaxies. The galaxies color-coded with red indicate that the galaxy have positive peculiar velocity, while galaxies color-coded with blue indicate that the galaxy have negative peculiar velocity. FIGURE 5.12 is the IRSF K_s band peculiar velocity map with a mean peculiar velocity of 615 ± 1921 km s^{-1} and the number of galaxies for this analysis was $N = 121$. FIGURE 5.13 is the 2MASS K_s band peculiar velocity map with a mean peculiar velocity of 1096 ± 2196 km s^{-1} and the number of galaxies for this analysis was $N = 115$. The WISE W1 band peculiar velocity maps in FIGURE 5.14, 5.15, 5.16 & 5.17 has a mean peculiar velocity of 1636 ± 1393 km s^{-1}, 570 ± 1776 km s^{-1}, 723 ± 1640 km s^{-1} and 455 ± 1867 km s^{-1} respectively and the number of galaxies for these analysis were $N = 124$. FIGURE 5.18 & 5.19 shows WISE W2 band peculiar velocity map with a mean peculiar velocity of 462 ± 1727 km s^{-1} and 599 ± 1607 km s^{-1} respectively and the number of galaxies for these analysis were $N = 123$. The peculiar velocity maps have three prominent infall in region around the Great attractor, the region around Puppis cluster and the region between Hydra and Antlia clusters as seen in FIGURE $5.12 - 5.19$. Therefore, from the mapping analysis in this work we have shown that the Great Attractor is the major over density strongly influencing the motion of galaxies in the ZoA region as seen in FIGURE $5.12 - 5.19$. The range of distribution of the peculiar velocities in FIGURE $5.12 - 5.19$ shows that the WISE bands as compared to IRSF and 2MASS bands is more suitable for mapping ZoA cosmic flow.

The peculiar velocity mapping of ZoA galaxies in this work is in agreement with the published work of Kolatt et al. (1995). Kolatt et al. (1995) studied the large-scale mass distribution behind the Galactic plane and found that the main dynamical features at a distance ~ 4000 km s^{-1} are the peak of Great Attractor connecting Centaurus and Pavo at $l \simeq 300$ and a large void from the southern Galactic hemisphere into the ZoA near the direction of Puppis at $l \simeq 220° - 270°$. Kolatt et al. (1995), also found a moderate bridge connecting Perseus-Pisces and Cepheus at $l \simeq 140°$ as one main dynamical features in the local group which is not covered by this work. This work is in agreement with the results of Said (2013) which shows that Local Universe shows a clear infall into the Great Attractor.

FIGURE 5.12: IRSF K_s band peculiar velocity map using Said (2013) Tully-Fisher relation calibration. These galaxies are color-coded based on their peculiar velocities and the background color is the interpolation of the data.

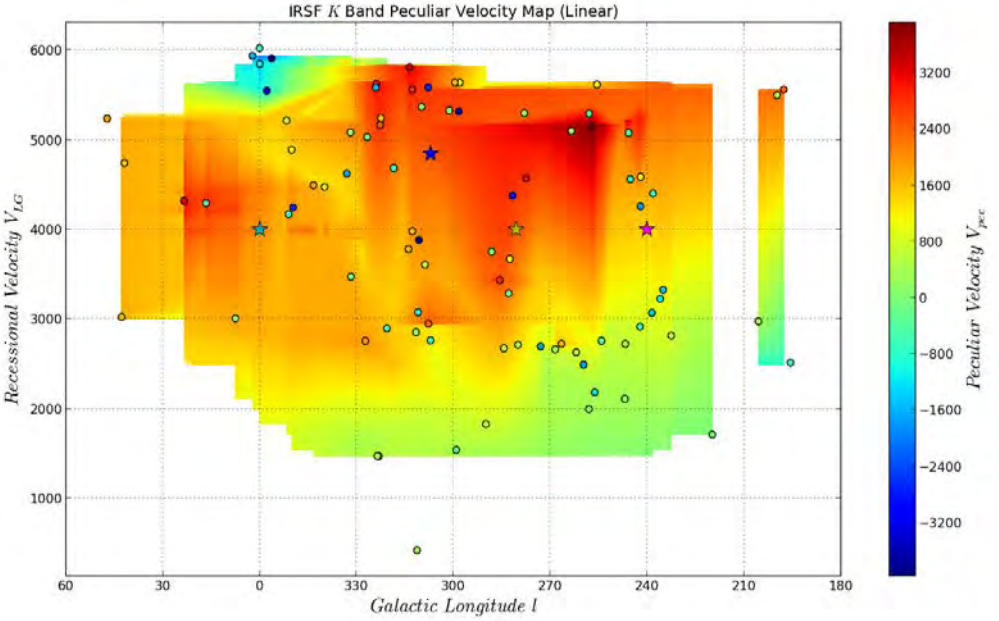

FIGURE 5.13: 2MASS K_s band peculiar velocity map using Said (2013) Tully-Fisher relation calibration. These galaxies are color-coded based on their peculiar velocities and the background color is the interpolation of the data.

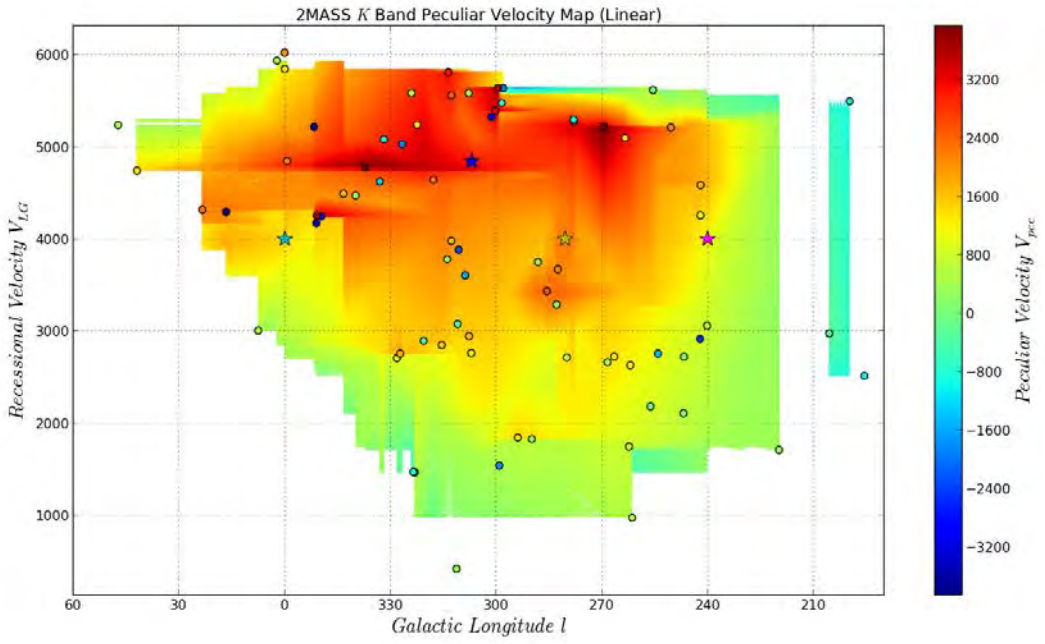

FIGURE 5.14: WISE W1 band peculiar velocity map using Lagattuta et al. (2013) WISE W1 Tully-Fisher relation calibration. These galaxies are color-coded based on their peculiar velocities and the background color is the interpolation of the data.

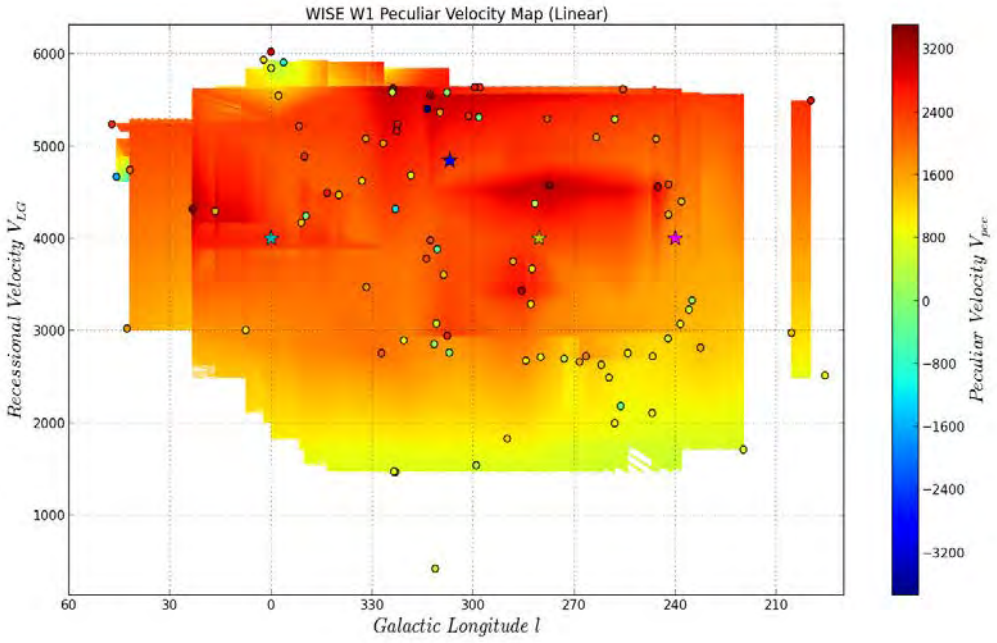

FIGURE 5.15: WISE W1 band peculiar velocity map using Sorce et al. (2013) 3.6 μm Tully-Fisher relation calibration. These galaxies are color-coded based on their peculiar velocities and the background color is the interpolation of the data.

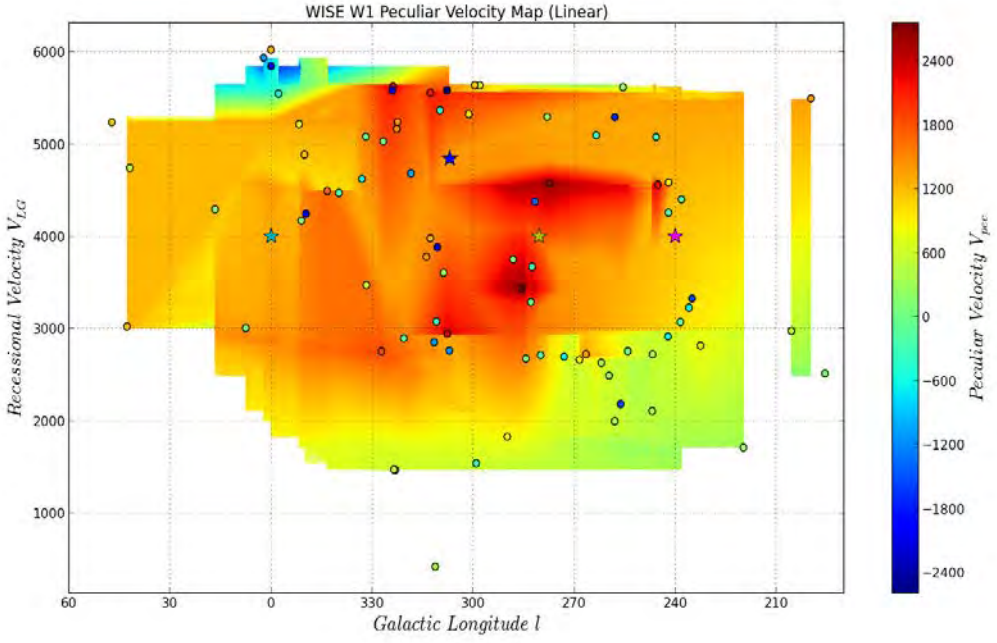

FIGURE 5.16: WISE W1 band peculiar velocity map using Cosmic Flow Program WISE W1 Tully-Fisher relation calibration. These galaxies are color-coded based on their peculiar velocities and the background color is the interpolation of the data.

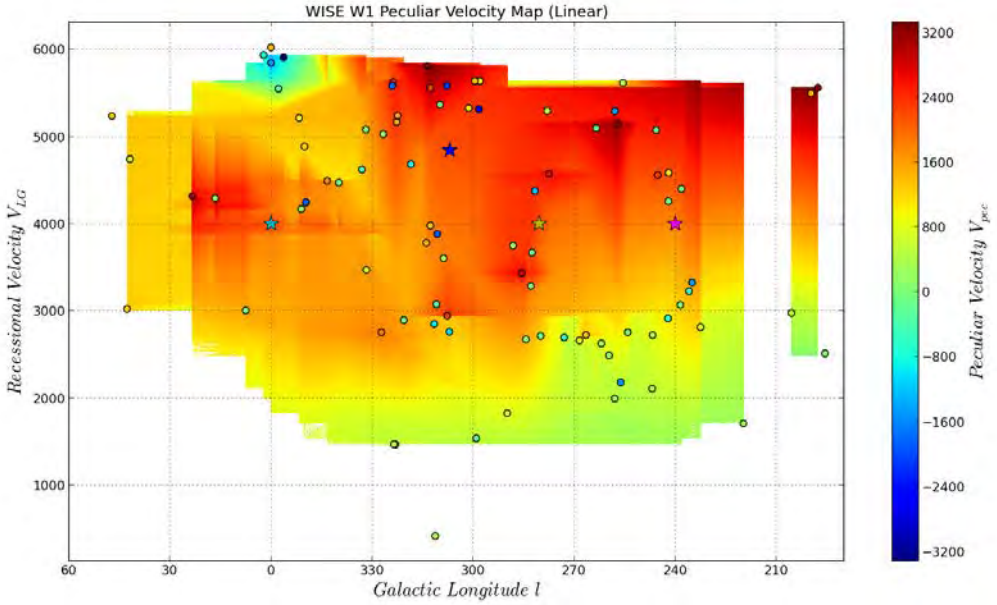

FIGURE 5.17: WISE W1 band peculiar velocity map using Cosmic Flow Program *I* band conversion of WISE W1 Tully-Fisher relation calibration. These galaxies are color-coded based on their peculiar velocities and the background color is the interpolation of the data.

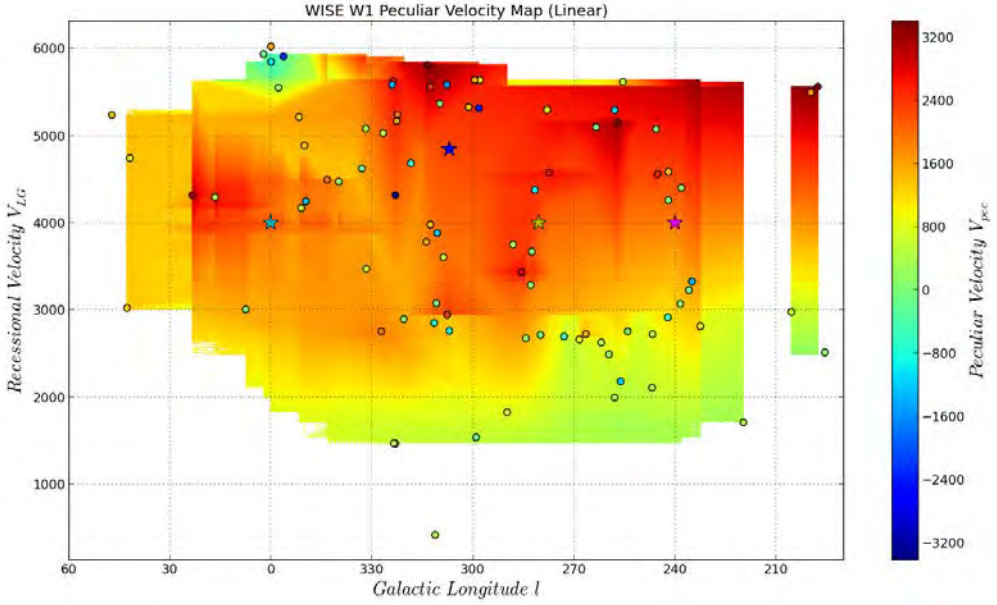

FIGURE 5.18: WISE W2 band peculiar velocity map using Cosmic Flow Program WISE W2 Tully-Fisher relation calibration. These galaxies are color-coded based on their peculiar velocities and the background color is the interpolation of the data.

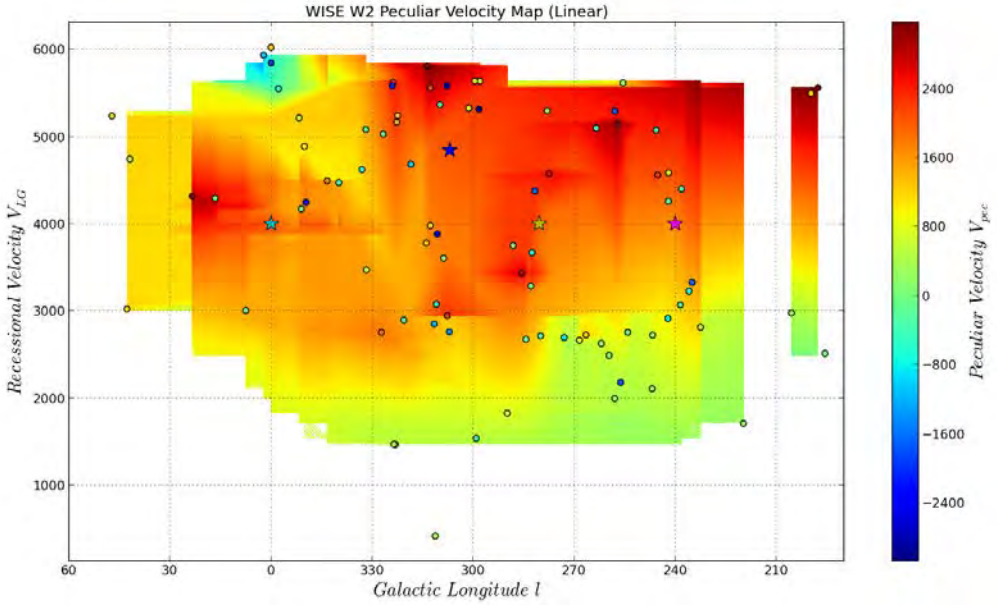

FIGURE 5.19: WISE W2 band peculiar velocity map using Cosmic Flow Program *I* band conversion of WISE W2 Tully-Fisher relation calibration. These galaxies are color-coded based on their peculiar velocities and the background color is the interpolation of the data.

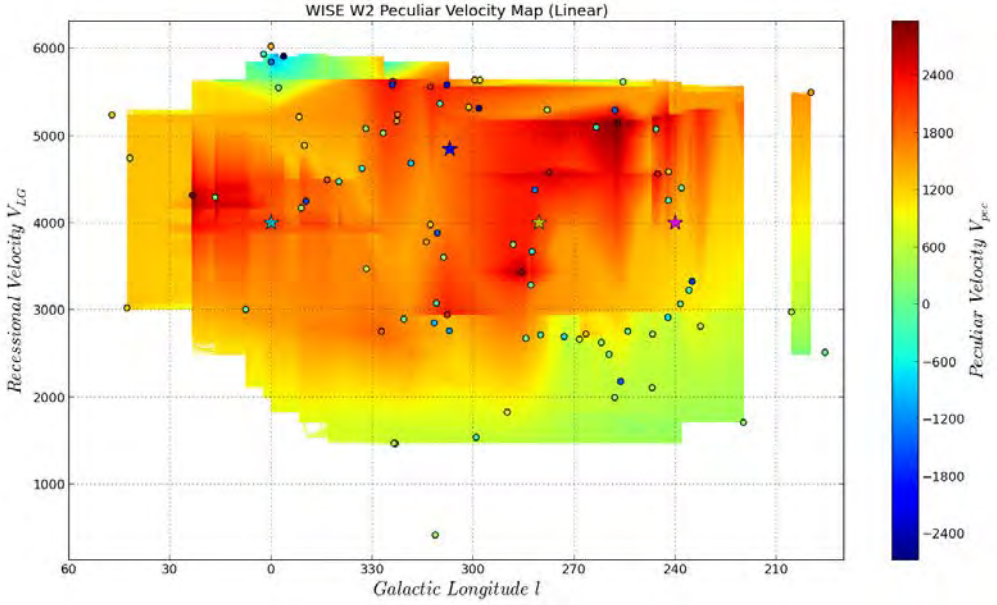

5.3.2 Radial Velocity Field Analysis of ZoA Galaxies

The radial velocity field analysis was done by projection in the supergalactic coordinate positions of the radial velocity component of our sample galaxies. The supergalactic longitude SGL and supergalactic latitude SGB were obtained using the relation given as

$$SGB = \sin^{-1}(\sin b \cos 83^{\circ}.68 + \cos b \sin 83^{\circ}.68 \cos(l - 47^{\circ}.37)), \quad (5.13)$$

$$SGL = 89^{\circ}.92 - \sin^{-1}\left(\frac{\cos b \sin(l - 47^{\circ}.37)}{\sin(SGB)}\right). \quad (5.14)$$

Where l and b Galactic longitude and latitude respectively. Therefore, for a galaxy at a distance R the supergalactic coordinates in 3-dimensions are

$$SGX = R\cos(SGB)\cos(SGL), \quad (5.15)$$

$$SGY = R\cos(SGB)\sin(SGL), \quad (5.16)$$

$$SGZ = R\sin(SGB). \quad (5.17)$$

We plotted the SGY on SGX, SGZ on SGY and SGZ on SGX to understand the different radial velocity field associated with ZoA galaxies in three dimensional supergalactic coordinates. The direction of the radial velocity field was plotted using a python module called quiver. The results of the cosmic velocity field plots for the supergalactic plane is given in FIGURE 5.20-5.27. The plots shows that ZoA galaxies radial velocity field are mostly in the region of high mass concentration. The flow around the supergalactic center and the Great Attractor indicate a region of high matter density concentration as seen in FIGURE 5.20-5.27. If we observe the distribution of our sampled galaxies distances in the supergalactic plane especially the SGZ on SGX and the SGZ on SGY plots. We would find an inflow into a massive concentration and an outflow into another more massive concentration which is not covered by the scope of this work. The mass concentration regions are labelled with star as seen in FIGURE 5.20-5.27. The blue star (★) is the position of the Great Attractor, the green star (★) is the Virgo supercluster and the cyan star (★) is the Supergalactic center. The radial velocity field plots in FIGURE 5.20-5.27 also show the evidence of a large-scale streaming towards a distance of about $\sim$ 100 Mpc in the direction behind the Great Attractor. The radial velocity field plots in FIGURE 5.20 - 5.27 describe nearly the same direction of motion for all the Tully-Fisher relation calibrations used in these radial velocity field analysis. Thereby, suggesting that the ZoA galaxies motion is characterized with both an inflow into a mass concentration and outflow into a more massive concentration behind the Great Attractor. The inflow into a mass concentration is centered around the Great

Attractor and the Virgo cluster. The outflow into this more massive concentration is not covered by the scope of the ZoA work.

Linear perturbation theory predicts that the Local Group peculiar velocity is induced by anisotropies in the surrounding matter distribution. Therefore, It is widely accepted that the CMB dipole is due to a Doppler effect arising from the motion of the Local Group through the cosmological reference frame. Kogut et al. (1993) showed that the CMB dipole indicates that our Local Group moves with a velocity of 627 ± 22 km s^{-1} towards the direction of $l = 276°$, $b = 30°$ in Galactic coordinates. The ZoA mean peculiar velocity galaxies results obtained in this research work in section 5.3.1 is consistent with this value. The Local group cosmic flow obtained in these research work is in agreement with the published work of Tonry et al. (2000) who found using surface brightness fluctuation that the motion of the Local Group is as a result of two flow, one into the Hydra-Centaurus supercluster and a second flow toward a more distance source which was later identified as Shapley supercluster. Furthermore, Lavaux et al. (2010) studies from cosmic flow from 2MASS redshift survey is consistent with ZoA flow field analysis in FIGURE 5.20-5.27. Pomarède et al. (2013) used information from the Extragalactic Distance Database V8k redshift catalog and peculiar velocities from the Cosmicflows-1 survey and the recent results obtained on the reconstruction of cosmic flows with the Wiener Filter approach to show the visualization of three-dimensional large-scale structures and cosmic flows. The three major components of the Milky Way motion are the expulsion from the Local Void, the infall toward the Virgo cluster, and the bulk flow of the Local supercluster toward the Great Attractor. The radial velocity field analysis in this work is in agreement with published work of Cosmic Flow Project by Pomarède et al. (2013) on large-scale structure cosmic flow field. Kocevski & Ebeling (2006) showed using the combination of X-ray selected clusters galaxies from the ROSAT-ESO Flux Limited X-ray (REFLEX) catalog in the southern hemisphere, the extended Brightest Cluster Sample (eBCS) sample in the north, and the Clusters In the Zone of Avoidance (CIZA) survey in the Galactic plane. They found using the dipole anisotropy present in the cluster distribution that 44 % of the Local Group's peculiar velocity is due to infall into the Great Attractor region, while 56 % is in the form of a large-scale flow induced by more distant overdensities between 130 and 180 h^{-1} Mpc away. Also, they showed that the Shapley supercluster is the only single overdensity most likely responsible for the increase in the dipole amplitude beyond 130 h^{-1} Mpc, generating 30.4 % of the large-scale contribution. This results is in agreement with the radial velocity field analysis in this research work. The results in this work agree favorably with the work of Tully et al. (2008), who found that the Milky Way participates in the bulk motion of the Local Sheet away from the Local Void which collectively add up to 631 km s^{-1}. The component of motion is attributed to the Virgo cluster and its surroundings at 17 Mpc away, the

attraction at 3000 km s^{-1} near the direction of the Centaurus cluster. Importantly, flow maps are used to constrain the mean mass density of the Universe Ω_m as well as to examine the degree to which the distribution of galaxies follows the distribution of mass. Current results shows that the mean mass density parameter value $\Omega_m \approx 0.2$.

FIGURE 5.20: IRSF K_s band radial velocity field projection in the supergalactic plane using Said (2013) Tully-Fisher relation calibration. The stars are the Great Attractor (★), the Virgo supercluster (★) and the Supergalactic center (★). The dots are ZoA galaxies color-coded based on their peculiar velocities with the arrow describing their direction.

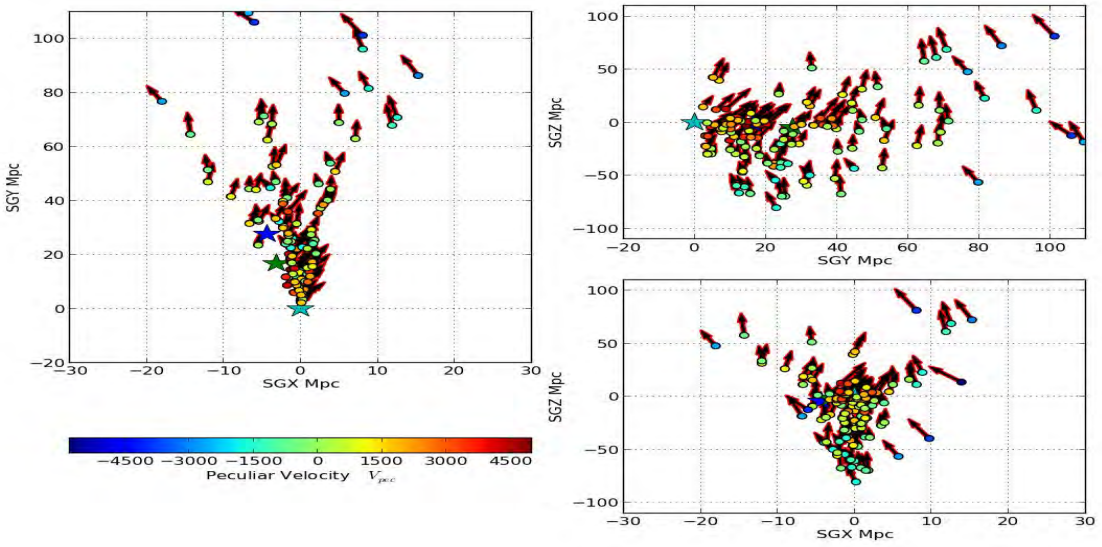

FIGURE 5.21: 2MASS K_s band radial velocity field projection in the supergalactic plane using Said (2013) Tully-Fisher relation calibration. The stars are the Great Attractor (★), the Virgo supercluster (★) and the Supergalactic center (★). The dots are ZoA galaxies color-coded based on their peculiar velocities with the arrow describing their direction.

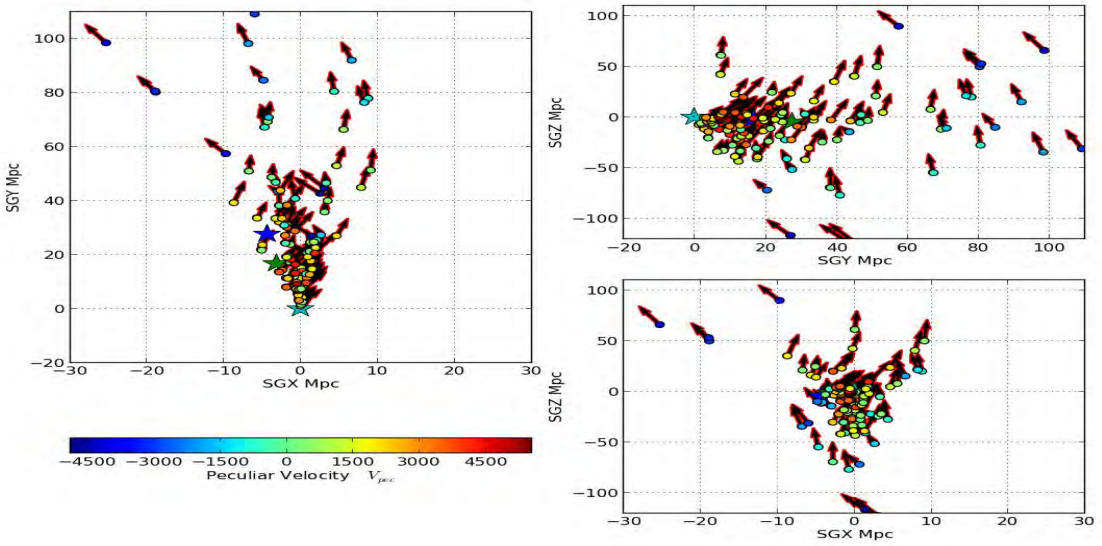

FIGURE 5.22: WISE W1 band radial velocity field projection in the supergalactic plane Lagattuta et al. (2013) WISE W1 Tully-Fisher relation calibration. The stars are the Great Attractor (★), the Virgo supercluster (★) and the Supergalactic center (★). The dots are ZoA galaxies color-coded based on their peculiar velocities with the arrow describing their direction.

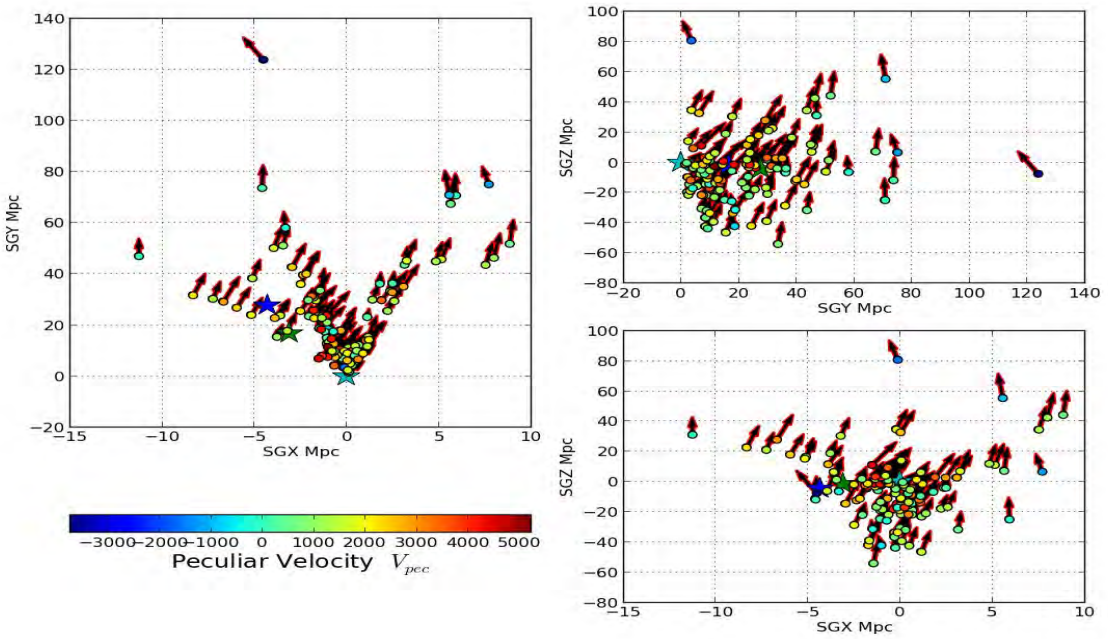

FIGURE 5.23: WISE W1 band radial velocity field projection in the supergalactic plane using Sorce et al. (2013) 3.6 μm Tully-Fisher relation calibration. The stars are the Great Attractor (★), the Virgo supercluster (★) and the Supergalactic center (★). The dots are ZoA galaxies color-coded based on their peculiar velocities with the arrow describing their direction.

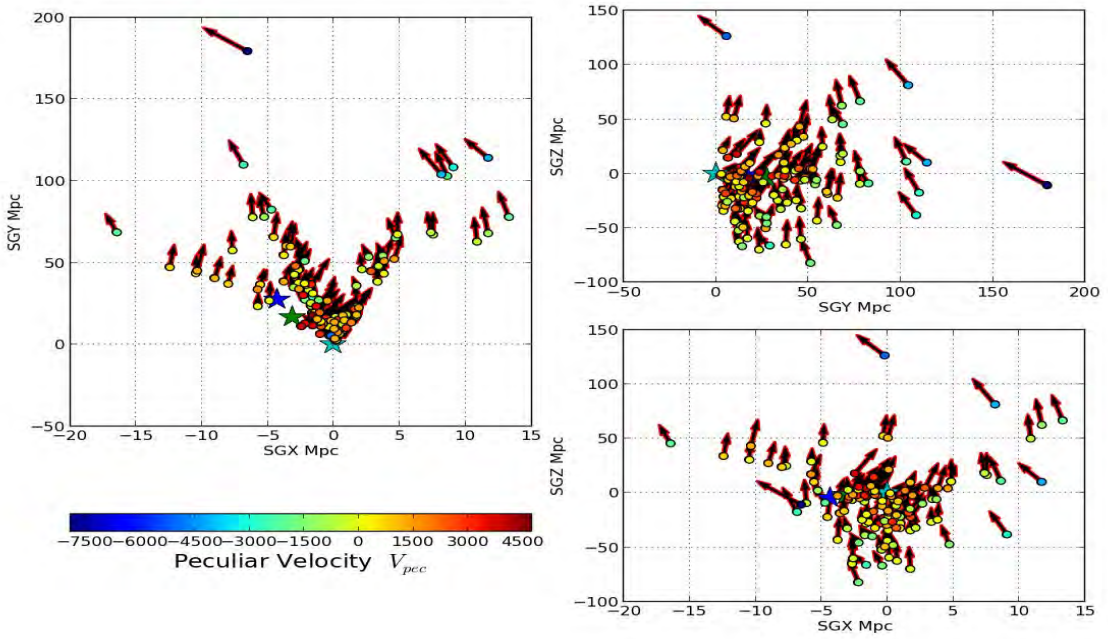

FIGURE 5.24: WISE W1 band radial velocity field projection in the supergalactic plane using Cosmic Flow Program WISE W1 Tully-Fisher relation calibration. The stars are the Great Attractor (★), the Virgo supercluster (★) and the Supergalactic center (★). The dots are ZoA galaxies color-coded based on their peculiar velocities with the arrow describing their direction.

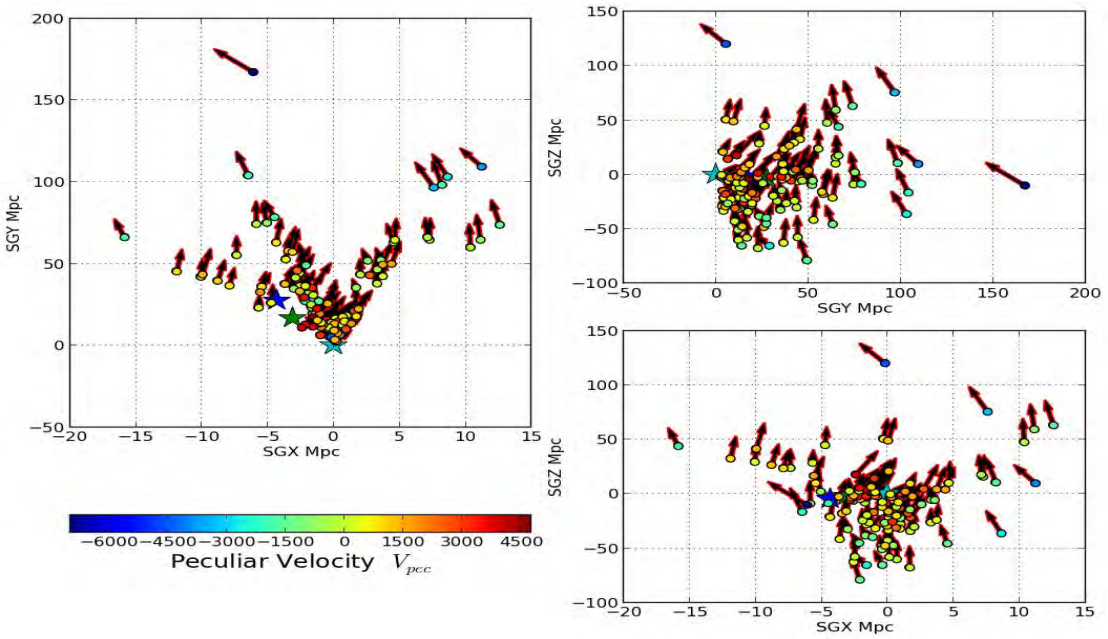

FIGURE 5.25: WISE W1 band radial velocity field projection in the supergalactic plane using Cosmic Flow Program I band conversion of WISE W1 Tully-Fisher relation calibration. The stars are the Great Attractor (★), the Virgo supercluster (★) and the Supergalactic center (★). The dots are ZoA galaxies color-coded based on their peculiar velocities with the arrow describing their direction.

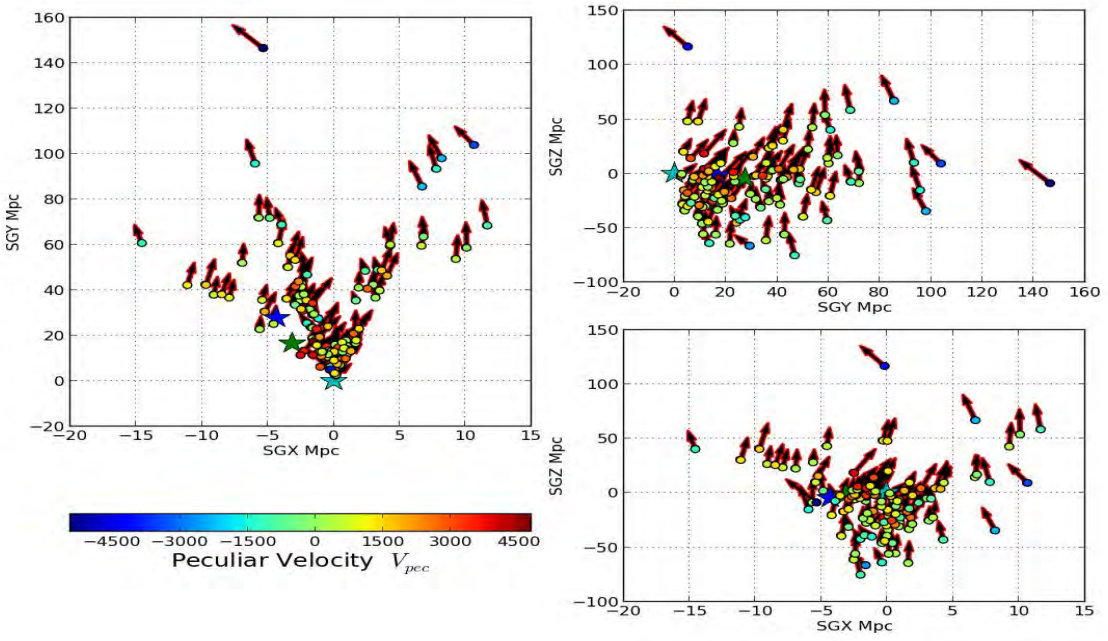

FIGURE 5.26: The stars are the Great Attractor (★), the Virgo supercluster (★) and the Supergalactic center (★). The dots are ZoA galaxies color-coded based on their peculiar velocities with the arrow describing their direction.

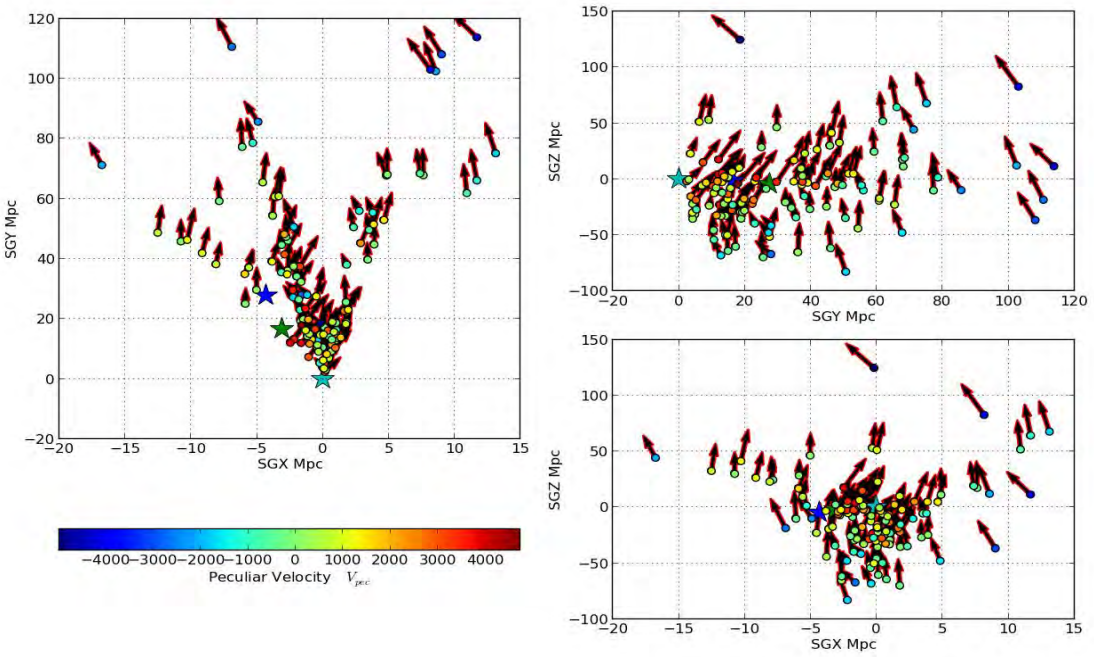

FIGURE 5.27: WISE W2 band radial velocity field projection in the supergalactic plane using Cosmic Flow Program *I* band conversion of WISE W2 Tully-Fisher relation calibration. The stars are the Great Attractor (★), the Virgo supercluster (★) and the Supergalactic center (★). The dots are ZoA galaxies color-coded based on their peculiar velocities with the arrow describing their direction.

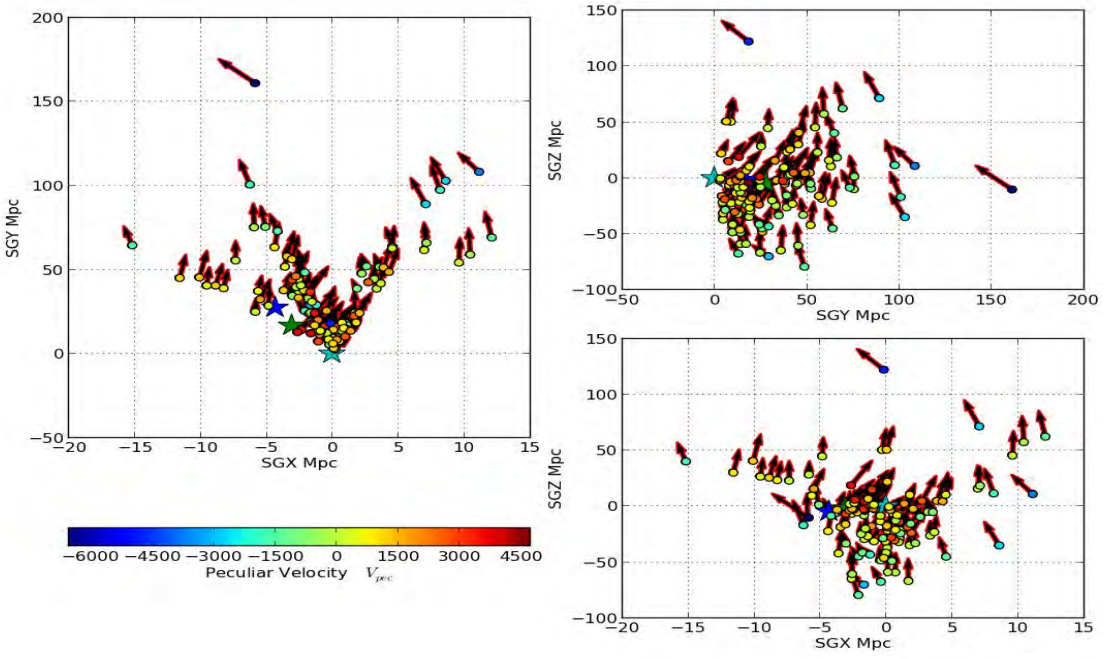

5.3.3 Peculiar Velocity Comparison

The peculiar velocities of galaxies are a unique cosmological probe. Providing an unbiased estimate of the distribution of matter on scale much larger than the depth of the survey. We compare the K_s band derived peculiar velocities with the WISE W1 band peculiar velocities the result shows that the K_s band and WISE W1 band have similar peculiar velocities as seen in FIGURE 5.28. Therefore, they both trace similar star formation history.

FIGURE 5.28: Comparison between IRSF K_s and WISE W1 peculiar velocity parameters.

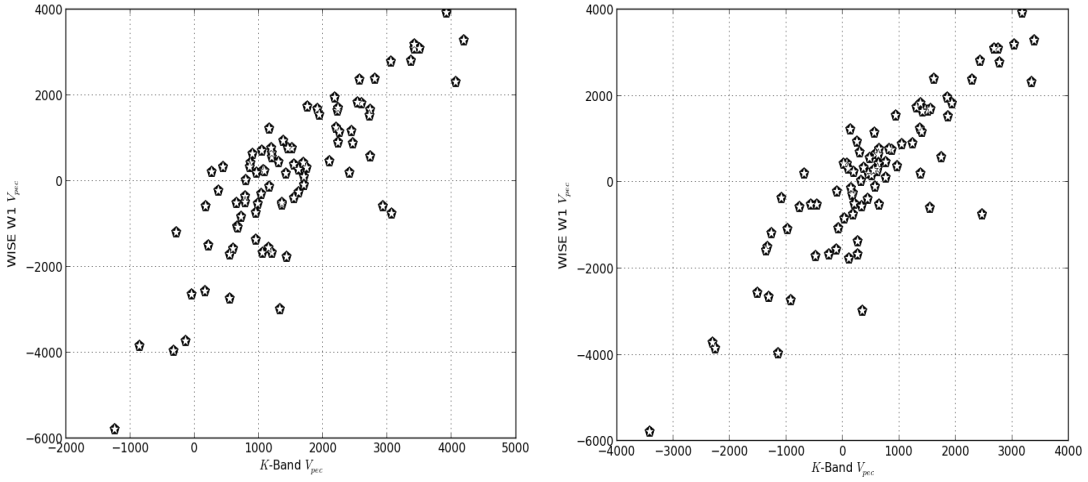

(a) WISE W1 band peculiar velocities from Cosmic Flow Program and IRSF K_s band peculiar velocities from Said (2013).

(b) WISE W1 band peculiar velocities from Cosmic Flow Program I band conversion and IRSF K_s band peculiar velocities from Said (2013).

5.4 Error Budget

The errors were obtained by taking the standard deviation of galaxies peculiar velocities of selected ZoA regions discussed in the previous sections. The errors associated with peculiar velocity distribution using Said (2013) Tully-Fisher relation calibration for IRSF and 2MASS K_s bands are 1921 km s^{-1} and 2196 km s^{-1} respectively as explained in the caption of FIGURE 5.3 & 5.4. For WISE W1 band the errors associated with peculiar velocity distribution for Lagattuta et al. (2013), Sorce et al. (2013) and Cosmic Flow Program Tully-Fisher relation calibrations are 1393 km s^{-1}, 1776 km s^{-1}, 1940 km s^{-1} and 1867 km s^{-1} respectively, while the errors from WISE W2 calibrations of the Cosmic Flow Program have 1727 km s^{-1} and 1607 km s^{-1} respectively as explained in the caption of FIGURE 5.5 & 5.6.

Also, the errors associated with galactic absorption estimate of Δm in WISE W1 and W2 are $0^{\rm m}.001$ and $0^{\rm m}.002$ respectively. These values are small when compared to the $0^{\rm m}.010$ values obtained for 2MASS JHK_s bands as seen in TABLE 3.3.

From the Tully-Fisher distance used in the projection of supergalactic coordinate on the radial velocity component for ZoA galaxies, we estimated the mean distance to ZoA region using WISE W1 and W2 bands and the K_s band of 2MASS and IRSF. For WISE W1 and W2 band the ZoA mean distance estimate are 52.41 ± 28.25 Mpc and 53.91 ± 26.97 Mpc respectively, while the K_s band of 2MASS and IRSF are 39.21 ± 30.88 Mpc and 47.07 ± 29.63 Mpc respectively. These shows that WISE bands provide more accurate mean distance estimate of distance to ZoA region when compared to Near-Infrared K_s band estimate of 2MASS and IRSF.

Using the scatter from the Tully-Fisher relation calibration of Said (2013) for K_s band, Lagattuta et al. (2013) Tully-Fisher relation calibration for WISE W1 band, Cosmic Flow Program Tully-Fisher relation calibrations from Neill et al. (2014) for WISE W1 and W2 band and Sorce et al. (2013) Tully-Fisher relation calibration for 3.6 μm bands, We compared the Near-Infrared scatter from Said (2013) calibration with the Mid-Infrared scatter from Lagattuta et al. (2013), Sorce et al. (2013) and the Cosmic Flow Program calibrations. We found that the new Tully-Fisher relation calibrations and scatters with WISE and 3.6 μm calibration brings an improvement when compared to 2MASS calibration and scatter given in the appendix of this work.

5.5 Conclusion

In details, we have described the cosmic flow associated with ZoA galaxies using the K_s band, WISE W1 and W2 bands galaxy magnitudes together with linewidth-magnitude calibration of Said (2013) for the K_s band, Lagattuta et al. (2013); Sorce et al. (2013) and Cosmic Flow Program calibrations for WISE W1 band and the Cosmic Flow Program calibrations for WISE W2 band. The mean peculiar velocity of the ZoA galaxies obtained from using these calibrations is between $\sim 455 - 723$ km s^{-1} except for Lagattuta et al. (2013) calibrations which is around 1636 km s^{-1} and 2MASS calibration which are around ~ 1096 km s^{-1} for galaxies with $\log W \geq 2.0$. For galaxies selected with $\log W \geq 2.3$ the mean peculiar velocity is between $\sim 65-437$ km s^{-1} except for Lagattuta et al. (2013) calibrations which is around 1425 km s^{-1}. We have shown that the ZoA cosmic flow arises from an inflow into a massive concentration which comprising of the the Great Attractor, the Virgo cluster and the Supergalactic center and an outflow into a more massive clusters behind the Great Attractor. Also, the major overdensity in the ZoA are mostly associated with regions of massive clusters. These include the region

around the Great Attractor, the region around Puppis clusters and the region between Hydra and Antlia clusters.

Chapter 6

Discussion & Conclusion

We selected ZoA galaxies using the observed IRSF counterparts of HIZoA possible galaxies. We obtained the WISE W1-W4 bands resolved galaxies and online photometry, the online 2MASS JHK_s bands extended source photometry of our selected sample galaxies as seen in FIGURE 2.2. We applied the formalism of Cameron (1990) and Riad et al. (2010) to studied the effect of Galactic absorption on 2MASS JHK_s bands and WISE W1-W4 bands galaxies. We found that the effect of Galactic absorption decreases from J band to WISE W4 band. The Galactic absorption effect for WISE W3 and W4 bands galaxies are quite negligible. We found that the Galactic absorption in the K_s band is about 8.8 % of the Galactic absorption in the B band, while the Galactic absorption in WISE W1 and W2 bands is about 0.59 % & 1.03 % of the extinction in the B band respectively. For the cosmic flow analysis we selected galaxies with IRSF K_s band axial ratio less than 0.7 from the initial Tully-Fisher relation data and then obtained the peculiar velocity map and radial velocity field plots using various calibrations. We found that the cosmic flow associated with the ZoA galaxies is as a result of inflow into a mass concentration which is centered around the Great Attractor, Virgo clusters and an outflow into a more massive concentration which is most likely associated with the Shapley supercluster. Using the various peculiar velocity models, we found that the peculiar velocity model of the Local Universe provide the best model for explaning the cosmic flow associated with the ZoA galaxies. The radial velocity field plots in FIGURE 5.12-5.23 are consistent with the results of the 2MASS cosmic flow field from redshift survey by Lavaux et al. (2010), the works of Kolatt et al. (1995); Tonry et al. (2000); Pomarède et al. (2013); Kocevski & Ebeling (2006); Said (2013) and Tully et al. (2008). The mean peculiar velocity for ZoA region are given in FIGURE 5.11. Lagattuta et al. (2013) WISE W1 Tully-Fisher relation calibration was over estimated when compared to the Tully-Fisher relation calibrations given by the Cosmic Flow Program for WISE W1 and the 3.6 μm Tully-Fisher relation calibration of Sorce et al. (2013). Therefore,

we found a higher mean peculiar velocity for the Lagattuta et al. (2013) WISE W1 Tully-Fisher relation calibration.

One major setback in mapping the cosmic flow of galaxies in the ZoA region is mostly associated with the difficulties in uncovering galaxies in this region because of the effect of extinction. The conclusion we have drawn from these analysis are that cosmic flows in the ZoA region are more difficult to study in the near-infrared IRSF JHK_s and 2MASS JHK_s band due to high obscuration from dust and stellar crowding around the Galactic bulge. WISE bands observations and results analysis provide a more compelling tools for mapping the cosmic flows in the ZoA regions due to small effect of extinction.

In the future, we hope to use more distant ZoA galaxies to determine the cosmic flows. This will help us understand the influence of various ZoA overdensity on the motion of the Local Universe. In this work we combined data from HI, K_s band IRSF, K_s band 2MASS and WISE W1-W2 bands data to understand the cosmic flow associated with the ZoA galaxies. Also, we could extend this work with $3.6\mu m$ band data using $3.6\mu m$ Tully-Fisher relation calibration from Sorce et al. (2013). Furthermore, we could extend this work to include the all-sky cosmic flow. This would involve selecting galaxies from all regions of the sky for the cosmic flow analysis.

Appendix A

ZoA Cosmic Flow Data

The complete data for the cosmic flow analysis used in this project can be downloaded at http://www.ast.uct.ac.za/~affadi/patrick/patrick.html. Also, the images and rededuced WISE and IRSF photometry can be downloaded at this site. The description of the column parameters in TABLE *A*.1 are:

Column 1: ZoA name of the galaxy

Column 2: HI name of the galaxy

Column 3 & **4**: l & b is the Galactic longitude and Galactic lactitude respectively

Column 5: ϵ_K is the K_s band ellipticity

Column 6, 7 & **8**: M_J, M_H & M_K are IRSF J, H & K_s bands magnitudes

Column 9, 10, 11 & **12**: M_{W1}, M_{W2}, M_{W3}, & M_{W4} are WISE W1-W4 bands magnitudes

Column 13: V_{obs} is the heliocentric velocity

Column 14: W_{50} is the 50% line-width

Column 15: E(B-V) values from Schlafly & Finkbeiner (2011)

A.1 Near-Infrared K_s band Calibrations

Said (2013) K_s band Tully-Fisher relation calibration

$$M_K = -21.959 - 10.523(\log W_{mx} - 2.5), \tag{A.1}$$

with scatter given as $\sigma = 0.716 - 2.369(\log W_{mx} - 2.5)$.

A.2 WISE W1 band Calibrations

Lagattuta et al. (2013) WISE W1 band Tully-Fisher relation calibration

$$M_{W1} = -22.240 - 10.050(\log W_{mx} - 2.5), \tag{A.2}$$

with scatter of $\sigma_{WISE} = 0.686$.
Cosmic Flow Program of [1] WISE W1 band Tully-Fisher relation calibration

$$M_{W1} = -23.049 - 9.580(\log W_{mx} - 2.5), \tag{A.3}$$

with scatter of $\sigma_{W1} = 0.54$.
Cosmic Flow Program I band conversion for WISE W1 band Tully-Fisher relation calibration

$$M_{W1} = -22.929 - 9.080(\log W_{mx} - 2.5), \tag{A.4}$$

with scatter of $\sigma_{W1} = 0.46$.

A.3 3.6μm band Calibration

Sorce et al. (2013) 3.6μm band Tully-Fisher relation calibration

$$M_{3.6} = -22.125 - 9.740(\log W_{mx} - 2.5), \tag{A.5}$$

with scatter of $\sigma_{3.6\mu\mathrm{m}} = 0.49$.

A.4 WISE W2 band Calibrations

Cosmic Flow Program WISE W2 band Tully-Fisher relation calibration

$$M_{W2} = -23.119 - 9.750(\log W_{mx} - 2.5), \tag{A.6}$$

with scatter of $\sigma_{W2} = 0.56$.
Cosmic Flow Program I band conversion for WISE W2 band Tully-Fisher relation has a scatter of $\sigma_{W2} = 0.46$ and the calibration is given as

$$M_{W2} = -22.999 - 9.070(\log W_{mx} - 2.5). \tag{A.7}$$

[1] Cosmic Flow Program calibrations is from Neill et al. (2014).

TABLE A.1: IRSF JHK_s bands and resolved galaxies WISE W1-W4 bands parameters for ZoA selected galaxies samples of our cosmic flow analysis.

ZOA Name	HI Name	l °	b °	ϵ_K arc	M_J mag	M_H mag	M_K mag	M_{W1} mag	M_{W2} mag	M_{W3} mag	M_{W4} mag	V_{obs} kms^{-1}	W_{50} kms^{-1}	E(B-V) mag
ZOA061518.189+	J0614+12	197.7	-2.2	0.43	12.8 ± 0.02	11.9 ± 0.02	12.5 ± 0.02	10.8 ± 0.01	10.8 ± 0.01	7.8 ± 0.03	5.7 ± 0.05	5553 ± 2	217 ± 7	1.0 ± 0.37
ZOA061545.021+	J0615+11	198.9	-2.7	0.07	14.0 ± 0.02	13.2 ± 0.02	12.8 ± 0.02	12.0 ± 0.02	11.8 ± 0.03	8.4 ± 0.08	6.3 ± 0.07	5446 ± 5	184 ± 14	0.8 ± 0.03
ZOA062128.888+	J0621+11	199.7	-1.5	0.60	15.3 ± 0.03	14.6 ± 0.02	14.2 ± 0.03	11.7 ± 0.02	11.7 ± 0.02	8.5 ± 0.04	7.7 ± 0.15	5599 ± 2	188 ± 5	0.9 ± 0.04
ZOA062226.284+	J0622+04	205.6	-4.4	0.62	11.6 ± 0.02	10.7 ± 0.02	10.4 ± 0.02	9.8 ± 0.01	9.7 ± 0.01	6.2 ± 0.01	4.4 ± 0.02	2958 ± 3	306 ± 12	0.6 ± 0.01
ZOA062258.091+	J0622+11B	199.8	-1.1	0.62	12.9 ± 0.02	11.9 ± 0.02	11.3 ± 0.02	10.4 ± 0.01	10.1 ± 0.01	6.1 ± 0.01	4.0 ± 0.02	5493 ± 1	366 ± 2	1.1 ± 0.04
ZOA063015.648+	J0630+16	195.6	3.0	0.66	13.2 ± 0.02	12.1 ± 0.02	12.3 ± 0.02	10.9 ± 0.01	10.9 ± 0.02	8.6 ± 0.08	8.6 ± 0.33	2532 ± 3	258 ± 8	0.6 ± 0.00
ZOA063626.882+	J0636+00	210.4	-2.9	0.06	14.2 ± 0.03	13.2 ± 0.03	12.6 ± 0.03	10.6 ± 0.01	10.4 ± 0.01	6.3 ± 0.01	3.3 ± 0.01	2723 ± 1	144 ± 2	1.5 ± 0.05
ZOA065802.880-	J0657-05B	218.4	-1.0	0.08	11.8 ± 0.02	10.7 ± 0.02	10.2 ± 0.02	9.6 ± 0.01	9.5 ± 0.01	5.9 ± 0.01	4.1 ± 0.02	2721 ± 3	108 ± 6	1.3 ± 0.02
ZOA070024.539-	J0700-04	217.7	0.1	0.06	19.4 ± 0.22	18.9 ± 0.15	18.7 ± 0.41	14.6 ± 0.04	13.9 ± 0.05	10.7 ± 0.09	7.1 ± 0.09	297 ± 3	74 ± 6	1.0 ± 0.12
ZOA070934.590-	J0709-05	219.8	1.5	0.56	11.7 ± 0.02	10.5 ± 0.02	10.4 ± 0.02	9.4 ± 0.01	9.4 ± 0.01	6.6 ± 0.01	5.0 ± 0.04	1719 ± 5	262 ± 10	0.5 ± 0.01
ZOA071248.588-	J0712-09	223.6	0.5	0.60	13.5 ± 0.02	12.5 ± 0.02	12.1 ± 0.02	11.5 ± 0.01	11.5 ± 0.02	7.9 ± 0.02	5.7 ± 0.05	2437 ± 9	98 ± 19	0.7 ± 0.04
ZOA071650.760-	J0716-18C	232.6	-3.1	0.91	13.3 ± 0.02	12.0 ± 0.02	11.4 ± 0.02	10.5 ± 0.01	10.4 ± 0.01	7.1 ± 0.01	5.3 ± 0.04	2807 ± 5	267 ± 10	1.9 ± 0.15
ZOA072143.868-	J0721-16	231.2	-1.1	0.94	15.3 ± 0.04	14.3 ± 0.03	13.9 ± 0.04	12.8 ± 0.02	12.5 ± 0.02	9.5 ± 0.03	7.2 ± 0.08	2710 ± 13	171 ± 26	1.8 ± 0.04
ZOA072545.358-	J0725-17	232.7	-0.8	0.10	12.0 ± 0.02	10.9 ± 0.02	10.5 ± 0.02	10.1 ± 0.01	10.1 ± 0.01	7.3 ± 0.02	5.7 ± 0.05	2760 ± 4	103 ± 7	1.4 ± 0.07
ZOA072729.171-	J0727-23	238.2	-3.3	0.70	12.2 ± 0.02	11.1 ± 0.02	10.7 ± 0.02	10.1 ± 0.01	10.0 ± 0.01	7.4 ± 0.02	5.9 ± 0.05	4395 ± 4	412 ± 8	1.1 ± 0.07
ZOA073153.035-	J0732-16	232.6	0.9	0.68	9.4 ± 0.02	13.8 ± 0.02	13.1 ± 0.02	12.3 ± 0.02	12.1 ± 0.02	8.6 ± 0.04	− ± −	4320 ± 9	80 ± 19	13.2 ± 3.28
ZOA073331.236-	J0733-13	230.2	2.7	0.54	14.2 ± 0.02	13.5 ± 0.02	13.1 ± 0.02	12.5 ± 0.02	12.4 ± 0.02	9.3 ± 0.04	7.3 ± 0.12	3257 ± 16	151 ± 31	0.4 ± 0.02
ZOA073626.054-	J0736-18	234.1	1.3	0.82	14.7 ± 0.03	13.8 ± 0.02	13.4 ± 0.02	12.8 ± 0.02	12.8 ± 0.02	10.3 ± 0.06	9.0 ± 0.21	4461 ± 9	119 ± 19	0.9 ± 0.03
ZOA073951.074-	J0739-24	240.2	-1.2	0.24	13.2 ± 0.02	12.4 ± 0.02	12.0 ± 0.02	11.2 ± 0.01	11.1 ± 0.02	7.6 ± 0.02	5.9 ± 0.05	3057 ± 4	227 ± 8	0.8 ± 0.01
ZOA074059.570-	J0740-22	238.8	-0.1	0.54	12.9 ± 0.02	12.1 ± 0.02	11.7 ± 0.02	10.9 ± 0.01	10.8 ± 0.01	7.0 ± 0.01	5.0 ± 0.03	3054 ± 8	169 ± 15	0.6 ± 0.01
ZOA074020.456-	J0740-30A	245.8	-4.2	0.81	13.3 ± 0.02	12.4 ± 0.02	12.0 ± 0.02	11.5 ± 0.01	11.4 ± 0.01	8.3 ± 0.02	7.0 ± 0.08	5071 ± 8	323 ± 15	0.5 ± 0.01
ZOA074058.810-	J0740-32	246.8	-4.6	0.59	11.9 ± 0.02	11.1 ± 0.02	10.8 ± 0.02	10.2 ± 0.01	10.1 ± 0.01	6.6 ± 0.01	5.0 ± 0.02	2715 ± 6	278 ± 12	0.6 ± 0.01
ZOA074141.201-	J0741-22	238.6	0.2	0.80	11.3 ± 0.02	10.2 ± 0.02	9.7 ± 0.02	8.9 ± 0.01	8.6 ± 0.01	5.1 ± 0.01	3.2 ± 0.01	3073 ± 4	466 ± 9	0.7 ± 0.01
ZOA074157.604-	J0741-26	241.7	-1.5	0.16	14.7 ± 0.03	13.8 ± 0.02	13.1 ± 0.02	12.7 ± 0.02	12.6 ± 0.02	12.8 ± 0.28	9.9 ± 0.74	3508 ± 8	142 ± 16	0.9 ± 0.01
ZOA074153.241-	J0741-30B	245.3	-3.5	0.64	12.2 ± 0.02	11.7 ± 0.02	11.4 ± 0.02	9.2 ± 0.01	9.2 ± 0.01	7.9 ± 0.02	6.7 ± 0.07	4556 ± 5	349 ± 10	0.6 ± 0.02
ZOA074158.081-	J0742-26	242.2	-1.8	0.61	13.6 ± 0.03	12.9 ± 0.02	12.4 ± 0.03	11.6 ± 0.02	11.5 ± 0.02	9.0 ± 0.04	8.8 ± 0.25	2913 ± 7	247 ± 14	0.9 ± 0.04
ZOA074252.007-	J0742-31	246.9	-4.2	0.46	11.2 ± 0.02	10.4 ± 0.02	9.7 ± 0.02	8.8 ± 0.01	8.9 ± 0.01	9.6 ± 0.02	9.4 ± 0.24	2102 ± 3	305 ± 5	0.8 ± 0.05
ZOA074330.966-	J0743-18	235.1	2.7	0.30	14.3 ± 0.02	13.6 ± 0.02	13.3 ± 0.02	12.4 ± 0.02	12.4 ± 0.03	9.9 ± 0.05	8.8 ± 0.24	3338 ± 4	189 ± 9	0.6 ± 0.02
ZOA074434.244-	J0744-13	230.7	5.5	0.28	12.9 ± 0.02	12.3 ± 0.02	11.9 ± 0.02	10.6 ± 0.01	10.7 ± 0.01	7.8 ± 0.02	5.9 ± 0.06	2305 ± 4	123 ± 7	0.3 ± 0.02
ZOA074423.844-	J0744-25	241.9	-1.0	0.31	12.5 ± 0.02	11.5 ± 0.02	11.0 ± 0.02	10.5 ± 0.01	10.4 ± 0.01	7.1 ± 0.01	5.1 ± 0.03	4039 ± 13	158 ± 26	1.0 ± 0.06
ZOA074752.048-	J0747-18	236.0	3.4	0.80	10.1 ± 0.02	9.3 ± 0.02	8.9 ± 0.02	8.6 ± 0.01	8.6 ± 0.01	5.7 ± 0.01	4.1 ± 0.02	3240 ± 5	513 ± 11	0.4 ± 0.00
ZOA074717.031-	J0747-25	242.1	-0.3	0.34	14.2 ± 0.03	13.4 ± 0.02	13.2 ± 0.03	11.8 ± 0.02	11.9 ± 0.02	9.3 ± 0.04	8.2 ± 0.17	4261 ± 9	216 ± 19	0.5 ± 0.01
ZOA074713.308-	J0747-26A	242.5	-0.6	0.05	13.0 ± 0.02	11.5 ± 0.02	11.8 ± 0.02	10.4 ± 0.02	10.3 ± 0.02	6.7 ± 0.01	5.0 ± 0.03	883 ± 3	145 ± 5	0.7 ± 0.03
ZOA074813.893-	J0748-18	236.0	3.5	0.67	17.3 ± 0.06	16.7 ± 0.05	16.7 ± 0.10	11.7 ± 0.02	12.3 ± 0.03	10.5 ± 0.09	11.5 ± 1.76	920 ± 5	174 ± 10	0.4 ± 0.01
ZOA075110.784-	J0751-35	250.5	-4.3	0.22	15.5 ± 0.04	14.5 ± 0.03	14.1 ± 0.03	11.3 ± 0.02	11.1 ± 0.02	7.6 ± 0.02	5.8 ± 0.05	5207 ± 7	268 ± 13	1.6 ± 0.08
ZOA075220.625-	J0752-25A	242.1	1.0	0.50	10.9 ± 0.02	10.2 ± 0.02	9.8 ± 0.02	9.6 ± 0.01	9.6 ± 0.01	6.8 ± 0.01	5.3 ± 0.03	4591 ± 6	361 ± 13	0.4 ± 0.01
ZOA075448.396-	J0754-38	254.2	-5.6	0.70	13.4 ± 0.02	12.4 ± 0.02	12.0 ± 0.02	11.0 ± 0.01	11.0 ± 0.01	7.7 ± 0.02	6.0 ± 0.04	2751 ± 5	270 ± 11	0.8 ± 0.01
ZOA075747.381-	J0757-26	244.2	1.2	0.62	19.5 ± 0.20	18.9 ± 0.15	17.7 ± 0.17	13.6 ± 0.05	13.9 ± 0.09	14.8 ± 1.53	10.2 ± 0.87	954 ± 5	74 ± 10	0.6 ± 0.02
ZOA080610.996-	J0805-27	245.7	2.4	0.51	10.4 ± 0.02	9.4 ± 0.02	8.9 ± 0.02	7.6 ± 0.01	7.4 ± 0.01	4.0 ± 0.01	2.2 ± 0.01	1024 ± 3	41 ± 6	0.4 ± 0.01
ZOA080953.826-	J0809-41	258.1	-4.6	0.87	12.0 ± 0.02	10.8 ± 0.02	10.3 ± 0.02	9.4 ± 0.01	9.2 ± 0.01	5.8 ± 0.01	4.0 ± 0.02	1993 ± 3	316 ± 6	1.2 ± 0.04
ZOA081848.024-	J0818-29A	248.9	3.6	0.40	15.2 ± 0.03	14.4 ± 0.02	13.9 ± 0.03	13.5 ± 0.02	13.4 ± 0.04	11.5 ± 0.11	9.8 ± 0.60	1521 ± 18	99 ± 36	0.3 ± 0.01
ZOA081844.267-	J0818-29B	248.9	3.6	0.63	15.8 ± 0.04	15.1 ± 0.03	14.8 ± 0.04	14.1 ± 0.05	14.3 ± 0.09	13.4 ± 0.46	10.0 ± 0.77	2514 ± 5	165 ± 9	0.3 ± 0.01
ZOA081839.478-	J0818-33	252.3	1.3	0.48	13.6 ± 0.02	12.7 ± 0.02	12.4 ± 0.02	11.3 ± 0.02	11.2 ± 0.02	8.0 ± 0.02	6.3 ± 0.08	2013 ± 12	104 ± 24	0.7 ± 0.02
ZOA082139.675-	J0821-39	257.1	-1.3	0.44	13.6 ± 0.02	12.5 ± 0.02	11.9 ± 0.02	11.5 ± 0.01	11.4 ± 0.01	11.5 ± 0.12	10.9 ± 1.36	5148 ± 13	188 ± 25	2.1 ± 0.06
ZOA082627.102-	J0826-44	261.9	-3.6	0.83	14.7 ± 0.03	13.5 ± 0.02	13.0 ± 0.02	12.1 ± 0.03	12.4 ± 0.03	9.2 ± 0.04	7.8 ± 0.15	1024 ± 3	184 ± 6	1.5 ± 0.04
ZOA082737.362-	J0827-43	261.2	-2.8	0.42	17.7 ± 0.08	16.4 ± 0.04	15.8 ± 0.06	14.1 ± 0.02	14.2 ± 0.05	13.0 ± 0.32	9.9 ± 0.73	2740 ± 3	66 ± 6	2.1 ± 0.07
ZOA083439.531-	J0834-40	259.4	0.1	0.09	10.0 ± 0.02	9.5 ± 0.02	9.3 ± 0.02	8.4 ± 0.01	8.3 ± 0.01	5.7 ± 0.01	4.0 ± 0.02	2772 ± 3	167 ± 6	2.1 ± 0.02
ZOA084008.955-	J0839-34	255.6	4.4	0.61	14.2 ± 0.02	13.4 ± 0.02	13.1 ± 0.02	12.6 ± 0.02	12.6 ± 0.02	9.5 ± 0.04	8.3 ± 0.17	5626 ± 11	235 ± 23	0.4 ± 0.01
ZOA084014.403-	J0840-32	254.4	5.4	0.64	16.8 ± 0.04	16.2 ± 0.03	16.0 ± 0.05	13.2 ± 0.03	13.5 ± 0.05	14.4 ± 0.85	11.8 ± 2.89	1397 ± 10	69 ± 19	0.3 ± 0.00
ZOA084033.110-	J0840-37	258.0	2.7	0.81	13.4 ± 0.02	12.7 ± 0.02	12.2 ± 0.02	12.1 ± 0.01	12.3 ± 0.02	9.5 ± 0.03	7.5 ± 0.12	5298 ± 6	315 ± 12	0.6 ± 0.02
ZOA084421.997-	J0844-34	256.3	5.0	0.39	11.6 ± 0.02	10.8 ± 0.02	10.4 ± 0.02	10.1 ± 0.01	10.1 ± 0.01	6.8 ± 0.01	4.5 ± 0.02	2190 ± 12	291 ± 24	0.4 ± 0.00
ZOA084408.888-	J0844-35	256.8	4.5	0.44	15.0 ± 0.03	14.3 ± 0.02	13.8 ± 0.03	13.0 ± 0.02	12.8 ± 0.02	9.0 ± 0.03	7.9 ± 0.11	2242 ± 5	156 ± 10	0.5 ± 0.03
ZOA084521.622-	J0845-42	262.4	0.4	0.24	13.5 ± 0.03	11.3 ± 0.02	11.0 ± 0.02	8.8 ± 0.01	8.5 ± 0.01	5.0 ± 0.01	3.4 ± 0.02	1748 ± 6	305 ± 11	3.0 ± 0.12
ZOA084821.230-	J0848-39	260.6	2.6	0.55	15.6 ± 0.04	14.7 ± 0.03	14.3 ± 0.03	13.1 ± 0.04	13.1 ± 0.05	13.4 ± 0.36	10.5 ± 0.96	1832 ± 5	177 ± 10	1.1 ± 0.03
ZOA085601.214-	J0856-37	259.7	5.2	0.73	13.9 ± 0.02	12.9 ± 0.02	12.9 ± 0.02	10.9 ± 0.01	10.9 ± 0.01	8.0 ± 0.02	6.1 ± 0.05	2498 ± 7	252 ± 15	0.6 ± 0.01

ZOA Name	HI Name	l	b	ϵ_K	M_J	M_H	M_K	M_{W1}	M_{W2}	M_{W3}	M_{W4}	V_{obs}	W_{50}	E(B-V)
		°	°	arc	mag	mag	mag	mag	mag	mag	mag	kms^{-1}	kms^{-1}	mag
ZOA085640.039-	J0856-48	268.5	-2.1	0.66	14.2 ± 0.02	12.3 ± 0.02	11.5 ± 0.02	10.1 ± 0.01	9.7 ± 0.01	5.7 ± 0.01	2.9 ± 0.01	2664 ± 8	261 ± 17	1.6 ± 0.05
ZOA085728.473-	J0857-39	261.5	4.1	0.08	9.2 ± 0.02	8.3 ± 0.02	8.0 ± 0.02	7.0 ± 0.01	7.0 ± 0.01	5.8 ± 0.01	5.4 ± 0.02	979 ± 4	320 ± 7	0.8 ± 0.04
ZOA085838.795-	J0858-42	264.1	2.1	0.44	12.0 ± 0.02	10.1 ± 0.02	9.3 ± 0.02	8.5 ± 0.01	8.3 ± 0.01	8.5 ± 0.02	7.7 ± 0.07	2948 ± 11	71 ± 22	4.5 ± 1.49
ZOA085813.978-	J0858-45A	266.6	-0.1	0.66	12.6 ± 0.02	11.2 ± 0.02	10.5 ± 0.02	9.7 ± 0.01	9.1 ± 0.01	4.6 ± 0.01	1.5 ± 0.01	2726 ± 8	268 ± 15	2.7 ± 0.09
ZOA085915.276-	J0859-52	272.0	-4.5	0.55	15.2 ± 0.03	14.3 ± 0.02	13.7 ± 0.03	13.2 ± 0.02	13.2 ± 0.02	12.0 ± 0.14	12.4 ± 4.91	4802 ± 8	136 ± 17	1.0 ± 0.02
ZOA090033.110-	J0900-39	262.0	4.4	0.41	10.8 ± 0.02	10.2 ± 0.02	9.7 ± 0.02	9.3 ± 0.01	9.2 ± 0.01	5.7 ± 0.01	4.0 ± 0.01	2634 ± 4	295 ± 7	0.7 ± 0.04
ZOA090145.761-	J0901-41	263.5	3.4	0.41	14.6 ± 0.03	13.6 ± 0.02	13.1 ± 0.02	12.4 ± 0.02	12.3 ± 0.02	9.8 ± 0.05	8.5 ± 0.19	5102 ± 10	222 ± 19	1.2 ± 0.06
ZOA090323.536-	J0903-41	263.8	3.6	0.34	12.0 ± 0.02	11.1 ± 0.02	10.6 ± 0.02	9.9 ± 0.01	9.8 ± 0.01	6.2 ± 0.01	4.2 ± 0.02	5443 ± 3	72 ± 6	1.2 ± 0.06
ZOA090720.153-	J0907-48	269.4	-0.5	0.18	14.4 ± 0.03	12.2 ± 0.02	11.4 ± 0.02	10.7 ± 0.01	10.4 ± 0.01	6.8 ± 0.03	5.0 ± 0.07	5224 ± 13	181 ± 26	2.6 ± 0.15
ZOA091047.158-	J0910-44	267.0	2.5	0.30	13.6 ± 0.02	12.7 ± 0.02	12.3 ± 0.02	11.5 ± 0.01	11.3 ± 0.02	8.6 ± 0.02	7.3 ± 0.10	1875 ± 10	115 ± 19	1.1 ± 0.03
ZOA091645.205-	J0916-54B	274.9	-3.6	0.71	9.6 ± 0.02	9.3 ± 0.02	9.3 ± 0.02	10.8 ± 0.01	10.5 ± 0.01	6.2 ± 0.01	3.9 ± 0.01	4057 ± 5	207 ± 9	0.9 ± 0.05
ZOA091651.023-	J0916-55	275.9	-4.6	0.16	15.9 ± 0.04	15.1 ± 0.03	14.5 ± 0.03	13.2 ± 0.03	13.1 ± 0.04	9.5 ± 0.04	9.4 ± 0.33	1205 ± 17	154 ± 34	0.6 ± 0.03
ZOA091730.512-	J0917-53	274.3	-2.9	0.68	13.1 ± 0.02	12.1 ± 0.02	11.7 ± 0.02	10.9 ± 0.01	10.8 ± 0.01	7.7 ± 0.02	5.1 ± 0.03	945 ± 3	179 ± 6	0.9 ± 0.02
ZOA092334.428-	J0923-42	267.4	5.3	0.26	12.7 ± 0.02	11.9 ± 0.02	12.1 ± 0.02	10.5 ± 0.01	10.4 ± 0.01	6.7 ± 0.01	4.9 ± 0.03	2984 ± 10	141 ± 21	0.6 ± 0.02
ZOA092745.693-	J0927-55	277.1	-3.7	0.71	16.8 ± 0.06	15.9 ± 0.04	15.2 ± 0.04	10.9 ± 0.02	9.3 ± 0.27	7.0 ± 0.02	6.6 ± 0.08	1154 ± 3	140 ± 6	0.8 ± 0.04
ZOA092806.021-	J0928-56	277.6	-4.0	0.30	12.8 ± 0.02	11.9 ± 0.02	11.5 ± 0.02	10.9 ± 0.01	10.7 ± 0.01	6.9 ± 0.01	5.1 ± 0.03	4579 ± 8	183 ± 15	1.3 ± 0.08
ZOA093024.231-	J0930-55	277.4	-3.4	0.30	15.2 ± 0.03	14.1 ± 0.02	13.4 ± 0.02	9.0 ± 0.33	8.2 ± 0.47	4.8 ± 0.01	3.6 ± 0.02	2746 ± 5	96 ± 10	1.6 ± 0.06
ZOA093257.563-	J0933-58	279.7	-5.4	0.26	13.8 ± 0.02	13.0 ± 0.02	12.6 ± 0.02	11.2 ± 0.02	12.2 ± 0.02	12.0 ± 0.11	16.0 ± –	4471 ± 13	128 ± 26	0.6 ± 0.01
ZOA093639.331-	J0936-54	277.1	-1.8	0.10	13.0 ± 0.02	12.1 ± 0.02	11.5 ± 0.02	10.9 ± 0.01	10.7 ± 0.01	7.0 ± 0.01	4.6 ± 0.02	2742 ± 5	113 ± 10	1.9 ± 0.04
ZOA094622.473-	J0946-46	273.1	5.2	0.79	13.4 ± 0.02	12.6 ± 0.02	12.2 ± 0.02	11.0 ± 0.01	11.1 ± 0.01	9.1 ± 0.03	9.3 ± 0.25	2697 ± 4	289 ± 9	0.5 ± 0.02
ZOA094916.505-	J0949-47A	274.3	4.5	0.09	9.7 ± 0.02	9.0 ± 0.02	8.7 ± 0.02	8.3 ± 0.01	8.2 ± 0.01	6.2 ± 0.01	4.7 ± 0.02	1932 ± 5	188 ± 11	0.4 ± 0.00
ZOA094944.198-	J0949-47B	273.8	5.2	0.05	14.2 ± 0.02	13.6 ± 0.02	13.5 ± 0.03	11.5 ± 0.02	11.6 ± 0.02	9.2 ± 0.04	9.7 ± 0.54	5360 ± 6	192 ± 12	0.4 ± 0.02
ZOA094952.868-	J0949-56	279.8	-2.1	0.30	11.4 ± 0.02	10.3 ± 0.02	9.6 ± 0.02	8.4 ± 0.01	8.2 ± 0.01	4.6 ± 0.01	1.7 ± 0.01	1762 ± 3	218 ± 7	2.1 ± 0.09
ZOA095034.078-	J0950-49	275.6	3.3	0.32	12.7 ± 0.02	12.1 ± 0.02	11.7 ± 0.02	11.1 ± 0.02	11.1 ± 0.02	7.6 ± 0.02	– ± –	3771 ± 7	164 ± 14	0.5 ± 0.01
ZOA095144.281-	J0951-59	281.7	-4.0	0.68	13.5 ± 0.02	12.6 ± 0.02	12.4 ± 0.02	11.3 ± 0.02	11.3 ± 0.02	8.8 ± 0.04	7.4 ± 0.13	4384 ± 4	338 ± 7	1.0 ± 0.04
ZOA095300.679-	J0952-61	283.3	-5.7	0.15	13.9 ± 0.02	13.1 ± 0.02	12.6 ± 0.02	11.4 ± 0.01	11.3 ± 0.01	6.7 ± 0.02	5.0 ± 0.04	4441 ± 5	55 ± 11	0.5 ± 0.01
ZOA095310.882-	J0953-49	275.7	3.9	0.48	15.5 ± 0.03	14.8 ± 0.03	14.6 ± 0.03	13.4 ± 0.04	13.3 ± 0.04	10.6 ± 0.07	8.8 ± 0.25	2264 ± 9	97 ± 18	0.4 ± 0.01
ZOA095509.072-	J0955-60	282.9	-4.8	0.54	13.1 ± 0.02	12.2 ± 0.02	12.0 ± 0.02	11.2 ± 0.02	11.2 ± 0.02	8.0 ± 0.02	6.3 ± 0.04	3295 ± 5	249 ± 10	0.5 ± 0.03
ZOA095711.087-	J0957-48	275.9	4.6	0.38	16.3 ± 0.04	15.5 ± 0.03	15.3 ± 0.04	13.1 ± 0.04	13.4 ± 0.05	10.8 ± 0.11	9.5 ± 0.34	3727 ± 3	43 ± 6	0.6 ± 0.02
ZOA100008.790-	J1000-58A	282.2	-2.8	0.66	13.0 ± 0.02	11.9 ± 0.02	11.4 ± 0.02	11.0 ± 0.02	10.9 ± 0.02	9.8 ± 0.04	8.2 ± 0.11	2682 ± 2	118 ± 4	1.4 ± 0.06
ZOA100356.868-	J1004-58	282.6	-2.6	0.38	13.3 ± 0.02	12.1 ± 0.02	11.6 ± 0.02	11.1 ± 0.02	10.9 ± 0.03	7.9 ± 0.03	7.0 ± 0.28	3676 ± 4	290 ± 7	3.7 ± 0.50
ZOA100629.201-	J1006-50A	277.9	4.4	0.10	12.1 ± 0.02	11.3 ± 0.02	11.0 ± 0.02	10.6 ± 0.01	10.5 ± 0.01	7.2 ± 0.01	5.5 ± 0.03	5272 ± 8	276 ± 17	0.5 ± 0.01
ZOA100606.464-	J1006-50B	278.1	4.1	0.58	12.9 ± 0.02	12.2 ± 0.02	11.9 ± 0.02	11.3 ± 0.01	11.2 ± 0.01	7.8 ± 0.01	6.2 ± 0.04	5296 ± 6	298 ± 11	0.5 ± 0.01
ZOA101212.032-	J1012-62	285.7	-5.1	0.63	10.8 ± 0.02	10.1 ± 0.02	9.7 ± 0.02	8.9 ± 0.01	8.4 ± 0.01	3.9 ± 0.01	0.6 ± 0.01	3444 ± 14	229 ± 27	0.3 ± 0.00
ZOA101345.674-	J1013-52B	280.0	3.4	0.37	11.9 ± 0.02	11.1 ± 0.02	10.7 ± 0.02	10.5 ± 0.01	10.4 ± 0.01	7.0 ± 0.01	5.3 ± 0.03	2713 ± 3	251 ± 6	0.5 ± 0.04
ZOA102445.376-	J1024-54	282.8	2.2	0.72	13.5 ± 0.02	12.9 ± 0.02	12.5 ± 0.02	11.8 ± 0.02	11.7 ± 0.03	10.6 ± 0.07	7.3 ± 0.11	1080 ± 4	140 ± 8	0.6 ± 0.05
ZOA103157.298-	J1031-63	288.2	-4.9	0.49	11.7 ± 0.02	11.0 ± 0.02	10.6 ± 0.02	10.1 ± 0.01	10.1 ± 0.01	6.8 ± 0.01	5.2 ± 0.03	3762 ± 6	320 ± 12	0.5 ± 0.01
ZOA103718.096-	J1037-54	284.4	3.0	0.72	11.5 ± 0.02	10.6 ± 0.02	10.2 ± 0.02	10.1 ± 0.21	9.5 ± 0.03	7.3 ± 0.02	6.0 ± 0.04	2673 ± 3	313 ± 7	0.8 ± 0.04
ZOA103815.920-	J1038-54	284.2	3.7	0.44	14.4 ± 0.02	13.6 ± 0.02	13.2 ± 0.02	12.5 ± 0.02	12.4 ± 0.03	9.2 ± 0.03	7.5 ± 0.10	2810 ± 10	60 ± 21	0.5 ± 0.03
ZOA103956.322-	J1039-54	284.5	3.6	0.78	14.8 ± 0.03	14.0 ± 0.02	13.7 ± 0.03	12.7 ± 0.03	12.7 ± 0.03	9.4 ± 0.04	7.2 ± 0.08	2755 ± 3	117 ± 6	0.7 ± 0.02
ZOA105345.693-	J1053-62	290.0	-3.0	0.69	11.6 ± 0.02	10.7 ± 0.02	9.9 ± 0.02	9.1 ± 0.01	8.9 ± 0.01	5.8 ± 0.01	4.1 ± 0.02	1836 ± 3	271 ± 6	0.9 ± 0.04
ZOA114118.278-	J1141-64	295.5	-2.6	0.43	15.1 ± 0.03	13.8 ± 0.02	13.1 ± 0.02	12.3 ± 0.04	12.1 ± 0.03	9.4 ± 0.04	8.8 ± 0.19	2025 ± 3	186 ± 5	1.8 ± 0.04
ZOA114606.371-	J1145-56	293.9	5.3	0.27	10.0 ± 0.02	9.3 ± 0.02	8.8 ± 0.02	7.9 ± 0.01	7.7 ± 0.01	3.8 ± 0.01	1.6 ± 0.01	1835 ± 5	272 ± 9	0.4 ± 0.00
ZOA114955.786-	J1149-57	294.8	4.2	0.14	14.9 ± 0.03	14.2 ± 0.02	14.0 ± 0.03	13.3 ± 0.02	13.4 ± 0.03	10.6 ± 0.05	8.2 ± 0.11	1802 ± 13	82 ± 25	0.5 ± 0.04
ZOA114948.692-	J1149-64	296.2	-1.9	0.41	11.7 ± 0.02	10.4 ± 0.02	9.7 ± 0.02	8.9 ± 0.01	8.5 ± 0.01	4.6 ± 0.01	2.6 ± 0.01	2119 ± 7	188 ± 14	2.4 ± 0.09
ZOA120424.172-	J1204-67	298.4	-4.7	0.30	14.2 ± 0.02	13.5 ± 0.02	13.2 ± 0.02	12.4 ± 0.02	12.2 ± 0.03	9.0 ± 0.03	6.8 ± 0.08	5330 ± 9	241 ± 19	0.5 ± 0.02
ZOA120821.250-	J1208-65	298.5	-3.0	0.27	12.3 ± 0.02	11.2 ± 0.02	10.8 ± 0.02	10.8 ± 0.02	10.8 ± 0.02	7.8 ± 0.03	6.6 ± 0.07	5489 ± 3	364 ± 7	0.9 ± 0.03
ZOA121425.627-	J1214-58	298.1	4.1	0.77	13.8 ± 0.02	12.9 ± 0.02	12.4 ± 0.02	11.8 ± 0.01	11.5 ± 0.01	7.5 ± 0.01	5.5 ± 0.03	5631 ± 6	287 ± 11	0.6 ± 0.02
ZOA122238.290-	J1222-58	299.2	4.0	0.72	9.7 ± 0.02	8.9 ± 0.02	8.6 ± 0.02	8.3 ± 0.01	8.2 ± 0.01	6.3 ± 0.01	4.5 ± 0.02	1531 ± 6	374 ± 12	0.6 ± 0.01
ZOA122524.509-	J1225-59	299.6	3.5	0.30	12.9 ± 0.02	12.2 ± 0.02	11.7 ± 0.02	11.2 ± 0.02	11.1 ± 0.02	7.7 ± 0.02	6.1 ± 0.05	5633 ± 7	238 ± 14	0.7 ± 0.07
ZOA122830.949-	J1228-58	299.9	4.1	0.13	13.0 ± 0.02	12.2 ± 0.02	11.6 ± 0.02	11.2 ± 0.02	11.2 ± 0.02	8.5 ± 0.02	6.9 ± 0.07	5562 ± 7	195 ± 14	0.6 ± 0.03
ZOA122948.708-	J1229-61	300.3	1.6	0.19	12.4 ± 0.02	11.5 ± 0.02	10.8 ± 0.02	9.6 ± 0.02	9.5 ± 0.02	6.6 ± 0.02	5.1 ± 0.03	5391 ± 8	333 ± 16	1.9 ± 0.08
ZOA123311.226-	J1232-59	300.6	3.6	0.21	12.6 ± 0.02	11.7 ± 0.02	11.3 ± 0.02	11.0 ± 0.02	10.9 ± 0.02	8.5 ± 0.04	7.6 ± 0.12	5437 ± 11	165 ± 22	1.2 ± 0.09
ZOA123906.653-	J1239-59	301.4	3.2	0.67	12.5 ± 0.02	11.5 ± 0.02	11.0 ± 0.02	10.3 ± 0.01	10.0 ± 0.01	6.0 ± 0.01	4.1 ± 0.02	5321 ± 4	379 ± 9	0.9 ± 0.02
ZOA130612.957-	J1305-57	304.9	5.3	0.34	11.8 ± 0.02	11.0 ± 0.02	10.8 ± 0.02	10.2 ± 0.01	10.1 ± 0.01	6.5 ± 0.01	3.7 ± 0.01	5902 ± 8	181 ± 17	0.4 ± 0.00
ZOA131245.901-	J1312-60	305.5	1.9	0.26	13.8 ± 0.02	12.0 ± 0.02	11.3 ± 0.02	11.3 ± 0.05	11.3 ± 0.05	9.0 ± 0.07	7.9 ± 0.20	2322 ± 3	238 ± 6	2.5 ± 0.33
ZOA131509.704-	J1314-58	306.0	3.8	0.34	12.4 ± 0.02	11.1 ± 0.02	10.9 ± 0.02	10.4 ± 0.02	10.2 ± 0.01	6.3 ± 0.01	4.0 ± 0.02	2338 ± 5	156 ± 9	0.9 ± 0.03
ZOA132723.827-	J1327-57	307.8	5.0	0.73	10.9 ± 0.02	9.8 ± 0.02	9.3 ± 0.02	8.7 ± 0.01	8.1 ± 0.01	3.8 ± 0.01	0.5 ± 0.01	2932 ± 5	255 ± 11	0.8 ± 0.02

ZOA Name	HI Name	l	b	ϵ_K	M_J	M_H	M_K	M_{W1}	M_{W2}	M_{W3}	M_{W4}	V_{obs}	W_{50}	E(B-V)
		°	°	arc	mag	mag	mag	mag	mag	mag	mag	kms^{-1}	kms^{-1}	mag
ZOA132933.164-	J1329-58	307.9	3.7	0.47	12.5 ± 0.02	11.6 ± 0.02	11.4 ± 0.02	11.0 ± 0.02	10.9 ± 0.02	7.9 ± 0.02	6.6 ± 0.06	5575 ± 5	388 ± 10	0.7 ± 0.05
ZOA133148.660-	J1331-65	307.1	-2.7	0.31	11.9 ± 0.02	10.9 ± 0.02	10.5 ± 0.02	10.1 ± 0.02	10.1 ± 0.02	8.1 ± 0.03	6.9 ± 0.09	2773 ± 3	292 ± 5	1.3 ± 0.05
ZOA133724.550-	J1337-58B	308.9	3.5	0.67	11.5 ± 0.02	10.5 ± 0.02	10.1 ± 0.02	9.9 ± 0.01	9.9 ± 0.01	10.0 ± 0.03	9.6 ± 0.28	3598 ± 6	361 ± 11	1.1 ± 0.02
ZOA133744.189-	J1337-58C	309.0	4.1	0.38	14.4 ± 0.03	13.5 ± 0.02	13.3 ± 0.03	13.6 ± 0.07	13.2 ± 0.07	8.8 ± 0.03	7.0 ± 0.09	5906 ± 12	130 ± 24	0.8 ± 0.05
ZOA134154.816-	J1341-58	309.4	3.4	0.31	13.8 ± 0.02	12.5 ± 0.02	12.5 ± 0.02	11.9 ± 0.03	11.9 ± 0.04	8.8 ± 0.05	7.2 ± 0.11	3865 ± 6	174 ± 11	1.0 ± 0.06
ZOA134229.543-	J1342-61	309.1	1.2	0.13	13.3 ± 0.02	11.8 ± 0.02	10.9 ± 0.02	10.0 ± 0.01	9.7 ± 0.01	7.1 ± 0.02	5.3 ± 0.05	3946 ± 7	340 ± 14	3.1 ± 0.39
ZOA134343.558-	J1343-56	310.1	5.5	0.27	14.1 ± 0.02	13.1 ± 0.02	13.0 ± 0.02	12.9 ± 0.04	12.4 ± 0.03	9.9 ± 0.04	7.8 ± 0.07	5218 ± 7	62 ± 14	0.6 ± 0.02
ZOA134345.417-	J1343-57	309.9	4.6	0.31	14.0 ± 0.02	13.2 ± 0.02	12.9 ± 0.02	12.3 ± 0.02	12.1 ± 0.03	8.5 ± 0.02	6.8 ± 0.07	5355 ± 6	207 ± 12	0.6 ± 0.02
ZOA134436.279-	J1344-58	309.9	3.9	0.25	12.2 ± 0.02	11.4 ± 0.02	11.0 ± 0.02	10.1 ± 0.01	10.0 ± 0.01	6.8 ± 0.01	5.3 ± 0.04	5434 ± 6	252 ± 11	1.0 ± 0.07
ZOA135138.534-	J1351-58	310.7	3.4	0.52	10.2 ± 0.02	9.3 ± 0.02	8.9 ± 0.02	8.4 ± 0.01	8.3 ± 0.01	6.1 ± 0.01	4.9 ± 0.03	3874 ± 5	635 ± 10	1.0 ± 0.05
ZOA140156.320-	J1401-55	312.8	5.7	0.52	12.0 ± 0.02	11.2 ± 0.02	10.9 ± 0.02	10.5 ± 0.01	10.5 ± 0.02	7.3 ± 0.01	5.8 ± 0.04	3962 ± 5	274 ± 9	0.5 ± 0.01
ZOA140224.271-	J1402-57	312.5	4.5	0.51	15.5 ± 0.03	14.8 ± 0.03	14.5 ± 0.03	13.7 ± 0.04	13.5 ± 0.05	10.7 ± 0.08	9.6 ± 0.48	5561 ± 11	118 ± 21	0.5 ± 0.02
ZOA140513.269-	J1405-65	310.5	-3.8	0.71	13.6 ± 0.02	12.4 ± 0.02	12.4 ± 0.02	12.0 ± 0.04	11.9 ± 0.04	8.9 ± 0.06	7.4 ± 0.14	2838 ± 15	64 ± 29	0.6 ± 0.03
ZOA140610.192-	J1406-57	312.8	3.6	0.70	12.2 ± 0.02	11.3 ± 0.02	11.0 ± 0.02	10.8 ± 0.01	10.8 ± 0.02	9.6 ± 0.06	8.3 ± 0.20	5551 ± 7	304 ± 14	0.7 ± 0.02
ZOA140745.677-	J1407-58	312.7	2.7	0.46	13.7 ± 0.02	12.7 ± 0.02	12.2 ± 0.02	13.9 ± 0.06	13.5 ± 0.05	10.1 ± 0.06	7.5 ± 0.10	3214 ± 4	53 ± 7	2.0 ± 0.11
ZOA141036.181-	J1410-65	311.0	-4.0	0.52	10.4 ± 0.02	9.5 ± 0.02	9.1 ± 0.02	8.7 ± 0.01	8.6 ± 0.01	6.7 ± 0.02	5.5 ± 0.04	3092 ± 6	437 ± 12	0.6 ± 0.01
ZOA141232.785-	J1412-56A	314.0	4.5	0.53	11.4 ± 0.02	10.6 ± 0.02	10.3 ± 0.02	9.9 ± 0.02	9.8 ± 0.02	6.5 ± 0.01	4.7 ± 0.03	3767 ± 13	282 ± 25	0.7 ± 0.01
ZOA141309.873-	J1413-65	311.3	-3.8	0.50	7.5 ± 0.02	6.5 ± 0.02	6.1 ± 0.02	4.7 ± 0.01	4.2 ± 0.01	1.1 ± 0.01	-2.0 ± 0.01	435 ± 4	254 ± 7	1.5 ± 0.21
ZOA141421.901-	J1414-58	313.6	2.8	0.60	13.5 ± 0.02	12.5 ± 0.02	11.9 ± 0.02	11.0 ± 0.02	10.7 ± 0.02	7.1 ± 0.02	5.3 ± 0.04	5804 ± 10	249 ± 20	1.3 ± 0.06
ZOA141552.098-	J1415-58	313.7	2.2	0.80	12.6 ± 0.02	11.3 ± 0.02	10.6 ± 0.02	10.2 ± 0.01	10.1 ± 0.02	8.9 ± 0.04	7.4 ± 0.12	5396 ± 6	713 ± 12	2.1 ± 0.20
ZOA141604.868-	J1416-65	311.6	-3.8	0.52	11.2 ± 0.02	10.3 ± 0.02	9.9 ± 0.02	10.2 ± 0.02	10.2 ± 0.02	8.9 ± 0.05	7.9 ± 0.15	2868 ± 8	330 ± 16	0.8 ± 0.01
ZOA142023.463-	J1419-55	315.5	5.6	0.18	11.5 ± 0.02	11.1 ± 0.02	10.9 ± 0.02	10.3 ± 0.01	10.2 ± 0.01	6.5 ± 0.01	4.7 ± 0.02	2829 ± 8	237 ± 16	0.6 ± 0.00
ZOA142042.940-	J1420-58	314.5	2.7	0.04	12.4 ± 0.02	11.7 ± 0.02	10.9 ± 0.02	10.9 ± 0.02	10.8 ± 0.02	8.2 ± 0.04	7.2 ± 0.15	5483 ± 4	216 ± 9	1.6 ± 0.06
ZOA142403.045-	J1423-65	312.2	-4.7	0.69	14.3 ± 0.02	13.3 ± 0.02	12.8 ± 0.02	12.1 ± 0.03	12.2 ± 0.02	10.0 ± 0.06	9.2 ± 0.25	3088 ± 9	155 ± 18	0.7 ± 0.02
ZOA143016.491-	J1429-54	317.0	5.5	0.14	15.2 ± 0.03	14.4 ± 0.02	14.1 ± 0.03	13.3 ± 0.04	13.2 ± 0.05	11.5 ± 0.19	10.9 ± 1.73	3017 ± 6	110 ± 11	0.7 ± 0.05
ZOA143158.829-	J1431-55	316.9	4.7	0.05	10.3 ± 0.02	9.5 ± 0.02	9.0 ± 0.02	8.6 ± 0.01	8.5 ± 0.01	4.9 ± 0.01	3.0 ± 0.01	3109 ± 3	176 ± 7	0.9 ± 0.03
ZOA143927.759-	J1439-55	317.9	4.3	0.21	11.2 ± 0.02	10.4 ± 0.02	10.0 ± 0.02	9.8 ± 0.01	9.7 ± 0.01	6.4 ± 0.02	4.7 ± 0.03	4631 ± 9	328 ± 18	0.7 ± 0.03
ZOA144429.934-	J1444-55	318.5	4.0	0.33	13.7 ± 0.02	12.7 ± 0.02	12.4 ± 0.02	11.9 ± 0.03	11.8 ± 0.03	8.4 ± 0.04	7.0 ± 0.12	4671 ± 7	237 ± 13	0.6 ± 0.01
ZOA145007.770-	J1450-55	319.4	3.8	0.03	12.5 ± 0.02	11.5 ± 0.02	11.0 ± 0.02	10.8 ± 0.02	10.7 ± 0.02	7.0 ± 0.02	5.3 ± 0.04	5527 ± 4	160 ± 8	1.0 ± 0.03
ZOA145709.815-	J1457-54	320.7	4.1	0.55	10.0 ± 0.02	9.1 ± 0.02	8.7 ± 0.02	8.3 ± 0.01	8.2 ± 0.01	5.7 ± 0.01	4.1 ± 0.02	2881 ± 3	475 ± 7	0.8 ± 0.01
ZOA145822.080-	J1458-55	320.5	3.3	0.61	13.3 ± 0.02	12.4 ± 0.02	11.9 ± 0.02	11.6 ± 0.02	11.5 ± 0.02	8.4 ± 0.04	5.1 ± 0.04	5216 ± 12	181 ± 23	0.9 ± 0.03
ZOA150556.328-	J1506-54	321.8	3.5	0.68	15.5 ± 0.03	14.6 ± 0.03	14.3 ± 0.03	14.1 ± 0.07	14.0 ± 0.07	10.6 ± 0.12	8.7 ± 0.22	2943 ± 4	146 ± 7	1.0 ± 0.03
ZOA150928.962-	J1509-52	323.2	4.8	0.76	9.2 ± 0.02	8.4 ± 0.02	8.0 ± 0.02	7.6 ± 0.01	7.5 ± 0.01	5.1 ± 0.01	3.5 ± 0.01	1451 ± 5	346 ± 9	0.8 ± 0.03
ZOA151434.147-	J1514-53	323.6	4.0	0.77	8.9 ± 0.02	7.9 ± 0.02	7.4 ± 0.02	6.7 ± 0.01	6.6 ± 0.01	3.2 ± 0.01	1.5 ± 0.01	1457 ± 3	431 ± 7	1.0 ± 0.05
ZOA153927.174-	J1539-44	331.8	8.7	0.75	14.1 ± 0.02	13.3 ± 0.02	13.0 ± 0.02	11.8 ± 0.04	11.5 ± 0.04	9.0 ± 0.10	8.1 ± 0.19	3434 ± 0	224 ± 0	0.3 ± 0.01
ZOA153931.522-	J1539-59B	322.8	-3.3	0.65	12.4 ± 0.02	11.4 ± 0.02	11.0 ± 0.02	10.6 ± 0.03	10.5 ± 0.03	8.8 ± 0.04	9.0 ± 0.25	5178 ± 5	110 ± 10	1.0 ± 0.02
ZOA154006.589-	J1540-50	328.1	3.6	0.38	11.9 ± 0.02	11.0 ± 0.02	10.7 ± 0.02	10.0 ± 0.02	9.7 ± 0.01	5.9 ± 0.01	3.4 ± 0.01	5325 ± 3	72 ± 7	0.8 ± 0.02
ZOA154327.789-	J1543-60	322.8	-4.2	0.61	13.7 ± 0.02	12.9 ± 0.02	12.5 ± 0.02	12.2 ± 0.03	12.2 ± 0.03	8.9 ± 0.06	6.7 ± 0.08	5186 ± 7	230 ± 14	0.7 ± 0.01
ZOA154526.828-	J1545-61	322.5	-4.9	0.51	11.5 ± 0.02	10.6 ± 0.02	10.1 ± 0.02	9.7 ± 0.01	9.5 ± 0.01	6.1 ± 0.01	3.8 ± 0.01	5264 ± 10	365 ± 19	0.7 ± 0.03
ZOA154644.877-	J1546-42	334.2	9.6	0.24	12.7 ± 0.02	12.0 ± 0.02	11.7 ± 0.02	11.2 ± 0.01	11.1 ± 0.02	7.6 ± 0.03	6.1 ± 0.06	4637 ± 0	172 ± 0	0.4 ± 0.01
ZOA154710.889-	J1547-59	323.9	-3.5	0.61	11.3 ± 0.02	10.7 ± 0.02	10.1 ± 0.02	10.1 ± 0.52	9.5 ± 0.01	6.3 ± 0.02	4.4 ± 0.02	5644 ± 4	341 ± 9	0.6 ± 0.01
ZOA155100.942-	J1550-59	324.0	-4.2	0.28	13.9 ± 0.02	13.2 ± 0.02	12.9 ± 0.02	11.9 ± 0.03	11.8 ± 0.03	8.5 ± 0.05	6.1 ± 0.07	4989 ± 12	110 ± 23	0.5 ± 0.01
ZOA155357.476-	J1553-61	323.1	-5.8	0.32	14.4 ± 0.03	13.5 ± 0.02	13.4 ± 0.02	12.4 ± 0.03	12.2 ± 0.03	9.7 ± 0.05	8.9 ± 0.28	4345 ± 5	263 ± 10	0.4 ± 0.01
ZOA155414.198-	J1554-59	324.1	-4.7	0.42	13.6 ± 0.02	13.0 ± 0.02	12.7 ± 0.02	12.2 ± 0.03	12.2 ± 0.03	8.5 ± 0.03	6.9 ± 0.09	5607 ± 9	272 ± 18	0.5 ± 0.01
ZOA155657.592-	J1556-42	335.5	8.3	0.64	14.6 ± 0.03	13.6 ± 0.02	13.2 ± 0.02	12.2 ± 0.02	11.9 ± 0.03	8.3 ± 0.04	6.2 ± 0.08	5755 ± 0	86 ± 0	0.9 ± 0.05
ZOA160449.497-	J1604-41	337.2	7.9	0.50	11.4 ± 0.02	10.7 ± 0.02	10.3 ± 0.02	9.7 ± 0.01	9.7 ± 0.01	7.1 ± 0.03	5.5 ± 0.05	4743 ± 0	200 ± 0	0.7 ± 0.02
ZOA160627.540-	J1606-57	326.8	-4.0	0.78	12.0 ± 0.02	11.1 ± 0.02	10.8 ± 0.02	10.4 ± 0.01	10.3 ± 0.01	7.2 ± 0.01	5.8 ± 0.05	5051 ± 7	398 ± 14	0.6 ± 0.02
ZOA161031.033-	J1610-38	340.3	9.6	0.89	14.3 ± 0.03	13.7 ± 0.02	13.2 ± 0.03	12.0 ± 0.02	12.1 ± 0.03	8.9 ± 0.12	6.6 ± 0.09	4503 ± 0	142 ± 0	0.8 ± 0.03
ZOA161319.695-	J1613-56	328.3	-3.8	0.25	10.9 ± 0.02	10.7 ± 0.02	9.7 ± 0.02	10.0 ± 0.02	10.0 ± 0.02	7.1 ± 0.02	5.1 ± 0.03	2726 ± 4	318 ± 8	0.5 ± 0.02
ZOA161616.704-	J1616-40	339.9	7.7	0.59	12.0 ± 0.02	11.1 ± 0.02	10.8 ± 0.02	10.8 ± 0.02	10.7 ± 0.02	7.9 ± 0.07	6.5 ± 0.10	4438 ± 0	344 ± 0	1.0 ± 0.04
ZOA161710.749-	J1617-58	327.3	-5.5	0.58	10.8 ± 0.02	10.0 ± 0.02	9.8 ± 0.02	9.2 ± 0.01	9.0 ± 0.01	5.4 ± 0.01	2.6 ± 0.01	2783 ± 10	231 ± 21	0.3 ± 0.01
ZOA162101.624-	J1621-36	343.4	9.8	0.57	10.8 ± 0.02	10.1 ± 0.02	9.7 ± 0.02	9.4 ± 0.01	9.4 ± 0.01	8.0 ± 0.03	9.3 ± 0.32	4447 ± 0	370 ± 0	0.7 ± 0.02
ZOA162530.063-	J1625-42	339.5	4.7	0.43	13.5 ± 0.02	12.3 ± 0.02	11.9 ± 0.02	11.5 ± 0.02	11.2 ± 0.02	7.5 ± 0.03	5.1 ± 0.04	2394 ± 10	141 ± 21	1.3 ± 0.05
ZOA162653.388-	J1626-53	331.8	-3.0	0.05	13.2 ± 0.02	12.1 ± 0.02	12.1 ± 0.02	12.0 ± 0.05	11.8 ± 0.05	8.3 ± 0.12	5.7 ± 0.06	2631 ± 10	91 ± 21	0.7 ± 0.04
ZOA162808.701-	J1628-29	349.7	13.5	0.61	11.8 ± 0.02	11.0 ± 0.02	10.7 ± 0.02	10.3 ± 0.01	10.3 ± 0.01	9.8 ± 0.22	9.3 ± 0.34	4180 ± 0	426 ± 0	0.4 ± 0.01
ZOA162949.964-	J1629-26	351.7	14.8	0.45	11.7 ± 0.02	11.0 ± 0.02	10.6 ± 0.02	10.2 ± 0.02	9.6 ± 0.01	6.7 ± 0.03	4.8 ± 0.03	5143 ± 0	334 ± 0	0.5 ± 0.03
ZOA163007.748-	J1630-30	348.9	12.2	0.81	14.2 ± 0.02	13.4 ± 0.02	13.2 ± 0.02	12.6 ± 0.02	12.5 ± 0.03	12.6 ± 0.75	9.4 ± 0.34	4109 ± 0	207 ± 0	0.4 ± 0.02
ZOA163140.118-	J1631-28	351.0	13.6	0.29	10.8 ± 0.02	10.1 ± 0.02	9.6 ± 0.02	8.9 ± 0.01	8.7 ± 0.01	5.0 ± 0.01	3.0 ± 0.01	4188 ± 0	243 ± 0	0.7 ± 0.04

ZOA Name	HI Name	l °	b °	ϵ_K arc	M_J mag	M_H mag	M_K mag	M_{W1} mag	M_{W2} mag	M_{W3} mag	M_{W4} mag	V_{obs} kms^{-1}	W_{50} kms^{-1}	E(B-V) mag
ZOA163211.878-	J1632-28	351.1	13.5	0.71	10.3 ± 0.02	9.4 ± 0.02	9.1 ± 0.02	8.7 ± 0.01	8.7 ± 0.01	- ± -	5.6 ± 0.14	4104 ± 0	518 ± 0	0.6 ± 0.04
ZOA163237.158-	J1632-29B	350.1	12.6	0.78	13.0 ± 0.02	12.2 ± 0.02	11.9 ± 0.02	11.3 ± 0.01	11.2 ± 0.02	8.7 ± 0.12	6.7 ± 0.10	4827 ± 0	282 ± 0	0.5 ± 0.05
ZOA163401.796-	J1634-27	351.7	13.5	0.58	13.0 ± 0.02	12.2 ± 0.02	11.9 ± 0.02	11.6 ± 0.01	11.6 ± 0.02	11.6 ± 0.30	– ± –	4231 ± 0	99 ± 0	0.5 ± 0.02
ZOA164421.521-	J1644-55	331.9	-6.3	0.70	11.4 ± 0.02	10.4 ± 0.02	10.0 ± 0.02	10.0 ± 0.01	9.8 ± 0.01	6.8 ± 0.01	5.0 ± 0.03	5114 ± 0	441 ± 0	0.3 ± 0.01
ZOA164808.402-	J1648-54	333.1	-6.1	0.65	13.9 ± 0.02	13.2 ± 0.02	12.8 ± 0.02	11.8 ± 0.03	11.7 ± 0.02	8.8 ± 0.03	6.5 ± 0.07	4654 ± 0	282 ± 0	0.4 ± 0.01
ZOA165820.881-	J1658-21B	0.1	13.0	0.46	14.7 ± 0.03	13.8 ± 0.02	13.7 ± 0.03	12.1 ± 0.02	12.2 ± 0.03	10.9 ± 0.52	8.9 ± 0.42	5959 ± 0	233 ± 0	0.4 ± 0.01
ZOA170231.682-	J1702-52	335.7	-6.7	0.25	14.0 ± 0.02	13.2 ± 0.02	13.2 ± 0.02	12.6 ± 0.04	12.4 ± 0.04	9.1 ± 0.05	6.9 ± 0.12	4445 ± 0	110 ± 0	0.4 ± 0.01
ZOA170836.263-	J1708-56	333.2	-9.7	0.07	13.4 ± 0.02	12.8 ± 0.02	12.6 ± 0.02	11.9 ± 0.02	11.8 ± 0.03	8.6 ± 0.03	7.3 ± 0.11	4671 ± 0	101 ± 0	0.2 ± 0.00
ZOA171136.926-	J1711-47	340.8	-4.8	0.11	12.7 ± 0.02	11.6 ± 0.02	11.0 ± 0.02	11.9 ± 0.03	11.8 ± 0.04	9.2 ± 0.17	7.3 ± 0.14	2187 ± 3	226 ± 7	0.7 ± 0.02
ZOA171229.285-	J1712-15	7.6	14.0	0.48	13.2 ± 0.02	12.5 ± 0.02	12.4 ± 0.02	11.6 ± 0.01	11.4 ± 0.02	8.4 ± 0.09	6.5 ± 0.08	2937 ± 0	206 ± 0	0.4 ± 0.02
ZOA171923.686-	J1719-45	342.9	-4.9	0.28	11.3 ± 0.02	10.6 ± 0.02	10.4 ± 0.02	10.3 ± 0.02	10.3 ± 0.02	7.1 ± 0.02	5.2 ± 0.04	5807 ± 10	249 ± 20	0.6 ± 0.03
ZOA173228.425-	J1732-43	346.4	-5.4	0.33	12.5 ± 0.02	11.9 ± 0.02	11.6 ± 0.02	10.8 ± 0.01	10.8 ± 0.02	7.3 ± 0.02	4.7 ± 0.03	2516 ± 6	174 ± 13	0.5 ± 0.03
ZOA173309.442-	J1733-09	15.2	12.6	0.62	14.7 ± 0.03	14.0 ± 0.02	13.5 ± 0.02	12.7 ± 0.02	12.6 ± 0.03	9.8 ± 0.12	7.8 ± 0.16	5502 ± 0	138 ± 0	0.9 ± 0.06
ZOA174402.614-	J1744-09	16.7	10.4	0.38	13.0 ± 0.02	12.4 ± 0.02	12.6 ± 0.02	11.4 ± 0.02	11.3 ± 0.02	11.5 ± 0.71	7.4 ± 0.13	4245 ± 0	238 ± 0	1.1 ± 0.01
ZOA175453.601-	J1755-34	356.4	-4.5	0.43	11.0 ± 0.02	10.3 ± 0.02	9.8 ± 0.02	9.8 ± 0.02	9.5 ± 0.02	6.0 ± 0.02	3.7 ± 0.02	5935 ± 8	543 ± 16	0.7 ± 0.02
ZOA180031.811-	J1800-03	23.4	9.4	0.72	12.5 ± 0.02	11.5 ± 0.02	10.9 ± 0.02	10.2 ± 0.01	9.8 ± 0.01	5.8 ± 0.02	2.9 ± 0.01	4276 ± 0	227 ± 0	1.4 ± 0.05
ZOA181022.611+	J1810+01	29.6	9.9	0.65	12.4 ± 0.02	11.8 ± 0.02	11.2 ± 0.02	10.8 ± 0.01	10.7 ± 0.01	10.3 ± 0.29	6.7 ± 0.08	1860 ± 0	74 ± 0	0.5 ± 0.03
ZOA182226.663-	J1822-35	357.9	-10.1	0.58	11.0 ± 0.02	10.1 ± 0.02	9.8 ± 0.02	9.1 ± 0.01	8.9 ± 0.01	6.2 ± 0.01	4.7 ± 0.03	5604 ± 0	542 ± 0	0.1 ± 0.00
ZOA182423.339-	J1824-34	359.4	-9.8	0.28	11.1 ± 0.02	10.4 ± 0.02	10.1 ± 0.02	9.7 ± 0.01	9.6 ± 0.01	6.1 ± 0.03	4.2 ± 0.02	4901 ± 0	335 ± 0	0.1 ± 0.00
ZOA182641.621-	J1826-33	0.0	-10.0	0.32	12.3 ± 0.02	11.5 ± 0.02	11.3 ± 0.02	11.1 ± 0.02	11.0 ± 0.02	7.4 ± 0.04	5.5 ± 0.05	5900 ± 0	315 ± 0	0.2 ± 0.00
ZOA183155.989-	J1831-31	2.3	-10.1	0.42	11.2 ± 0.02	10.6 ± 0.02	10.3 ± 0.02	10.0 ± 0.01	10.0 ± 0.01	6.8 ± 0.02	5.5 ± 0.05	5992 ± 0	426 ± 0	0.2 ± 0.01
ZOA185347.519+	J1853+09	42.0	4.0	0.63	12.4 ± 0.02	11.5 ± 0.02	11.0 ± 0.02	10.9 ± 0.02	10.7 ± 0.02	7.8 ± 0.02	6.2 ± 0.07	4729 ± 1	320 ± 3	0.9 ± 0.04
ZOA190004.970+	J1900+13	46.0	4.3	0.45	16.6 ± 0.04	15.6 ± 0.03	15.8 ± 0.06	13.7 ± 0.06	13.7 ± 0.07	11.6 ± 0.17	10.1 ± 0.84	4658 ± 2	234 ± 4	0.8 ± 0.02
ZOA191724.683+	J1917+07	42.9	-2.2	0.32	11.4 ± 0.02	10.4 ± 0.02	9.9 ± 0.02	9.7 ± 0.01	9.5 ± 0.01	5.6 ± 0.01	3.7 ± 0.02	3033 ± 2	226 ± 6	2.0 ± 0.04
ZOA193351.647+	J1933+10	47.3	-4.4	0.65	13.6 ± 0.02	12.8 ± 0.02	12.5 ± 0.02	12.0 ± 0.02	11.8 ± 0.02	8.3 ± 0.02	6.7 ± 0.10	5255 ± 3	240 ± 8	0.5 ± 0.01

A.5 WISE Pipeline Photometry Output Table

TABLE A.2: WISE resolved galaxy photometry output parameters from the pipeline. The units marc^{-2} represent mag arcsec^{-2}, while arc represent arcsec.

WISE resolved galaxy Photometry Output Parameters		
name	units	Description
desig	—	name of object/galaxy
ra	deg	Right Ascension, degrees J2000
dec	deg	Declination, degrees J2000
Riso,R2iso,R3iso,R4iso	arc	W1,W2,W3,W4 1-sigma isophote radius aperture
ba	—	axis ratio based on the W1 3-sigma isophote
pa	deg	position angle based on the W1 3-sigma isophote
flux_1,flux_2,flux_3,flux_4	mJy	W1,W2,W3,W4 integrated flux density
err_1,err_2,err_3,err_4	mJy	W1,W2,W3,W4 integrated flux density uncertainty
mag_1,mag_2,mag_3,mag_4	mag	W1,W2,W3,W4 integrated magnitude
merr_1,merr_2,merr_3,merr_4	mag	W1,W2,W3,W4 integrated magnitude uncertainty
flg1,flg2,flg3,flg4	—	W1,W2,W3,W4 photometry confusion flag
W1W2, W1W2er	mag	W1-W2 color & uncertainty 1-sigma isophote
W2W3,W2W3er	mag	W2-W3 color & uncertainty 1-sigma isophote
W1W3,W1W3er	mag	W1-W3 color & uncertainty 1-sigma isophote
W3W4, W3W4er	mag	W3-W4 color & uncertainty 1-sigma isophote
meanSB_1,meanSB_2,meanSB_3,meanSB_4	marc^{-2}	W1,W2,W3,W4 mean surface brightness
sky_1,sky_2,sky_3,sky_4	dn	W1,W2,W3,W4 local background sky level
sig_1,sig_2,sig_3,sig_4	dn	W1,W2,W3,W4 local background sky RMS
R1iso,R2iso,R3iso,R4iso	arc	W1,W2,W3,W4 1-sigma isophotal radius
SB_1,SB_2,SB_3,SB_4	marc^{-2}	W1,W2,W3,W4 1-sigma local sky brightness
Scale_1a,Scale_2a,Scale_3a,Scale_4a	arc	W1,W2,W3,W4 scale length (1st Sérsic fit, bulge)
Scale_1b,Scale_2b,Scale_3b,Scale_4b	arc	W1,W2,W3,W4 scale length (2nd Sérsic fit, disk)
beta_1a,beta_2a,beta_3a,beta_4a	arc	W1,W2,W3,W4 scale length (1st Sérsic fit, bulge)
beta_1b,beta_2b,beta_3b,beta_4b	arc	W1,W2,W3,W4 scale length (2nd Sérsic fit, disk)
Rtot_1,Rtot_2,Rtot_3,Rtot_4	arc	W1,W2,W3,W4 total radius
ftot_1,ftot_2,ftot_3,ftot_4	mJy	W1,W2,W3,W4 total flux density
mtot_1,mtot_2,mtot_3,mtot_4	mag	W1,W2,W3,W4 total magnitude
Reff_1,Reff_2,Reff_3,Reff_4	arc	W1,W2,W3,W4 effective radius
SBeff_1,SBeff_2,SBeff_3,SBeff_4	marc^{-2}	W1,W2,W3,W4 effective surface brightness
con_1,con_2,con_3,con_4	—	W1,W2,W3,W4 concentration index
R1conv,R2conv,R3conv,R4conv	arc	W1,W2,W3,W4 inflection radius
W1conv,W2conv,W3conv,W4conv	mag	W1,W2,W3,W4 inflection magnitude
uW1conv,uW2conv,uW3conv,uW4conv	mag	W1,W2,W3,W4 inflection magnitude uncertainty
Rinner	arc	Local background annulus, inner radius
Router	arc	Local background annulus, outer radius
w1zero,w2zero,w3zero,w4zero	mag	W1,W2,W3,W4 zero point (calibration) magnitude
w1mpro,w2mpro,w3mpro,w4mpro	mag	W1,W2,W3,W4 mpro (profile-fit) photometry
dw1mpro,dw2mpro,dw3mpro,dw4mpro	mag	W1,W2,W3,W4 mpro uncertainty
w1rchi,w2rchi,w3rchi,w4rchi	mag	W1,W2,W3,W4 reduce χ^2 photometry
xscprox	arc	Proximity (radius) from the nearest 2MASS galaxy
Rmoments	arc	W1 1$^{\mathbf{st}}$ moment radius
Rminor	arc	W1 1$^{\mathbf{st}}$ moment radius along minor axis
Rfuzzy	arc	W1 1$^{\mathbf{st}}$ fuzzy radius, indicator for resolved emission

Appendix B

S0 Redshift Template Data

The complete S0 redshift data used to determine the K-correction in this project can be downloaded at http://www.ast.uct.ac.za/~affadi/patrick/patrick.html. The description of the column parameters in TABLE A.1 are:
Column 1: z redshift
Column 2, 3 & **4**: J, H & K_s are IRSF J, H & K_s bands magnitudes
Column 5, 6, 7 & **8**: W1, W2, W3, & W4 are WISE W1-W4 bands magnitudes
Column 9, 10, 11, 12 & **13**: $J - K_s$, $H - K_s$, W1-W2, W2-W3 & W3-W4 are WISE W1-W4 bands colors in magnitudes

B.1 Low z K-Correction Equations

Given the scaling factor f_s, the rest wavelength flux f_{rest} is given as

$$f_{\text{rest}} = f_{\text{observed}} \times f_s. \tag{B.1}$$

While for colors $(\lambda_1 - \lambda_2)$ given in magnitude units the correction is given as

$$(\lambda_1 - \lambda_2)_{\text{rest}} = (\lambda_1 - \lambda_2)_{\text{observed}} \times (\lambda_1 - \lambda_2)_{\text{correction}}. \tag{B.2}$$

The low-z cosmological K-correction equation is given as

$$k(z) = m_{z(i)} - m_{z(0)} - 2.5 \log 10(1 + z). \tag{B.3}$$

B.2 Rest Wavelengths

The rest wavelengths flux for JHK_s bands and WISE W1-W4 and colors of $J - K_s$, $H - K_s$, W1-W2, W2-W3 & W3-W4.

$$F_{W1} = 242.935, \quad F_J = 520.304, \quad H - K_s = 0.183,$$
$$F_{W2} = 143.874, \quad F_H = 619.260, \quad W1 - W2 = 0.070,$$
$$F_{W3} = 91.390, \quad F_{Ks} = 477.421, \quad W2 - W3 = 1.343,$$
$$F_{W4} = 101.513, \quad J - K_s = 0.851, \quad W3 - W4 = 1.560.$$

TABLE B.1: S0 redshift template data of Jarrett et al. (2013).

z	J	H	K_s	W1	W2	W3	W4	J-K_s	H-K_s	W1-W2	W2-W3	W3-W4
kms^{-1}	mag	mag	mag	mag	mag	mag	mag	mag	mag	mag	mag	mag
0.000	1.000	1.000	1.000	1.000	1.000	1.000	1.000	0.000	0.000	0.000	0.000	0.000
0.003	0.977	0.984	0.977	0.976	0.975	0.979	0.984	0.008	0.000	0.000	-0.004	-0.006
0.005	0.983	0.986	0.976	0.977	0.973	0.980	0.990	0.011	0.008	0.005	-0.008	-0.011
0.007	0.973	0.979	0.965	0.967	0.961	0.971	0.985	0.015	0.008	0.007	-0.012	-0.016
0.009	0.975	0.980	0.961	0.964	0.957	0.970	0.988	0.021	0.015	0.009	-0.015	-0.020
0.011	0.968	0.974	0.954	0.957	0.947	0.963	0.986	0.023	0.016	0.011	-0.018	-0.025
0.013	0.966	0.971	0.948	0.951	0.939	0.958	0.985	0.026	0.020	0.013	-0.022	-0.030
0.015	0.962	0.970	0.944	0.945	0.932	0.954	0.985	0.030	0.021	0.016	-0.025	-0.034
0.017	0.961	0.968	0.940	0.941	0.926	0.950	0.985	0.032	0.024	0.018	-0.028	-0.040
0.019	0.956	0.964	0.934	0.935	0.917	0.944	0.983	0.035	0.026	0.020	-0.031	-0.044
0.021	0.953	0.962	0.929	0.929	0.910	0.939	0.981	0.038	0.027	0.023	-0.035	-0.048
0.023	0.951	0.960	0.924	0.924	0.903	0.935	0.981	0.041	0.031	0.026	-0.038	-0.052
0.025	0.948	0.958	0.920	0.920	0.896	0.931	0.980	0.044	0.032	0.028	-0.041	-0.056
0.027	0.945	0.956	0.915	0.914	0.889	0.926	0.978	0.048	0.036	0.031	-0.044	-0.059
0.029	0.943	0.955	0.911	0.910	0.883	0.922	0.978	0.051	0.038	0.033	-0.046	-0.064
0.031	0.942	0.952	0.907	0.906	0.876	0.918	0.976	0.054	0.041	0.036	-0.051	-0.067
0.033	0.937	0.950	0.901	0.899	0.868	0.912	0.974	0.058	0.042	0.038	-0.053	-0.072
0.035	0.936	0.950	0.897	0.895	0.862	0.909	0.973	0.062	0.046	0.041	-0.058	-0.074
0.037	0.932	0.947	0.893	0.890	0.856	0.904	0.972	0.064	0.047	0.043	-0.059	-0.079
0.039	0.930	0.947	0.888	0.885	0.849	0.900	0.970	0.070	0.050	0.045	-0.064	-0.081
0.041	0.926	0.944	0.883	0.880	0.842	0.895	0.968	0.072	0.052	0.048	-0.067	-0.085
0.043	0.924	0.943	0.879	0.875	0.836	0.892	0.967	0.076	0.054	0.050	-0.070	-0.088
0.045	0.921	0.941	0.874	0.870	0.829	0.887	0.966	0.081	0.057	0.053	-0.073	-0.093
0.047	0.918	0.939	0.870	0.866	0.823	0.884	0.965	0.083	0.058	0.056	-0.078	-0.095
0.049	0.916	0.938	0.866	0.862	0.816	0.880	0.964	0.087	0.060	0.058	-0.081	-0.099
0.051	0.912	0.936	0.862	0.857	0.810	0.875	0.962	0.090	0.062	0.060	-0.084	-0.102
0.053	0.909	0.935	0.857	0.852	0.804	0.872	0.960	0.094	0.064	0.064	-0.088	-0.105
0.055	0.906	0.934	0.853	0.848	0.798	0.867	0.959	0.098	0.066	0.066	-0.091	-0.109
0.057	0.904	0.933	0.848	0.843	0.792	0.864	0.958	0.103	0.069	0.068	-0.095	-0.112
0.059	0.901	0.932	0.845	0.839	0.786	0.861	0.957	0.107	0.070	0.071	-0.099	-0.114
0.061	0.899	0.931	0.840	0.835	0.780	0.857	0.955	0.112	0.073	0.074	-0.102	-0.118
0.063	0.895	0.929	0.836	0.830	0.774	0.853	0.954	0.114	0.074	0.077	-0.107	-0.121
0.065	0.894	0.928	0.832	0.826	0.768	0.850	0.952	0.119	0.078	0.079	-0.110	-0.124
0.067	0.890	0.926	0.828	0.822	0.762	0.846	0.950	0.122	0.079	0.082	-0.113	-0.127
0.069	0.888	0.926	0.824	0.818	0.756	0.842	0.949	0.127	0.081	0.085	-0.116	-0.130
0.071	0.885	0.924	0.820	0.814	0.751	0.838	0.947	0.131	0.083	0.087	-0.119	-0.134
0.073	0.882	0.923	0.816	0.809	0.745	0.834	0.946	0.134	0.085	0.090	-0.123	-0.137
0.075	0.879	0.923	0.812	0.805	0.739	0.830	0.944	0.139	0.086	0.093	-0.126	-0.139
0.077	0.877	0.921	0.807	0.801	0.734	0.826	0.941	0.143	0.090	0.095	-0.129	-0.142
0.079	0.875	0.920	0.804	0.798	0.729	0.823	0.939	0.147	0.092	0.099	-0.132	-0.144
0.081	0.872	0.919	0.800	0.793	0.723	0.819	0.937	0.150	0.094	0.101	-0.135	-0.146
0.083	0.869	0.918	0.796	0.789	0.718	0.815	0.935	0.155	0.096	0.104	-0.138	-0.149
0.085	0.867	0.916	0.792	0.785	0.713	0.811	0.932	0.159	0.099	0.106	-0.140	-0.152
0.087	0.865	0.914	0.788	0.782	0.707	0.807	0.931	0.162	0.101	0.109	-0.143	-0.155
0.089	0.862	0.914	0.784	0.778	0.702	0.804	0.928	0.166	0.103	0.112	-0.147	-0.156
0.091	0.860	0.912	0.780	0.775	0.697	0.799	0.925	0.170	0.106	0.115	-0.148	-0.160
0.093	0.858	0.912	0.776	0.771	0.692	0.796	0.924	0.176	0.109	0.118	-0.152	-0.162
0.095	0.856	0.909	0.772	0.767	0.687	0.791	0.921	0.178	0.112	0.120	-0.154	-0.165
0.097	0.853	0.909	0.768	0.763	0.682	0.787	0.919	0.183	0.115	0.123	-0.156	-0.168
0.099	0.852	0.907	0.764	0.760	0.677	0.783	0.917	0.187	0.118	0.126	-0.158	-0.171
0.102	0.848	0.905	0.758	0.754	0.669	0.777	0.912	0.192	0.121	0.130	-0.162	-0.174
0.106	0.844	0.901	0.750	0.747	0.659	0.769	0.908	0.200	0.129	0.136	-0.167	-0.180
0.110	0.840	0.899	0.741	0.740	0.649	0.761	0.902	0.210	0.135	0.142	-0.173	-0.184
0.115	0.834	0.895	0.732	0.732	0.639	0.753	0.895	0.218	0.141	0.148	-0.179	-0.188
0.120	0.829	0.891	0.724	0.724	0.628	0.745	0.887	0.226	0.148	0.155	-0.186	-0.189
0.124	0.824	0.887	0.714	0.716	0.617	0.736	0.879	0.236	0.155	0.162	-0.193	-0.193
0.129	0.818	0.884	0.704	0.707	0.606	0.727	0.870	0.247	0.164	0.168	-0.197	-0.195
0.135	0.813	0.878	0.694	0.699	0.595	0.717	0.859	0.256	0.173	0.175	-0.203	-0.195
0.140	0.808	0.874	0.683	0.691	0.584	0.708	0.847	0.268	0.182	0.183	-0.209	-0.195
0.146	0.802	0.869	0.671	0.681	0.572	0.698	0.831	0.280	0.193	0.190	-0.216	-0.189
0.152	0.797	0.864	0.660	0.672	0.560	0.688	0.814	0.293	0.205	0.197	-0.222	-0.183
0.158	0.791	0.859	0.648	0.662	0.549	0.678	0.796	0.306	0.217	0.203	-0.229	-0.174
0.164	0.786	0.854	0.636	0.652	0.537	0.668	0.776	0.320	0.230	0.211	-0.238	-0.162

z	J	H	K_s	W1	W2	W3	W4	J-K_s	H-K_s	W1-W2	W2-W3	W3-W4
kms^{-1}	mag	mag	mag	mag	mag	mag	mag	mag	mag	mag	mag	mag
0.171	0.782	0.847	0.623	0.641	0.525	0.657	0.755	0.334	0.246	0.217	-0.244	-0.150
0.178	0.776	0.841	0.611	0.630	0.514	0.648	0.735	0.347	0.260	0.222	-0.252	-0.136
0.185	0.770	0.834	0.598	0.619	0.501	0.638	0.715	0.361	0.274	0.229	-0.262	-0.124
0.192	0.766	0.827	0.585	0.608	0.490	0.630	0.699	0.375	0.292	0.234	-0.273	-0.114
0.200	0.759	0.819	0.572	0.595	0.479	0.620	0.682	0.389	0.306	0.236	-0.281	-0.102
0.208	0.754	0.810	0.560	0.582	0.467	0.612	0.665	0.401	0.323	0.239	-0.293	-0.089
0.216	0.748	0.800	0.548	0.569	0.455	0.603	0.650	0.412	0.339	0.243	-0.305	-0.082
0.225	0.743	0.792	0.535	0.555	0.444	0.591	0.637	0.425	0.355	0.241	-0.310	-0.080
0.234	0.738	0.782	0.523	0.541	0.433	0.583	0.626	0.436	0.373	0.241	-0.322	-0.078
0.244	0.733	0.771	0.512	0.527	0.421	0.572	0.616	0.445	0.389	0.243	-0.331	-0.080
0.254	0.728	0.761	0.502	0.512	0.411	0.561	0.609	0.453	0.404	0.238	-0.336	-0.090
0.264	0.724	0.750	0.490	0.498	0.400	0.553	0.599	0.463	0.424	0.238	-0.351	-0.088
0.275	0.719	0.740	0.481	0.482	0.389	0.544	0.593	0.468	0.437	0.233	-0.365	-0.093
0.286	0.714	0.730	0.471	0.467	0.379	0.535	0.587	0.475	0.452	0.227	-0.376	-0.099
0.297	0.712	0.719	0.462	0.452	0.368	0.526	0.580	0.480	0.469	0.224	-0.388	-0.106
0.309	0.711	0.708	0.454	0.436	0.357	0.519	0.577	0.482	0.486	0.216	-0.405	-0.114
0.322	0.710	0.698	0.447	0.421	0.347	0.516	0.578	0.483	0.502	0.209	-0.430	-0.124
0.335	0.710	0.687	0.441	0.406	0.337	0.506	0.579	0.480	0.516	0.202	-0.442	-0.146
0.348	0.705	0.676	0.437	0.389	0.327	0.500	0.580	0.474	0.520	0.188	-0.461	-0.160
0.362	0.702	0.665	0.433	0.375	0.317	0.492	0.579	0.467	0.525	0.182	-0.475	-0.177
0.377	0.703	0.655	0.430	0.359	0.308	0.486	0.590	0.458	0.535	0.168	-0.497	-0.211
0.392	0.701	0.644	0.426	0.345	0.299	0.478	0.593	0.448	0.541	0.153	-0.508	-0.235
0.408	0.701	0.633	0.423	0.329	0.289	0.465	0.592	0.436	0.548	0.141	-0.517	-0.261
0.424	0.700	0.621	0.421	0.313	0.280	0.456	0.586	0.423	0.552	0.122	-0.528	-0.273
0.442	0.699	0.610	0.418	0.298	0.271	0.448	0.596	0.411	0.560	0.104	-0.547	-0.308
0.459	0.697	0.598	0.413	0.284	0.261	0.444	0.601	0.403	0.569	0.091	-0.577	-0.328
0.478	0.695	0.586	0.408	0.268	0.253	0.435	0.598	0.395	0.579	0.066	-0.590	-0.346
0.497	0.693	0.575	0.403	0.253	0.243	0.420	0.601	0.385	0.588	0.042	-0.591	-0.390
0.517	0.695	0.563	0.398	0.239	0.235	0.406	0.593	0.377	0.605	0.016	-0.593	-0.411
0.538	0.694	0.553	0.392	0.226	0.226	0.395	0.589	0.375	0.621	-0.004	-0.603	-0.435
0.560	0.697	0.544	0.383	0.213	0.219	0.385	0.535	0.380	0.649	-0.026	-0.615	-0.356
0.583	0.694	0.535	0.374	0.202	0.212	0.368	0.501	0.388	0.669	-0.051	-0.600	-0.335
0.606	0.691	0.526	0.365	0.192	0.204	0.353	0.470	0.396	0.692	-0.067	-0.595	-0.312
0.631	0.688	0.519	0.355	0.181	0.197	0.329	0.441	0.412	0.718	-0.091	-0.557	-0.318
0.656	0.685	0.511	0.345	0.172	0.189	0.317	0.414	0.426	0.744	-0.099	-0.560	-0.292
0.683	0.684	0.505	0.337	0.165	0.180	0.306	0.390	0.440	0.770	-0.095	-0.577	-0.264
0.710	0.683	0.500	0.328	0.157	0.171	0.286	0.367	0.459	0.796	-0.091	-0.559	-0.269
0.739	0.680	0.498	0.319	0.150	0.161	0.268	0.320	0.483	0.822	-0.079	-0.553	-0.192
0.769	0.674	0.496	0.311	0.143	0.150	0.261	0.280	0.508	0.840	-0.051	-0.602	-0.075
0.800	0.673	0.500	0.303	0.137	0.140	0.246	0.263	0.544	0.867	-0.021	-0.613	-0.073
0.832	0.670	0.497	0.295	0.130	0.128	0.232	0.247	0.566	0.891	0.017	-0.641	-0.071
0.866	0.668	0.494	0.287	0.123	0.120	0.219	0.243	0.591	0.918	0.033	-0.654	-0.114
0.901	0.660	0.493	0.279	0.118	0.110	0.207	0.229	0.619	0.935	0.077	-0.684	-0.114
0.937	0.657	0.494	0.270	0.112	0.101	0.196	0.228	0.654	0.963	0.112	-0.716	-0.165
0.975	0.648	0.496	0.262	0.108	0.093	0.185	0.228	0.694	0.984	0.162	-0.751	-0.223
1.014	0.648	0.494	0.255	0.103	0.085	0.176	0.245	0.718	1.013	0.203	-0.787	-0.356
1.055	0.642	0.490	0.248	0.099	0.079	0.168	0.253	0.739	1.034	0.248	-0.826	-0.446
1.098	0.645	0.486	0.242	0.095	0.072	0.161	0.247	0.757	1.065	0.296	-0.867	-0.467
1.142	0.651	0.485	0.237	0.092	0.068	0.154	0.264	0.777	1.097	0.330	-0.894	-0.587
1.189	0.658	0.487	0.233	0.089	0.062	0.139	0.263	0.801	1.129	0.386	-0.877	-0.690
1.237	0.668	0.485	0.230	0.086	0.057	0.134	0.265	0.811	1.158	0.447	-0.924	-0.739
1.287	0.675	0.481	0.228	0.085	0.054	0.121	0.270	0.811	1.180	0.495	-0.887	-0.867
1.339	0.682	0.477	0.227	0.084	0.050	0.117	0.244	0.806	1.194	0.549	-0.918	-0.797
1.393	0.698	0.478	0.227	0.081	0.046	0.106	0.221	0.806	1.217	0.610	-0.898	-0.797
1.449	0.709	0.475	0.227	0.078	0.044	0.096	0.200	0.804	1.238	0.633	-0.857	-0.797
1.507	0.723	0.469	0.226	0.076	0.040	0.093	0.182	0.791	1.261	0.681	-0.911	-0.722
1.568	0.750	0.462	0.228	0.073	0.038	0.085	0.165	0.767	1.294	0.711	-0.867	-0.722
1.632	0.774	0.455	0.228	0.071	0.036	0.077	0.133	0.749	1.327	0.744	-0.822	-0.594
1.698	0.804	0.452	0.224	0.068	0.033	0.070	0.120	0.762	1.386	0.776	-0.799	-0.594
1.766	0.838	0.450	0.222	0.065	0.032	0.068	0.123	0.768	1.443	0.787	-0.831	-0.641
1.837	0.913	0.453	0.223	0.063	0.031	0.062	0.111	0.770	1.531	0.772	-0.754	-0.641
1.912	1.010	0.456	0.222	0.060	0.029	0.056	0.101	0.781	1.644	0.784	-0.700	-0.641
1.989	1.105	0.471	0.220	0.058	0.028	0.051	0.105	0.828	1.754	0.796	-0.643	-0.786
2.069	1.263	0.489	0.220	0.057	0.028	0.046	0.095	0.865	1.896	0.780	-0.551	-0.786
2.153	1.475	0.498	0.220	0.054	0.027	0.042	0.101	0.886	2.064	0.753	-0.485	-0.954
2.240	1.654	0.507	0.217	0.053	0.026	0.041	0.091	0.922	2.206	0.767	-0.502	-0.867
2.330	1.824	0.515	0.213	0.052	0.025	0.035	0.083	0.959	2.332	0.782	-0.340	-0.954
2.425	2.109	0.531	0.211	0.049	0.024	0.031	0.091	1.003	2.501	0.791	-0.301	-1.151

Bibliography

Aaronson, M., Huchra, J., & Mould, J. 1979, ApJ, 229, 1

Aaronson, M., Huchra, J., Mould, J., Schechter, P. L., & Tully, R. B. 1982, ApJ, 258, 64

Aaronson, M., Huchra, J., Mould, J. R., et al. 1982, ApJS, 50, 241

Arnaud, M. 2005, Background Microwave Radiation and Intracluster Cosmology, 77

Balkowski, C., Bottinelli, L., Chamaraux, P., Gouguenheim, L., & Heidmann, J. 1974, A&A, 34, 43

Bertschinger, E., & Dekel, A. 1989, ApJ, 336, L5

Bistolas, V., & Hoffman, Y. 1998, ApJ, 492, 439

Binney, J. & Merrifield, M. 1998, Galactic Astronomy: Princeton University Press, 1998. (Princeton series in astrophysics) QB857 .B522 1998, ed. J. Binney, & M. Merrifield

Böhringer, H., Schuecker, P., Komossa, S., et al. 2000, ASPC, Vol. 218, Mapping the Hidden Universe: The Universe behind the Mily Way - The Universe in HI, ed. by R. C. Kraan-Korteweg, P. A. Henning & H. Andernach, 93

Bohlin, R. C., Savage, B. D., & Drake, J. F. 1978, ApJ, 224, 132

Bothun, G. D., & Mould, J. R. 1987, ApJ, 313, 629

Branchini, E., Plionis, M., & Sciama, D. W. 1996, ApJ, 461, L17

Burke, D. L., Axelrod, T., Blondin, S., Claver, C. 2010, AJ, 720, 811

Burstein, D., & Raychaudhury, S. 1989, ApJ, 343, 18

Cardelli, J. A., Clayton, G. C., & Mathis, J. S. 1989, ApJ, 345, 245

Caon, N., Capaccioli, M., & D'Onofrio, M. 1993, MNRAS, 265, 1013

Cameron, L. M. 1990, A&A, 233, 16

Ciotti, L. 1991, A&A, 249, 99

Colless, M., Dalton, G., Maddox, S., et al. 2001, MNRAS, 328, 1039

Colless, M., Peterson, B. A., Jackson, C., et al. 2003, arXiv, arXiv:astro-ph/0306581

Courteau, S., Dutton, A. A., van den Bosch, F. C., et al. 2007, ApJ, 671, 203

Courteau, S., Willick, J. A., Strauss, M. A., Schlegel, D., & Postman, M. 2000, ASPC, Vol. 201, Cosmic Flows Workshop, ed. by S. Courteau & J. Willick, 17

Cutri, R. M., Strutskie, M. F., van Dyk, S., et al. 2003, "The IRSA 2MASS All-Sky Point Source Catalog, NASA/IPAC Infrared Science Archive. http://irsa.ipac.caltech.edu/applications/Gator/"

Davis, M., Efstathiou, G., Frenk, C. S., & White, S. D. M. 1985, ApJ, 292, 371

Davis, M., & Geller, M. J. 1976, ApJ, 208, 13

Dekel, A., Eldar, A., Kolatt, T., et al. 1999, ApJ, 522, 1

Dekel, A., & Lahav, O. 1999, ApJ, 520, 24

de Vaucouleurs, G. 1982, Nature, 299, 303

de Vaucouleurs, G., de Vaucouleurs, A., & Buta, R. 1981, AJ, 86, 1429

de Vaucouleurs, G. 1972, IAUS, External Galaxies and Quasi-Stellar Objects, Symposium no 44, ed. by D. S. Evans, D. Wills & B. J. Wills, 353

Diplas, A., & Savage, B. D. 1994, ApJ, 427, 274

Donley, J. L., Staveley-Smith, L., Kraan-Korteweg, R. C., et al. 2005, AJ, 129, 220

Doyle, M. T., Drinkwater, M. J., Rohde, D. J., et al. 2005, MNRAS, 361, 34

Dressler, A., & Sandage, A. 1983, ApJ, 265, 664

Dressler, A. 1980, ApJ, 236, 351

Ellis, G. F. R. 1975, QJRAS, 16, 245

Enßlin, T. A., Frommert, M., & Kitaura, F. S. 2009, Phys. Rev. D, 80, 105005

Epchtein, N., de Batz, B., Capoani, L., et al. 1997, The Messenger, 87, 27

Ewen, H. I., & Purcell, E. M. 1951, Nature, 168, 356

Faber, S. M., & Burstein, D. 1988, Large-Scale Motions in the Universe: A Vatican study Week, 115

Fabian, A. C. 1994, ASPC, Vol. 67, Unveiling Large-Scale Structures Behind the Milky Way, ed. by C. Balkowski & R. C. Kraan-Korteweg, 73

Fairall, A. P., & Kraan-Korteweg, R. C. 2000, ASPC, Vol.218, Mapping the Hidden Universe: The Universe behind the Milky Way - The Universe in HI, ed. by R. C. Kraan-Korteweg, P. A. Henning & H. Andernach, 35

Feldman, H. A., Watkins, R., & Hudson, M. J. 2010, MNRAS, 407, 2328

Fisher, K. B., Lahav, O., Hoffman, Y., Lynden-Bell, D., & Zaroubi, S. 1995, MNRAS, 272, 885

Fisher, J. R., & Tully, R. B. 1981, ApJS, 47, 139

Fixsen, D. J., Cheng, E. S., Gales, J. M., et al. 1996, ApJ, 473, 576

Flaherty, K. M., Pipher, J. L., Megeath, S. T., et al. 2007, ApJ, 663, 1069

Frei, Z., & Gunn, J. E. 1994, AJ, 108, 1476

Giovanelli, R., Haynes, M. P., da Costa, L. N., et al. 1997, ApJ, 477, L1

Giovanelli, R., Haynes, M. P., Freudling, W., et al. 1998, ApJ, 505, L91

Giovanelli, R., Dale, D. A., Haynes, M. P., Hardy, E., & Campusano, L. E. 1999, ApJ, 525, 25

Geller, M. J., & Huchra, J. P. 1983, ApJS, 52, 61

Geller M. J., & Huchra, J. P. 1989, Science, 246, 897

Glass, I. S., & Nagata, T. 2000, Monthly Notes of the Astronomical Society of South Africa, 59, 110

Gordon, K. D., Clayton, G. C., Misselt, K. A., Landolt, A. U., & Wolff, M. J. 2003, ApJ, 594, 279

Gudehus, D. H. 2000, ASPC, Vol. 201, Cosmic Flows Workshop, ed. by S. Courteau, J. Willick, 286

Hart, L., & Davies, R. D. 1982, Nature, 297, 191

Hauschildt, M. 1987, A&A, 184, 43

Haynes, M. P., van Zee, L., Hogg, D. E., Roberts, M. S., & Maddalena, R. J. 1998, AJ, 115, 62

He, L., Whittet, D. C. B., Kilkenny, D., & Spencer Jones, J. H. 1995, ApJS, 101, 335

Henning, P. A., Kraan-Korteweg, R. C., Rivers, A. J., Loan, A. J., Lahav, O. & Burton, W. B., 1998, AJ, 115, 584

Henning, P. A., Staveley-Smith, L., Ekers, R. D., et al. 2000, AJ, 119, 2686

Hoffman, Y. 1994, ASPC, Vol. 67, Unveiling Large-Scale Structures Behind the Milky Way, ed. by C. Balkowski & R. C. Kraan-Korteweg, 185

Hoffman, G. L., Salpeter, E. E., Lamphier, C., & Roos, T. 1992, ApJ, 388, L5

Hoffman, Y., & Zaroubi, S. 2000, ApJ, 535, L5

Holmberg, E. 1958, Meddelanden fran Lunds Astronomiska Observatorium Serie II, 136, 1

Horvath, I., Hakkila, J., & Bagoly, Z. 2013, arXiv, arXiv:1311.1104

Huang, J.-S., Ashby, M. L. N., Barmby, P., et al. 2007, ApJ, 664, 840

Hubble, E. P. 1936, Realm of the Nebulae, by E.P. Hubble. New Haven: Yale University Press, 1936. ISBN 9780300025002

Hudson, M. J., Smith, R. J., Lucey, J. R., & Branchini, E. 2004, MNRAS, 352, 61

Jacoby, G. H., Branch, D., Ciardullo, R., et al. 1992, PASP, 104, 599

Jarrett, T. H., Chester, T., Cutri, R., et al. 2000a, AJ, 119, 2498

Jarrett, T.-H., Chester, T., Cutri, R., et al. 2000b, AJ, 120, 298

Jarrett, T. H., Chester, T., Cutri, R., Schneider, S. E., & Huchra, J. P. 2003, AJ, 125, 525

Jarrett, T. H., Cohen, M., Masci, F., et al. 2011, ApJ, 735, 112

Jarrett, T. H., Masci, F., Tsai, C. W., et al. 2013, AJ, 145, 6

Jerjen, H., & Tammann, G. A. 1993, A&A, 276, 1

Johnston, M. D., Bradt, H. V., Doxsey, R. E., et al. 1981, ApJ, 245, 799

Juraszek, S. J., Staveley-Smith, L., Kraan-Korteweg, R. C., et al. 2000, AJ, 119, 1627

Jurić, M., Ivezić, Ž., Brooks, A., et al. 2008, ApJ, 673, 864

Kalberla, P. M. W., Burton, W. B., Hartmann, D., et al. 2005, A&A, 440, 775

Kaiser, N. 1984, ApJ, 284, L9

Kannappan, S. J., Fabricant, D. G., & Franx, M. 2002, AJ, 123, 2358

Kauffmann, G., Nusser, A., & Steinmetz, M. 1997, MNRAS, 286, 795

Kennicutt, R. C., Jr., Armus, L., Bendo, G., et al. 2003, PASP, 115, 928

Kocevski, D. D. & Ebeling, H. 2006, ApJ, 645, 1043

Kogut, A., Lineweaver, C., Smoot, G. F., et al. 1993, ApJ, 419, 1

Kolatt, T., Dekel A., Lahav O. 1995, MNRAS, 275, 797

Kolatt, T., & Dekel, A. 1995, arXiv, arXiv:astro-ph/9512132

Komberg, B. V., Kravtsov, A. V., & Lukash, V. N. 1996, arXiv, arXiv:astro-ph/9602090

Koribalski, B. S., Staveley-Smith, L., Kilborn, V. A., Ryder, S. D., Kraan-Korteweg, R. C., Ryan-Weber, E. V., Ekers, R. D., Jerjen, H., et al. 2004, AJ, 128, 16

Kraan-Korteweg, R. C. 2000a, Guanajuato Lectures on Astrophysics, Vol. 556, From the Sun to the Great Attractor, ed. by D. Pageand, J. G. Hirsch, 301

Kraan-Korteweg, R. C. 2000b, A&AS, 141, 123

Kraan-Korteweg, R. C., & Jarrett, T. 2005, ASPC, Vol. 329, Nearby Large-Scale Structures and the Zone of Avoidance, ed. by K. P. Fairall and P. A. Woudt, 119

Kraan-Korteweg, R. C., & Juraszek, S. 2000, PASA, 17, 6

Kraan-Korteweg, R. C., & Lahav, O. 2000, A&A Rev., 10, 211

Kraan-Korteweg, R. C., Loan, A. J., Burton, W. B., et al. 1994, Nature, 372, 77

Kraan-Korteweg, R. C., Woudt, P. A., Cayatte, V., et al. 1996, Nature, 379, 519

Lagattuta, D. J., Mould, J. R., Staveley-Smith, L., et al. 2013, ApJ, 771, 88

Lahav, O., Brosch, N., Goldberg, E., et al. 1998, MNRAS, 299, 24

Lahav, O., Fisher, K. B., Hoffman, Y., Scharf, C. A., & Zaroubi, S. 1994, ApJ, 423, L93

Lahav, O., Yamada, T., Scharf, C., & Kraan-Korteweg, R. C. 1993, MNRAS, 262, 711

Lavaux, G., Tully, R. B., Mohayaee, R., & Colombi, S. 2010, ApJ, 709, 483

Lercher, G., Kerber, F., & Weinberger, R. 1996, A&AS, 117, 369

Lindner, U., Einasto, J., Einasto, M., et al. 1995, A&A, 301, 329

Lucey, J., Radburn-Smith, D., & Hudson, M. 2005, ASPC, Vol. 329, Nearby Large-Scale Structures and the Zone of Avoidance, ed. A.P. Fairall & P. A. Woudt, 21

Lynden-Bell, D., Faber, S. M., Burstein, D., et al. 1988, ApJ, 326, 19

Mamon, G. A. 1994, ASPC, Vol. 67, Unveiling Large-Scale Structures Behind the Milky Way, ed. by C. Balkowski & R. C. Kraan-Korteweg, 53

Mathewson, D. S., & Ford, V. L. 1994, ApJ, 434, L39

Mathewson, D. S., Ford, V. L., & Buchhorn, M. 1992, ApJ, 389, L5

Matthews, L. D., van Driel, W., & Gallagher, J. S., III 1998, AJ, 116, 1169

Masters, K. L. 2008, ASPC, Vol. 395, Frontiers of Astrophysics: A Celebration of NRAO's 50th Anniversary, ed. by A. H. Bridle, J. J. Condon, & G. C. Hunt, 137

Masters, K. L., Giovanelli, R., & Haynes, M. P. 2003, AJ, 126, 158

Masters, K. L., Springob, C. M., Haynes, M. P., & Giovanelli, R. 2006, ApJ, 653, 861

Masters, K. L., Springob, C. M., & Huchra, J. P. 2008, AJ, 135, 1738

Meyer, M. J., Zwaan, M. A., Webster, R. L., et al. 2004, MNRAS, 350, 1195

Mould, J. R., Huchra, J. P., Freedman, W. L., et al. 2000a, ApJ, 529, 786

Mould, J. R., Huchra, J. P., Freedman, W. L., et al. 2000b, ApJ, 545, 547

Mould, J. R., Hughes, S. M. G., Stetson, P. B., et al. 2000c, ApJ, 528, 655

Nagayama, T. Woudt, P. A., Nagashima, C., Nakajima, Y., Kato, D., Kurita, M., Nagata, T., Nakaya, H., Tamura, M., Sugitani, K., Wakamatsu, K., & Sato, S. 2004, MNRAS, 354, 980

Neill, J. D., Seibert M., et al. 2014, ApJ, 792, 129

Newman, P. R., Long, D. C., Snedden, S. A., et al. 2004, SPIE, 5492, 533

Nusser, A., & Davis, M. 1995, MNRAS, 276, 1391

Oke, J. B., & Gunn, J. E. 1983, ApJ, 266, 713

Oke, J. B. 1974, ApJS, 27, 21

Peebles, P. J. E. 1976, Ap&SS, 45, 3

Pierce, M. 2006, EAA, DOI:10.1888/0333750888/2622 edited by Murdin, P.

Pomarède, D., Courtois, H., & Tully, R. B. 2013, IAU Symposium, 289, 323

Poggianti, B. M. 1997, A&AS, 122, 399

Proctor, R. 1878, The Universe of Stars (London: Longman, Green and Co.), 41

Radburn-Smith, D. J., Lucey, J. R., Woudt, P. A., Kraan-Korteweg, R. C., & Watson, F. G. 2006, MNRAS, 369, 1131

Riad, I. F., Kraan-Korteweg, R. C. & Woudt, P. A. 2010, MNRAS, 401, 924-932

Roberts, M. S. 1969, AJ, 74, 859

Roberts, M. S. 1978, AJ, 83, 1026

Robin, A., & Creze, M. 1986, A&A, 157, 71

Robin, A. C., Marshall, D. J., Schultheis, M., & Reylé, C. 2012, A&A, 538, A106

Rogstad, D. H., & Shostak, G. S. 1972, ApJ, 176, 315

Said, K. 2013, Master's thesis, University of Cape Town

Sandage, A. 1996, AJ, 111, 18

Sandage, A. 1999, AJ, 117, 157

Sandage, A. 1999, ApJ, 527, 479

Sandage, A. 1973, ApJ, 183, 711

Saurer, W., Seeberger, R., & Weinberger, R. 1997, A&AS, 126, 247

Savage, B. D., Massa, D., Meade, M., & Wesselius, P. R. 1985, ApJS, 59, 397

Scharf, C., Hoffman, Y., Lahav, O., & Lynden-Bell, D. 1992, MNRAS, 256, 229

Schechter, P. L. 1980, AJ, 85, 801

Schlafly, E. F., & Finkbeiner, D. P. 2011, ApJ, 737, 103

Schlegel, D. J., Finkbeiner, D. P., & Davis, M. 1998, ApJ, 500, 525

Schneider, D. P., Richards, G. T., Fan, X., et al. 2002, AJ, 123, 567

Schröder, A., Kraan-Korteweg, R. C., & Mamon, G. A. 2000, ASPC, Vol. 218, Mapping the Hidden Universe: The Universe behind the Milky Way - The Universe in HI, ed. by R. C. Kraan-Korteweg, P. A. Henning & H. Andernach, 119

Schröder, A. C., Mamon, G. A., Kraan-Korteweg, R. C., & Woudt, P. A. 2007, A&A, 466, 481-499

Schultz, G. V., & Wiemer, W. 1975, A&A, 43, 133

Seeberger, R., Saurer, W., & Weinberger, R. 1996, A&AS, 117, 1

Sérsic, J. L. 1963, Boletin de la Asociacion Argentina de Astronomia La Plata Argentina, 6, 41

Sérsic, J. L. 1968, Cordoba, Argentina: Observatorio Astronomico, 1968

Shapley, H. 1961, Cambridge, Harvard University Press, 159, 1961. Rev. ed.,

Shaya, E. J. 1984, ApJ, 280, 470

Shostak, G. S. 1975, ApJ, 198, 527

Skrutskie, M. F., Cutri, R. M., Stiening, R., et al. 2006, AJ, 131, 1163

Sneden, C., Gehrz, R. D., Hackwell, J. A., York, D. G., & Snow, T. P. 1978, ApJ, 223, 168

Sorce, J. G., Courtois, H. M., Tully, R. B., et al. 2013, ApJ, 765, 94

Sorce, J. G., Tully, R. B., & Courtois, H. M. 2012, ApJ, 758, L12

Springob, C. M., Haynes, M. P., Giovanelli, R., & Kent, B. R. 2005, ApJS, 160, 149

Staveley-Smith, L. 1997, PASA, 14, 111

Staveley-Smith, L., Juraszek, S., Koribalski, B, S., Ekers, R, D., Haynes, R. F., Henning, P, A., Kesteven, M. J., et al. 1998, AJ, 116, 2717

Staveley-Smith, L., Wilson, W. E., Bird, T. S., et al. 1996, PASA, 13, 243

Stecher, T. P. 1965, ApJ, 142, 1683

Stecher, T. P. 1969, ApJ, 157, L125

Takata, T., Yamada, T., & Saito, M. 1996, ApJ, 457, 693

Teerikorpi, P. 1984, A&A, 141, 407

Tegmark, M., & Bromley, B. C. 1999, ApJ, 518, L69

Tonry, J. L., Blakeslee, J. P., Ajhar, E. A., & Dressler, A. 2000, ApJ, 530, 625

Tonry, L. J., Dressler, A., Blakeslee, P. J., Ajhar, A. E., Fletcher, B. A., Luppino, A. G., Metzger, R. M., Moore, B. C.. 2001, ApJ, 546, 681

Trumpler, R. J. 1930, Lick Observatory Bulletin, 14, 154

Tully, R. B., & Fisher, J. R. 1977, A&A, 54, 661

Tully, R. B., & Fouque, P. 1985, ApJS, 58, 67

Tully, R. B., & Pierce, M. J. 2000, ApJ, 533, 744

Tully, R. B., Shaya, E. J., Karachentsev, I. D., et al. 2008, ApJ, 676, 184

van Dokkum, P. G., Peletier, R. F., de Grijs, R., & Balcells, M. 1994, A&A, 286, 415

Webster, A. 1982, MNRAS, 199, 683

Webster, M., Lahav, O., & Fisher, K. 1997, MNRAS, 287, 425

Werner, M. W., Roellig, T. L., Low, F. J., et al. 2004, ApJS, 154, 1

Weinberger, R., Saurer, W., & Seeberger, R. 1995, A&AS, 110, 269

Williams, W. L. 2011, Master's thesis, University of Cape Town

Willick, J. A. 1990, ApJ, 351, L5

Willick, J. A. 1994, ApJS, 92, 1

Willick, J. A., Courteau, S., Faber, S. M., et al. 1997, ApJS, 109, 333

Whittet, D. C. B. 1988, Dust in the Universe, 25

Woudt, P. A., Fairall, A., Kraan-Korteweg, R. C., et al. 2005, ASPC, Vol. 329, Nearby Large-Scale Structures and the Zone of Avoidance, ed. by K. P. Fairall & P. A. Woudt, 147

Wright, E. L., Eisenhardt, P. R. M., Mainzer, A. K., et al. 2010, AJ, 140, 1868

Yahil, A. 1985, in European Southern Observatory Conference and Workshop Proceedings, Vol. 20, ESO Workshop on the Virgo Cluster of Galaxies, ed. O. -G. Richter & B. Binggeli, 359-373

Yahil, A., Strauss, M. A., Davis, M., & Huchra, J. P. 1991, ApJ, 372, 380

Yanny, B., & Gardner, S. 2013, ApJ, 777, 91

Zaroubi, S., Hoffman, Y., & Dekel, A. 1999, ApJ, 520, 413

Zaroubi, S., Hoffman, Y., Fisher, K. B., & Lahav, O. 1995, ApJ, 449, 446

Zwaan, M. A., Meyer, M. J., Webster, R. L., et al. 2004, MNRAS, 350, 1210